APPLIED COMPUTATIONAL ELECTROMAGNETICS SOCIETY JOURNAL

December 2016
Vol. 31 No. 12
ISSN 1054-4887

The ACES Journal is abstracted in INSPEC, in Engineering Index, DTIC, Science Citation Index Expanded, the Research Alert, and to Current Contents/Engineering, Computing & Technology.

The illustrations on the front cover have been obtained from the research groups at the Department of Electrical Engineering, The University of Mississippi.

EMERITUS EDITORIAL ASSISTANTS

DECEMBER 2016 REVIEWERS

THE APPLIED COMPUTATIONAL ELECTROMAGNETICS SOCIETY

JOURNAL

Vol. 31 No. 12 December 2016

TABLE OF CONTENTS

Reconstruction of the Antenna Far-Field Pattern through a Fast Plane-Polar Scanning

F. D'Agostino, F. Ferrara, C. Gennarelli, R. Guerriero, and M. Migliozzi

Dipartimento di Ingegneria Industriale
University of Salerno, via Giovanni Paolo II, 132 - 84084 Fisciano, Italy
fdagostino@unisa.it, flferrara@unisa.it, cgennarelli@unisa.it, rguerriero@unisa.it, mmigliozzi@unisa.it

Abstract ― This paper provides the experimental validation of a fast and accurate technique, which allows the reconstruction of the antenna radiation pattern from a minimum number of near-field measurements collected through a plane-polar scanning. This near-field to far-field (NFTFF) transformation technique relies on a nonredundant sampling representation of the voltage acquired by the probe, achieved by modeling the antenna with a double bowl, a very flexible model particularly suitable to deal with antennas having a quasi-planar geometry. The NF data required by the standard plane-rectangular NFTFF transformation are efficiently reconstructed from the nonredundant plane-polar ones by using an optimal sampling interpolation algorithm, thus making possible to get a considerable measurement time saving. The accuracy and practical efficacy of the described technique are assessed by experimental tests carried out at the Antenna Characterization Lab of the University of Salerno.

Index Terms ― Antenna measurements, nonredundant sampling representations, plane-polar near-field to far-field transformation.

I. INTRODUCTION

Since the beginning of 70s, near-field to far-field (NFTFF) transformation techniques [1-6] are a widely employed and recognized tool for the precise measurement of the FF radiation characteristics of antennas, whose sizes in terms of wavelengths do not allow the fulfillment of the Fraunhofer distance requirements in an anechoic camber. Among these techniques, the standard NFTFF with plane-rectangular scanning [7, 8] can be conveniently employed when measuring high gain antennas exhibiting pencil beam radiation patterns. For this kind of antennas, a convenient and appealing alternative to such a classical transformation is that using the plane-polar scanning [9-11]. Such a scan (see Fig. 1) is simpler than the plane-rectangular one from the mechanical point of view, since it involves a linear displacement of the probe and a rotation of the antenna under test (AUT). Other advantages are: a larger measurement zone as compared with the plane-rectangular scanning case, for a fixed extent of the anechoic chamber; a "fine chamber tuning", because the AUT always points in the same direction; a more accurate testing of gravitationally sensitive spaceborne antennas [9], since the scanning can be easily accomplished in a horizontal plane. However, in the former approach [9, 10], the antenna far-field was evaluated by employing a Jacobi-Bessel expansion, so that a large computational time was needed. Such a drawback has been surmounted in [11], by reconstructing the NF data required to perform the standard plane-rectangular NFTFF transformation from the collected plane-polar ones, through a very simple bivariate Lagrange interpolation formula. This has made possible the exploitation of the fast Fourier transform (FFT) algorithm to efficiently reconstruct the antenna far-field. Unfortunately, because of the generic nature of such an interpolation formula, very close spacings were required to minimize the interpolation error. A more effective interpolation algorithm, requiring a significantly lower number of data with respect to the previous approaches [9-11], has been developed in [12], by properly taking into account that the radiated or scattered electromagnetic (EM) fields are spatially quasi-bandlimited functions [13] and employing the optimal sampling interpolation (OSI) expansions, able to minimize the truncation error for a fixed number of nearest considered samples.

The measurement time reduction is nowadays one of the hottest issues related to the NFTFF transformation techniques, since the time required to acquire the NF data is remarkably greater than the computer time needed to perform the NFTFF transformation. To this end, the nonredundant sampling representations of EM fields [14, 15] have been usefully applied to develop NFTFF transformations with plane-rectangular [16, 17] and plane-polar scans [18, 19] using a minimum number of NF measurements. In particular, the fast and accurate sampling representation, which allows the efficient reconstruction of the near-field data required by the standard plane-rectangular NFTFF transformation from the acquired plane-polar samples, has been obtained by considering the AUT as enclosed in a "double bowl" [18]

Submitted On: March 30, 2016
Accepted On: October 7, 2016

or in an oblate ellipsoid [19]. Both these representations contain as particular case that relevant to the spherical modeling [20], but, when considering quasi-planar antennas, they allow to obtain a further reduction of the required NF data number and to locate the scanning plane at a distance less than one half of the antenna maximum dimension, thus lowering the error due to the truncation of the measurement zone. In fact, according to the nonredundant representations [14], the observation surface must be external to the surface modeling the AUT. It is worthy to note that the sample spacings required by the nonredundant approaches [18-20] are larger than those derived in [21, 22] by a rigorous sampling theorem in plane-polar coordinates.

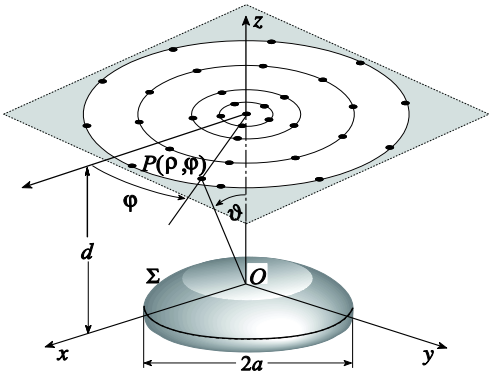

Fig. 1. Plane-polar scanning.

The aim of this paper is to experimentally validate the nonredundant NFTFF transformation with plane-polar scan, adopting a double bowl to model an antenna with a quasi-planar geometry. The experimental tests have been performed in the Antenna Characterization Lab of the University of Salerno, equipped with a plane-polar NF scanning system. It is worth noting that the experimental validation of the NFTFF transformation based on the oblate ellipsoidal modeling of the AUT has been already provided in [23].

II. NONREDUNDANT PROBE VOLTAGE REPRESENTATION ON A PLANE

Let an AUT be considered as contained in a rotational surface Σ delimiting a convex domain and the voltage be acquired by a nondirective probe on a plane at $z = d$, where (x, y, z) is a Cartesian coordinate system with the origin at the AUT centre (Fig. 1). A spherical reference system (r, ϑ, φ) is used for denoting any observation point, whereas a point P lying on the plane can be also specified by the plane-polar coordinates (ρ, φ). The nonredundant sampling representations of EM fields [14] can be applied to the probe voltage V, since the voltage acquired by a nondirective probe is characterized by the same effective spatial bandwidth of the antenna field [24]. Accordingly, it is advantageous to describe each of the curves C (radial lines and rings), representing the plane in a plane-polar frame, in terms of an optimal parameter ξ and to define the "reduced voltage":

$$\tilde{V}(\xi) = V(\xi)\mathrm{e}^{\mathrm{j}\gamma(\xi)}, \tag{1}$$

wherein $V(\xi)$ is the voltage acquired by the probe (V_φ) or the probe rotated by 90° around its longitudinal axis (V_ρ) and $\gamma(\xi)$ is a proper phase factor. The error resulting when approximating $\tilde{V}(\xi)$ by a bandlimited function can be effectively reduced by imposing that this function has a properly increased bandwidth $\chi' W_\xi$, with W_ξ being a critical value and $\chi' > 1$ the excess bandwidth factor [14].

When considering a radial line, the bandwidth W_ξ, the parameterization ξ and the corresponding phase function γ are [14]:

$$W_\xi = \beta \ell'/2\pi, \tag{2}$$

$$\gamma = (\beta/2)\left[R_1 + R_2 + s_1' - s_2'\right], \tag{3}$$

$$\xi = (\pi/\ell')\left[R_1 - R_2 + s_1' + s_2'\right], \tag{4}$$

wherein ℓ' is the length of the intersection curve C' between the meridian plane passing through the observation point P and Σ, β is the wavenumber, $R_{1,2}$ are the distances from P to the two tangency points $P_{1,2}$ between C' and the cone having the vertex at P, and $s_{1,2}'$ their curvilinear abscissas.

When the curve C is a ring, the angle φ can be conveniently adopted as optimal parameter, whereas γ is constant. The related bandwidth W_φ is [14]:

$$W_\varphi = \frac{\beta}{2}\max_{z'}(R^+ - R^-) = \frac{\beta}{2}\max_{z'}\left(\sqrt{(\rho+\rho'(z'))^2 + (z-z')^2} - \sqrt{(\rho-\rho'(z'))^2 + (z-z')^2}\right), \tag{5}$$

where $\rho'(z')$ specifies the surface Σ and R^+, R^- are the maximum and minimum distances of C from the circumference of Σ at z'. As shown in [14], the maximum is achieved on that zone of Σ, which lies on the same side of C with respect to its maximum transverse circumference.

According to the theoretical results in [14], the surface Σ must fit very well the AUT shape in order to minimize the number of needed samples. The antennas characterized by using a planar NF scanning system have usually a quasi-planar geometry, so that an oblate ellipsoid [19, 23] or a "double bowl" [18] can be conveniently employed as AUT models to get effective sampling representations on the plane. Although these models are particularly tailored for quasi-planar antennas, they are quite general and contain the spherical modeling as particular case. The choice of which of them has to be adopted to shape a given AUT depends only on the modeling which better fits its actual geometry.

The nonredundant sampling representation using the "double bowl" modeling is detailed in the following. The double bowl is a surface consisting of two circular bowls with the same aperture radius a, but with radii h and h' of

the upper and lower arcs which may differ for a better fitting of the actual AUT geometry (Figs. 1 and 2). The bandwidth, the parameterization, and the phase function relevant to a radial line are obtained from relations (2) – (4) by taking into account that $\ell' = 2[b + b' + (h + h')\pi/2]$ and substituting in them the appropriate values of $R_{1,2}$ and $s'_{1,2}$ [18]. It is easy to verify that, for $\rho < a$, the tangency points $P_{1,2}$ are both situated on the upper bowl (Fig. 2 (a)) and it results [18]:

$$R_1 = \sqrt{d^2 - h^2 + (\rho + b)^2}\,; \qquad s'_1 = -(b + h\alpha_1)\,, \quad (6)$$

$$\alpha_1 = \tan^{-1}(R_1/h) - \tan^{-1}[(\rho + b)/d]\,, \quad (7)$$

$$R_2 = \sqrt{d^2 - h^2 + (b - \rho)^2}\,; \qquad s'_2 = b + h\alpha_2\,, \quad (8)$$

$$\alpha_2 = \tan^{-1}(R_2/h) - \tan^{-1}[(b - \rho)/d]\,, \quad (9)$$

whereas, for $\rho > a$, P_2 is on the lower bowl so that R_1 and s'_1 are still given by (6), while

$$R_2 = \sqrt{d^2 - h'^2 + (\rho - b')^2}\,; \quad s'_2 = b + h\pi/2 + h'\alpha_2\,, \quad (10)$$

$$\alpha_2 = \tan^{-1}(R_2/h') + \tan^{-1}[(\rho - b')/d] - \pi/2\,. \quad (11)$$

For what concerns the evaluation of the maximum in relation (5) allowing the determination of W_φ, it is convenient to express z' and ρ' in terms of the angle δ (Fig. 2 (b)) as $z' = h\cos\delta$, $\rho' = b + h\sin\delta$. As shown in [18], such a maximum is the solution of the following equation:

$$bd(\cos^2\delta - \sin^2\delta) + [\rho^2 + d^2 - b^2]\sin\delta\cos\delta + \\ -h(b\cos\delta + d\sin\delta) = 0\,,$$

belonging to the interval $[0, \pi/2]$.

In light of the above results, the voltage at any point $P(\vartheta, \varphi)$ on the plane can be efficiently reconstructed by means of the two-dimensional OSI expansion [18]:

$$V(\xi(\vartheta), \varphi) = \mathrm{e}^{-\mathrm{j}\gamma(\xi)} \sum_{n=n_0-q+1}^{n_0+q} \Bigg\{ A(\xi, \xi_n, \bar{\xi}, N, N'') \cdot \\ \sum_{m=m_0-p+1}^{m_0+p} \tilde{V}(\xi_n, \varphi_{m,n})\, A(\varphi, \varphi_{m,n}, \bar{\varphi}, M_n, M''_n) \Bigg\}, \quad (12)$$

where $2q \times 2p$ is the number of retained reduced voltage samples $\tilde{V}(\xi_n, \varphi_{m,n})$, $n_0 = \mathrm{Int}(\xi/\Delta\xi)$, $m_0 = \mathrm{Int}(\varphi/\Delta\varphi_n)$,

$$\xi_n = n\Delta\xi = 2\pi n/(2N''+1)\,; \quad N'' = \mathrm{Int}(\chi N') + 1\,, \quad (13)$$

$$N' = \mathrm{Int}(\chi' W_\xi) + 1\,; \quad N = N'' - N'\,; \quad \bar{\xi} = q\Delta\xi\,, \quad (14)$$

$$\varphi_{m,n} = m\Delta\varphi_n = 2\pi m/(2M''_n+1);\; M''_n = \mathrm{Int}(\chi M'_n) + 1\,, \quad (15)$$

$$M'_n = \mathrm{Int}[\chi^* W_\varphi(\xi_n)] + 1\,; \quad M_n = M''_n - M'_n\,, \quad (16)$$

$$\chi^* = 1 + (\chi' - 1)[\sin\vartheta(\xi_n)]^{-2/3}\,; \quad \bar{\varphi} = p\Delta\varphi_n\,, \quad (17)$$

χ is an oversampling factor controlling the truncation error [14], Int(x) denotes the integer part of x, and

$$A(\alpha, \alpha_\ell, \bar{\alpha}, L, L'') = \Omega_L(\alpha - \alpha_\ell, \bar{\alpha})\, D_{L''}(\alpha - \alpha_\ell)\,, \quad (18)$$

is the OSI interpolation function. Moreover,

$$D_{L''}(\alpha) = \frac{\sin[(2L''+1)\alpha/2]}{(2L''+1)\sin(\alpha/2)}\,, \quad (19)$$

and

$$\Omega_L(\alpha, \bar{\alpha}) = \frac{T_L\left[2\cos^2(\alpha/2)/\cos^2(\bar{\alpha}/2) - 1\right]}{T_L\left[2/\cos^2(\bar{\alpha}/2) - 1\right]}\,, \quad (20)$$

are the Dirichlet and Tschebyscheff sampling functions [14], $T_L(\alpha)$ being the Tschebyscheff polynomial of degree L.

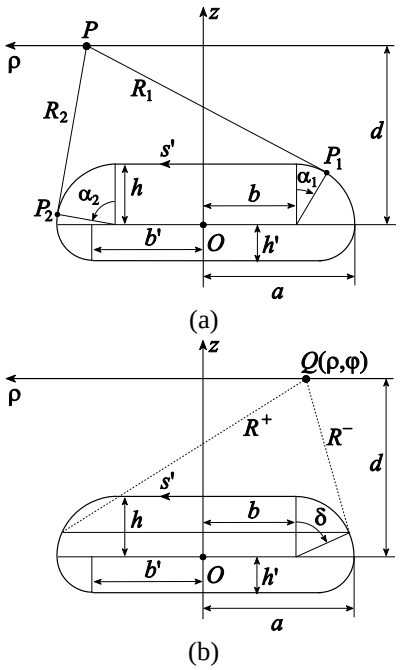

Fig. 2. Double bowl modeling: (a) relevant to the evaluation of γ and ξ; (b) relevant to the evaluation of W_φ.

It must be stressed that the two-dimensional OSI expansion (12) has the interesting features to reduce the truncation error for a given number of retained samples and to avoid the propagation of the errors affecting the samples [12, 18]. Accordingly, it can be properly exploited to accurately recover the voltages V_φ and V_ρ at any point in the measurement circle and, in particular, at those needed by the classical probe compensated NFTFF transformation with plane-rectangular scanning [8]. Unfortunately, the probe corrected formulas in [8] (whose expressions in the here adopted reference system are shown in the next section) are valid as long as the probe maintains its orientation with respect to the AUT and this requires its co-rotation with it. A probe having a far-field characterized by a first-order φ-dependence can be properly used for avoiding such a co-rotation. As a matter of fact, in this case, the voltages V_V and V_H (acquired with co-rotation by the probe and rotated probe) can be

determined from V_φ and V_ρ as follows:

$$V_V = V_\varphi \cos\varphi - V_\rho \sin\varphi\,;\quad V_H = V_\varphi \sin\varphi + V_\rho \cos\varphi\,. \quad (21)$$

III. PLANE-RECTANGULAR NFTFF TRANSFORMATION

For reader's convenience, this section reports the key formulas of the probe-corrected NFTFF transformation with plane-rectangular scanning [8], particularized for the here considered reference system (see Fig. 1) when an open-ended rectangular waveguide is adopted as measurement probe.

As shown in [7, 8], by properly applying the Lorentz reciprocity theorem and the plane wave spectrum representation of EM fields, the antenna far-field components E_ϑ, E_φ are related to the two-dimensional Fourier transforms I_V, I_H of the output probe voltages V_V, V_H and to the far-field components $E'_{\vartheta V}$, $E'_{\varphi V}$ and $E'_{\vartheta H}$, $E'_{\varphi H}$ of the electric field radiated by the probe and the probe rotated by 90°, when operating in the transmitting mode, by the following expressions:

$$E_\vartheta(\vartheta,\varphi) = \left(I_H E'_{\varphi V}(\vartheta,-\varphi) - I_V E'_{\varphi H}(\vartheta,-\varphi)\right)\Big/\Delta\,, \quad (22)$$

$$E_\varphi(\vartheta,\varphi) = \left(I_H E'_{\vartheta V}(\vartheta,-\varphi) - I_V E'_{\vartheta H}(\vartheta,-\varphi)\right)\Big/\Delta\,, \quad (23)$$

where

$$\Delta = E'_{\vartheta H}(\vartheta,-\varphi)E'_{\varphi V}(\vartheta,-\varphi) - E'_{\vartheta V}(\vartheta,-\varphi)E'_{\varphi H}(\vartheta,-\varphi)\,, \quad (24)$$

$$I_{V,H} = B\cos\vartheta\, e^{j\beta d\cos\vartheta}\cdot \int_{-\infty}^{+\infty}\int_{-\infty}^{+\infty} V_{V,H}(x,y)\, e^{j\beta x\sin\vartheta\cos\varphi}\, e^{j\beta y\sin\vartheta\sin\varphi}\, dxdy\,, \quad (25)$$

B being an appropriate constant.

As shown in [25], the FF components of the electric field radiated by an $a'\times b'$ sized open-ended rectangular waveguide, wherein a TE_{10} mode is propagating, are:

$$E'_{\vartheta V} = f_\vartheta(\vartheta)\sin\varphi\,\frac{e^{-j\beta r}}{r} = A_E\,\frac{1+(k_z/\beta)\cos\vartheta}{1+(k_z/\beta)}\cdot \frac{\sin\left[\beta(b'/2)\sin\vartheta\right]}{\beta(b'/2)\sin\vartheta}\sin\varphi\,\frac{e^{-j\beta r}}{r}\,, \quad (26)$$

$$E'_{\varphi V} = f_\varphi(\vartheta)\cos\varphi\,\frac{e^{-j\beta r}}{r} = A_H\cos\left[\beta(a'/2)\sin\vartheta\right]\cdot \left\{\frac{\cos\vartheta + (k_z/\beta) + \Gamma\left[\cos\vartheta - (k_z/\beta)\right]}{(\pi/2)^2 - \left[\beta(a'/2)\sin\vartheta\right]^2} + C_0\right\}\cos\varphi\,\frac{e^{-j\beta r}}{r}\,, \quad (27)$$

where

$$A_E = A_H\left\{\frac{4}{\pi^2}\left[1+(k_z/\beta)+\Gamma\left(1-(k_z/\beta)\right)\right]+C_0\right\}, \quad (28)$$

$$A_H = -j\,\beta^2 a'b'E_0/8\,, \quad (29)$$

$k_z = [\beta^2 - (\pi/a')^2]^{1/2}$ is the propagation constant of the TE_{10} mode, E_0 is its amplitude, and Γ is the reflection coefficient at the end of the waveguide, whose measured values are shown in [25]. Moreover, C_0 is a real constant that can be numerically computed as described in [25]. The FF components of the electric field radiated by the rotated probe can be easily determined by straightforward evaluations, thus getting:

$$E'_{\vartheta H} = f_\vartheta(\vartheta)\cos\varphi\,\frac{e^{-j\beta r}}{r}\,, \quad (30)$$

$$E'_{\varphi H} = -f_\varphi(\vartheta)\sin\varphi\,\frac{e^{-j\beta r}}{r}\,. \quad (31)$$

IV. EXPERIMENTAL TESTING

Some experimental results validating the efficacy of the described nonredundant NFTFF transformation with plane-polar scanning are shown in this section. The experimental proofs have been carried out in the anechoic chamber ($8\text{m}\times5\text{m}\times4\text{m}$ sized) of the Antenna Characterization Lab of the University of Salerno, covered by pyramidal absorbers ensuring a reflectivity lower than –40 dB and equipped with a NF plane-polar scanning system, besides the cylindrical and spherical ones. The plane-polar scanning is achieved by mounting the AUT on a rotator and the probe (an open-ended WR90 rectangular waveguide) on a linear vertical scanner. A vector network analyzer is used to perform the amplitude and phase measurements of the voltages acquired by the probe. The employed AUT is a dual pyramidal horn antenna with horizontal polarization, placed on the plane z = 0 and operating at 10 GHz. The horns have a $8.9\text{cm}\times6.8\text{cm}$ sized aperture and the distance between the apertures centers is 26 cm. A photo of the plane-polar NF facility with the dual pyramidal horn antenna is reported in Fig. 3. Note that, in order to show the roll positioner and the AUT mounting, the photo has been taken before covering the rotator and AUT support with the necessary absorbers. The nonredundant plane-polar samples have been collected on a circle having radius 110 cm on a plane 17 cm away from the considered antenna, which has been shaped by a double bowl, whose geometric parameters are a = 18.6 cm and $h = h'$ = 2.85 cm.

The amplitude and phase of the voltage V_φ on the radial line at φ = 0°, recovered from the collected nonredundant plane-polar samples, are compared in Figs. 4 and 5 with the directly measured ones (references). The comparison between the reconstructed amplitude of the voltage V_ρ on the radial line at φ = 90° and that directly measured is shown in Fig. 6. The reconstructions of the amplitudes of V_φ and V_ρ on the radial line at φ = 30° are reported in Fig. 7, while that relevant to the phase of V_φ is shown in Fig. 8. All recoveries are resulted to be very good, except for small discrepancies occurring in the zones characterized by very low voltage levels, thus assessing the effectiveness of the OSI formulas. Note that, the recovered voltages show a smoother behavior than the

measured ones, since the spectral content of the noise at the spatial frequencies higher than the antenna spatial band-width are cut away owing to the low pass filtering characteristics of the OSI functions. As regards the choice of the OSI algorithm parameters, the excess bandwidth factor χ' has been chosen equal to 1.35 to make negligible the aliasing error with respect to the measurement one, whereas $\chi = 1.20$ and $p = q = 7$ have been used to neglect the truncation error [18].

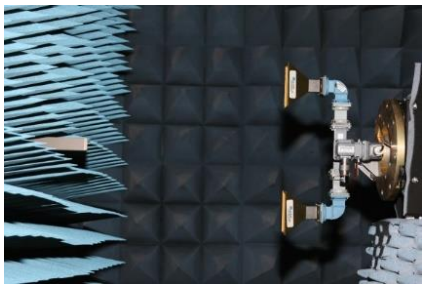

Fig. 3. Photo of the plane-polar NF facility with the dual pyramidal horn antenna.

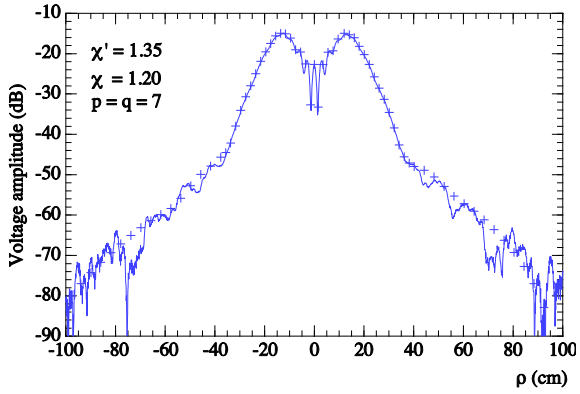

Fig. 4. Amplitude of V_φ on the radial line at φ = 0°. Solid line: reference. Crosses: reconstructed from the nonredundant plane-polar NF samples.

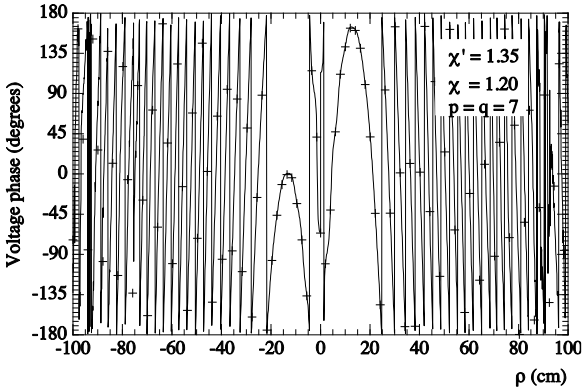

Fig. 5. Phase of V_φ on the radial line at φ = 0°. Solid line: reference. Crosses: reconstructed from the nonredundant plane-polar NF samples.

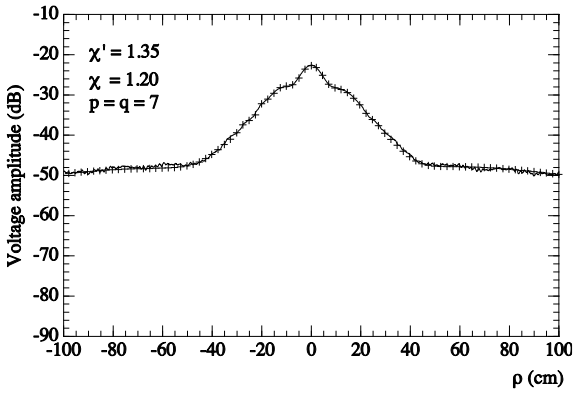

Fig. 6. Amplitude of V_ρ on the radial line at φ = 90°. Solid line: reference. Crosses: reconstructed from the nonredundant plane-polar NF samples.

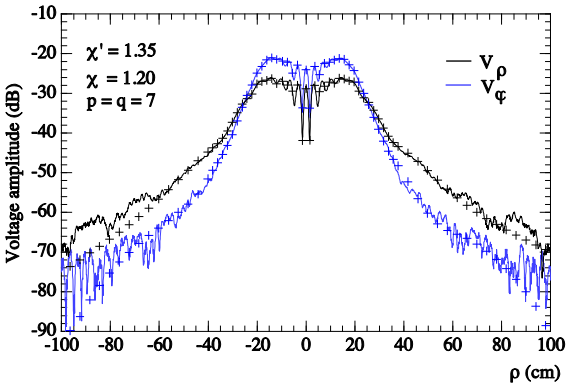

Fig. 7. Amplitudes of V_φ, V_ρ on the radial line at φ = 30°. Solid lines: references. Crosses: reconstructed from the nonredundant plane-polar NF samples.

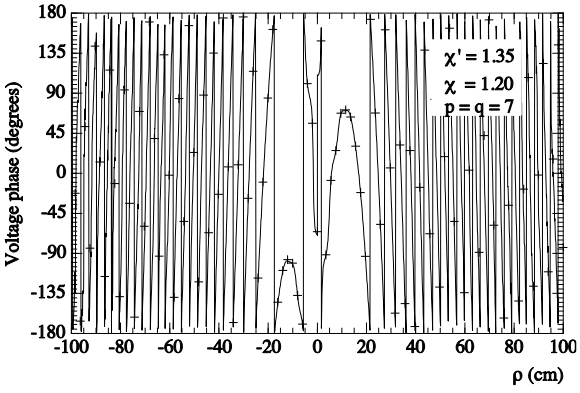

Fig. 8. Phase of V_φ on the radial line at φ = 30°. Solid line: reference. Crosses: reconstructed from the nonredundant plane-polar NF samples.

Finally, the overall efficacy of such a NFTFF transformation technique is validated by comparing the E- and H-planes FF patterns (see Figs. 9 and 10) recovered

from the acquired nonredundant plane-polar samples with the ones attained by using the NF cylindrical scanning system. Also in such a case, a very good agreement is found.

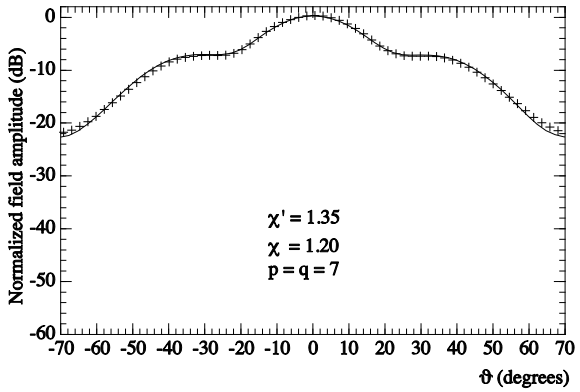

Fig. 9. E-plane pattern. Solid line: reference. Crosses: reconstructed from the nonredundant plane-polar NF samples.

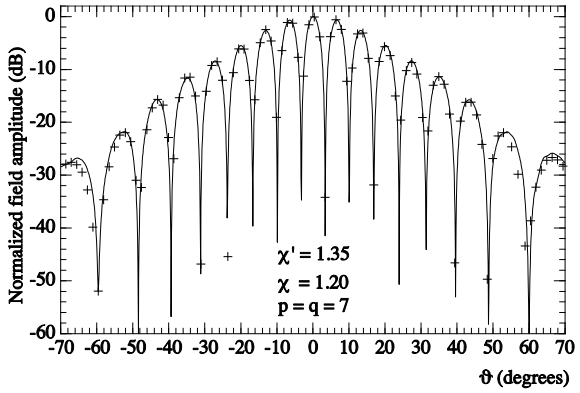

Fig. 10. H-plane pattern. Solid line: reference. Crosses: reconstructed from the nonredundant plane-polar NF samples.

It is noteworthy to compare the acquired NF samples number (1663) with that (33581) needed by the plane-polar scanning techniques [9-11] and with that (21609) required by the classical plane-rectangular NFTFF transformation [8].

The interested reader can find in [26] another set of experimental results relevant to a different AUT, which further assess the effectiveness of the proposed NFTFF transformation technique.

V. CONCLUSION

The experimental validation of the nonredundant plane-polar NFTFF transformation, using a double bowl to shape the AUT, is provided in this paper. Its effectiveness has been fully confirmed by the very good NF and FF reconstructions. It must be pointed out that the number of used NF measurements has resulted to be considerably smaller than those required when using the classical NFTFF transformations with plane-rectangular and plane-polar scans, thus showing that such a NFTFF transformation allows a significant measurement time reduction without any loss in accuracy.

REFERENCES

[1] A. D. Yaghjian, "An overview of near-field antenna measurements," *IEEE Trans. Antennas Prop*., vol. AP-34, pp. 30-45, Jan. 1986.

[2] J. Appel-Hansen, J. D. Dyson, E. S. Gillespie, and T. G. Hickman, *Antenna Measurements*, in *The Handbook of Antenna Design*, A. W. Rudge, K. Milne, A. D. Olver, and P. Knight, Eds., chapter 8, Peter Peregrinus, London, UK 1986.

[3] E. S. Gillespie, Ed., "Special Issue on near-field scanning techniques," *IEEE Trans. Antennas Prop*., vol. 36, pp. 727-901, June 1988.

[4] M. H. Francis and R. W. Wittmann, *Near-Field Scanning Measurements: Theory and Practice*, in *Modern Antenna Handbook*, C. A. Balanis, Ed., chapter 19, John Wiley & Sons, Hoboken, NJ, USA, 2008.

[5] M. H. Francis, Ed., *IEEE Recommended Practice for Near-Field Antenna Measurements*, IEEE Standard 1720-2012, 2012.

[6] C. Gennarelli, A. Capozzoli, L. Foged, J. Fordham, and D. J. van Rensburg, Eds., "Recent advances in near-field to far-field transformation techniques," *Int. Jour. Antennas Prop*., vol. 2012, ID 243203, 2012.

[7] D. T. Paris, W. M. Leach, Jr., and E. B. Joy, "Basic theory of probe-compensated near-field measurements," *IEEE Trans. Antennas Prop*., vol. AP-26, pp. 373-379, May 1978.

[8] E. B. Joy, W. M. Leach, Jr., G. P. Rodrigue, and D. T. Paris, "Application of probe-compensated near-field measurements," *IEEE Trans. Antennas Prop*., vol. AP-26, pp. 379-389, May 1978.

[9] Y. Rahmat-Samii, V. Galindo Israel, and R. Mittra, "A plane-polar approach for far-field construction from near-field measurements," *IEEE Trans. Antennas Prop*., vol. AP-28, pp. 216-230, Mar. 1980.

[10] Y. Rahmat-Samii and M. S. Gatti, "Far-field patterns of spaceborne antennas from plane-polar near-field measurements," *IEEE Trans. Antennas Prop*., vol. AP-33, pp. 638-648, June 1985.

[11] M. S. Gatti and Y. Rahmat-Samii, "FFT applications to plane-polar near-field antenna measurements," *IEEE Trans. Antennas Prop*., vol. 36, pp. 781-791, June 1988.

[12] O. M. Bucci, C. Gennarelli, and C. Savarese, "Fast and accurate near-field far-field transformation by sampling interpolation of plane-polar measurements," *IEEE Trans. Antennas Prop*., vol.

39, pp. 48-55, Jan. 1991.

[13] O. M. Bucci and G. Franceschetti, "On the spatial bandwidth of scattered fields," *IEEE Trans. Antennas Prop*., vol. AP-35, pp. 1445-1455, Dec. 1987.

[14] O. M. Bucci, C. Gennarelli, and C. Savarese, "Representation of electromagnetic fields over arbitrary surfaces by a finite and non redundant number of samples," *IEEE Trans. Antennas Prop*., vol. 46, pp. 351-359, Mar. 1998.

[15] O. M. Bucci and C. Gennarelli, "Application of nonredundant sampling representations of electromagnetic fields to NF-FF transformation techniques," *Int. Jour. Antennas Prop*., vol. 2012, ID 319856, 14 pages, 2012.

[16] F. Ferrara, C. Gennarelli, R. Guerriero, G. Riccio, and C. Savarese, "An efficient near–field to far–field transformation using the planar wide–mesh scanning," *Jour. Electr. Waves Appl.*, vol. 21, pp. 341-357, 2007.

[17] F. D'Agostino, I. De Colibus, F. Ferrara, C. Gennarelli, R. Guerriero, and M. Migliozzi, "Far-field pattern reconstruction from near-field data collected via a nonconventional plane-rectangular scanning: Experimental testing," *Int. Jour. Antennas Prop*., vol. 2014, ID 763687, 9 pages, 2014.

[18] O. M. Bucci, C. Gennarelli, G. Riccio, and C. Savarese, "Near–field – far–field transformation from nonredundant plane-polar data: effective modellings of the source," *IEE Proc. Microw., Antennas Prop.*, vol. 145, pp. 33-38, Feb. 1998.

[19] O. M. Bucci, F. D'Agostino, C. Gennarelli, G. Riccio, and C. Savarese, "NF–FF transformation with plane-polar scanning: Ellipsoidal modelling of the antenna," *Automatika*, vol. 41, pp. 159-164, 2000.

[20] O. M. Bucci, C. Gennarelli, G. Riccio, and C. Savarese, "Fast and accurate far-field evaluation from a non redundant, finite number of plane-polar measurements," *Proc. of 1994 IEEE AP-S Int. Symp.*, Seattle, USA, pp. 540-543, June 1994.

[21] A. D. Yaghjian, "Antenna coupling and near-field sampling in plane-polar coordinates," *IEEE Trans. Antennas Prop*., vol. 40, pp. 304-312, Mar. 1992.

[22] A. D. Yaghjian and M. B. Woodworth, "Sampling in plane-polar coordinates," *IEEE Trans. Antennas Prop*., vol. 44, pp. 696-700, May 1996.

[23] F. D'Agostino, F. Ferrara, C. Gennarelli, R. Guerriero, and M. Migliozzi, "Far-field pattern reconstruction from a nonredundant plane-polar near-field sampling arrangement: Experimental testing," *IEEE Antennas Wireless Prop. Lett.*, vol. 15, pp. 1345-1348, 2016.

[24] O. M. Bucci, G. D'Elia, and M. D. Migliore, "Advanced field interpolation from plane-polar samples: Experimental verification," *IEEE Trans. Antennas Prop*., vol. 46, pp. 204-210, Feb. 1998.

[25] A. D. Yaghjian, "Approximate formulas for the far field and gain of open-ended rectangular waveguide," *IEEE Trans. Antennas Prop*., vol. AP-32, pp. 378-384, Apr. 1984.

[26] F. D'Agostino, F. Ferrara, C. Gennarelli, R. Guerriero, and M. Migliozzi, "An efficient NF-FF transformation technique with plane-polar scanning: Experimental assessments," in *Proc. of LAPC '14*, Loughborough, UK, pp. 231-235, Nov. 2014.

Francesco D'Agostino was born near Salerno (Italy) in 1965. He received the Laurea degree in Electronic Engineering from the University of Salerno in 1994, where in 2001 he received the Ph.D. degree in Information Engineering. From 2002 to 2005 he was Assistant Professor at the Engineering Faculty of the University of Salerno where, in October 2005, he was appointed Associate Professor of Electromagnetics and joined the Department of Industrial Engineering, where he is currently working. His research activity includes application of sampling techniques to electromagnetics and to innovative NF–FF transformations, diffraction problems radar cross section evaluations, Electromagnetic Compatibility. In this area, D'Agostino has co-authored 4 books and over 150 scientific papers, published in peer-reviewed international journals and conference proceedings. He is a regular Reviewer for several journals and conferences and has chaired some international events and conferences. D'Agostino is a Member of AMTA, EurAAP, and IEEE.

Flaminio Ferrara was born near Salerno, Italy, in 1972. He received the Laurea degree in Electronic Engineering from the University of Salerno in 1999. Since the same year, he has been with the Research Group in Applied Electromagnetics at the University of Salerno. He received the Ph.D. degree in Information Engineering at the same University, where he is presently an Assistant Professor of Electromagnetic Fields. His interests include: application of sampling techniques to the efficient reconstruction of electromagnetic fields and to NF–FF transformation techniques; monostatic radar cross section evaluations of corner reflectors. Ferrara is co-author of more than 180 scientific papers, mainly in international journals and conference proceedings. He is Reviewer for several

international journals and Member of the Editorial board of the International Journal of Antennas and Propagation. He is Member of the IEEE society.

Claudio Gennarelli was born in Avellino, Italy, in 1953. He received the Laurea degree (*summa cum laude*) in Electronic Engineering from the University of Naples, Italy, in 1978. From 1978 to 1983, he worked with the Research Group in Electromagnetics at the Electronic Engineering Department of the University "Federico II" of Naples. In 1983, he became Assistant Professor at the Istituto Universitario Navale (IUN), Naples. In 1987, he was appointed Associate Professor of Antennas, formerly at the Engineering Faculty of Ancona University and subsequently at the Engineering Faculty of Salerno University. In 1999, he has been appointed Full Professor at the same University. The main topics of his scientific activity are: reflector antennas analysis, antenna measurements, diffraction problems, radar cross section evaluations, scattering from surface impedances, application of sampling techniques to electromagnetics and to NF–FF transformations. Gennarelli is co-author of more than 370 scientific papers, mainly in international journals and conference proceedings. In particular, he is co-author of four books on NF–FF transformation techniques. He is a Senior Member of the IEEE and Member of the Editorial board of the Open Electrical and Electronic Engineering Journal and of the International Journal of Antennas and Propagation.

Rocco Guerriero received the Laurea degree in Electronic Engineering and the Ph.D. degree in Information Engineering from the University of Salerno in 2003 and 2007, respectively. Since 2003, he has been with the Reaserch Group in Applied Electromagnetics of University of Salerno, where he is currently an Assistant Professor of Electromagnetic Fields. His interests include: application of sampling techniques to the efficient reconstruction of electromagnetic fields and to near-field-far-field transformation techniques; antenna measurements; inversion of ill-posed electromagnetic problems; analysis of microstrip reflectarrays; diffraction problems. Guerriero is co-author of more than 135 scientific papers, mainly in international journals and conference proceedings. He is Reviewer for several international journals and Member of the Editorial board of the International Journal of Antennas and Propagation. Since 2015, he is Member IEEE.

Massimo Migliozzi received the Laurea degree in Electronic Engineering from the University of Salerno, in 1999. He received the Ph.D. degree in Information Engineering at the same University, where at the present time he is a Research Fellow in Electromagnetic Fields. His scientific interests include: application of sampling techniques to the efficient reconstruction of electromagnetic fields and to NF–FF transformation techniques; antenna measurements; electromagnetic compatibility; antenna design; diffraction problems. Migliozzi is co-author of about 100 scientific papers, mainly in international journals and conference proceedings and Reviewer for several international journals.

The Fourth-Order One-Step Leapfrog HIE-FDTD Method

Mian Dong, Anxue Zhang, Juan Chen, Songlin Zhang, and Yuchen He

School of Electrical and Information Engineering
Xi'an Jiaotong University, Xi'an 710049, People's Republic of China
Chen.juan.0201@mail.xjtu.edu.cn

Abstract ─ A new fourth-order one-step leapfrog hybrid implicit-explicit finite-difference time-domain (HIE-FDTD) method has been proposed in this paper. This new method investigates the use of a second-order accurate in time and a fourth-order accurate in space. Because of the utilize of the one-step leapfrog theory, the proposed algorithm not only has the same formulation as that used for the traditional FDTD, but also require only one-step computations. The 2-D formulation of the method is presented and the time stability condition of the method is certified. Simulation results show that the proposed method is 6.8 times faster than the traditional second-order FDTD method and is 2.2 times faster than the second-order HIE-FDTD method, which shows that the proposed method has very high computational efficiency. On the other hand, the proposed method also has less dispersion error by comparing with traditional second-order FDTD method and the second-order HIE-FDTD method.

Index Terms ─ Computational efficiency, dispersive error, Finite-Difference Time-Domain (FDTD), fourth order, Hybrid Implicit- and Explicit-FDTD (HIE-FDTD), one-step leapfrog.

I. INTRODUCTION

It is well known that the Courant-Friedrich-Levy (CFL) stability condition restricts the applications of the FDTD [1-2] method when it is used to simulate structures where fine mesh needs. In order to remove the CFL limit, many improved method has been developed such as alternating direction implicit FDTD (ADI-FDTD) [3-8], Crank-Nicloson FDTD (CN-FDTD) [9], locally one-dimensional FDTD (LOD-FDTD) [10-13] and hybrid implicit and explicit-FDTD (HIE-FDTD) [14-18]. The HIE-FDTD method is weakly conditionally stable. Its time step size is not determined by fine space discretization, so, the method allows larger time step size than the conventional FDTD method, which is extremely useful for problems with very fine structures in one direction.

However, in the HIE-FDTD method, the cell size could not be larger than 1/10 of the wavelength, otherwise the numerical dispersion inherent in the classical Yee FDTD algorithm will introduce significant errors. So, when solving the electrically large problems, a large number of cells (10-20 cells per wavelength) are required to decrease the dispersion error, which would increase the computation time inevitably.

To reduce the computation time, two approaches are used in this paper. One is to use more terms in the Taylor series to approximate the spatial derivatives. Fang [19] was the first to present this approach in conjunction with solving Maxwell's equations. He investigated the use of a second-order accurate in time and a fourth-order accurate in space FDTD algorithm, which we denote as the FDTD (2, 4) algorithm [20-24], [5], [6]. The other one is to use the one-step leapfrog method. Cooke [25] firstly presented this approach into the ADI-FDTD method. With the one-step leapfrog, electric field terms arise only on the half time step, while the magnetic field terms arise only on the full time step. Consequently, the one-step leapfrog ADI-FDTD method is much simpler and more efficient than the traditional ADI-FDTD method.

In this paper, a novel fourth-order one-step leapfrog HIE-FDTD is developed. The fourth-order one-step leapfrog HIE-FDTD method not only has the second-order accurate in time and the fourth order accurate in space, but also has the one-step leapfrog schemes. Therefore, since the use of the fourth order accurate in space, the proposed method would provide a higher accuracy than the traditional second-order FDTD method [1-2] and second-order HIE-FDTD method [15]. What's more, the proposed method would spend much less computational time because of the use of one-step leapfrog schemes and the weak stability than the fourth-order FDTD method [24].

Numerical examples in this paper demonstrate that the proposed algorithm has lower dispersion error than the conventional FDTD method even when the cell size is equal to 1/5 of the wavelength in solving some EM problems. For simplicity, the two-dimensional (2-D) fourth-order one-step leapfrog HIE-FDTD update equations are discussed in this paper. The formulations for 3-D fourth-order HIE-FDTD method can be developed

Submitted On: January 14, 2016
Accepted On: June 17, 2016

following a similar procedure.

The organization of this paper is as follows. In Section II, the formulation of the proposed algorithm is presented. The stability condition is certified in Section III. The numerical dispersion analysis and numerical results applied to the EM problems are presented in the Sections IV and V.

II. FORMULATION

For simplicity, the two-dimensional TE model with respect to z-direction is considered in this paper. The numerical formulations of the Maxwell's equations in a lossless and isotropic medium are presented as follows:

$$\frac{\partial}{\partial \mathrm{t}}(\Psi)=(R)(\Psi). \tag{1}$$

Here, $(\Psi)=\left(E_{\mathrm{x}},E_{\mathrm{y}},H_{\mathrm{z}}\right)^{T}$, (R) can be expressed as follows:

$$(R)=\begin{pmatrix} 0 & 0 & (1/\varepsilon)\delta_{\mathrm{y}} \\ 0 & 0 & -(1/\varepsilon)\delta_{\mathrm{x}} \\ (1/\mu)\delta_{\mathrm{y}} & -(1/\mu)\delta_{\mathrm{x}} & 0 \end{pmatrix}, \tag{2}$$

while $\delta_{\mathrm{m}}=\partial/\partial m, m=x,y.$

By applying the one-step leapfrog technique [25] and the hybrid implicit-explicit FDTD (HIE-FDTD) [14-18] method, a set of time marching equations are derived as follows.

The space operator (R) is split into two parts, just as $(R)=\left(R_1\right)+\left(R_2\right)$, where

$$\left(R_1\right)=\begin{pmatrix} 0 & 0 & (1/\varepsilon)\delta_{\mathrm{y}} \\ 0 & 0 & -(1/\varepsilon)\delta_{\mathrm{x}} \\ (1/\mu)\delta_{\mathrm{y}} & 0 & 0 \end{pmatrix},$$

$$\left(R_2\right)=\begin{pmatrix} 0 & 0 & 0 \\ 0 & 0 & 0 \\ 0 & -(1/\mu)\delta_{\mathrm{x}} & 0 \end{pmatrix}.$$

By using the Peaceman-Rachford theory, Eq. (1) is split into two parts as shown in Eqs. (3) and (4), where time marching over one full time step is broken into two procedures. The first updating procedure involves the advancement from the n th time step to the $n+1/2$ th time step, and in the second procedure, the fields are updated from $n+1/2$ th time step to the $n+1$ th time step.

$$\begin{aligned}&\left(I-(\Delta t/2)\left(R_1\right)\right)\Psi^{n+1/2}\\&\quad=\left(I+(\Delta t/2)\left(R_2\right)\right)\Psi^{n}.\end{aligned} \tag{3}$$

$$\begin{aligned}&\left(I-(\Delta t/2)\left(R_2\right)\right)\Psi^{n+1}\\&\quad=\left(I+(\Delta t/2)\left(R_1\right)\right)\Psi^{n+1/2}.\end{aligned} \tag{4}$$

By substituting $\left[R_1\right]$ and $\left[R_2\right]$ into (3), we obtain

$$E_x^{n+1/2}-(\Delta t/2\varepsilon)\delta_y H_z^{n+1/2}=E_x^{n}, \tag{5-1}$$

$$E_{\mathrm{y}}^{n+1/2}+(\Delta t/2\varepsilon)\delta_x H_z^{n+1/2}=E_y^{n}, \tag{5-2}$$

$$\begin{aligned}&-(\Delta t/2\mu)\delta_y E_x^{n+1/2}+H_z^{n+1/2}\\&\quad=-(\Delta t/2\mu)\delta_y E_y^{n}+H_z^{n}.\end{aligned} \tag{5-3}$$

By substituting $\left[R_1\right]$ and $\left[R_2\right]$ into (4), we obtain

$$E_x^{n+1}=E_x^{n+1/2}+(\Delta t/2\varepsilon)\delta_y H_z^{n+1/2}, \tag{6-1}$$

$$E_{\mathrm{y}}^{n+1}=E_y^{n+1/2}-(\Delta t/2\varepsilon)\delta_x H_z^{n+1/2}, \tag{6-2}$$

$$\begin{aligned}&(\Delta t/2\mu)\delta_x E_y^{n+1}+H_z^{n+1}\\&\quad=(\Delta t/2\mu)\delta_y E_x^{n+1/2}+H_z^{n+1/2}.\end{aligned} \tag{6-3}$$

By replacing n with $n-1$ in (6-1)-(6-3), respectively, we obtain:

$$E_x^{n}=E_x^{n-1/2}+(\Delta t/2\varepsilon)\delta_y H_z^{n-1/2}, \tag{7-1}$$

$$E_{\mathrm{y}}^{n}=E_y^{n-1/2}-(\Delta t/2\varepsilon)\delta_x H_z^{n-1/2}, \tag{7-2}$$

$$\begin{aligned}&(\Delta t/2\mu)\delta_x E_y^{n}+H_z^{n}\\&\quad=(\Delta t/2\mu)\delta_y E_x^{n-1/2}+H_z^{n-1/2}.\end{aligned} \tag{7-3}$$

Substituting (7-3) into (7-1), we have:

$$\begin{aligned}E_x^{n}&=(1-(\Delta t^2/4\varepsilon\mu)\delta_y^2)E_x^{n-1/2}\\&+(\Delta t^2/4\varepsilon\mu)\delta_x\delta_y E_y^{n}+(\Delta t/2\varepsilon)\delta_y H_z^{n}.\end{aligned} \tag{8}$$

By substituting (5-3) and (8) into (5-1), the updating equation for E_x is obtained below:

$$\begin{aligned}&(1-(\Delta t^2/4\varepsilon\mu)\delta_y^2)E_x^{n+1/2}\\&=(1-(\Delta t^2/4\varepsilon\mu)\delta_y^2)E_x^{n-1/2}+(\Delta t/2\varepsilon)\delta_y H_z^{n}.\end{aligned} \tag{9}$$

Substituting (7-3) into (7-2), we have:

$$\begin{aligned}&\left(1+(\Delta t^2/4\varepsilon\mu)\delta_{\mathrm{x}}^2\right)E_y^{n}=E_y^{n-1/2}\\&-(\Delta t/2\mu)\delta_x H_z^{n}+(\Delta t^2/4\varepsilon\mu)\delta_x\delta_y E_x^{n-1/2}.\end{aligned} \tag{10}$$

By substituting (5-3) and (10) into (5-2), the updating equation for E_y is obtained below:

$$\begin{aligned}E_y^{n+1/2}&=E_y^{n-1/2}-(\Delta t/2\varepsilon)\delta_x H_z^{n}\\&-(\Delta t^2/4\varepsilon\mu)\delta_x\delta_y(E_x^{n+1/2}-E_x^{n-1/2}).\end{aligned} \tag{11}$$

By substituting (6-2), (5-2) and (5-3) into (6-3), the updating equation for H_z is obtained below:

$$\begin{aligned}H_{\mathrm{z}}^{n+1}&=H_z^{n}\\&+(\Delta t/2\mu)\left(\delta_y E_x^{n+1/2}-\delta_x E_y^{n+1/2}\right).\end{aligned} \tag{12}$$

In Eqs. (9), (11) and (12) it often uses the finite difference to approximate the spatial derivate [21], [23]. For example:

$$\begin{aligned}&\frac{\partial f(x,y,t)}{\partial x}\Big|_{x=i\Delta x}^{\mathrm{n}+1/2}\approx\frac{1}{\Delta x}\sum_{\iota=0}^{N-1}\alpha(l)\cdot\\&\left[f\Big|_{i+\iota+1/2,j}^{\mathrm{n}+1/2}-f\Big|_{i-\iota-1/2,j}^{\mathrm{n}+1/2}\right],\end{aligned} \tag{13}$$

where $\alpha(\iota)$ can be obtained in reference [20],

$$\alpha(\iota)=\frac{(-1)^{\iota}}{2(\iota+1/\iota)^2}\bullet\frac{\left[(2N-1)!!\right]}{(2N-2-2\iota)!!}\bullet\frac{\left[(2N-1)!!\right]}{(2N+2\iota)!!}.$$

If N is equal to 1, the order of the one-step leapfrog HIE-FDTD algorithm is equal to 2. When N is equal to 2, the order of the HIE-FDTD algorithm is equal to 4. Then according to the definition of the constant $\alpha(\iota)$ and by substituting (13) into (9), (11) and (12), the fourth-order one-step leapfrog HIE-FDTD algorithm's equations are obtained as followed.

To further simplify, the auxiliary field variables *e* and *h* are introduced as:

$$e_m^{n+1/2}=E_m^{n+1/2}-E_m^{n-1/2}, m=x,y,z, \tag{14-1}$$

$$h_m^{n+1}=H_m^{n+1}-H_m^{n}, m=x,y,z. \tag{14-2}$$

The final updating equation for E_x of the proposed method is obtained below:

$$\begin{aligned}&(1+\mathrm{c}_1)\mathrm{e}_{\mathrm{x}}\big|_{i+1/2,j}^{n+1/2}\\&-c_2\left(\mathrm{e}_{\mathrm{x}}\big|_{i+1/2,j+1}^{n+1/2}+\mathrm{e}_{\mathrm{x}}\big|_{i+1/2,j-1}^{n+1/2}\right)\\&-c_3\left(\mathrm{e}_{\mathrm{x}}\big|_{i+1/2,j+2}^{n+1/2}+\mathrm{e}_{\mathrm{x}}\big|_{i+1/2,j-2}^{n+1/2}\right)\\&-c_4\left(\mathrm{e}_{\mathrm{x}}\big|_{i+1/2,j+3}^{n+1/2}+\mathrm{e}_{\mathrm{x}}\big|_{i+1/2,j-3}^{n+1/2}\right)\\&=c_5\left(\mathrm{H}_{\mathrm{z}}\big|_{i+1/2,j+1/2}^{n}-\mathrm{H}_{\mathrm{z}}\big|_{i+1/2,j-1/2}^{n}\right)\\&\text{-}c_6\left(\mathrm{H}_{\mathrm{z}}\big|_{i+1/2,j+3/2}^{n}-\mathrm{H}_{\mathrm{z}}\big|_{i+1/2,j-3/2}^{n}\right),\end{aligned} \tag{15}$$

where

$$\begin{aligned}c_1&=365\Delta t^2/576\varepsilon\mu\Delta \mathrm{y}^2,\\c_2&=87\Delta t^2/256\varepsilon\mu\Delta \mathrm{y}^2,\\c_3&=3\Delta t^2/128\varepsilon\mu\Delta \mathrm{y}^2,\\c_4&=\Delta t^2/2304\varepsilon\mu\Delta \mathrm{y}^2,\\c_5&=9\Delta t/8\varepsilon\mu\Delta \mathrm{y},\\c_6&=\Delta t/24\varepsilon\mu\Delta \mathrm{y}.\end{aligned}$$

The other updating equations of the proposed method can be obtained similarly and are not shown here for simplicity.

III. STABALITY ANALYSIS OF FOURTH ORDER HIE-FDTD METHOD

From Eqs. (3) and (4), we obtain:

$$\begin{aligned}&\Psi^{n+1}\\&=\left(I-(\Delta t/2)(R_2)\right)^{-1}\cdot\left(I+(\Delta t/2)(R_1)\right)\\&\cdot\left(I-(\Delta t/2)(R_1)\right)^{-1}\cdot\left(I+(\Delta t/2)(R_2)\right)\Psi^n\\&=(A)^{-1}(B)(A_1)^{-1}(B_1)\Psi^n,\end{aligned} \tag{16}$$

while

$$(A)=\left(I-(\Delta t/2)(R_2)\right)=\begin{pmatrix}1&0&0\\0&1&0\\0&m_x/2\mu&1\end{pmatrix},$$

$$(A_1)=\left(I-(\Delta t/2)(R_1)\right)=\begin{pmatrix}1&0&-m_y/2\varepsilon\\0&1&m_x/2\varepsilon\\-m_y/2\mu&m_x/2\mu&1\end{pmatrix},$$

$$(B)=\left(I+(\Delta t/2)(R_1)\right)=\begin{pmatrix}1&0&m_y/2\varepsilon\\0&1&-m_x/2\varepsilon\\m_y/2\mu&0&1\end{pmatrix},$$

$$(B_1)=\left(I+(\Delta t/2)(R_2)\right)=\begin{pmatrix}1&0&0\\0&1&0\\0&-m_x/2\varepsilon&1\end{pmatrix},$$

$$m_{\mathrm{p}}=\frac{\Delta t}{\Delta p}\sum_{\iota=0}^{N-1}\alpha(\iota)2\hat{j}\sin\left(\frac{2\iota+1}{2}k_p\Delta p\right),\ p=x,y,$$

$$\alpha(0)=\frac{9}{8},\ \alpha(1)=-\frac{1}{24}.$$

For simplification, we obtain the formulation of *M* in (17), shown at the bottom of this page:

$$M=(A)^{-1}(B)(A_1)^{-1}(B_1)=\begin{pmatrix}\varepsilon\mu+\frac{1}{4}m_y^2&-\frac{1}{2}m_xm_y&\mu m_y\\-\frac{1}{2}m_xm_y&\varepsilon\mu-\frac{1}{4}m_y^2+\frac{1}{2}m_x^2&\mu m_y\\\varepsilon m_y+\frac{1}{4\mu}m_x^2m_y-\varepsilon m_x-\frac{1}{2\mu}m_x^3&\varepsilon\mu-\frac{1}{4}m_y^2+\frac{1}{2}m_x^2\end{pmatrix}\times\frac{4}{4\varepsilon\mu-m_y^2}. \tag{17}$$

By substituting (17) into (16), we have $\Psi^{n+1}=(M)\Psi^n$. By setting the determinant of $\left[I_{3\times3}\xi-M\right]$ to be zero, as that $\left|I_{3\times3}\xi-M\right|=0$. ξ represents the growth factor.

For simplification, the above equation can be represented as follows:

$$\xi^3-\frac{12\varepsilon\mu+4m_x^2+m_y^2}{4\varepsilon\mu-m_y^2}\xi+\frac{12\varepsilon\mu+4m_x^2+m_y^2}{4\varepsilon\mu-m_y^2}-1=0. \tag{18}$$

By solving (18), the values of the growth factor ξ are obtained:

$$\xi_1 = 1,$$

$$\xi_{2,3} = \frac{(8\varepsilon\mu + m_y^2 + 4m_x^2)}{2(4\varepsilon\mu - m_y^2)} \pm \frac{\sqrt{(4\varepsilon\mu + m_y^2 + 2m_x^2)^2 - (4\varepsilon\mu - m_y^2)^2}}{(4\varepsilon\mu - m_y^2)}.$$

In order to satisfy the stability condition during field advancement, the module of growth factor ξ must be less than or equal to 1. It is apparent that when the relation $(4\varepsilon\mu + m_y^2 + 2m_x^2)^2 \le (4\varepsilon\mu - m_y^2)^2$ is satisfied, the condition $|\xi_{2,3}| = 1$ would be obtained. When $(4\varepsilon\mu + m_y^2 + 2m_x^2)^2 \le (4\varepsilon\mu - m_y^2)^2$, we can obtain that $-4\varepsilon\mu - m_y^2 - 2m_x^2 \le 4\varepsilon\mu - m_y^2$, as well as $-m_x^2 \le 4\varepsilon\mu$.

By substituting the value of m_x, we have:

$$\left(\frac{\Delta t \sum_{\iota=0}^{N-1} \alpha(\iota) \sin(((2\iota+1)/2) k_x \Delta x))}{\Delta x/2} \right)^2$$

$$\le \frac{\left(\Delta t \sum_{\iota=0}^{N-1} |\alpha(\iota)| \right)^2}{(\Delta x/2)^2} \le 4\varepsilon\mu$$

$$\Rightarrow \Delta t \le \frac{1}{c \sum_{\iota=0}^{N-1} |\alpha(\iota)| \sqrt{(1/\Delta x)^2}},$$

where $c = 1/\sqrt{\varepsilon_0 \mu_0}$ is the speed of light in the vacuum. The values of constant $\alpha(0)$ and $\alpha(1)$ are equal to 9/8 and -1/24, respectively. So through the analysis above, the stability condition of the proposed algorithm is presented as follows:

$$\Delta t \le \frac{6/7}{c\sqrt{(1/\Delta x)^2}}. \tag{19}$$

IV. NUMERICAL DISPERSION ANALYSIS

We now study the numerical dispersion in the proposed algorithm. Substitute $\zeta = e^{j\omega\Delta t}$ into (1), it can be obtained:

$$(\sin(\omega\Delta t/2))^2 = \frac{-(m_x^2 + m_y^2)}{4\varepsilon\mu - m_y^2}, \tag{20}$$

while

$$m_x = \frac{\left[\frac{9}{4} \sin(\frac{k_x \Delta x}{2}) - \frac{1}{12} \sin(\frac{3k_x \Delta x}{2}) \right]}{-\hat{j}\Delta x/\Delta t},$$

$$m_y = \frac{\left[\frac{9}{4} \sin(\frac{k_y \Delta y}{2}) - \frac{1}{12} \sin(\frac{3k_y \Delta y}{2}) \right]}{-\hat{j}\Delta y/\Delta t}.$$

Suppose that a wave propagating at angle θ is in the spherical coordinate system. Then,

$$k_x = k_0 \cos(\theta),\ k_y = k_0 \sin(\theta),$$

where k_0 is the physical wave number. By substituting them into dispersion relation (20), the wave number $k = \omega/c$ can be obtained, while c is the light speed in the vacuum.

The global phase error:

$$\Phi = \frac{1}{4\pi} \int_0^{\pi} \left[\frac{k_0 - k(\theta)}{k_0} \right]^2 \sin\theta \, d\theta. \tag{21}$$

The cell size $\Delta x = \Delta y = \lambda / N$, λ is the operating wavelength and N is the constant.

It can be seen from Fig.1. (a) that when CFLN value is 2, as the increase of the N, the global phase error of the proposed algorithm decreases gradually. Fig.1. (b) shows that when N value is 14, the global phase error of the proposed algorithm increases gradually as the increase of the CFLN.

When the N value becomes bigger, the cell sizes of the proposed algorithm would become smaller so that the algorithm would have much bigger computing accuracy and lower global phase error, which agree well with the Fig.1. (a) When the CFLN value becomes bigger, the time step size of the proposed algorithm would become bigger so that the algorithm have much lower computing accuracy and larger global phase error, which agree well with the Fig.1. (b).

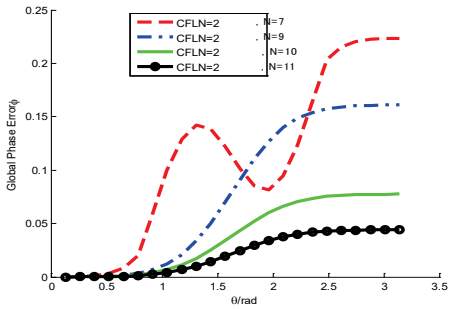

(a)

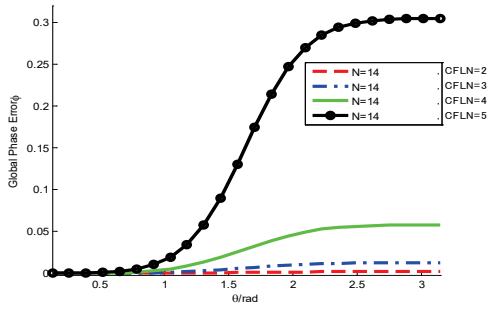

(b)

Fig. 1. (a) the relation between the global phase error and constant N, the relation between the global phase error and constant CFLN.

V. NUMERICAL RESULTS

To verify the computational efficiency and the dispersive error of the fourth-order one-step leapfrog HIE-FDTD method, two examples are presented in this section. For comparison, numerical results calculated by using the traditional second-order FDTD algorithm, the fourth-order FDTD algorithm and the second-order HIE-FDTD algorithm are also presented.

(1) Computational Efficiency

In order to verify the validity and computational efficiency of the fourth-order one-step leapfrog HIE-FDTD algorithm, the simulation of the proposed method with pulse source is presented in this sub section.

A 2-D computational domain with the dimension 360 mm×36 mm is shown in Fig. 2 (a). The cell sizes are $\Delta x = 6$ mm and $\Delta y = 0.6$ mm. So the total meshes are 60×60. 10 cell-thick CPML layers are used to terminate the computational domain. A small current source is placed at the center of the domain. Observation point P_1 is located at the grid (45, 30), as shown in Fig. 2 (a). The time dependence of the source is as follows:

$$P(t) = \cos(2\pi f_0 t)\exp(-4\pi(\frac{t-t_0}{\tau})^2),$$

where $f_0 = 5\,GHz$, $t_0 = 3\times10^{-9}$ s, $\tau = 3\times10^{-9}$ s; thus, the wavelength of the source is about 60 mm.

The electric field values E_y at point P_1 are calculated by using the fourth-order one-step leapfrog HIE-FDTD method and are plotted in Fig. 2 (b). For comparison, the results calculated by using the traditional second-order FDTD method, the fourth-order FDTD method and the second-order HIE-FDTD method are also presented in this figure. The time stability conditions of these four methods are: $\Delta t \le 1/c\sqrt{(1/\Delta x)^2+(1/\Delta y)^2} = 1.99\,ps$ (second-order FDTD method [1]), $\Delta t \le (6/7)0/c\sqrt{(1/\Delta x)^2+(1/\Delta y)^2} = 1.71$ (fourth-order FDTD method [10]), $\Delta t \le 1/c\sqrt{(1/\Delta x)^2} = 20\,ps$ (second-order HIE-FDTD method [7]) and $\Delta t \le (6/7)/c\sqrt{(1/\Delta x)^2} = 17.14\,ps$ (fourth-order one-step leapfrog HIE-FDTD method), respectively. In this simulation, the time step sizes of the above four algorithms all take the maximum time step size that satisfy their stability conditions.

Figure 2 (b) illustrates that the result of the fourth-order one-step leapfrog HIE-FDTD algorithm is well consistent with these of the second-order FDTD algorithm, the fourth-order FDTD algorithm, and the second-order HIE-FDTD algorithm.

To complete this simulation, the computer costs of these methods are presented in Table 1. Because the fourth-order one-step leapfrog HIE-FDTD algorithm as well as the second-order HIE-FDTD algorithm can take much larger time step size than the FDTD algorithm, the computer costs of these two methods are much less than the FDTD algorithm. From Table 1, it can see that the proposed method is 6.8 and 14.54 faster than the traditional second-order FDTD method and the fourth-order FDTD method, respectively. What is more, although the maximum time step size of the proposed algorithm is just 6/7 times as that of the second-order HIE-FDTD algorithm, the computer cost of the fourth-order one-step HIE-FDTD algorithm also be less than that of the second-order HIE-FDTD algorithm. It is 2.2 times faster than the second-order HIE-FDTD algorithm. In conclusion, the proposed fourth-order one-step leapfrog HIE-FDTD algorithm can save computational time greatly when solving the fine electromagnetic problems as presented in Table 1.

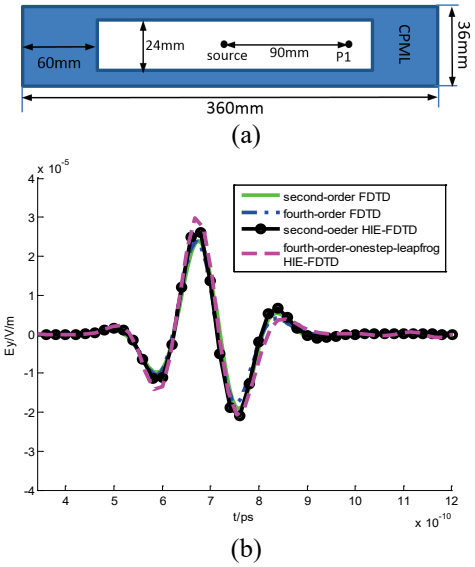

Fig. 2. (a) Free space truncated by CPML, and (b) the electric field values at point P_1.

Table 1: Computer costs of the FDTD algorithm and HIE-FDTD algorithm

	$\Delta t(ps)$	CPU Time (s)
Second-order FDTD	1.990	14.40
Fourth-order FDTD	1.71	30.69
Second-order HIE-FDTD	20.0	4.66
One-step-leapfrog Fourth-order HIE-FDTD	17.14	2.11

(2) Dispersion Error

In order to verify the lower dispersive error of the fourth-order one-step leapfrog HIE-FDTD algorithm,

another numerical example is presented in this sub section. 10-cell-thick CPML layers are used to terminate a 2-D computational domain with the dimensions 360 mm×360 mm. A small current source is placed at the center of the domain. Observation point P_2 is 117 mm far away from source point, as shown in Fig. 3 (a).

The time dependence of the source is as follows:

$$P(\mathrm{t}) = \sin(2\pi ft),$$

where f=10 GHz, thus the wavelength of the source is 30 mm.

It uses the fourth-order one-step leapfrog HIE-FDTD method, the second-order HIE-FDTD method and the second-order FDTD method to compute the field value E_y at point P_2, the results are shown in Fig. 3 (b). The cell sizes of the x-direction and y-direction of the fourth-order one-step leapfrog HIE-FDTD algorithm are $\Delta x = \Delta y = 6$ mm, which are equal to 1/5 of the wavelength. For comparison, there are two kinds of cell sizes used in the second-order FDTD algorithm. One is $\Delta x = \Delta y = 3$ mm, which are equal to 1/10 of the wavelength; the other is $\Delta x = \Delta y = 6$ mm, which are equal to the values of the fourth-order one-step leapfrog HIE-FDTD algorithm. The cell sizes of the second-order HIE-FDTD method are also $\Delta x = \Delta y = 6$ mm.

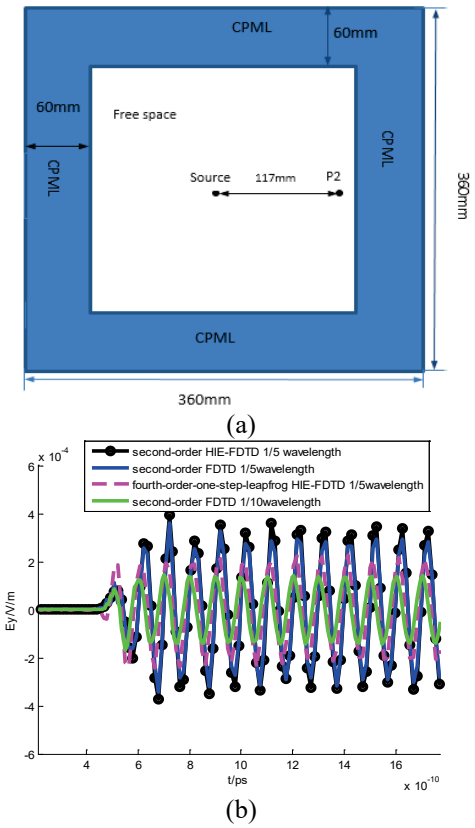

Fig. 3. (a) Free space truncated by CPML, and (b) the electric field values at point P_2.

It is well known that as the cell sizes increase, the dispersive error of the FDTD method would increase. It means that the accuracy of the FDTD method would decrease as the cell sizes increase, especially when the cell size is larger than 1/10 of the wavelength. So, in Fig. 3 (b), we think the result of the second-order FDTD algorithm whose cell size is equal to 1/10 of the wavelength is accurate. From Fig. 3 (b), it is clear that as the cell sizes increase, the result of the second-order FDTD algorithm and the second-order HIE-FDTD algorithm whose cell size are equal to 1/5 wavelength are not well consistent with the accurate result. However, the result of the fourth-order one-step leapfrog HIE-FDTD algorithm although its cell size is also equal to 1/5 of the wavelength agrees much well with the accurate result. It demonstrates that the fourth-order HIE-FDTD algorithm has much less dispersive error than the second-order FDTD algorithm method and second-order HIE-FDTD method when the cell size increases. Since the cell size could take larger values, the fourth-order one-step leapfrog HIE-FDTD algorithm is more suitable to solve electrically large problems.

VI. CONCLUSION

This paper firstly introduces the fourth-order one-step leapfrog theories into the HIE-FDTD algorithm. It is found that the technique is weakly conditionally stable and supports time step size greater than the CFL limit. The computer cost of the fourth-order one-step leapfrog HIE-FDTD algorithm is much less than the second-order, fourth-order FDTD algorithm and the second-order HIE-FDTD even though the maximum time step size of the proposed algorithm is smaller than that of the second-order HIE-FDTD algorithm. It means that the fourth-order one-step leapfrog HIE-FDTD method has higher computational efficiency than the FDTD algorithm and second-order HIE-FDTD algorithm. Numerical simulations show that the fourth-order one-step leapfrog HIE-FDTD algorithm has higher calculation accuracy and low computational error, even when the cell size is equal to 1/5 of the wavelength. Therefore the fourth-order one-step leapfrog HIE-FDTD algorithm is very suitable to solve problems where both fine and electrically large structures are needed.

ACKNOWLEDGMENT

This work was supported by National Natural Science Foundations of China (No. 61231003 and 61471292), and also supported by the Fundamental Research Funds for the Central Universities.

REFERENCES

[1] K. S. Yee, "Numerical solution of initial boundary value problems involving Maxwell's equations in isotropic media," *IEEE Trans. Antennas Propagat.*, vol. AP-14, pp. 302-307, 1966.

[2] A. Taflove, *Computational Electrodynamics*. Norwood, MA: Artech House, 1995.

[3] Z. Chen, "A finite-difference time-domain method without the Courant stability conditions," IEEE Microwave Guided Wave Lett., vol. 9, pp. 441-443, 1999.

[4] S. Staker, C. Holloway, A. Bhobe, and M. Piket-May, "ADI formulation of the FDTD method: Algorithm and material dispersion implementation," *IEEE Trans. Electromagn. Compat*., vol. 45, no. 2, pp. 156-166, 2003.

[5] N. V. Kantartzis, "Multi-frequency higher-order ADI-FDTD solvers for signal integrity predictions and interference modeling in general EMC applications."

[6] Y. Zhang, S. Lu, and J. Zhang, "Reduction of numerical dispersion of 3-D higher order ADI-FDTD method with artificial anisotropy," *IEEE Trans. Microw. Theory Tech*., vol. 57, no. 10, pp. 2416-28, Oct. 2009. *ACES Journal*, vol. 25, no. 12, pp. 1046 1060, 2010.

[7] H. Zheng and K. Leung, "A nonorthogonal ADI-FDTD algorithm for solving 2-D scattering problems," *IEEE Trans. Antennas Propag*., vol. 57, no. 12, pp. 3981-3902, Dec. 2009.

[8] M. Darms, R. Schuhmann, H. Spachmann, and T. Weiland, "Dispersion and asymmetry effects of ADI-FDTD," *IEEE Microw. Wireless Compon. Lett*., vol. 12, no. 12, pp. 491-493, Dec. 2002.

[9] H. Zheng, L. Feng, and Q. Wu, "3-D non-orthogonal ADI-FDTD algorithm for the full-wave analysis of microwave circuit devices," *IEEE Trans. Microw. Theory Tech*., vol. 58, no. 1, pp. 128-135, Jan. 2010.

[10] J. Chen and J. G. Wang, "Two approximate Crank–Nicolson finite-difference time-domain method for TE(z) waves," *IEEE Transactions on Antennas Propagation*, vol. 57, pp. 3375-3378, 2009.

[11] E. Li, I. Ahmed, and R. Vahldieck, "Numerical dispersion analysis with an improved LOD FDTD method," *IEEE Microw. Wireless Compon. Lett*., vol. 17, no. 5, pp. 319-321, May 2007.

[12] N. V. Kantartzis, T. Ohtani, and Y. Kanai, "Accuracy-adjustable nonstandard LOD-FDTD schemes for the design of carbon nanotube interconnects and nanocomposite EMC shields," *IEEE Trans. Magn*., vol. 49, no. 5, pp. 1821 1824, 2013.

[13] T. T. Zygiridis, N. V. Kantartzis, and T. D. Tsiboukis, "Parallel LOD-FDTD method with error-balancing properties," *IEEE Trans. Magn*., vol. 51, no. 3, art. no. 7205804, 2015.

[14] J. Shibayama, "Efficient implicit FDTD algorithm based on locally one-dimensional scheme," *Electron. Lett*., vol. 44, pp. 1046-1047, 2005.

[15] J. Chen and J. Wang, "A 3-D hybrid implicit-explicit FDTD scheme with weakly conditional stability," *Microwave Opt. Technol. Lett*., vol. 48, pp. 2291-2294, 2006.

[16] B. Huang and G. Wang, "A hybrid implicit-explicit FDTD scheme with weakly conditional stability," *Microwave Opt. Technol. Lett*., vol. 39, pp. 97-101, 2003.

[17] J. Chen and J. G. Wang, "A three-dimensional semi-implicit FDTD scheme for calculation of shielding effectiveness of enclosure with thin slots," *IEEE Transactions on Electromagnetic Compatibility*, vol. 49, pp. 354-360, 2007.

[18] J. Chen and J. G. Wang, "Numerical simulation using HIE–FDTD method to estimate various antennas with fine scale structures," *IEEE Trans-actions on Antennas Propagation*, vol. 55, pp. 3603-3612, 2007

[19] J. Fang, "Time domain finite difference computation for Maxwell's equations," *Ph.D. Dissertation, Univ. of California at Berkeley*, CA, 1989.

[20] M. L. Ghrist, "High order difference methods for wave equations," *[D]. University of Colorado*, 1997.

[21] M. Fujii and W. J. R Hoefer, "A wavelet formulation of finite difference method: Full vector analysis of optical waveguide junctions," *IEEE J. Quantum Electron*., vol. 37, pp. 1015-1029, Aug. 2011.

[22] N. V. Kantartzis, "Hybrid unconditionally stable high-order nonstandard schemes with optimal error-controllable spectral resolution for complex microwave problems," *Int. J. Num. Modelling: Electronic Networks, Devices and Fields*, vol. 25, no. 5, 6, pp. 621-644, 2012.

[23] M. Krumpholz and L. P. B. Katehi, "MRTD: New time-domain schems based on multiresolution analysis," *IEEE Trans. Microwave Theory Tech*., vol. 44, pp. 555-571, Apr. 1996.

[24] T. Deveze, L. Beaulieu, and W. Tabbara, "A fourth order scheme for the fdtd algorithm applied to Maxwell's equations*," IEEE APS Int. Symp. Proc*., Chicago, IL, vol. 7, pp. 346-349, 1992.

[25] S. J. Cooke, M. Botton, T. M. Antonsen, and B. Levush, "A leapfrog formulation of the 3D ADI-FDTD algorithm," *Int. J. Numer. Model*, vol. 22, no. 2, pp. 187-200, 2009.

A Speeding up Technique for Lossy Anisotropic Algorithm in FDTD Method

Fatih Kaburcuk [1] and Atef Z. Elsherbeni [2]

[1] Electrical and Electronic Engineering Department
Erzurum Technical University, Erzurum, 25700, Turkey
fkaburcu@syr.edu, fatih.kaburcuk@erzurum.edu.tr

[2] Electrical Engineering and Computer Science Department
Colorado School of Mines, Golden, CO 80401, USA
aelsherb@mines.edu

Abstract ─ In this paper, a speeding up technique for the lossy anisotropic (Lossy-ANI) algorithm integrated into the finite-difference time-domain (FDTD) method is proposed. The speeding up technique provides remarkable reduction in the computation time of the Lossy-ANI algorithm. This algorithm is applied to a line-fed microstrip patch antenna (MPA) with anisotropic substrate and a lossy anisotropic scattering object. Numerical results show that the anisotropy effects the resonant frequencies of the MPA and the bistatic RCS of the scattering object.

Index Terms ─ FDTD, lossy anisotropic medium.

I. INTRODUCTION

A generalized 3D FDTD algorithm is formulated based on Lossy-ANI algorithm with a speeding up technique. The Lossy-ANI algorithm was first proposed in [1] for a one-dimensional Lossy-ANI scatterer with permittivity and electric conductor tensors. This algorithm was extended in [2-4] for the 3D Lossy-ANI scatterer with permittivity, permeability, magnetic, and electric conductor tensors. Algorithms for complex lossy mediums and lossy dielectric mediums with off-diagonal permittivity and conductivity tensors were proposed in [5] and [6], respectively. The 3D FDTD algorithm for the analysis of anisotropic materials faces a lot of challenges, such as requirement of large computer memory and long computation time. A speeding up technique, proposed in this paper to reduce the computation time is achieved by dividing the computation of fields into two parts in the FDTD simulation: one is the fields produced by off-diagonal elements of anisotropic tensors, and the other is the fields produced by diagonal elements of anisotropic tensors. Then, the sum of the fields are considered as the total fields for the next time-step in the simulation. This technique provides remarkable reduction in the computation time.

A line-fed MPA with uniaxial anisotropic substrate was presented in [7]. Then, the MPA with anisotropic substrate was analyzed in [8-9] using the lossless anisotropic algorithm based on the relationships between *D*-, *E*-, *B*-, and *H*-fields. This example will be tested here but after the presentation of the new process of updating the FDTD equations.

In this paper, a detailed analysis of Lossy-ANI algorithm and speeding up technique are presented in Section II. The computational domain in the presented algorithm are terminated by the convolution perfectly matched layers (CPML). A line-fed MPA with anisotropic substrate and a lossy anisotropic scattering object are analyzed to investigate the simulation verification and its performance. Numerical results show that the scattering parameter of the MPA and the bistatic RCS of the scattering object are effected by the anisotropy as expected.

II. LOSSY-ANI ALGORITHM

A. Maxwell equations for 3D Lossy-ANI medium

The Maxwell equations for Lossy-ANI medium are:

$$\nabla \times H = \bar{\bar{\varepsilon}} \frac{\partial E}{\partial t} + \bar{\bar{\sigma}}^e E \text{ and } \nabla \times E = -\bar{\bar{\mu}} \frac{\partial H}{\partial t} - \bar{\bar{\sigma}}^m H, \quad (1)$$

where $\bar{\bar{\varepsilon}}$, $\bar{\bar{\mu}}$, $\bar{\bar{\sigma}}^e$, and $\bar{\bar{\sigma}}^m$ are permittivity, permeability, electric and magnetic conductivity tensors, respectively. After some mathematical manipulation, one can obtain:

$$\begin{aligned} E^{n+1} &= \bar{\bar{p}}_e \cdot (\Delta \times H)^{n+\frac{1}{2}} + \bar{\bar{r}}_e \cdot E^n \\ H^{n+\frac{1}{2}} &= \bar{\bar{p}}_m \cdot (\Delta \times E)^n + \bar{\bar{r}}_m \cdot H^{n-\frac{1}{2}}, \end{aligned} \quad (2)$$

where

$$\begin{aligned} \bar{\bar{p}}_e &= \left(\frac{\bar{\bar{\varepsilon}}}{\Delta t} + \frac{\bar{\bar{\sigma}}^e}{2}\right)^{-1}, \bar{\bar{r}}_e = \bar{\bar{p}}_e \cdot \left(\frac{\bar{\bar{\varepsilon}}}{\Delta t} - \frac{\bar{\bar{\sigma}}^e}{2}\right) \\ \bar{\bar{p}}_m &= \left(\frac{\bar{\bar{\mu}}}{\Delta t} + \frac{\bar{\bar{\sigma}}^m}{2}\right)^{-1}, \bar{\bar{r}}_m = p_m \cdot \left(\frac{\bar{\bar{\mu}}}{\Delta t} - \frac{\bar{\bar{\sigma}}^m}{2}\right) \end{aligned}. \quad (3)$$

The *x*-component of the *E*- and *H*-fields in (2) are obtained after discretizing in space by the following equations:

Submitted On: September 2, 2016
Accepted On: October 11, 2016

$$E_x\big|_{i-\frac{1}{2},j,k}^{n+1} = \begin{pmatrix} p_{e11}\left(\frac{\partial H_z}{\partial y}\Big|_{i-\frac{1}{2},j,k}^{n+\frac{1}{2}} - \frac{\partial H_y}{\partial z}\Big|_{i-\frac{1}{2},j,k}^{n+\frac{1}{2}}\right) \\ +p_{e12}\left(\frac{\partial H_x}{\partial z}\Big|_{i-\frac{1}{2},j,k}^{n+\frac{1}{2}} - \frac{\partial H_z}{\partial x}\Big|_{i-\frac{1}{2},j,k}^{n+\frac{1}{2}}\right) \\ +p_{e13}\left(\frac{\partial H_y}{\partial x}\Big|_{i-\frac{1}{2},j,k}^{n+\frac{1}{2}} - \frac{\partial H_x}{\partial y}\Big|_{i-\frac{1}{2},j,k}^{n+\frac{1}{2}}\right) \\ +r_{e11}E_x\big|_{i-\frac{1}{2},j,k}^{n} + r_{e12}E_y\big|_{i-\frac{1}{2},j,k}^{n} + r_{e13}E_z\big|_{i-\frac{1}{2},j,k}^{n} \end{pmatrix}, \quad (4)$$

$$H_x\big|_{i,j-0.5,k-0.5}^{n+0.5} = \begin{pmatrix} -p_{m11}\left(\frac{\partial E_z}{\partial y}\Big|_{i,j-0.5,k-0.5}^{n+0.5} - \frac{\partial E_y}{\partial z}\Big|_{i,j-0.5,k-0.5}^{n+0.5}\right) \\ -p_{m12}\left(\frac{\partial E_x}{\partial z}\Big|_{i,j-0.5,k-0.5}^{n+0.5} - \frac{\partial E_z}{\partial x}\Big|_{i,j-0.5,k-0.5}^{n+0.5}\right) \\ -p_{m13}\left(\frac{\partial E_y}{\partial x}\Big|_{i,j-0.5,k-0.5}^{n+0.5} - \frac{\partial E_x}{\partial y}\Big|_{i,j-0.5,k-0.5}^{n+0.5}\right) \\ -r_{m11}H_x\big|_{i,j-0.5,k-0.5}^{n-0.5} - r_{m12}H_y\big|_{i,j-0.5,k-0.5}^{n-0.5} \\ -r_{m13}H_z\big|_{i,j-0.5,k-0.5}^{n-0.5} \end{pmatrix}, \quad (5)$$

where the first subscript of the coefficients (p_{e11}, r_{e11} p_{m11}, and r_{e11}) refers to the type of the field (electric or magnetic) and the second and third subscripts refer the element number of the matrix in (3).

Similarly, other components of E- and H-fields can be obtained. It is realized that i, j, and k indices used in Equations (4)-(5) are not meant to give exact location where the fields are available. We must consider the exact location of the fields. Thus, linear interpolation [1-4] is used to obtain the right location of fields in the Yee's grid. $E_y^n(i,j,k)$ and $E_z^n(i,j,k)$ in (4) are interpolated from neighboring quantities as follows:

$$E_y^n(i,j,k) = \frac{1}{4}\begin{pmatrix} E_y^n(i+1,j+1,k) + E_y^n(i,j+1,k) \\ +E_y^n(i+1,j,k) + E_y^n(i,j,k) \end{pmatrix}, \quad (6.a)$$

$$E_z^n(i,j,k) = \frac{1}{4}\begin{pmatrix} E_z^n(i+1,j,k+1) + E_z^n(i,j,k+1) \\ +E_z^n(i+1,j,k) + E_z^n(i,j,k) \end{pmatrix}. \quad (6.b)$$

The spatial derivatives of H-fields in (4) can be obtained using the following approximations:

$$\frac{\partial H_z^{n+\frac{1}{2}}(i,j,k)}{\partial y} = \frac{1}{dy}\left(H_z^n(i,j+1,k) - H_z^n(i,j,k)\right), \quad (7.a)$$

$$\frac{\partial H_y^{n+\frac{1}{2}}(i,j,k)}{\partial z} = \frac{1}{dz}\left(H_y^n(i,j,k) - H_y^n(i,j,k-1)\right), \quad (7.b)$$

$$\frac{\partial H_x^{n+\frac{1}{2}}(i,j,k)}{\partial z} = \frac{0.25}{dz}\begin{pmatrix} H_x^n(i+1,j+1,k) + H_x^n(i,j+1,k) \\ +H_x^n(i+1,j,k) + H_x^n(i,j,k) \\ -H_x^n(i,j+1,k-1) - H_x^n(i+1,j,k-1) \\ -H_x^n(i+1,j+1,k-1) - H_x^n(i,j,k-1) \end{pmatrix}, \quad (7.c)$$

$$\frac{\partial H_x^{n+\frac{1}{2}}(i,j,k)}{\partial y} = \frac{0.25}{dy}\begin{pmatrix} H_x^n(i+1,j+1,k) + H_x^n(i,j+1,k) \\ +H_x^n(i+1,j,k-1) + H_x^n(i,j,k) \\ -H_x^n(i+1,j+1,k-1) - H_x^n(i,j+1,k-1) \\ -H_x^n(i+1,j,k-1) - H_x^n(i,j,k-1) \end{pmatrix}, \quad (7.d)$$

$$\frac{\partial H_z^{n+\frac{1}{2}}(i,j,k)}{\partial x} = \frac{0.25}{dx}\begin{pmatrix} H_x^n(i+2,j+1,k) + H_x^n(i+2,j,k) \\ -H_x^n(i,j+1,k) - H_x^n(i,j,k) \end{pmatrix}, \quad (7.e)$$

$$\frac{\partial H_y^{n+\frac{1}{2}}(i,j,k)}{\partial x} = \frac{0.25}{dx}\begin{pmatrix} H_y^n(i+2,j,k) + H_y^n(i+2,j,k-1) \\ -H_y^n(i,j,k) - H_y^n(i,j,k-1) \end{pmatrix}. \quad (7.f)$$

Now the x-component of the E-field in (4) can be updated using (6) and (7). Similarly, other component of the E- and H-fields can be updated. The spatial derivatives in the Yee's grids used in this paper have more complicated implementations compared to the Lebedev grids in [10].

B. Speeding up technique

With this Lossy-ANI algorithm, the E- and H-fields are produced by off-diagonal elements of anisotropic tensors are calculated in the entire computational domain as in [1-4]. It is realized that a considerable amount of computation time is spent for the calculation of these fields. Therefore, a speeding up technique is proposed here to reduce the computation time. In this technique, the fields produced by off-diagonal elements of anisotropic tensors are calculated in the region-ANI shown in Fig. 1 that contains anisotropic object, whereas the fields produced by diagonal elements of anisotropic tensors are calculated in the entire computational domain. Then, the sum of these fields are considered as the total fields for the next time-step in the simulation. This technique provides more than 70% reduction in the computation time of the Lossy-ANI algorithm.

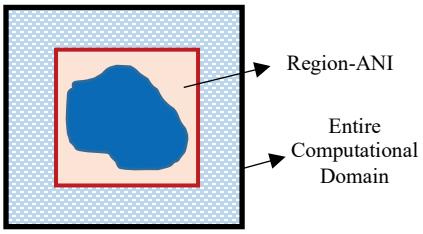

Fig. 1. Configuration of the FDTD computational domain for the Lossy-ANI algorithm.

III. NUMERICAL RESULT

In this section, we test the performance of the Lossy-ANI algorithm with the speeding up technique for solving a line-fed MPA [11] with anisotropic substrate and an anisotropic scattering object. The computer being used in this work has Intel® Core™ i7-4790 CPU and 8 GB DDR RAM. The program is based on [12] and is written and compiled in 64-bit MATLAB version 8.2.0.701 (R2013b).

A. A line-fed MPA with anisotropic substrate

A line-fed MPA with anisotropic substrate shown in Fig. 2 is analyzed to verify the efficiency of the Lossy-ANI algorithm with the speeding up technique. The discretization of the antenna in each direction are set to

dx=0.3891 mm, dy=0.4 mm, and dz=0.1985 mm. The rectangular patch size is (31 dx)×(40 dy). The size of the feed line is (6 dx)×(30 dy). The source and port position are located at the edge of the antenna. A Gaussian pulse is chosen as a source for the antenna. The simulation is performed for 6000 time steps.

The line-fed MPA with isotropic (ε_r=2.2 and μ_r=1) substrate is analyzed to prove the validity of the Lossy-ANI algorithm in comparison with that generated using the regular FDTD method. The scattering parameter (S_{11}) of the MPA, shown in Fig. 3, shows good agreement. The operating resonant lowest and highest frequencies are 7.68 GHz and 18.04 GHz, respectively.

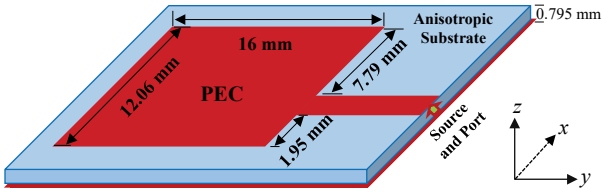

Fig. 2. A line-fed MPA with anisotropic substrate.

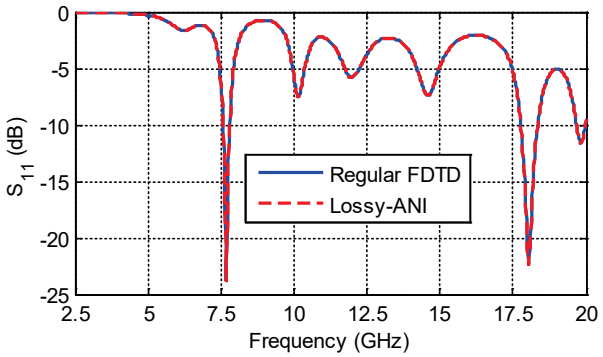

Fig. 3. S_{11} of the MPA with isotropic substrate obtained using the Lossy-ANI and the regular FDTD method.

Two different cases for the anisotropic substrate are then considered in new simulations. In the first case, the elements of permittivity and permeability tensors for the anisotropic substrate are given as follows:

$$\varepsilon_{xx} = \varepsilon_1 \cos^2\theta + \varepsilon_2 \sin^2\theta, \varepsilon_{yy} = \varepsilon_1, \varepsilon_{zz} = \varepsilon_1 \sin^2\theta + \varepsilon_2 \cos^2\theta$$
$$\varepsilon_{xz} = \varepsilon_{zx} = (\varepsilon_1 - \varepsilon_2) \sin\theta \cos\theta, \varepsilon_{xy} = \varepsilon_{yx} = \varepsilon_{yz} = \varepsilon_{zy} = 0$$
$$\mu_{xx} = \mu_1 \cos^2\theta + \mu_2 \sin^2\theta, \mu_{yy} = \mu_1, \mu_{zz} = \mu_1 \sin^2\theta + \mu_2 \cos^2\theta,$$
$$\mu_{xz} = \mu_{zx} = (\mu_1 - \mu_2) \sin\theta \cos\theta, \mu_{xy} = \mu_{yx} = \mu_{yz} = \mu_{zy} = 0 \quad (8)$$

where θ is the angle between the optical axis and the x-direction. For the second case, the elements of permittivity and permeability tensors for the anisotropic substrate are then given as follows:

$$\varepsilon_{xx} = \varepsilon_1, \varepsilon_{yy} = \varepsilon_1 \cos^2\phi + \varepsilon_2 \sin^2\phi, \varepsilon_{zz} = \varepsilon_1 \sin^2\phi + \varepsilon_2 \cos^2\phi$$
$$\varepsilon_{yz} = \varepsilon_{zy} = (\varepsilon_1 - \varepsilon_2) \sin\phi \cos\phi, \varepsilon_{xy} = \varepsilon_{yx} = \varepsilon_{xz} = \varepsilon_{xz} = 0$$
$$\mu_{xx} = \mu_1, \mu_{yy} = \mu_1 \cos^2\phi + \mu_2 \sin^2\phi, \mu_{zz} = \mu_1 \sin^2\phi + \mu_2 \cos^2\phi,$$
$$\mu_{yz} = \mu_{zy} = (\mu_1 - \mu_2) \sin\phi \cos\phi, \mu_{xy} = \mu_{yx} = \mu_{xz} = \mu_{zx} = 0 \quad (9)$$

where ϕ is the angle between the optical axis and the y-direction. The material parameters in (8) and (9) are set to ε_1=2.35, ε_2=2.05, μ_1=1.15, and μ_2=0.85.

In the first case for the anisotropic substrate, the S_{11} as a function of θ obtained using the Lossy-ANI algorithm is shown in Fig. 4. From Fig. 4, it can be observed that the lowest operating resonant frequency of the MPA is increasing if the angle θ is decreasing from $\pi/2$ to zero, whereas the highest operating resonant frequency of the MPA is decreasing. If the angle θ is chosen to be zero, $\pi/4$, and $\pi/2$, the operating resonant frequencies of the MPA at the lowest operating resonant are 7.4, 7.22, and 6.88 GHz, respectively, whereas at the highest operating resonant, they are 17.44, 18.25, and 18.9 GHz, respectively. The ratio of the number of cells in the region-ANI to that in the entire computational domain is 6.46%.

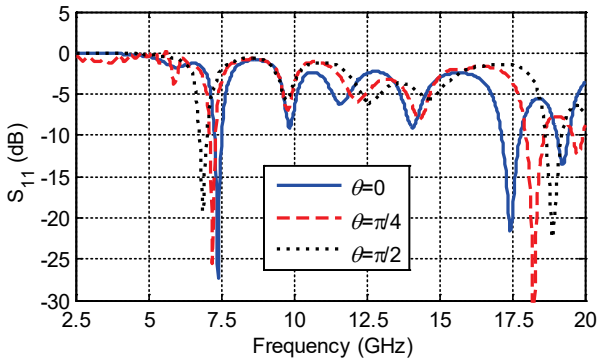

Fig. 4. S_{11} of the MPA as a function of θ obtained using the Lossy-ANI algorithm.

In the second case for the anisotropic substrate with the same material parameters used in (9), the S_{11} as a function of ϕ obtained using the Lossy-ANI algorithm is shown in Fig. 5. It can be observed from Fig. 5 that the operating resonance frequencies of the MPA are effected by the anisotropy in the substrate as those in the first case. The computation time of the MPA with the speeding up technique is 13 min 55 s, whereas those without the speeding up technique is 49 min 57 s. Therefore, the speeding up technique provides 72% reduction in the computation time.

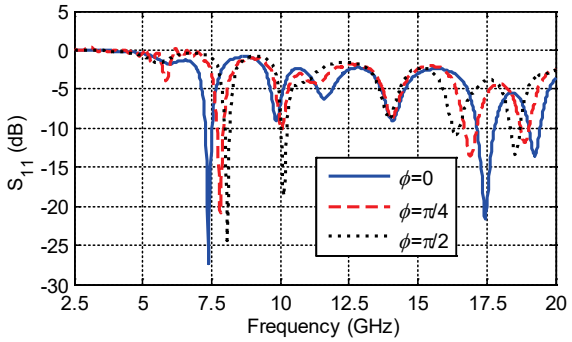

Fig. 5. S_{11} of the MPA as a function of ϕ obtained using the Lossy-ANI algorithm.

B. Lossy-ANI scattering object

To further verify the efficiency of the Lossy-ANI algorithm with the speeding up technique, a lossy anisotropic sphere with radius of 0.4 m, shown in Fig. 6, is analyzed. The discretization of the sphere in each direction is 0.025 m. This sphere is excited by a θ-polarized plane wave with θ^{inc}=90° and ϕ^{inc}=90°. The simulation is performed for 2000 time steps.

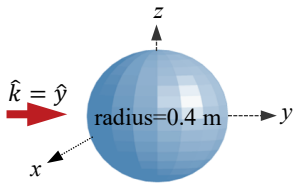

Fig. 6. Geometry of the lossy anisotropic sphere.

Three different cases for the anisotropic sphere are considered in this simulation. In the first case, the material parameters of the anisotropic sphere are given as follows:

$$\bar{\bar{\varepsilon}} = \varepsilon_o \begin{bmatrix} 2.2 & 1.8 & 0 \\ 1.8 & 2.2 & 0 \\ 0 & 0 & 2.2 \end{bmatrix}, \bar{\bar{\mu}} = \mu_o \begin{bmatrix} 2 & 1.6 & 0 \\ 1.6 & 2 & 0 \\ 0 & 0 & 2 \end{bmatrix}, \quad (10.a)$$

$$\bar{\bar{\sigma}}^e = \begin{bmatrix} 0.85 & 0.7 & 0 \\ 0.7 & 0.85 & 0 \\ 0 & 0 & 0.85 \end{bmatrix} \frac{s}{m}, \bar{\bar{\sigma}}^m = \begin{bmatrix} 0.65 & 0.5 & 0 \\ 0.5 & 0.65 & 0 \\ 0 & 0 & 0.65 \end{bmatrix} \frac{\Omega}{m}, \quad (10.b)$$

where $\bar{\bar{\varepsilon}}$, $\bar{\bar{\mu}}$, $\bar{\bar{\sigma}}^e$, and $\bar{\bar{\sigma}}^m$ are permittivity, permeability, electric and magnetic conductivity tensors, respectively. In the second case, the material parameters of the anisotropic sphere are given as follows:

$$\bar{\bar{\varepsilon}} = \varepsilon_o \begin{bmatrix} 2.2 & 0 & 1.8 \\ 0 & 2.2 & 0 \\ 1.8 & 0 & 2.2 \end{bmatrix}, \bar{\bar{\mu}} = \mu_o \begin{bmatrix} 2 & 0 & 1.6 \\ 0 & 2 & 0 \\ 1.6 & 0 & 2 \end{bmatrix}, \quad (11.a)$$

$$\bar{\bar{\sigma}}^e = \begin{bmatrix} 0.85 & 0 & 0.7 \\ 0 & 0.85 & 0 \\ 0.7 & 0 & 0.85 \end{bmatrix} \frac{s}{m}, \bar{\bar{\sigma}}^m = \begin{bmatrix} 0.65 & 0 & 0.5 \\ 0 & 0.65 & 0 \\ 0.5 & 0 & 0.65 \end{bmatrix} \frac{\Omega}{m}, \quad (11.b)$$

In the third case, the material parameters of the anisotropic sphere are given as follows:

$$\bar{\bar{\varepsilon}} = \varepsilon_o \begin{bmatrix} 2.2 & 0 & 0 \\ 0 & 2.2 & 1.8 \\ 0 & 1.8 & 2.2 \end{bmatrix}, \bar{\bar{\mu}} = \mu_o \begin{bmatrix} 2 & 0 & 0 \\ 0 & 2 & 1.6 \\ 0 & 1.6 & 2 \end{bmatrix}, \quad (12.a)$$

$$\bar{\bar{\sigma}}^e = \begin{bmatrix} 0.85 & 0 & 0 \\ 0 & 0.85 & 0.7 \\ 0 & 0.7 & 0.85 \end{bmatrix} \frac{s}{m}, \bar{\bar{\sigma}}^m = \begin{bmatrix} 0.65 & 0 & 0 \\ 0 & 0.65 & 0.5 \\ 0 & 0.5 & 0.65 \end{bmatrix} \frac{\Omega}{m}, \quad (12.b)$$

The bistatic RCSs for the three plane cuts (*xy*, *xz*, and *yz*) in Fig. 7 are computed at 300 MHz using the scattering fields from the anisotropic sphere for the three cases with the material parameters in (10)-(12) and compared with that generated using the scattering fields from the isotropic sphere when the material parameters are set to ε_r=2.2, μ_r=2, σ^e=0.85, and σ^m=0.65. It can be seen from Fig. 7 that the anisotropy in the sphere effects the magnitude of the RCS. The computation time of the anisotropic sphere with the speeding up technique is 4 min 12 s, whereas those without the speeding up technique 14 min 56 s. Therefore, the speeding up technique provides 72% reduction in the computation time for this scattering problem. The ratio of the number of cells in the region-ANI to that in the entire computational domain is 12.5%.

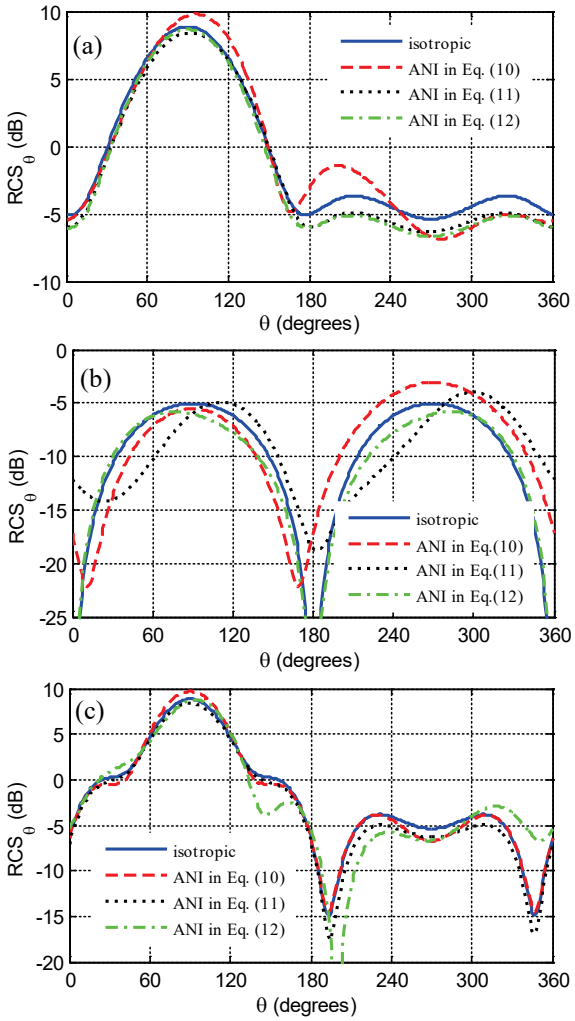

Fig. 7. Bistatic RCSs for: (a) *xy*, (b) *xz*, and (c) *yz* plane cuts.

IV. CONCLUSION

In this paper, the performance of a 3D FDTD algorithm based on the Lossy-ANI algorithm is presented in terms of computation time for solving the line-fed MPA with anisotropic substrate and the lossy anisotropic scattering object. The speeding up technique proposed here provides remarkable reduction in the computation time for configurations containing lossy anisotropic material. Numerical results show that the operating resonant frequencies of the MPA and magnitude of the bistatic RCS obtained from the scattering object are effected by the anisotropy of the material used.

REFERENCES

[1] J. Schneider and S. Hudson, "The finite-difference time-domain method applied to anisotropic material," *IEEE Trans. on Antennas and Propagation*, vol. 41, pp. 994-999, July 1993.

[2] D. Ge, L. Yang, B. Wei, N. Ge, and K. Zheng, "FDTD applied to lossy anisotropic medium and its parallel computing," *Proceedings of ISAP2005*, Seoul, Korea.

[3] L. X. Yang, G. Wang, and S. Yan, "Parallel ANI-FDTD implementation for electromagnetic scattering by both electric and magnetic anisotropic medium," *Microwave and Optical Technology Letters*, vol. 50, no. 5, May 2008.

[4] H. Zhang, Z. Li, Y. Wang, and J. Wang, "Studying on the parallel FDTD algorithm for calculating the EM scattering from anisotropic ellipsoid," *Cross Strait Quad-Regional Radio Science and Wireless Technology Conference (CSQRWC) IEEE, 2011*, vol. 1, 2011.

[5] D. Vidacic, "Assesment of FDTD Model Parameters for Lossy Media," *Diss. University of New Hampshire*, 2003.

[6] K.-Y. Jung, F. L. Teixeira, and R. Lee, "Complex envelope PML-ADI-FDTD method for lossy anisotropic dielectrics," *IEEE Antennas. Wireless Propag. Lett*., vol. 6, pp. 643-46, 2007.

[7] S. D. Gedney, "An anisotropic perfectly matched layer-absorbing medium for the truncation of FDTD lattices," *IEEE Trans. Antennas Propag*., vol. 44, no. 12, pp. 1630-1639, Dec. 1996.

[8] A. P. Zhao, J. Juntunen, and A. V. Raisanen, "An efficient FDTD algortihm for the analysis of microstrip patch antennas printed on a general anisotropic substrate," *IEEE Trans. Microwave Theory Tech.*, vol. 47, pp. 1142-1146, 1999.

[9] L. Dou and A. R. Sebak, "3D FDTD method for arbitrary anisotropic materials," *Microw. Opt. Technol. Lett.*, vol. 48, no. 10, pp. 2083-2090, 2006.

[10] M. Nauta, M. Okoniewski, and M. Potter, "FDTD method on a Lebedev grid for anisotropic materials," in *IEEE Trans. Antennas Propag*., vol. 61, no. 6, pp. 3161-3171, June 2013.

[11] D. M. Sheen, S. M. Ali, M. D. Abouzahra, and J. A. Kong, "Application of the three-dimensional finite-difference time-domain method to the analysis of planar microstrip circuits," *IEEE Trans. Microwave Theory Tech.*, vol. 38, pp. 849-857, July 1990.

[12] A. Z. Elsherbeni and V. Demir, *The Finite-Difference Time-Domain Method for Electromagnetics with MATLAB Simulations*. Second edition, ACES Series on Computational Electromagnetics and Engineering, SciTech Publishing, an Imprint of IET, Edison, NJ, 2016.

Fatih Kaburcuk was born in 1984, in Sivas, Turkey. He received both the M.Sc. and Ph.D. degrees from Syracuse University, Syracuse, New York in 2011 and 2014, respectively, all in Electrical Engineering. He worked as a Research Assistant for PPC-Belden, Inc., Syracuse, New York in 2013. He worked as a Visiting Research Scholar in the Electrical Engineering and Computer Science Department at the Colorado School of Mines in 2014. Currently, Kaburcuk is working as an Assistant Professor at the Department of Electrical and Electronics Engineering at Erzurum Technical University, Erzurum, Turkey. His research interest includes electromagnetic scattering and microwaves.

Atef Z. Elsherbeni received his Ph.D. degree in Electrical Engineering from Manitoba University, Winnipeg, Manitoba, Canada, in 1987. He was with the University of Mississippi from 1987 to 2013 and was a Finland Distinguished Professor from 2009 to 2011. In August 2013 he became the Dobelman Distinguished Chair Professor of Electrical Engineering at Colorado School of Mines. His research interest includes the scattering and diffraction of EM waves, finite-difference time-domain analysis of antennas and microwave devices, field visualization and educational software development, interactions of EM waves with human body, RFID and sensor integrated FRID systems, printed antennas and antenna arrays, and measurement of material properties. Elsherbeni is a Fellow Member of IEEE and ACES. He is the Editor-in-Chief for ACES Journal. He was the General Chair for the 2014 APS-URSI Symposium and was the President of ACES Society from 2013 to 2015.

Full-Wave Analysis of Microstrip Circuits with Reciprocal Matrix Compression Technique

Mengmeng Li [1,2], Chenhui Xia [1], and Rushan Chen [1]

[1] Communication Engineering
Nanjing University of Science and Technology, Nanjing, 210094, China
limengmeng@njust.edu.cn

[2] State Key Laboratory of Millimeter Waves
Najing, 210094, China

Abstract ─ We propose an efficient full-wave simulation method for microstrip circuits with reciprocal multilevel matrix compression method (rMLMCM). The mixed potential integral equation (MPIE) with the layered media Green's function is applied to the exterior layers of the packed interconnects. With quadtree structure, the dense impedance matrix is split up into the "near" and "far" terms according to the admission condition. The "near" term block matrices are full-rank, they are evaluated by the method of moments (MoM) directly. While the "far" term block matrices are low-rank, they are sparse filled and compressed by the rMLMCM. The rMLMCM low-rank approximation precisions of the block impedance matrices with respect to the decomposition thresholds are tested in detail. The current densities on the large-scale interconnects at high frequency are extracted much more effectively with the rMLMCM over the standard rank based methods. Numerical results demonstrate the validity of the proposed method.

Index Terms ─ Integral equation, matrix compression, microstrip circuits.

I. INTRODUCTION

The full wave electromagnetic (EM) simulations of microstrip interconnects are becoming more and more important in electronic packing with the continuing increase of the operating frequency and decrease of the sizes of modern high-speed integrated circuits. The full wave simulations of the high high-density interconnects on printed circuit boards (PCBs) attracted many researches [1]-[3].

The method of moments (MoM) [4] with the layered media Green's functions [5] has been a preferred method for the problem of interconnects in the exterior layers of PCBs. However, the MoM solver leads to the generation of a linear matrix equation $\mathbf{Zx} = \mathbf{V}$, where $\mathbf{Z}$ is a dense matrix. The solution of which requires $O(N^3)$ operations and $O(N^2)$ memory storage when to solve it directly, where N refers to the number of unknowns. The size of the MoM matrix increases so rapidly with the increase of the number of unknowns that the computation will be intractable for the computational capacity.

Therefore a suitable fast method is required to overcome the difficulties. Recently, the kernel independent methods such as IES^3 [6], adaptive cross approximation (ACA) [7], [8], multilevel matrix decomposition algorithm (MLMDA) [9], [10], H-matrix [11], and UV method [12]-[14], are widely researched because they are purely algebraic, kernel function independent and easy to be applied to accelerate the existing MoM codes. The rank-based methods take advantage of the rank-deficient nature of the coupling matrix blocks representing well-separated interactions. The interaction matrix $\mathbf{Z}_{m\times n}$ between two well separated groups can be approximated by the multiplication of matrices $\mathbf{U}_{m\times r}$ and $\mathbf{V}_{r\times n}$. r is the truncation rank of the interaction matrix, which is evaluated by means of predetermined threshold.

For the standard rank based methods [6]-[14], the low rank decomposition will be repeatedly implemented on each pair of far coupling groups, which leads to time and memory consuming process. In [15], a new multilevel matrix compression method (MLMCM) is proposed, where only one receiving matrix $\mathbf{U}$ and radiation matrix $\mathbf{V}$ are defined respectively, and the relative smaller dimension translators are defined between two coupling groups, when coupling with a cluster of its far interaction groups. As a result, the memory requirements and solution time can be saved significantly over the standard methods [6]-[14]. In [16], the radiation matrix is defined as the transpose of the receiving matrix, denoted as reciprocal MLMCM (rMLMCM), to further reduce the low rank approximation time and memory. Then it is employed to compress the near region of the standard multilevel fast multipole algorithm (MLFMA) [18], [19] for the electric field

Submitted On: July 24, 2015
Accepted On: October 11, 2016

integral equation (EFIE) when simulating the high-fidelity multiscale problems.

The contributions of the proposed work are: first, with the rMLMCM, we need to compute the low rank decomposition only once for each groups over the standard low rank method [6]-[14]; second, the rMLMCM proposed for the modeling of perfect electric conductor previously [16], is explored to accelerate the mixed potential integral equation (MPIE) with layered media Green's function. The rMLMCM low rank approximation precisions of the impedance matrices produced by two far coupling groups at different frequencies are first tested and validated in detail. Then the current densities on the large-scale interconnects are extracted with the standard rank based method (e.g., ACA) and the proposed rMLMCM, respectively, to show its advantages.

The remainder of the paper is organized as follows. The proposed algorithm for the simulation of the densely packed interconnects is described in Section II; numerical results in Section III demonstrate the validity of the proposed method. Finally, a brief conclusion is given in Section IV.

II. THEORY

Since the layered media Green's function is used, only the metallic surface of the microstrip circuits has to be meshed as the number of unknowns [5]. The surface of the interconnects are firstly discretized into triangular elements. The induced current on the metallic interconnects can be solved by the MPIE:

$$j\omega u_0 \hat{z}\times[\mathbf{A}(\mathbf{r})+\frac{1}{k_0^2}\nabla\Phi(\mathbf{r})]=\hat{z}\times\mathbf{E}^{inc}(\mathbf{r}), \quad (1)$$

where u_0 is the magnetic permeability, ω is the angular frequency. The vector and scalar potentials can be expressed as:

$$\mathbf{A}(\mathbf{r})=\iint_S \mathbf{G}^A(\mathbf{r},\mathbf{r}')\cdot J(\mathbf{r}')ds', \quad (2)$$

$$\Phi(\mathbf{r})=\iint_S G^q(\mathbf{r},\mathbf{r}')\cdot\nabla'\cdot\mathbf{J}(\mathbf{r}')ds', \quad (3)$$

$\mathbf{G}^A$ is the magnetic vector potential dyadic Green's function due to an electric current source and G^q is the Green's function of the scalar electric potential due to an electric charge. Then the current is expanded with Rao-Wilton-Glisson (RWG) basis functions [17]. The final linear matrix equation can be written as:

$$\mathbf{Zx}=\mathbf{V}, \quad (4)$$

where the elements of the impedance matrix $\mathbf{Z}$ and vector $\mathbf{V}$ are given by:

$$Z_{m,n}=j\omega u_0\iint_{T_m}\iint_{T_n}\mathbf{f}_m(r)\cdot\mathbf{f}_n(r')G^A(r,r')dr'dr + j\omega u_0\iint_{T_m}\iint_{T_n}\frac{1}{k_0^2}\nabla\cdot\mathbf{f}_m(r)\cdot\nabla'\cdot\mathbf{f}_n(r')G^q(r,r')dr'dr, \quad (5)$$

$$V_m=\iint_{T_m}E^{inc}(r)\cdot\mathbf{f}_m(r)dr. \quad (6)$$

It is known that the MoM matrix contains many low-rank sub-blocks which represent the interactions between two well-separated groups [6]-[16]. With this in mind, the rMLMCM starts by grouping the basis functions by the quadtree structure [13], [18], [19]. The grouping of basis functions splits the impedance matrix into a collection of submatrix blocks. In general, the submatrix is full-rank when the observation groups are in the near field of the source group, while the submatrix between them is low-rank when the observation groups are in the far field, the near and far region are defined according to the admission condition following. The rMLMCM is implemented in the case of low-rank submatrix. When accelerating the far part evaluation by the rMLMCM, the matrix-vector product $\mathbf{ZI}$ can be written as:

$$\mathbf{ZI}=\mathbf{Z}_N\mathbf{I}+\mathbf{Z}_F\mathbf{I}, \quad (7)$$

where $\mathbf{Z}_N$ is the near interaction part and $\mathbf{Z}_F$ is the far interaction part of $\mathbf{Z}$, respectively.

The quadtree structure of a densely packed interconnect with 31% interconnect fractional area is shown in Fig. 1. The admissibility condition is a criterion for judging whether a submatrix allows for a low rank approximation. A standard admissibility condition [7] is given as:

$$\mathrm{Min}\{diam(i), diam(j)\}\le\eta dist(i,j), \quad (8)$$

where *diam* and *dist* denote the group size and distance of the center of the two interaction groups respectively, and η is a parameter to control the region of the far coupling groups. In this paper, η is set to be 1. If groups i and j satisfy the admissibility condition, with the proposed MLMCM, the interaction matrix $\mathbf{Z}_{m\times n}$ can be expressed as:

$$[\mathbf{Z}_{i,j}]_{m\times n}=[\mathbf{U}_i]_{m\times r}[\mathbf{D}_{i,j}]_{r\times r}[\mathbf{V}_j]_{r\times n}, \quad (9)$$

where m, n is the number of source and testing basis functions in groups i and j respectively; r is the number of ε-rank with MGS and $r\ll\min(m,n)$.

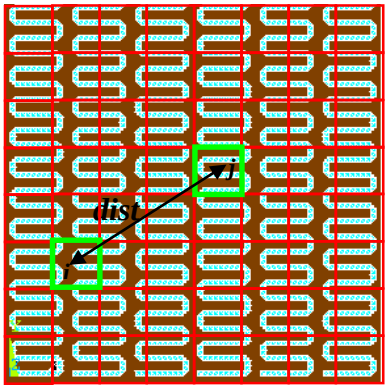

Fig. 1. The quadtree structure of a densely packed interconnect with 31% interconnect fractional area.

To construct the receiving matrix $[\mathbf{U}_i]$ for group i, as shown in Fig. 1, sampling fill the collection of columns of $[\mathbf{Z}_{i,1}, \mathbf{Z}_{i,2}, \mathbf{Z}_{i,3} \cdots]$ produced by group i against its far region groups with ACA, then a modified Gram-Schmidt (MGS) algorithm is used to the columns to get the orthogonal vectors, as the receiving matrix:

$$[\mathbf{U}_i] = \mathrm{MGS}[\mathbf{Z}_{i,1}, \mathbf{Z}_{i,2}, \mathbf{Z}_{i,3} \cdots]. \quad (10)$$

For the radiation matrix $[\mathbf{V}_j]$, it can be constructed repeatedly as in [15] from the collection of the columns $[\mathbf{Z}_{1,i}, \mathbf{Z}_{2,i}, \mathbf{Z}_{3,i} \cdots]^{\mathrm{T}}$. While in this work, we obtained from a more elegant way, it is defined as the transpose of the receiving matrix [16], [20], [21]:

$$[\mathbf{V}_j] = [\mathbf{U}_j]^{\mathrm{T}}. \quad (11)$$

Unlike (9), the receiving matrix now is now defined as:

$$[\mathbf{U}_i] = \mathrm{MGS}[\mathbf{Z}_{i,1}, \mathbf{Z}_{i,2}, \mathbf{Z}_{i,3} \cdots \mathbf{Z}_{1,i}{}^{\mathrm{T}}, \mathbf{Z}_{2,i}{}^{\mathrm{T}}, \mathbf{Z}_{3,i}{}^{\mathrm{T}} \cdots]. \quad (12)$$

For the the planar microstrip packaged interconnects in this work $\mathbf{Z}_{i,j} = \mathbf{Z}_{j,i}{}^{\mathrm{T}}$. As a result, (12) can be rewritten as:

$$[\mathbf{V}_j]^{\mathrm{T}} = [\mathbf{U}_j] = \mathrm{MGS}[\mathbf{Z}_{i,1}, \mathbf{Z}_{i,2}, \mathbf{Z}_{i,3} \cdots]. \quad (13)$$

Finally, the translator $[\mathbf{D}_{i,j}]$ can be defined as:

$$[\mathbf{D}_{i,j}] = [\mathbf{U}_i]^{\dagger}[\mathbf{U}_i][\mathbf{D}_{i,j}][\mathbf{V}_j][\mathbf{V}_j]^{\dagger} = [\mathbf{U}_i]^{\dagger}[\mathbf{Z}_{i,j}][\mathbf{V}_j]^{\dagger}, \quad (14)$$

where $[\bullet]^{\dagger}$ denotes the conjugate transpose; the ACA [7], [8] is used to compress $[\mathbf{Z}_{i,j}]$ this work.

Compared with the standard rank-based methods [6]-[14], for each group, we only construct one radiation matrix, and the truncated rank for the row and column spaces. The translator $[\mathbf{D}_{i,j}]$ with reduced dimension spans, up to a prescribed accuracy, both the row and column spaces of the original interaction matrix $[\mathbf{Z}_{i,j}]$. Compared with the MLMCM employed to simulate the scattering problems in free space [15], only one of the receiving and radiation matrices are stored, lead to about 1/3 time and memory consumption saving for the low rank decomposition. Furthermore, the rMLMCM is error controllable with the ε-rank and the threshold in ACA for multiscale problems [16], which guarantee the accuracy for the densely packed interconnects simulations.

III. NUMERICAL RESULTS

In this section, we show the results of the rMLMCM for the simulation of the densely packed interconnects. The truncation thresholds for the MGS and ACA decomposition are 10^{-4} if not specified, and the double floating point precision is used in the codes to guarantee the accuracy of the simulated results. All the simulations are performed on a personal computer with 2.8 GHz CPU and 8.0 GB RAM.

First, we test the rMLMCM low rank approximation error with respect to the threshold of the MGS and ACA. Without loss of generality, a square 20 mm × 20 mm microstrip patch, with thickness and dielectric constant of the substrates 1mm and 4, respectively, is tested. The simulated frequencies are 30, 15, 7.5, and 3.75 GHz, respectively, and the corresponding selected source/ testing group sizes are 0.5, 0.25, 0.125, and 0.0625 λ. There are 343 and 451 RWG basis functions in the selected source/testing groups. As shown in Fig. 2, we decrease the thresholds in the rMLMCM from 1e-3 to 1e-6, the low rank approximation error (defined as $\|\mathbf{Z}_{\mathrm{MoM}} - \mathbf{UDV}\|_2 / \|\mathbf{Z}_{\mathrm{MoM}}\|_2$, where $\|\cdot\|$ denotes the 2-norm) is decreasing with from 1e-2 to 1e-5, the order of the errors are decreasing in the same speed. This demonstrates the proposed rMLMCM is error controllable for the MPIE equation with layered media Green's function. It should be noted here, we use the predetermined threshold to compute **U**, **D**, and **V**, as a result, the error of the final low rank approximation will be enlarged compared with the predetermined threshold.

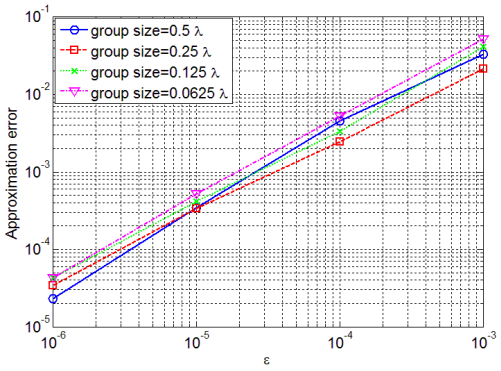

Fig. 2. Validation: the rMLMCM low rank approximation precision for the impedance matrix produced by two selected groups from a square miscrostrip patch with respect to the decomposition thresholds.

Next, a series of 4, 8, 16 and 32 meander lines traces with 31% interconnect fractional area as shown in Fig. 1 are simulated. The traces have a width of 1 mm, the thickness of the substrate is 0.25 mm, dielectric constant is 4 and the simulation frequency is 20 GHz. The numbers of unknowns are 1 628, 6 328, 24 943, and 99 040 respectively. The dimension of the simulated interconnects are 3.1 × 3.3, 6.3 × 6.5, 12.7 × 12.9 and 25.5 × 25.7 wavelengths. The minimum group size of the quadtree structure is 0.4 wavelengths, and the corresponding levels of the MLMCM chosen for the different electrical sizes are 2, 3, 4 and 5 respectively. The interconnects are excited by a delta gap voltage source on the lower end of the third trace. The amplitude and phase of the current densities along the excited trace of the 8 meander lines traces simulated by the MoM, three-level ACA and rMLMCM are plotted in Figs. 3 (a) and (b) respectively. Excellent agreements can be found. The relative error of

the ACA and the rMLMCM in the current densities versus the MoM is defined as $\|\mathbf{J}_{\text{Fast method}} - \mathbf{J}_{\text{MoM}}\|_2 / \|\mathbf{J}_{\text{MoM}}\|_2$. The norm errors are 1.1% and 1.0%, respectively. The amplitude and phase of the current densities along the excited trace of the large scale interconnects with 32 meander lines traces simulated by the five-level ACA and rMLMCM are plotted in Figs. 4 (a) and (b) respectively. Perfect agreements can also be found too. The relative error of the rMLMCM versus the ACA is 1.6%.

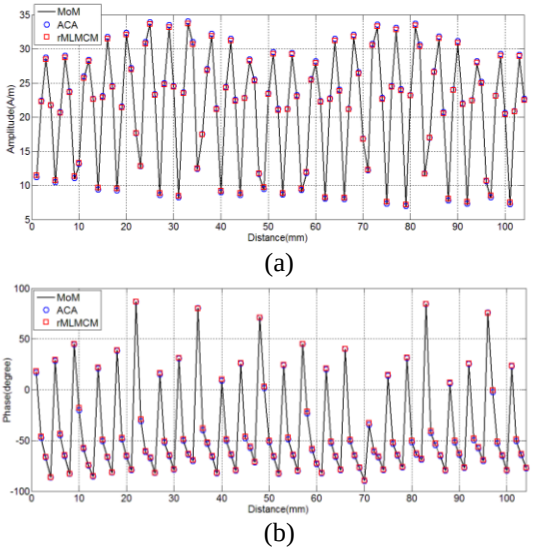

Fig. 3. The current densities along the excited trace at 20 GHz of the 8 meander lines traces simulated by the MoM, three-level ACA and rMLMCM respectively: (a) amplitude and (b) phase.

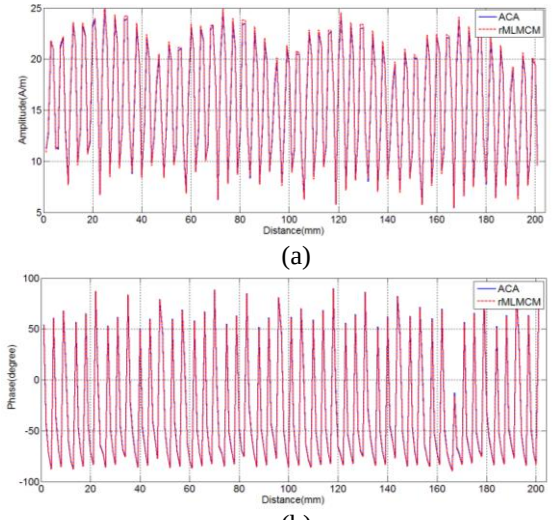

Fig. 4. The current densities along the excited trace at 20 GHz of the 32 meander lines traces simulated by five-level ACA and rMLMCM respectively: (a) amplitude and (b) phase.

Table 1 lists the memory requirements and CPU time when simulating the series of 4, 8, 16 and 32 meander lines traces by the ACA and the rMLMCM. The memory requirements of the near and far part are presented in column 3, significant reduction can be found in the far part by using the rMLMCM compared with the ACA. Therefore, total memory requirements are decreased significantly of the proposed rMLMCM. The set-up time to construct the low rank approximation matrices **U**, **D**, and **V** in column 4 of the rMLMCM is longer than the ACA, because the constructions of the radiation and translator matrices are based on the ACA low-rank decomposition, which requires additional operations of the matrices. The process can easily be accelerated by parallelization (e.g., OMP [22] or MPI [23]), as the low-ranked decompositions are evaluated independently with respect to each level and each group. Furthermore, this can be compensated by the more efficient matrix-vector product operation. It can be seen the total simulation time from the start to the end of the simulation (containing the near field evaluation, far field low rank approximation, and iterative solution) in column 5 will be reduced significantly, especially for larger number of traces.

Finally, we simulate the S parameters of the miniaturized band-pass microstrip filter, the dimension parameters can be found in Fig. 5, the permittivity and thickness of the substrate is 10.2 and 0.635 mm. The full MoM, two-level ACA, and two-level rMLMCM are employed to simulate the filter, respectively. The simulated frequency band is from 2 to 12 GHz, with discrete frequency points step of 0.25 GHz. Figure 6 plots the simulated S parameters with the two-level ACA, two-level rMLMCM, and measured data in [24]. Good agreement can be found between them. Table 2 list the computation time and memory consumption of the MoM, ACA, and rMLMCM at 6.75 GHz, it can be found with the proposed rMLMCM, both time and memory reduction can be obtained. When for the total 41 frequency points, significant total simulation time will be obtained. In this paper, we did not list the results of the MLFMA, because the MLFMA is Green's function dependent, the approximation of the layered Green's function will be more complex and less efficient when compared with the simulation of the problems in free space [25].

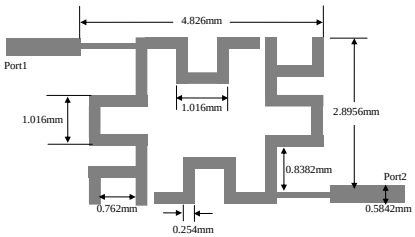

Fig. 5. Parameters of the band-pass microstrip filter.

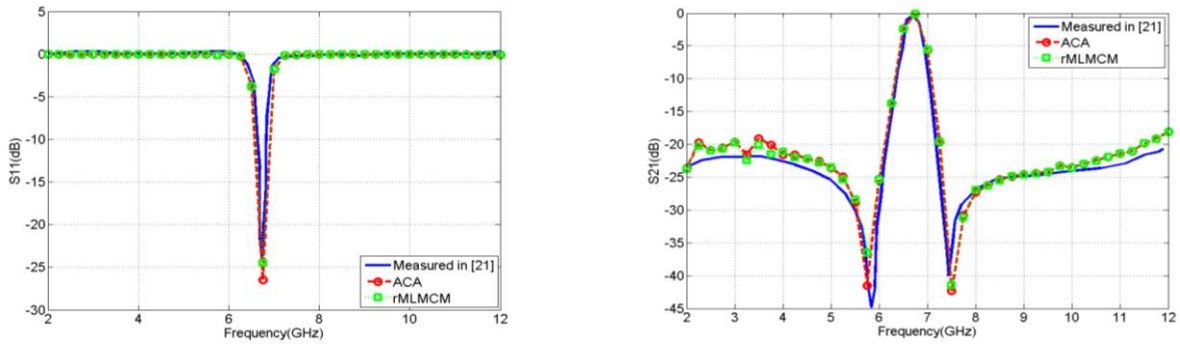

Fig. 6. Simulated results of the microstrip filter with two-level ACA and rMLMCM: (a) S11 and (b) S21.

Table 1: The memory and CPU time for the simulation of a series of 4, 8, 16 and 32 meander lines traces with ACA and rMLMCM

		Memory (MB) Near/Far Part	Set-up Time [mm:ss]	Total Time [hh:mm:ss]
4 traces	ACA	4.9/17.7	00:04	00:00:44
	rMLMCM	4.9/4.5	00:04	00:00:27
8 traces	ACA	19.8/129.4	00:31	00:06:15
	rMLMCM	19.8/23.5	00:32	00:03:11
16 traces	ACA	80.1/783.3	03:02	00:26:24
	rMLMCM	80.1/129.5	04:19	00:16:58
32 traces	ACA	320.9/4816.2	18:37	02:19:49
	rMLMCM	320.9/694.8	36:13	01:18:36

Table 2: The memory and CPU time for the simulation of the microstrip filter at 6.75 GHz with MoM, ACA, and rMLMCM

Methods	Frequency (GHz)	Far Memory (MB)	Solution Time [s]	Total Time [s]
MoM	6.75	53	199	347
ACA	6.75	8.3	117	176
rMLMCM	6.75	1.7	81	120

IV. CONCLUSION

In this paper, the rMLMCM is employed for the simulation of the large-scale microstrip circuits. The rMLMCM low-rank approximation precision is discussed in detail. When compared with the standard rank based method (e.g., ACA), the proposed rMLMCM is much more efficient for analyzing the large scale interconnects. Up to 32 meander lines traces with 31% interconnect fractional area are analyzed with moderate memory requirements and CPU time on a personal computer.

ACKNOWLEDGMENT

The authors would like to thank the support of Natural Science Foundation of 61501237, by the State Key Laboratory of Millimeter Waves Foundation under grant K201623, by the Fundamental Research Funds for the Central Universities under grant 30916015102 and NJ20160011.

REFERENCES

[1] Y. X. Sun, Q. Li, W. H. Yu, Q. H. Jiang, and Q. K. Zhuo, "Study on crosstalk between space transient interference microstrip lines using finite difference time domain method," *ACES Journal*, vol. 30, no. 8. pp. 891-897, Aug. 2015.

[2] M. Li, M. Chen, W. Zhuang, Z. Fan, and R. S. Chen, "Parallel SAI preconditioned adaptive integral method for analysis of large planar microstrip antennas," *ACES Journal*, vol. 25, no. 11, pp. 926-935, Nov. 2010.

[3] C. G. Parini, R. Dubrovka, and S. F. Gregson, "Computational electromagnetic modelling of compact antenna test range quiet zone probing," *ACES Express Journal*, vol. 1, no. 3, pp. 92-96, Mar. 2016.

[4] R. F. Harrington, *Field Computation by Moment Methods*. New York, MacMillan, 1968.

[5] Y. L. Chow, J. J. Yang, D. G. Fang, and G. E. Howard, "A closed-form spatial Green's function for the thick microstrip substrate," *IEEE Transaction on Microwave and Theory Technology*, vol. 3, pp. 588-592, 1991.

[6] S. Kapur and D. Long, "IES3: A fast integral equation solver for efficient 3-dimensional extraction," *in Proc. IEEE/ACM Int. Conf. Computer-Aided Design*, pp. 448-455, Nov. 1997.

[7] M. Bebendorf and S. Rjasanow, "Adaptive low-rank approximation of collocation matrices," *Computing*, no. 70, pp. 1-24, 2003.

[8] K. Zhao, M. N. Vouvakis, and J.-F. Lee, "The adaptive cross approximation algorithm for accelerated method of moments computations of EMC problems," *IEEE Trans. Electromagn. Compat*., vol. 47, no. 4, pp. 763-773, Nov. 2005.

[9] E. Michielssen and A. Boag, "A multilevel matrix decomposition algorithm for analyzing scattering from large structures," *IEEE Trans. Antennas Propag*., vol. 44, no. 8, pp. 1086-1093, Aug. 1996.

[10] J. M. Rius, J. Parrn, A. Heldring, J. M. Tamayo, and E. Ubeda, "Fast iterative solution of integral equations with method of moments and matrix decomposition algorithm-singular value decomposition," *IEEE Trans. Antennas Propag*., vol. 56, no. 8, pp. 2314-2324, Aug. 2008.

[11] S. Borm, L. Grasedyck, and W. Hackbusch, "Hierarchical Matrices," *Lecture note 21 of the Max Planck Institute for Mathematics in the Sciences*, 2003.

[12] L. Tsang, Q. Li, P. Xu, D. Chen, and V. Jandhyala, "Wave scattering with UV multilevel partitioning method: 2. Three-dimensional problem of non-penetrable surface scattering," *Radio Sci*., vol. 39, p. RS5011, 2004.

[13] M. Li, J. J. Ding, D. Z. Ding, Z. H. Fan, and R. S. Chen "Multiresolution preconditioned multilevel UV method for analysis of planar layered finite frequency selective surface," *Microw. Opt. Tech. Lett*., vol. 52, no. 7, pp. 1530-1536, July 2010.

[14] C.-J. Ong and L. Tsang, "Full-wave analysis of large-scale interconnects using the multilevel UV method with the sparse matrix iterative approach (SMIA)," *IEEE Trans. Adv. Packag*., vol. 31, no. 4, pp. 818-829, Nov. 2008.

[15] M. Li, C. Y. Li, C.-J. Ong, and W. C. Tang, "A novel multilevel matrix compression method for analysis of electromagnetic scattering from PEC targets," *IEEE Trans. Antennas Propag*., vol. 60, no. 3, pp. 1390-1399, Mar. 2012.

[16] M. Li, M. A. Francavilla, F. Vipiana, G. Vecchi, Z. H. Fan, and R. S. Chen, "A doubly hierarchical MoM for high-fidelity modeling of multiscale structures," *IEEE Trans. Electromagn. Compat.*, vol. 56, no. 5, pp. 1103-1111, Oct. 2014.

[17] S. M. Rao, D. R. Wilton, and A. W. Glisson, "Electromagnetic scattering by surfaces of arbitrary shape," *IEEE Trans. Antennas Propag*., vol. 30, no. 3, pp. 409-418, May 1982.

[18] J. M. Song and W. C. Chew, "Multilevel fast multipole algorithm for solving combined field integral equation of electromagnetic scattering," *Microw. Opt. Tech. Lett*., vol. 10, no. 1, pp. 14-19, Sep. 1995.

[19] J. M. Song, C. C. Lu, and W. C. Chew, "Multilevel fast multipole algorithm for electromagnetic scattering by large complex objects," *IEEE Trans. Antennas Propag*., vol. 45, no. 10, pp. 1488-1493, Oct. 1997.

[20] J.-G, Wei, Z. Peng, and J.-F. Lee, "A fast direct matrix solver for surface integral equation methods for electromagnetic wave scattering from non-penetrable targets," *Radio Sci*., vol. 47, pp. RS5003, 2012.

[21] P. G. Martinsson, "A fast randomized algorithm for computing a hierarchically semiseparable representation of a matrix," *SIAM J. Matrix Anal. Appl*., vol. 32, no. 4, pp. 1251-1274, 2011.

[22] L. Dagum and R. Menon, "OpenMP: An industry standard API for shared-memory programming," *Computational Science & Engineering, IEEE*, vol. 5, no. 1, pp. 46-55, 1998.

[23] *The MPI Forum*, "MPI: A Message-Passing Interface Standard," Knoxville, TN, USA, Tech. Rep., 1994.

[24] B. L. Oci, Y. Wang, and H. Y. Fong, "Experimental study of new planar filter without using cross-coupled effect," *IEE Proc.-Microw. Antennas Propag*., vol. 153, no. 3, pp. 226-230, June 2006.

[25] Y. P. Chen, J. L. Xiong, and W. C. Chew, "A mixed-form thin-stratified medium fast-multipole algorithm for both low and mid-frequency problems," *IEEE Trans. Antennas Propag*., vol. 59, no. 6, pp. 2341-2349, June 2011.

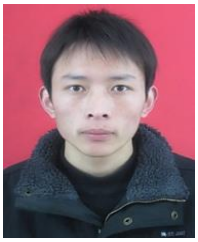

Mengmeng Li received the B.S. (Hons.) degree in Physics from Huaiyin Normal College, Huai'an, China, in 2007, and the Ph.D. degree in Electromagnetic Field and Microwave Technology from Nanjing University of Science and Technology, Nanjing, China, in 2014.

From 2012 to 2014, he carried out fast solver for multiscale simulations as a Visiting Student at the Electronics Department, Politecnico di Torino and Antenna and EMC Laboratory (LACE), Istituto

Superiore Mario Boella (ISMB), Torino, Italy. Since 2014, he has been with the Department of Communication Engineering, Nanjing University of Science and Technology, as an Assistant Professor. His research interests include fast solver algorithms, computational electromagnetic solvers for circuits, signal integrity analysis, and multiscale simulations.

Li was the recipient of the Student Paper Award (top 5 of 260) at the International Conference on Microwave and Millimeter Wave Technology in 2012.

Chenhui Xia received the B.Sc. degree in Electronic Engineering from Taizhou Institute of Science and Techbology in 2015. Now he is pursuing the master degree in Electromagnetic Field and Microwave Technology, His research interest is antenna design and optimization.

Rushan Chen received the B.Sc. and M.Sc. degrees from the Department of Radio Engineering, Southeast University, China, in 1987 and 1990, respectively, and the Ph.D. degree from the Department of Electronic Engineering, City University of Hong Kong, in 2001.

He joined the Department of Electrical Engineering, Nanjing University of Science and Technology (NJUST), China, where he became a Teaching Assistant in 1990 and a Lecturer in 1992. Since September 1996, he has been a Visiting Scholar with the Department of Electronic Engineering, City University of Hong Kong, first as Research Associate, then as a Senior Research Associate in July 1997, a Research Fellow in April 1998, and a Senior Research Fellow in 1999. From June to September 1999, he was also a Visiting Scholar at Montreal University, Canada. In September 1999, he was promoted to Full Professor and Associate Director of the Microwave and Communication Research Center in NJUST, and in 2007, he was appointed Head of the Department of Communication Engineering, NJUST. He was appointed as the Dean in the School of Communication and Information Engineering, Nanjing Post and Communications University in 2009. And in 2011 he was appointed as Vice Dean of the School of Electrical Engineering and Optical Technique, Nanjing University of Science and Technology. His research interests mainly include microwave/millimeter-wave systems, measurements, antenna, RF-integrated circuits, and computational electromagnetics. He has authored or co-authored more than 200 papers, including over 140 papers in international journals.

Chen received the 1992 Third-Class Science and Technology Advance Prize given by the National Military Industry Department of China, the 1993 Third-Class Science and Technology Advance Prize given by the National Education Committee of China, the 1996 Second-Class Science and Technology Aadvance Prize given by the National Education Committee of China, and the 1999 First-Class Science and Technology Advance Prize given by Jiangsu Province, as well as the 2001 Second-Class Science and Technology Advance Prize. He is the recipient of the Foundation for China Distinguished Young Investigators presented by the National Science Foundation (NSF) of China in 2003. In 2008, he became a Chang-Jiang Professor under the Cheung Kong Scholar Program awarded by the Ministry of Education, China. Besides, he was selected as a Member of Electronic Science and Technology Group by Academic Degree Commission of the State Council in 2009. Chen is a Senior Member of the Chinese Institute of Electronics (CIE), Vice-Presidents of Microwave Society of CIE and IEEE MTT/APS/EMC Nanjing Chapter. He serves as the Reviewer for many technical journals such as IEEE Trans. on AP and MTT, Chinese Physics etc., and now serves as an Associate Editor for the International Journal of Electronics.

Finite Element Analysis of Three Dimensional Complex Scatterers in Layered Media

Xuewei Ping [1], Xinghui Yin [1], Li Li [1], Changli Li [1], and Qingbo Li [2]

[1] College of Computer and Information Engineering
HoHai University, Nanjing, 211100, Jiangsu, China
xwping@hhu.edu.cn, xhyin@hhu.edu.cn, lili_lee@hhu.edu.cn, charlee@hhu.edu.cn

[2] Jiangsu Key Construction Laboratory of Modern Measurement Technology and Intelligent System
Huaiyin Normal University, Huai'an, 223300, China
qingboli12@126.com

Abstract ─ In this paper, an efficient three-dimensional finite-element method (FEM) is introduced to study the scattering from complex three-dimensional objects in the layered media. The proposed method is valid to targets which are located either close to or far away from the media interface. Furthermore, the interface can be either a planar or rough surface in the computational domain. To improve efficiency, the preconditioned conjugate gradient method for normal equations (CGN) are proposed to solve the FEM linear system. Numerical examples are presented to demonstrate the accuracy and efficiency of the presented method.

Index Terms ─ Complex objects, electromagnetic scattering, finite element method, layered media.

I. INTRODUCTION

The investigation of complex electromagnetic (EM) scattering characteristic of targets in the layered media has been of interest due to extensive applications, such as near-surface geophysical exploration, investigation of automobiles and other vehicles over road or terrain surfaces and landmine detection, etc. A viable and efficient way to deal with this kind of problem is to use analytical or numerical simulation methods. Ref. [1] developed the analytical expressions for calculating scattering from buried homogeneous objects in a low-contrast situation for several geometries. For complex media or complex structures, numerical methods have to be used. The method of moment (MOM)-based techniques [2-5], such as the multilevel fast multipole algorithm (MLFMA) [2-3], the conjugate gradient method and fast Fourier transform (CG-FFT) [4], are efficient ways for the numerical simulations of the perfectly electrical conducting (PEC) objects or homogeneous dielectric objects. The principle challenge of MOM to solve the scattering problems in half space or layered media is the evaluation of the spatial dyadic Green's function (SDGF), each component of which is expressed in an oscillatory Sommerfeld integration. Furthermore, these methods is most suitable for structures only contain perfectly conductors, and are less efficient in solving complex media.

Another efficient method to deal with scattering problems in layered media is the finite-difference time-domain (FDTD) method [6-8]. The deficiency of FDTD is that the stair-cased meshing can lead to inaccuracy in modeling complex geometries, though the application of conformal meshes can alleviate this deficiency for some extent. For problems containing complex structures or dispersion medium, the finite element method is the most suitable method. In this paper, a three-dimensional (3D) tangential vector finite element method (TVFEM) is introduced to simulate the scattering characteristics of targets in the presence of air-earth interface.

The advantage of TVFEM is that it can cope with material discontinuities as well as complex structures in a natural way. In the past a few decades, TVFEM has been paid much attention and have developed rapidly in theory and practical applications [9-12]. However, in most of the published FEM research contributions, the influence of the background medium is rarely considered. Some investigations on FEM simulation of buried scatterers are as follows. In [13], a 2D planar anisotropic perfectly matched layer for the FEM mesh truncation tool was investigated for electromagnetic scattering by buried objects. However, the detailed FEM process to simulate buried objects was not given. In [14], a 2-D FEM model is set up based on the Monte Carlo method for predicting the statistical properties of the electromagnetic scattering from objects on or above random rough sea surfaces. In [15-19], the combination of finite-element and the boundary-integral (FEBI) method are proposed. This kind of methods can solve complex structures. However, the sparsity of the FEM matrix will be destroyed, which will make the solution

Submitted On: April 18, 2016
Accepted On: October 25, 2016

of the FEM linear system difficult.

In this paper, we propose an efficient 3D FEM based on scattered electric field to solve the scattering problems in multi-layered media. From the FEM process given below, it can be seen that the computational efficiency of this method for targets in multi-layered media is comparable with that for targets in free space.

II. FORMULATION

The FEM computational domain for a typical scattering problem in layered media is shown in Fig. 1. The scattering target is formed with arbitrary media, such as inhomogeneous dielectrics, metals, etc. The permittivity and permeability of the media within any point of the computational domain are denoted as ε_r and μ_r respectively. In order to truncate the FEM computational domain, the outer boundary of the scattering target is lined with absorbing perfectly matched layers (PMLs). In order to consider the affection of the air-earth interface to the scattered field, the interface has to be included in the computational domain. For simplicity, the computational domain is denoted as Ω, the region occupied by the scatterer is denoted as Ω_{sc}, the bounding surface of the scatterer is denoted as S, the normal vector of the bounding surface is *n*. For simplicity, only plane wave is discussed in this paper. The incident wave is denoted as E_i, the reflected and transmitted fields due to E_i is denoted as E_r and E_t. For simplicity, the propagation direction of incident wave is supposed to be in the xz plane, and the incident angle is θ_i.

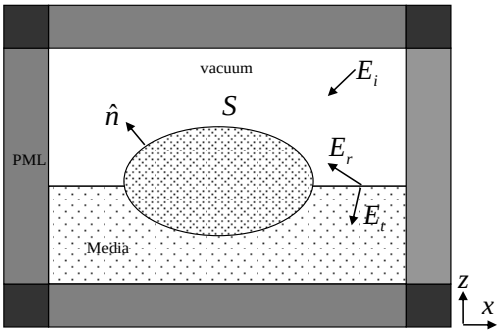

Fig. 1. Illustration of the FEM computational domain of scattering targets in layered media.

For TE modes, the incident, reflected and transmitted fields can be expressed as follows:

$$\begin{aligned} E_i &= E_0 \bar{y}\, e^{-jk_0(x\cdot\sin\theta_i + z\cdot\cos\theta_i)} \\ E_r &= R^{TE} E_0 \bar{y}\, e^{-jk_0(x\cdot\sin\theta_i - z\cdot\cos\theta_i)} \\ E_t &= T^{TE} E_0 \bar{y}\, e^{-jk_0\sqrt{\varepsilon_r\mu_r}(x\cdot\sin\theta_t + z\cdot\cos\theta_t)} \end{aligned} \quad . \tag{1}$$

For TM modes:

$$\begin{aligned} E_i &= E_0\, e^{jk_0(x\cdot\sin\theta_i + z\cdot\cos\theta_i)}\left(\cos\theta_i \bar{x} - \sin\theta_i \bar{z}\right) \\ E_r &= -R^{TM} E_0\, e^{jk_0(x\sin\theta_i - z\cos\theta_i)}\left(\cos\theta_i \bar{x} + \sin\theta_i \bar{z}\right) \\ E_t &= T^{TM} E_0\, e^{jk_0\sqrt{\varepsilon_r\mu_r}(x\cdot\sin\theta_t + z\cdot\cos\theta_t)}\left(\cos\theta_t \bar{x} - \sin\theta_t \bar{z}\right) \end{aligned} \quad . \tag{2}$$

If the propagation direction of incident wave is not in the xz plane, the expression of E_i, E_r and E_t can be obtained by Equation (1) and Equation (2) through coordinate rotation. The equivalent incident electric field on the surface of the targets above the air-earth interface can be obtained with the reflection coefficient approximation formulation:

$$E^{inc} = E_i + E_r . \tag{3}$$

And the equivalent incident electric field obtained with the reflection coefficient approximation below the air-earth interface is:

$$E^{inc} = E_t . \tag{4}$$

To derive the FEM formulation, the vector wave equation based on electric field is written:

$$\nabla\times\left(\mu_r^{-1}\cdot\nabla\times E\right) - k_0^2\varepsilon_r\cdot E = 0 , \tag{5}$$

where $k_0 = \omega\sqrt{\mu_0\varepsilon_0}$, E is the total electric field, which can be decomposed into two parts:

$$E = E^{sc} + E^{inc} , \tag{6}$$

where E^{sc} is the scattered field of the targets, E^{inc} is the equivalent incident field given by Equation (3) and Equation (4).

In FEM simulation, it is more efficient to work with the scattered electric field than the total electric field E. By substituting (6) into Equation (5), one obtains:

$$\begin{aligned} &\nabla\times\left(\mu_r^{-1}\cdot\nabla\times E^{sc}\right) - k_0^2\varepsilon_r\cdot E^{sc} \\ &= -\nabla\times\left(\mu_r^{-1}\cdot\nabla\times E^{inc}\right) + k_0^2\varepsilon_r\cdot E^{inc} \end{aligned} . \tag{7}$$

According to the generalized variational principle, the functional pertinent to the scattering field is written [9]:

$$\begin{aligned} F(E^{sc}) = \frac{1}{2}\int_{\Omega} &[(\nabla\times E^{sc})\cdot\mu_r^{-1}\cdot(\nabla\times E^{sc}) \\ &- k_0^2 E^{sc}\cdot\varepsilon_r\cdot E^{sc}]dV \\ &+ \int_{\Omega_{sc}} [(\nabla\times E^{sc})\cdot\mu_r^{-1}\cdot(\nabla\times E^{inc}) \\ &- k_0^2 E^{sc}\cdot\varepsilon_r\cdot E^{inc}]dV \\ &+ \int_{\Gamma_{sc}} \left[E^{sc}\cdot\hat{n}\times\nabla\times E^{inc}\right]dS \end{aligned} . \tag{8}$$

Note that in the derivation of Equation (8), the following formulation is used:

$$\nabla\times\nabla\times E^{inc} - k_0^2 E^{inc} = 0 . \tag{9}$$

In this paper, tetrahedron elements are used for mesh discretization, the scattered field within each element is expanded with H_0(curl) basis.

III. THE PRECONDITIONED CGN SOLVER

Using the Ritz variational or Galerkin method [9], a large sparse algebraic linear system is obtained, which can be written into the following form:

$$\mathbf{A}x = b, \tag{10}$$

with $\boldsymbol{A} \in \boldsymbol{C}^{n\times n}$, b, $x \in \boldsymbol{C}^{n}$.

As is well known, the efficiency of FEM is mainly determined by the efficiency of solving Equation (10). There are many different methods to solve Equation (10) [20-24]. For small problems, the multifrontal method always has satisfactory behavior. However, iterative methods are better choice, as which can save a great deal of memory compared with direct methods. In this paper, the preconditioned conjugate gradient for normal equations (PCGN) method [9] are proposed for the finite element solution of scattering problems. The FSAI-CGN solver proposed in [24] is especially investigated to solve the FEM linear systems generated from targets in the presence of air-earth interface. Though this method is less efficient than ICCG [23], however, it is very stable. What's more, it is very suitable for parallel, which is an important property as the ability to solve large 3D FEM linear systems is most meaningful.

IV. FURTHER DISCUSSIONS

In theory, the above process for the formation of the FEM linear system is applicable for any scatterers in the presence of air-earth interface. However, when the targets are placed far away from the interface, the whole computational domain will be very large and make the method very inefficient or even infeasible because both the targets and the region near the interface have to be included in the FEM computational domain. To overcome this difficulty, the simplified FEM model in Fig. 2 is recommended.

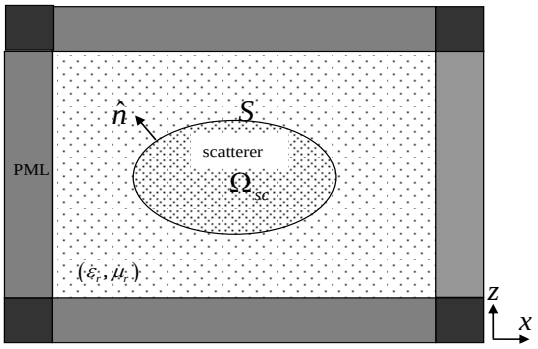

Fig. 2. Illustration of the FEM computational domain when scattering targets is far away from the interface.

In this model, only the region near the targets is included in the computational domain, the air-earth interface is not necessarily included. However, the total incident wave is still computed with Equations (3) and (4). In this model, the contribution of the interface to the scattered field is omitted. When the targets are placed far away from the interface, this simplification won't influence the accuracy of FEM. However, the efficiency is greatly enhanced.

In the deduction of the FEM formulations, the air-earth interface is assumed to be infinitely large and planar. However, this is not always the case in practical applications. In fact, the air-earth interface is not necessarily planar in the proposed algorithm. Let's see the problem shown in Fig. 3. In this problem, the interface above the scattering target is full of bumps and hollows; in other places, the interface is planar.

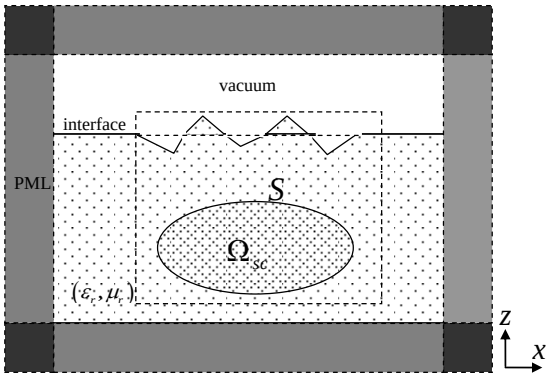

Fig. 3. Illustration of the FEM model when the air-earth interface is not planar in the computational domain.

This kind of problem can also be dealt with using the proposed method by treating the earth above the interface and the air below the interface as scatterers. If the far field and RCS are computed, the integration will be done on the surface expressed with the dashed line. If the air-earth interfaces are all rough in any places, the proposed method is no longer applicable because the excitation wave on the scatterers can no longer be expressed by Equation (3) and Equation (4).

In the next section, the proposed method is applied to analyze the scattering characteristics of some targets in the existence of layered media to validate the accuracy of the proposed method.

V. NUMERICAL RESULTS

The first example is the scattering characteristics of a perfectly conducting (PEC) sphere with radius 1.0λ half buried in the earth. The electric constant of the earth is $\varepsilon_r = 2.0 - 0.1j$, $\mu_r = 1.0$. The illustrated wireframe of the FEM model for this problem in the xz plane is shown in Fig. 4. In order to apply FEM simulation, the problem is divided into 550008 tetrahedrons, with the average mesh size 0.05λ. The number of FEM unknown edges generated is 676788. To validate the accuracy of 3D FEM, this problem is simulated with the software FEKO,

in which MOM combined with exact Sommerfeld integration is selected. The mesh in FEKO are also chosen to be 0.05λ, and the number of triangle meshes is 13868. In Fig. 5, the VV polarized bi-static radar cross sections of the PEC sphere is computed, the incident angle is $\theta = 0^o, \varphi = 0^o$. The comparison of FEM results with the simulated results by FEKO is depicted in the figure. Good agreements are found in both figures.

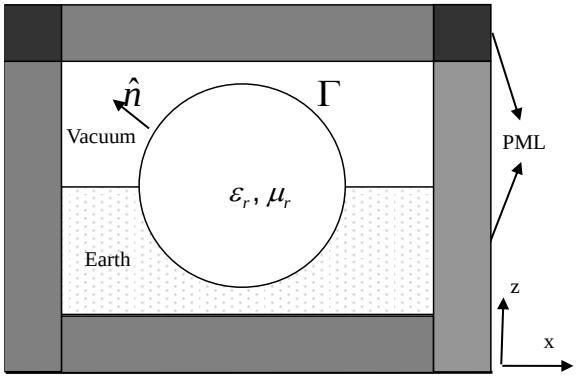

Fig. 4. Illustration of the FEM computational domain of a PEC sphere half buried in the earth.

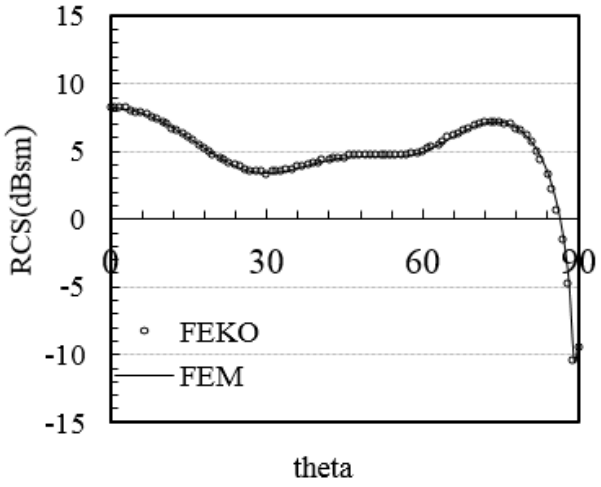

Fig. 5. Bi-static radar cross sections of the PEC sphere half buried in the earth.

In solving the finite element system, the comparison of different preconditioned CGN solvers are made. The convergence curves of D-CGN, SSOR-CGN and FSAI-CGN are shown in Fig. 6. In Table 1, the CPU time and memory are listed. From the table, it can be seen that the finite element method is more efficient than FEKO in solving this problem. It should be noted that, as the FEM matrix is symmetric, only half should be stored. The SSOR preconditioner is not necessary to be stored as it is the same as half of the matrix.

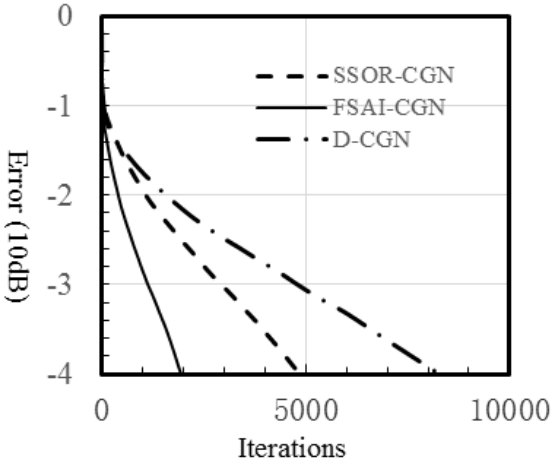

Fig. 6. Iterative behaviors of different solvers for finite element simulation of the PEC sphere half buried in the earth.

Table 1: CPU time and memory comparison of different methods

Solver		CPU Time (sec)	Memory (MB)
MOM		8415.8	3452
FEM	D-CGN	1360	283.0
	SSOR-CGN	1031	315.5
	FSAI-CGN	585	431.5

In the followings, the accuracy of the FEM algorithm for targets placed far away from the interface is tested. The same PEC sphere is placed 3.5λ below the interface. The simplified FEM model in Fig. 2 is used. The computation region is uniformly discretized with 0.05λ mesh size. For comparison, the FEKO is meshed with 0.05λ, the number of triangle meshes is 13868. The comparison of FEM results with the simulated results by FEKO is depicted in Fig. 7. Good agreements are found. This showed that 3D FEM can accurately simulate the targets placed far away from the air-earth interface. In this example, the CPU time used by FEKO is 8213 sec, the peak memory is 3.238 GB. The CPU time used by FEM with FSAI-CGN solver is 366 sec, the memory is 431.5 MB.

The third example tested is the bistatic scattering of a $2.5\lambda \times 2.5\lambda \times 0.2\lambda$ PEC brick buried below the earth. Assuming the electric constant of the earth is $\varepsilon_r = 4.0 - 0.2j$, $\mu_r = 1.0$. The incident angle is $\theta = 0^o$, $\varphi = 0^o$. In this case, the problem is uniformly discretized with the average mesh size 0.05λ. As a result, 802720 tetrahedrons and 954211 unknown edges are generated. Figure 8 showed the VV polarized bi-static RCS results simulated with 3D FEM and with FEKO. In this example, the mesh is 0.05λ in FEKO, the number of patches is

16220. The CPU time used by FEKO is 7591 sec. The peak memory is 4.4 GB. The CPU time used by FEM with FSAI-CGN solver is 1428 sec, the memory used is 616.5 MB.

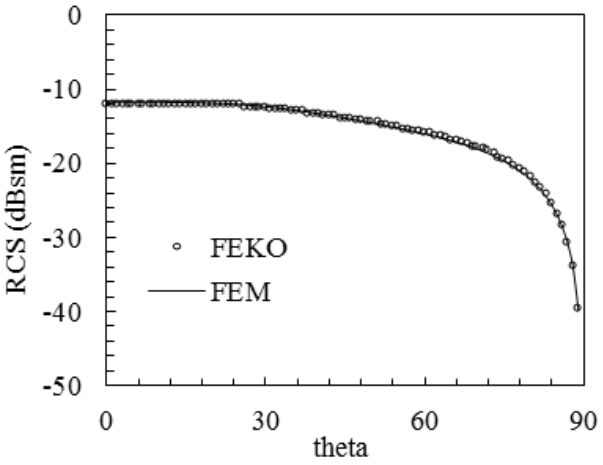

Fig. 7. Bi-static radar cross sections of the PEC sphere buried 3.5λ below the earth.

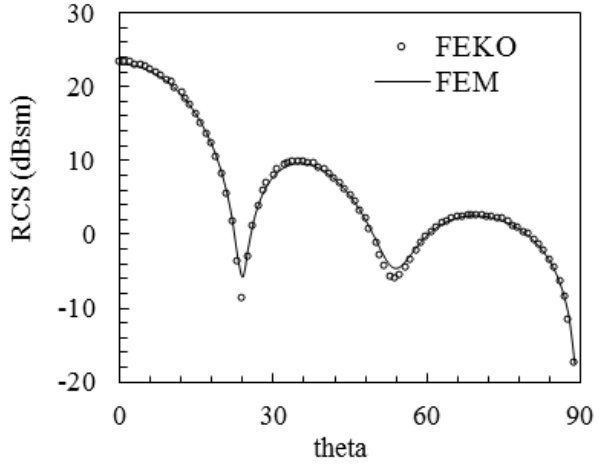

Fig. 8. Bi-static radar cross sections of a $2.5\lambda \times 2.5\lambda \times 0.2\lambda$ PEC cube buried below the earth.

As have been noted above, one advantage of FEM is that it can deal with complex dielectric materials. However, dielectric media buried under earth is hard to be simulated with FEKO. To validate the accuracy of FEM in simulating dielectrics, here a compound cube buried 0.1λ below the earth is computed. The cube is formed by a $2.5\lambda \times 2.5\lambda \times 0.2\lambda$ dielectric cube placed above the $2.5\lambda \times 2.5\lambda \times 0.2\lambda$ PEC cube. The permittivity of the dielectric cube is equal to the permittivity of the earth, i.e., $\varepsilon_r = 4.0 - 0.2j$. The incident angle is θ=0°, φ=0°. In Fig. 9, the RCS results of the compound cube and the RCS results of the PEC cube are compared, two results agreed quite well.

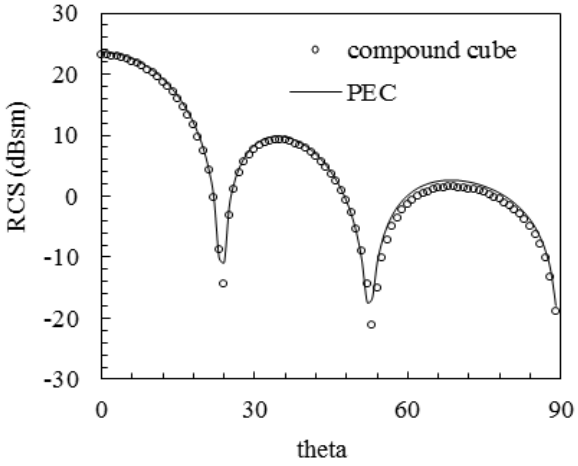

Fig. 9. Bi-static radar cross sections of the PEC cube and the compound cube buried 0.1λ below the earth.

Next, we assume the interface is not planar. There are many $0.1\lambda \times 0.1\lambda \times 0.2\lambda$ cavities uniformly distributed on the interface above the PEC brick, the distance between two nearest cavities is 0.1λ. The illustrated figure is shown in Fig. 10. The VV polarized Bi-static RCS results simulated with 3D FEM when the incident angle is θ=0° is shown in Fig. 11.

This problem cannot be simulated by FEKO. For comparison, the results for planar interface are also drawn in the figure. Two results are quite similar, but the RCS value for the interface with many cavities is a little smaller than that for plane interface in most angles. This is reasonable because the incident angle is perpendicular to the interface.

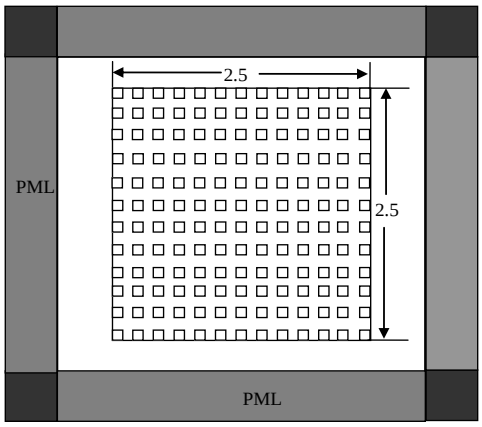

(a) Top view

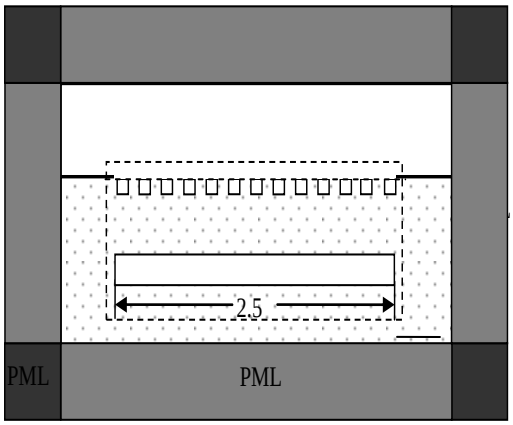

(b) Side view

Fig. 10. Illustration of the FEM computational domain of a PEC brick placed below the rough interface.

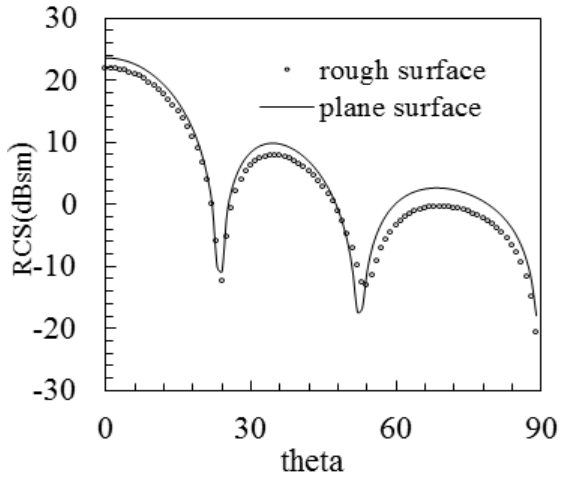

Fig. 11. Bi-static radar cross sections of the $2.5\lambda\times2.5\lambda\times0.2\lambda$ PEC brick when the air-earth interface is rough.

The next example tested is the bistatic scattering of a $5\lambda\times5\lambda\times5\lambda$ brick buried 0.3λ below the earth. Assuming the electric constant of the earth is $\varepsilon_r = 4.0-0.2j$, $\mu_r = 1.0$. The incident angle is θ=0^o, φ=0^o. Firstly, assuming the brick is PEC. The problem is uniformly discretized with the average mesh size 0.05λ, the generated tetrahedrons and unknown edges are respectively 4,072,000 and 4,662,546. Secondly, the brick is assumed to be dielectric with electric constant ε_r=2.0, μ_r=1.0. With mesh size 0.05λ, a total of 9,072,000 tetrahedrons and 10,752,846 unknowns are obtained. Figure 12 showed the simulated bi-static RCS results with VV polarization. As it is hard to solve a problem with such large electric-size by FEKO and dielectric media buried under earth cannot be simulated by FEKO, only 3D FEM results are given in the figure.

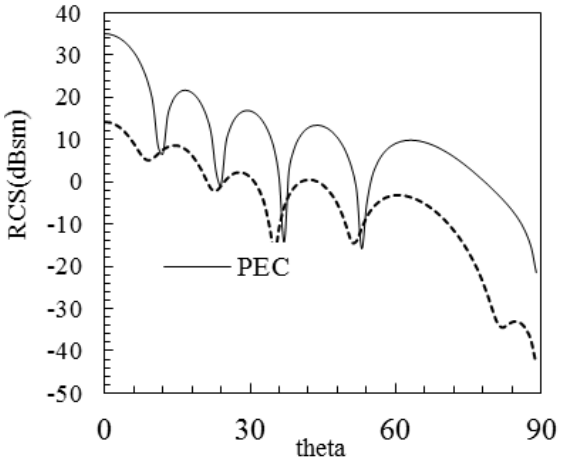

Fig. 12. Bi-static radar cross sections of a $5\lambda\times5\lambda\times5\lambda$ PEC brick and a dielectric brick buried 0.3λ below the earth.

The last example is the simulation of a cloak half buried below the earth. The relative permittivity of the earth is $\varepsilon_r = 1.5-0.2j$. Assuming the inner and outer boundary of the cloak are descripted by:

$$R_1 = 0.2+0.05\cos(3\theta)+0.01\cos(\theta),$$
$$R_2 = 0.3+0.05\cos(3\theta)+0.01\cos(\theta).$$

The relative permittivity and permeability of the cloak can be deduced with method described in [25-26] according to the above contour equations. In cylindrical coordinates, they are described by:

$$\bar{\bar{\varepsilon}}_r = \left[\varepsilon_{r,1}\,\mathrm{sgn}(z)+(\varepsilon_{r,2})\,\mathrm{sgn}(-z)\right]JJ^T/|J|,$$
$$\bar{\bar{\mu}}_r = JJ^T/|J|,$$

where $\varepsilon_{r,1}$ and $\varepsilon_{r,2}$ is the relative permittivity of media 1 and media 2, other parameters are defined by:

$$\mathrm{sgn}(z) = \begin{cases} 0 & z \le 0 \\ 1 & z > 0 \end{cases},$$

$$J_{xx} = cos^2\varphi sin\theta(R_3 sin\theta + R_4/r cos\theta) + (sin^2\varphi + cos^2\varphi cos^2\theta)r'/r,$$

$$J_{xy} = \sin\theta\sin(2\varphi)(\mathrm{R_4cos\theta\text{-}R_1sin\theta})/(2r),$$

$$J_{xz} = \text{-}\cos\varphi\sin\theta(\mathrm{R_1cos\theta + R_4sin\theta})/r,$$

$$J_{yx} = J_{xy},$$

$$J_{yy} = sin^2\varphi sin\theta(R_3 sin\theta + R_4/r cos\theta) + (cos^2\varphi + \cos^2\theta\sin^2\varphi)r'/r$$

$$J_{yz} = \text{-}\sin\varphi\sin\theta(\mathrm{R_1cos\theta + R_4sin\theta})/r$$

$$J_{zx} = \cos\varphi\cos\theta(\mathrm{R_4cos\theta\text{-}R_1sin\theta})/r$$

$$J_{zy} = \cos\theta\sin\varphi(\mathrm{R_4cos\theta\text{-}R_1sin\theta})/r$$

$$J_{zz} = cos\theta(R_3 cos\theta - R_4/r sin\theta) + r'/r sin^2\theta$$

With R_3, R_4 defined by:

$$R_3 = \frac{R_2 - R_1}{R_2}.$$

$$R_4 = \frac{\left[r' - R_1\right] \mathrm{R}_1 \, dR_2 / d\theta}{R_2\left[R_2 - R_1\right]} - \frac{\left[r' - R_2\right] \mathrm{R}_2 \, dR_1 / d\theta}{R_2\left[R_2 - R_1\right]}.$$

The value of the relative permittivity and permeability of the cloak in Cartesian coordinates can be obtained using the above formulation. Assuming the frequency of the incident plane wave is 1.0 *GHz*. The incident angle is $\theta = 30^o$, $\varphi = 0^o$. The problem is discretized with the average mesh size 0.05λ in free space and 0.02λ in the cloak. To investigate the effect of the cloak, the electric field distribution near the coordinate origin is plotted in Fig. 13. Figure 13 (a) is the electric field distribution without cloak. Figure 13 (b) is the electric field distribution with cloak. As can be seen, the field outside the cloak is almost unchanged. This agrees with the theoretical results.

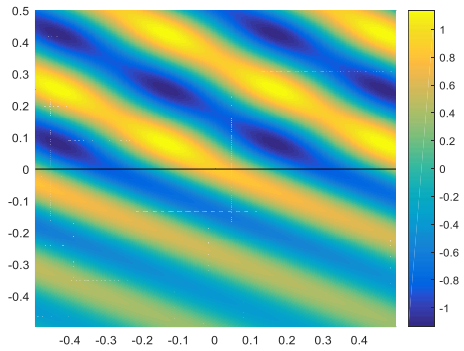

(a)

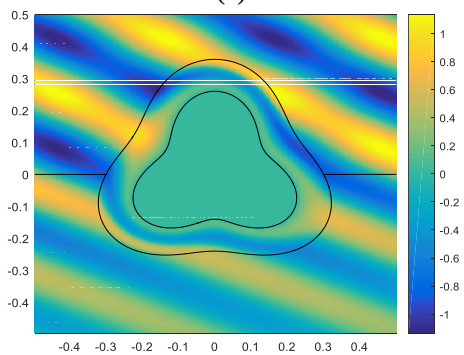

(b)

Fig. 13. The electric field distribution near the origin in the xoz plane when the plane wave incident from air to the loss media with the incident angle 30°. (a) Without the existence of the cloak, and (b) with the existence of the cloak.

VI. CONCLUSION

In this paper, the finite element method is used to analyze the scattering characteristics of 3D targets in the presence of air-earth interface. The FEM model for different cases including the targets placed near the interface, far away from the interface, and the interface is partially rough surface is discussed in the paper. The numerical results showed that the algorithm is very accurate and powerful for 3D targets in the presence of air-earth interface.

ACKNOWLEDGMENT

This work is supported in part by the Natural Science Foundation of Jiangsu Province under Grant BK20130854, in part by the Fundamental Research Funds for the Central Universities under Grant 2013B01914, in part by the National Science Foundation of China under Grant U1531101.

REFERENCES

[1] H. A. David, "Electromagnetic scattering by buried objects of low contrast," *IEEE Trans, Geosci. Remote Sens.*, vol. 26, pp. 195-203, 1988.

[2] N. Geng, A. Sullivan, and L. Carin, "Multilevel fast multipole algorithm for scattering from conducting targets above or embedded in a lossy half space," *IEEE Trans, Geosci. Remote Sens.*, vol. 38, pp. 1567-1579, 2000.

[3] Z. J. Liu, R. J. Adams, and L. Carin, "Well-conditioned MLFMA formulation for closed PEC targets in the vicinity of a half space," *IEEE Trans. Antennas Propagat.*, vol. 51, pp. 2822-2829, 2003.

[4] T. J. Cui and W. C. Chew, "Fast algorithm for electromagnetic scattering by buried 3-D dielectric objects of large size," *IEEE Trans. Geosci. Remote Sens.*, vol. 35, pp. 2597- 2608, 1999.

[5] B. Guan, J. F. Zhang, X. Y. Zhou, and T. J. Cui, "Electromagnetic scattering from objects above a rough surface using the method of moments with half-space green's function," *IEEE Trans. Geosci. Remote Sens.*, vol. 47, pp. 3399-3405, 2009.

[6] J. Li, L. X. Guo, and H. Zeng, "FDTD investigation on bistatic scattering from a target above two-layered rough surfaces using UPML absorbing condition," *Progress in Electromagnetics Research*, vol. 88, pp. 197-211, 2008.

[7] K. Demarest, R. Plumb, and Z. B. Huang, "FDTD modeling of scatterers in stratified media," *IEEE Trans. Antennas Propagat.*, vol. 43, pp. 1164-1168, 1995.

[8] P. B. Wong, G. L. Tyler, J. E. Baron, et al., "A three wave FDTD approach to surface scattering with applications to remote sensing of geophysical surfaces," *IEEE Trans. Antennas Propagat.*, vol. 44, pp. 504-514, 1996.

[9] J. M. Jin, *The Finite Element Method in Electromagnetics*. Wiley, New York, 1993.

[10] A. Aghabarati and J. P. Webb, "An algebraic multigrid method for the finite element analysis of large scattering problems," *IEEE Trans. Antennas*

Propagat., vol. 61, no. 2, pp. 809-817, 2013.

[11] X. C. Wei, E. P. Li, and Y. J. Zhang, "Efficient solution to the large scattering and radiation problem using the improved finite-element fast multipole method," *IEEE Trans. Magn*., vol. 41, pp. 1684-1687, 2005.

[12] W. G. Facco, E. J. Silva, A. S. Moura, N. Z. Lima, and R. R. Saldanha, "Handling material discontinuities in the generalized finite element method to solve wave propagation problems," *IEEE Trans. Magn*., vol. 48, pp. 607-610, 2012.

[13] S. Caorsi and M. Raffetto, "Perfectly matched layers for the truncation of finite element meshes in layered half-space geometries and applications to electromagnetic scattering by buried objects," *Microwave Opt. Technol. Lett.*, vol. 19, pp. 427-434, 1998.

[14] O. Ozgun and M. Kuzuoglu, "Monte Carlo-based characteristic basis finite-element method (MC-CBFEM) for numerical analysis of scattering from objects on/above rough sea surfaces," *IEEE Trans. Geosci. Remote Sens*., vol.50, pp. 769-783, 2012.

[15] D. H. Han, A. C. Polycarpou, and C. A. Balanis, "Ground effects for VHF/HF antennas on helicopter airframes," *IEEE Trans. Antennas Propagat*., vol. 49, pp. 402-412, 2001.

[16] E. Simsek, J. Liu, and Q. H. Liu, "A spectral integral method and hybrid SIM/FEM for layered media," *IEEE Transactions on Microwave Theory and Techniques*, vol. 54, no. 11, pp. 3878-3884, 2006.

[17] T. Eibert, Y. Erdemli, and J. Volakis, "Hybrid finite element-fast spectral domain multilayer boundary integral modeling of doubly periodic structures," *IEEE Transactions on Antennas and Propagation*, vol. 51, no. 9, pp. 2517-2520, Sept. 2003.

[18] R. Xu, L. Guo, and X. Meng, "Analysis of scattering from dielectric rough surfaces by hybrid FEM/BIE," *Progress In Electromagnetics Research M*, vol. 34, pp. 107-116, 2014.

[19] L. Guo and R. Xu "An efficient multiregion FEM-BIM for composite scattering from an arbitrary dielectric target above dielectric rough sea surfaces," *IEEE Transactions on Geoscience and Remote Sensing*, vol. 53, no. 7, pp. 3885-3896, 2015.

[20] B. M. Irons, "A frontal method solution program for finite element analysis," *Int. J. Numer. Meth. Eng*., vol. 2, pp. 5-32, 1970.

[21] Y. Saad, *Iterative Methods for Sparse Linear Systems*. PWS Publishing Company, Boston, 1995.

[22] M. Benzi, "Preconditioning techniques for large linear systems: A survey," *Journal of Computational Physics*, vol. 182, pp. 418-477, 2002.

[23] R. S. Chen, X. W. Ping, E. K. N. Yung, C. H. Chan, et al., "Application of diagonally perturbed incomplete factorization preconditioned conjugate gradient algorithms for edge finite element analysis of Helmholtz equations," *IEEE Trans. Antennas Propagat*., vol. 54, pp. 1604-1608, 2006.

[24] X. W. Ping and T. J. Cui, "The factorized sparse approximate inverse preconditioned conjugate gradient algorithm for finite element analysis of scattering problems," *Progress In Electromagnetics Research*, vol. 98, pp. 15-31, 2009.

[25] D. Schurig, J. B. Pendry, and D. R. Smith, "Calculation of material properties and ray tracing in transformation media," *Opt. Express*, vol. 14, pp. 9794-9804, 2006.

[26] C. Li, K. Yao, and F. Li, "Invisibility cloaks with arbitrary geometries for layered and gradually changing backgrounds," *J. Phys. D: Appl. Phys*., vol. 42, 185504, 2009.

Xuewei Ping received the B.S., M.S., and Ph.D. degrees from Nanjing University of Science and Technology, Nanjing, China, in 2001, 2004, and 2007, respectively. Since Dec 2012, he has been a Lector of HoHai University. His research interests include computational electromagnetics, radar cross-section analysis, electromagnetic design and analysis of magnetic resonance imaging components.

A New HIE-PSTD Method for Solving Problems with Fine and Electrically Large Structures Simultaneously

Jianying Guo, Juan Chen, Jianguo Wang, and Anxue Zhang

School of Electronic and Information Engineering
Xi'an Jiaotong University, Xi'an, 710049, People's Republic of China
gjyhn@126.com, chen.juan.0201@mail.xjtu.ed.cn, wanguiuc@163.com, anxuezhang@mail.xjtu.edu.cn

Abstract ─ A new hybrid implicit-explicit difference and pseudospectral (PS) scheme is presented for solving the electromagnetic problems which have fine features and are electrically large. The maximum time-step size in this method is only determined by two spatial discretization which only need two cells per wavelength. The formulation of the method is presented and the time stability condition of the method is demonstrated. This method is more efficient than the finite-difference time-domain (FDTD) method in terms of computer memory and computation time, which is demonstrated through numerical examples.

Index Terms ─ Courant limit, FDTD method, Fourier transform, hybrid implicit explicit difference.

I. INTRODUCTION

The finite-difference time-domain (FDTD) method [1]-[3] has been proven to be a simple algorithm that provides accurate predictions of electromagnetic field interaction. But in practice, the stability condition makes the FDTD method inefficient for some problems with fine or electrically large structures. So there are two prominent efforts that have been made recently to develop more efficient FDTD schemes. First, is to weaken the Courant limit on the time step size of the FDTD method. Second, is to overcome the limit of the wavelength on the space discretization. Among those proposed methods, the hybrid implicit-explicit difference FDTD (HIE-FDTD) method [4]-[6] and pseudospectral time-domain (PSTD) technique [7]-[8] are two kinds of representative algorithms. In the HIE-FDTD method, the time step size is not limited by the fine space discretization and is extremely useful for the analysis of structures with fine-scale dimensions. The PSTD technique uses a Fourier transform algorithm to represent spatial derivative and allows a coarse discretization of only two cells per wavelength[9]-[10], while the FDTD method requires a relatively large number of nodes (usually 10–20 nodes per minimum wavelength for a problem of moderate size) to achieve reasonably good accuracy. This makes the PSTD method more efficient than the FDTD method for problems with electrically large structures. However, many simulations of electromagnetic problems are both with fine and electrically large structures, such as the fine plane. So it is desirable to combine the HIE-FDTD and PSTD algorithms to efficiently handle this structure.

In this paper, we present a novel HIE-PSTD method which applies the hybrid implicit explicit difference technique in one direction and the pseudospectral scheme in the other two directions. The new method not only weakens the Courant limit on the time step size, but also overcomes the limit of the wavelength on the space discretization. The time step size in this method is not determined by the fine space discretization and the space discretization along the electrically large direction only need two cells per wavelength. First, the 3-D formula of the HIE-PSTD method is presented and the time stability condition of the method is discussed. Finally, the numerical performance of the method is demonstrated through numerical examples by comparing with the FDTD and HIE-FDTD methods.

II. FORMULAS

In a linear, non-dispersive, and lossless medium, the Maxwell's curl equations for full waves are as follows:

$$\varepsilon \frac{\partial E_x}{\partial t} = \frac{\partial H_z}{\partial y} - \frac{\partial H_y}{\partial z}, \tag{1.1}$$

$$\varepsilon \frac{\partial E_y}{\partial t} = \frac{\partial H_x}{\partial z} - \frac{\partial H_z}{\partial x}, \tag{1.2}$$

$$\varepsilon \frac{\partial E_z}{\partial t} = \frac{\partial H_y}{\partial x} - \frac{\partial H_x}{\partial y}, \tag{1.3}$$

$$\mu \frac{\partial H_x}{\partial t} = \frac{\partial E_y}{\partial z} - \frac{\partial E_z}{\partial y}, \tag{1.4}$$

$$\mu \frac{\partial H_y}{\partial t} = \frac{\partial E_z}{\partial x} - \frac{\partial E_x}{\partial z}, \tag{1.5}$$

$$\mu \frac{\partial H_z}{\partial t} = \frac{\partial E_x}{\partial y} - \frac{\partial E_y}{\partial x}. \tag{1.6}$$

Assuming that the fine structure is along the *z* direction and the electrically large structures are along

Submitted On: June 19, 2016
Accepted On: August 14, 2016

the *x* direction and the *y* direction. So the high-density cells in the *z* direction have to be used in order to accurately describe this fine structure. In order to make sure that the time step size have no relation with spatial increment Δz, apply the hybrid implicit explicit difference technique to the derivative in *z* direction. Meanwhile in the *x* direction and the *y* direction, the PSTD method is employed. We use the forward and inverse Fourier transforms to replace the derivative with respect to *x* and *y*. Being different from the standard Yee's algorithm, the HIE-PSTD method does not require the spatial staggered grid along the *x* direction and the *y* direction. The electromagnetic field components are arranged on the cells as shown in Fig. 1.

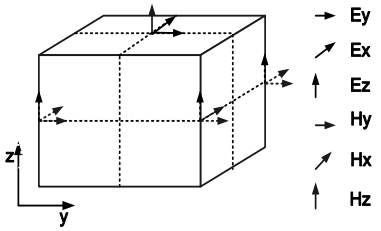

Fig. 1. Spatial grid of the field components in the HIE-PSTD method.

Thus, the difference updating Equations of (1) can be obtained as:

$$\varepsilon\frac{E_x^{n+1}\left(i+\frac{1}{2},j+\frac{1}{2},k\right)-E_x^{n}\left(i+\frac{1}{2},j+\frac{1}{2},k\right)}{\Delta t}=$$
$$\Im_y^{-1}\left\{\Im_y\left[\partial H_z^{n+1}\left(i+\frac{1}{2},j+\frac{1}{2},k\right)\Big/\partial y\right]\right\} \tag{2.1}$$
$$-\frac{1}{2\Delta z}\left[\begin{array}{l}H_y^{n+1}\left(i,j,k+\frac{1}{2}\right)-H_y^{n+1}\left(i,j,k-\frac{1}{2}\right)\\+H_y^{n}\left(i,j,k+\frac{1}{2}\right)-H_y^{n}\left(i,j,k-\frac{1}{2}\right)\end{array}\right],$$

$$\varepsilon\frac{E_y^{n+1}\left(i+\frac{1}{2},j+\frac{1}{2},k\right)-E_y^{n}\left(i+\frac{1}{2},j+\frac{1}{2},k\right)}{\Delta t}=$$
$$\frac{1}{2\Delta z}\left[\begin{array}{l}H_x^{n+1}\left(i,j,k+\frac{1}{2}\right)-H_x^{n+1}\left(i,j,k-\frac{1}{2}\right)\\+H_x^{n}\left(i,j,k+\frac{1}{2}\right)-H_x^{n}\left(i,j,k-\frac{1}{2}\right)\end{array}\right] \tag{2.2}$$
$$-\Im_x^{-1}\left\{\Im_x\left[\partial H_z^{n+1}\left(i+\frac{1}{2},j+\frac{1}{2},k\right)\Big/\partial x\right]\right\},$$

$$\varepsilon\frac{E_z^{n+1}\left(i,j,k+\frac{1}{2}\right)-E_z^{n}\left(i,j,k+\frac{1}{2}\right)}{\Delta t}$$
$$=\Im_x^{-1}\left\{\Im_x\left[\partial H_y^{n}\left(i,j,k+\frac{1}{2}\right)\Big/\partial x\right]\right\} \tag{2.3}$$
$$-\Im_y^{-1}\left\{\Im_y\left[\partial H_x^{n}\left(i,j,k+\frac{1}{2}\right)\Big/\partial y\right]\right\},$$

$$\mu\frac{H_x^{n+1}\left(i,j,k+\frac{1}{2}\right)-H_x^{n}\left(i,j,k+\frac{1}{2}\right)}{\Delta t}$$
$$=\frac{1}{2\Delta z}\left[\begin{array}{l}E_y^{n+1}\left(i+\frac{1}{2},j+\frac{1}{2},k+1\right)-E_y^{n+1}\left(i+\frac{1}{2},j+\frac{1}{2},k\right)\\+E_y^{n}\left(i+\frac{1}{2},j+\frac{1}{2},k+1\right)-E_y^{n}\left(i+\frac{1}{2},j+\frac{1}{2},k\right)\end{array}\right]$$
$$-\Im_y^{-1}\left\{\Im_y\left[\partial E_z^{n+1}\left(i,j,k+\frac{1}{2}\right)\Big/\partial y\right]\right\}, \tag{2.4}$$

$$\mu\frac{H_y^{n+1}\left(i,j,k+\frac{1}{2}\right)-H_y^{n}\left(i,j,k+\frac{1}{2}\right)}{\Delta t}=$$
$$\Im_x^{-1}\left\{\Im_x\left[\partial E_z^{n+1}\left(i,j,k+\frac{1}{2}\right)\Big/\partial x\right]\right\}$$
$$-\frac{1}{2\Delta z}\left[\begin{array}{l}E_x^{n+1}\left(i+\frac{1}{2},j+\frac{1}{2},k+1\right)-E_x^{n+1}\left(i+\frac{1}{2},j+\frac{1}{2},k\right)\\+E_x^{n}\left(i+\frac{1}{2},j+\frac{1}{2},k+1\right)-E_x^{n}\left(i+\frac{1}{2},j+\frac{1}{2},k\right)\end{array}\right], \tag{2.5}$$

$$\mu\frac{H_z^{n+1}\left(i+\frac{1}{2},j+\frac{1}{2},k\right)-H_z^{n}\left(i+\frac{1}{2},j+\frac{1}{2},k\right)}{\Delta t}=$$
$$\Im_y^{-1}\left\{\Im_y\left[\partial E_x^{n}\left(i+\frac{1}{2},j+\frac{1}{2},k\right)\Big/\partial y\right]\right\} \tag{2.6}$$
$$-\Im_x^{-1}\left\{\Im_x\left[\partial E_y^{n}\left(i+\frac{1}{2},j+\frac{1}{2},k\right)\Big/\partial x\right]\right\}.$$

Obviously, the updating of E_x and E_y, as shown in the Equations (2.1) and (2.2), needs the unknown H_x and H_y at the same time; thus, E_x and E_y have to be updated implicitly. By substituting the Equation (2.5) into (2.1) and the Equation (2.5) into (2.2), the equations for E_x and E_y are given as:

$$\left[1+\frac{\Delta t^2}{2\varepsilon\mu\Delta z^2}\right]E_x^{n+1}\left(i+\frac{1}{2},j+\frac{1}{2},k\right)-\frac{\Delta t^2}{4\varepsilon\mu\Delta z^2}\begin{bmatrix}E_x^{n+1}\left(i+\frac{1}{2},j+\frac{1}{2},k+1\right)\\+E_x^{n+1}\left(i+\frac{1}{2},j+\frac{1}{2},k-1\right)\end{bmatrix}$$
$$=E_x^n\left(i+\frac{1}{2},j+\frac{1}{2},k\right)+\frac{\Delta t}{\varepsilon}\Im_y^{-1}\left\{\Im_y\left[\partial H_z^{n+1}\left(i+\frac{1}{2},j+\frac{1}{2},k\right)\Big/\partial y\right]\right\}$$
$$+\frac{\Delta t^2}{4\varepsilon\mu\Delta z^2}\begin{bmatrix}E_x^n\left(i+\frac{1}{2},j+\frac{1}{2},k+1\right)-E_x^n\left(i+\frac{1}{2},j+\frac{1}{2},k\right)\\-E_x^n\left(i+\frac{1}{2},j+\frac{1}{2},k\right)+E_x^n\left(i+\frac{1}{2},j+\frac{1}{2},k-1\right)\end{bmatrix}$$
$$-\frac{\Delta t}{\varepsilon\Delta z}\left[H_y^n\left(i,j,k+\frac{1}{2}\right)-H_y^n\left(i,j,k-\frac{1}{2}\right)\right]$$
$$-\frac{\Delta t^2}{2\varepsilon\mu\Delta z}\begin{bmatrix}\Im_x^{-1}\left\{\Im_x\left[\partial E_z^{n+1}\left(i,j,k+\frac{1}{2}\right)\Big/\partial x\right]\right\}\\-\Im_x^{-1}\left\{\Im_x\left[\partial E_z^{n+1}\left(i,j,k-\frac{1}{2}\right)\Big/\partial x\right]\right\}\end{bmatrix}, \tag{2.7}$$

$$\left[1+\frac{\Delta t^2}{2\varepsilon\mu\Delta z^2}\right]E_y^{n+1}\left(i+\frac{1}{2},j+\frac{1}{2},k\right)$$
$$-\frac{\Delta t^2}{4\varepsilon\mu\Delta z^2}\begin{bmatrix}E_y^{n+1}\left(i+\frac{1}{2},j+\frac{1}{2},k+1\right)\\+E_y^{n+1}\left(i+\frac{1}{2},j+\frac{1}{2},k-1\right)\end{bmatrix}$$
$$=E_y^n\left(i+\frac{1}{2},j+\frac{1}{2},k\right)-\frac{\Delta t}{\varepsilon}\Im_x^{-1}\left\{\Im_x\left[\partial H_z^{n+1}\left(i+\frac{1}{2},j+\frac{1}{2},k\right)\Big/\partial x\right]\right\}$$
$$+\frac{\Delta t^2}{4\varepsilon\mu\Delta z^2}\begin{bmatrix}E_y^n\left(i+\frac{1}{2},j+\frac{1}{2},k+1\right)-E_y^n\left(i+\frac{1}{2},j+\frac{1}{2},k\right)\\-E_y^n\left(i+\frac{1}{2},j+\frac{1}{2},k\right)+E_y^n\left(i+\frac{1}{2},j+\frac{1}{2},k-1\right)\end{bmatrix}$$
$$+\frac{\Delta t}{\varepsilon\Delta z}\left[H_x^n\left(i,j,k+\frac{1}{2}\right)-H_x^n\left(i,j,k-\frac{1}{2}\right)\right]$$
$$-\frac{\Delta t^2}{2\varepsilon\mu\Delta z}\begin{bmatrix}\Im_y^{-1}\left\{\Im_y\left[\partial E_z^{n+1}\left(i,j+1,k+\frac{1}{2}\right)\Big/\partial y\right]\right\}\\-\Im_y^{-1}\left\{\Im_y\left[\partial E_z^{n+1}\left(i,j+1,k-\frac{1}{2}\right)\Big/\partial y\right]\right\}\end{bmatrix}, \tag{2.8}$$

where $\Im_\alpha$ and $\Im_\alpha^{-1}$ is forward and inverse Fourier transforms to variable α (where α is x or y). Taking spatial derivative $\partial E_x^{n+1}/\partial y$ as an example, the Fourier transforms can be obtained as:

$$\Im_y^{-1}\left\{\Im_y\left[\frac{\partial E_x^{n+1}\left(i+\frac{1}{2},j+\frac{1}{2},k\right)}{\partial y}\right]\right\}$$
$$=A\times B\times\begin{bmatrix}E_x^{n+1}\left(I+\frac{1}{2},1+\frac{1}{2},k\right)\\E_x^{n+1}\left(I+\frac{1}{2},2+\frac{1}{2},k\right)\\\cdot\\\cdot\\\cdot\\E_y^{n+1}\left(I+\frac{1}{2},\left(J-1+\frac{1}{2}\right),k\right)\end{bmatrix}, \tag{3}$$

where B is a $L\times I$ matrix, and $B_{l,i}=e^{-\hat{j}(k_{y,l})(i\Delta y)}\Delta y$, A is a $1\times L$ vector, and $A_{1,l}=\frac{1}{2\pi}\left(\hat{j}k_{y,l}\right)e^{\hat{j}(k_{y,l})(i\Delta y)}\Delta y$. The range of spectral k_y domain is from $-\frac{2\pi}{2\Delta y}$, to $\frac{2\pi}{2\Delta y}$, $k_{y,l}=-\frac{2\pi}{2\Delta y}+l\Delta k_y$, $\Delta k_y=\frac{2\pi}{L\Delta y}$, $L = I$ is the total mesh cell in the y direction.

Therefore, components E_z and H_z are explicitly updated first by using the Equations (2.3) and (2.6). Then, E_x and E_y components are updated implicitly by solving the tridiagonal matrix Equations (2.7) and (2.8). At last, H_x and H_y are explicitly updated straight forward by using the equations (2.4) and (2.5).

III. NUMERICAL STABILITY

We now study the numerical stability in the proposed HIE-PSTD algorithm. The field components of traveling-wave as shown:

$$E_p(i,j,k)=\zeta^n E_{p0}e^{\hat{j}\left(k_x i\Delta x+k_y j\Delta y+k_z k\Delta z\right)}, \tag{4}$$

$$H_p(i,j,k)=\zeta^n H_{p0}e^{\hat{j}\left(k_x i\Delta x+k_y j\Delta y+k_z k\Delta z\right)}, \tag{5}$$

where $p=x,y,z,\quad \hat{j}=\sqrt{-1},\quad E_{p0}$ and H_{p0} are the amplitudes of the field components respectively. k_x, k_y and k_z are wave numbers, and ζ indicates growth factor. We substitute the Equations (5) and (4) into (2.1)-(2.6), and obtain the equations as:

$$(\zeta-1)H_{x0}=\frac{\Delta t}{\mu}\left(\hat{j}\zeta k_y E_{z0}+(\zeta+1)\cdot\frac{E_{y0}}{\Delta z}\cdot\sin\left(\frac{k_z\Delta z}{2}\right)\right), \tag{6}$$

$$(\zeta-1)H_{y0}=\frac{\Delta t}{\mu}\left(-\hat{j}\zeta k_x E_{z0}-(\zeta+1)\cdot\frac{E_{x0}}{\Delta z}\cdot\sin\left(\frac{k_z\Delta z}{2}\right)\right), \tag{7}$$

$$(\zeta-1)H_{z0}=\frac{\Delta t}{\mu}\left(-\hat{j}\zeta k_y E_{x0}+\hat{j}\zeta k_x E_{y0}\right), \tag{8}$$

$$(\zeta-1)E_{x0}=\frac{\Delta t}{\varepsilon}\left(-\hat{j}\zeta k_y H_{z0}-(\zeta+1)\frac{H_{y0}}{\Delta z}\sin\left(\frac{k_z\Delta z}{2}\right)\right), \tag{9}$$

$$(\zeta-1)E_{y0}=\frac{\Delta t}{\varepsilon}\left(\hat{j}\zeta k_x H_{z0}+(\zeta+1)\frac{H_{x0}}{\Delta z}\sin\left(\frac{k_z\Delta z}{2}\right)\right), \tag{10}$$

$$(\zeta-1)E_{z0}=\frac{\Delta t}{\varepsilon}\left(\hat{j}k_y H_{x0}-\hat{j}k_x H_{y0}\right). \tag{11}$$

By substituting the Equations (6)-(8) into (9)-(11), and eliminating H_{x0}, H_{y0} and H_{z0}, we obtain three equations of E_{x0}, E_{y0} and E_{z0}. Then combining the three equations, and eliminating E_{x0}, E_{y0} and E_{z0}, we obtain:

$$(\zeta-1)^2\times\left[\begin{array}{l}\dfrac{abD^2}{4}(\zeta+1)^2\\ +\left(ab\left(\hat{j}k_x\right)^2+ab\left(\hat{j}k_y\right)^2\right)\zeta-(\zeta-1)^2\end{array}\right]^2=0, \quad (12)$$

where $a=\Delta t/\varepsilon$, $b=\Delta t/\mu$, $D=2\hat{j}\sin\left(k_z\Delta z/2\right)/\Delta z$. By solving the Equation (12), the growth factor ζ can be obtained:

$$\zeta_1=1,$$

$$\zeta_{2,3}=\frac{N\pm\sqrt{N^2-R^2}}{R},$$

where

$$R=abD^2/2-2,$$

$$N=-\left(abD^2/2+ab\left(\hat{j}k_y\right)^2+ab\left(\hat{j}k_x\right)^2+2\right).$$

To satisfy the stability condition during field advancement, the module of growth factor ζ cannot be larger than 1. Thus, it has

$$R^2\geq N^2\Rightarrow\frac{abk_y^2}{4}+\frac{abk_x^2}{4}\leq 1.$$

Due to the maximum value of k_x and k_y is $\dfrac{2\pi}{2\Delta x}$, it obtains:

$$\frac{ab}{4}\left(\frac{\pi}{\Delta y}\right)^2+\frac{ab}{4}\left(\frac{\pi}{\Delta x}\right)^2\leq 1\Rightarrow\Delta t\leq\frac{1}{c\sqrt{\left(\pi/2\Delta y\right)^2+\left(\pi/2\Delta x\right)^2}}. \quad (13)$$

From the Equation (13), we can see, the maximum time-step size in this method is only determined by spatial increments Δx and Δy. When the simulated structure has fine-scale dimensions in the *z* direction, this is especially useful. The spatial increments Δx and Δy. only needs to satisfy Nyquist sampling theorem which results the spatial discretization $\Delta x\leq\lambda/2$ and $\Delta y\leq\lambda/2$. Thus, for the electrically large dimensions in the *x* direction and the *y* direction, and thin dimensions in the *z* direction, the HIE-PSTD algorithm is more efficient than the FDTD method. For example, in the *z* direction, in order to accurately describe the fine structure, the spatial increments $\Delta z=\lambda/100$ for the FDTD method and the HIE-PSTD method. In the *x* direction and the *y* direction, for the FDTD method, considering the limit of the wavelength on the space discretization, the spatial discretization Δx and Δy are selected to be 1/10 of the wavelength, while for the HIE-PSTD method, spatial discretization Δx and Δy can be increased to 1/2 of the wavelength. With the space discretization determined beforehand, the maximum time-step size to satisfy the stability condition of the FDTD algorithm is Δt_0 and of the HIE-PSTD method is Δt_1. Then Δt_1 is 22.7 times of Δt_0. So the computation time requirement of the HIE-PSTD method is considerably reduced.

IV. NUMERICAL VALIDATION

To demonstrate the time stability condition of the HIE-PSTD method, a simple numerical example is presented. A computation domain with total mesh number 90×90×50 is discretized. To cut off the outer boundary, the perfectly matched layer (PML) proposed by Berenger [11] can be used. A small current source applied along the *x* direction is placed at the cell (20, 20, 20) of the computation domain. The time dependence of the excitation function is:

$$J_x(t)=\sin(2\pi f_0 t), \quad (14)$$

where $f_0=100\times10^9\,Hz$, thus the wavelength of the source is $0.003m$. The observation point is at the cell (30, 30, 40). We apply the FDTD and the HIE-PSTD methods to compute the electric field component E_x at the observation point. The spatial cell size is $\Delta x=\Delta y=10\Delta z=0.3mm$, corresponding to 1/10 of the wavelength. For FDTD method, the time step size is $\Delta t=1/c\sqrt{(1/0.0003)^2+(1/0.0003)^2+(1/0.00003)^2}=0.099ps$, which is the maximum time-step size to satisfy the stability condition of the FDTD algorithm. For the HIE-PSTD method, the time-step sizes are $\Delta t=2/c\sqrt{(\pi/0.0003)^2+(\pi/0.0003)^2}=0.45ps$. Figure 2 shows the electric field component E_x at observation point calculated by using the conventional FDTD and the HIE-PSTD methods.

It can be seen from the figure that the result calculated by using the HIE-PSTD method agrees very well with the result calculated by using the conventional FDTD method, which shows the HIE-PSTD method has high computational accuracy with a time step that permitted by the time stability condition.

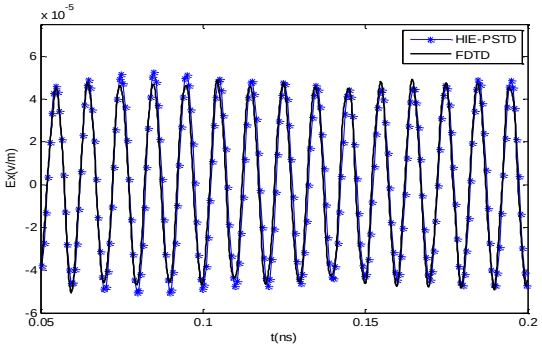

Fig. 2. Electric field component E_x at the observation point calculated by using the FDTD $(\Delta x=\Delta y=10\Delta z=0.03mm,\Delta t=0.099\,ps)$ and the HIE-PSTD $(\Delta x=\Delta y=10\Delta z=0.3mm,\Delta t=0.45\,ps)$ methods.

In the HIE-PSTD method, we apply the HIE finite-difference. This technique will bring a splitting error which is proportional to the time-step size [12], and is almost not affected by the increase of the space increment [13]-[15]. Now we study the computational accuracy of the HIE-PSTD method with different time-step size.

For the FDTD method, we set spatial increment $\Delta x = \Delta y = 10\Delta z = 0.3mm$ and the time-step $\Delta t_0 = 0.099\,ps$ which is the maximum time-step maximum to satisfy the stability condition of the FDTD algorithm. For the HID-PSTD method, we set spatial increment $\Delta z = 0.03mm$ unchanged and space increment Δx and Δy to be $0.15mm$ corresponding to $\lambda/2$ which is the maximum space increment. Define $CFLN = \Delta t/\Delta t_0$, where Δt is the time-step of the HIE-PSTD method. When $\Delta t = \Delta t_{\max}$, corresponding to the maximum time-step size to ensure the numerical stability in the HIE-PSTD method, *CFLN*=22. We set *CFLN* to be 8, 12, 20, and 22 (corresponding time-step size increases from 0.79*ps* to 2.25*ps*) and calculate the electric field component E_x at observation point by using the HIE-PSTD method with different *CFLN* respectively.

Figure 3 and Fig. 4 show the result calculated by using the HIE-PSTD method with different *CFLN*. For the comparison, the result calculated by using the FDTD method is shown in Fig. 3-Fig. 4 simultaneously.

It can be seen from Fig. 3 that, when *CFLN*=8, 12, the computational result of the HIE-PSTD method agrees well with the result of the FDTD method.

When *CFLN* is too large (*CFLN*=20, 22), as shown in the Fig. 4, the accuracy of the HIE-PSTD method began to decrease for the large time-step. Table l shows the simulation time of the FDTD and the HIE-PSTD methods.

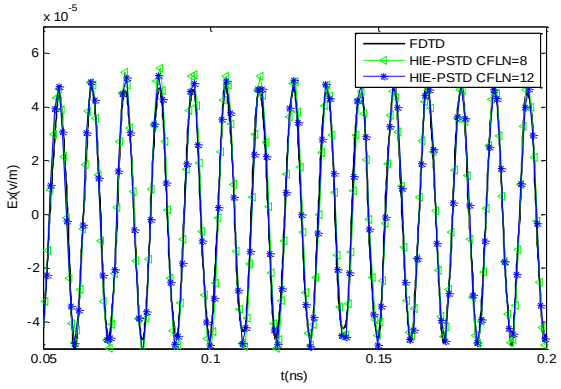

Fig. 3. Electric field component E_x at the observation point calculated by using the FDTD and the HIE-PSTD methods with different time step sizes.

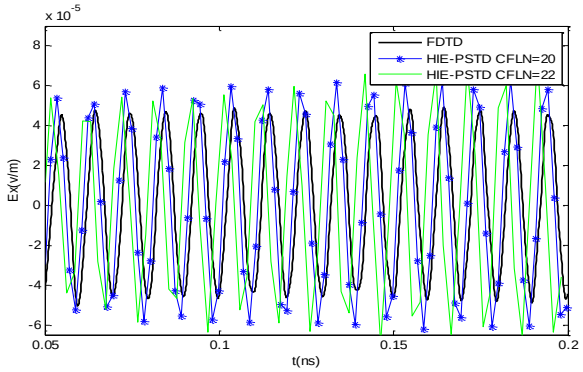

Fig. 4. Electric field component E_x at the observation point calculated by using the FDTD and the HIE-PSTD methods with different time step sizes.

Table 1: Error and computation time of the HIE-PSTD method for difference *CFLN*

Time	CFLN=1	CFLN=8	CFLN=12	CFLN=20	CFLN=22
FDTD	7893s				
HIE-PSTD	8929s	987s	706s	412s	344s

We can see, the HIE-PSTD takes much less time than that of the FDTD method. So in practice, the choice of *CFLN* (or Δt) in the HIE-PSTD method is dictated by the accuracy and efficiency rather than the stability consideration. In the situation with very stringent accuracy requirements, *CFLN* should not be larger than 12 usually.

V. SPECIFIC EXAMPLE

Considering the HIE-PSTD method is mainly useful in the simulations of electromagnetic problems which are both with fine structures and electrically large structure, another example with similar geometry is presented to demonstrate the accuracy and efficiency of the HIE-PSTD. We simulate a 3-D parallel-plate structure. The size of the plate is $0.06mm \times 90mm \times 90mm$ (as shown in Fig. 5). The distance between the plates is $12mm$. The *z* direction incident plane wave is Gauss pulse with the highest frequency of 100×10^9 *Hz*. Thus, the wavelength of the incident plane wave is about $3mm$. The polarization is along the *x* direction. The observation point is at the center of the gap between two parallel plates.

To demonstrate the numerical performance of the HIE-PSTD method, we perform the numerical simulations for a $0.1ns$ time history by using the FDTD and the HIE-PSTD methods. The plate has fine structure along the *z* direction, so we set $\Delta z = 0.03mm$. Considering the limit of the wavelength on the space discretization, for the FDTD method, the spatial

discretization $\Delta x = \Delta y = 0.3mm$ and for the HIE-PSTD method spatial discretization Δx and Δy can be increased to 1.5*mm*, corresponding to 1/2 of the wavelength. The time step size for FDTD method is $\Delta t = 1/c\sqrt{(1/0.0003)^2 + (1/0.0003)^2 + (1/0.00003)^2} = 0.099ps$, For the HIE-PSTD method, the time step size is the maximum time-step size to satisfy the stability condition of the HIE-PSTD algorithm, $\Delta t = 2/c\sqrt{(\pi/0.0015)^2 + (\pi/0.0015)^2} = 2.25ps$, namely, which is 22 times as that of the FDTD. Figure 6 shows the electric field component at the observation point calculated by using the FDTD, and the HIE-PSTD methods. It can be seen from Fig. 6 that the result of the HIE-PSTD method agrees very well with the result calculated by using the FDTD method.

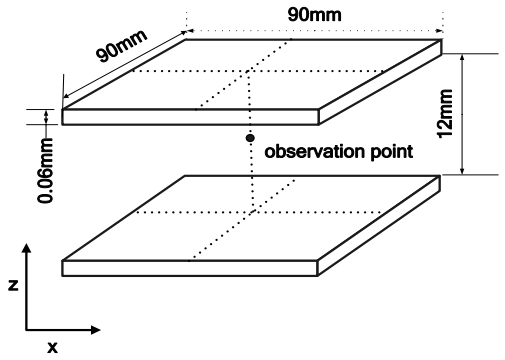

Fig. 5. The parallel-plate structure.

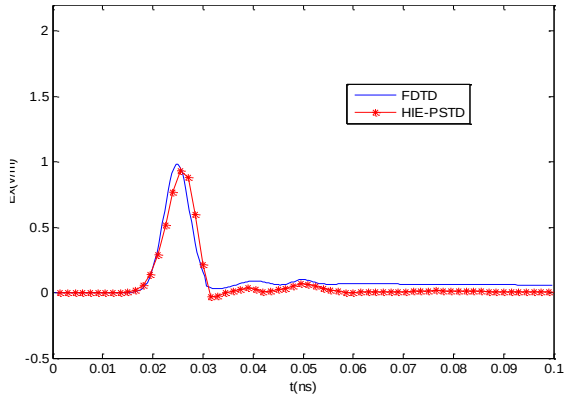

Fig. 6. Electric field component E_x at the observation point calculated by using the FDTD and HIE-PSTD methods.

The computation time and memory requirement of the simulation above are summarized in Table 2. It can be seen from this table that both the memory requirement and computational time for the HIE-PSTD method are reduced significantly compared with those of the FDTD method, due to large spatial discretization and large time step size applied, the memory requirement of the HIE-PSTD method is reduced by 42%, and the computation time is almost 1/16 of that of the FDTD method.

It should be noted that the standard DFT algorithm is only based on a uniform sampling. So the HIE-PSTD method is limited in application to the cases that require a non-uniform grid. To overcome this difficulty, non-uniform DFT have been suggested [16], these methods may add complexity and instability.

Table 2: Simulation time and memory requirement for the FDTD method and HIE-PSTD method

	Total Cells	Δt (ps)	Time (s)	Memory (Mb)
FDTD	360×360×74	0.099	7626	213.72
HIE-PSTD	130×130×74	2.25	473	90.15

VI. CONCLUSION

This paper introduces a HIE-PSTD method based on the hybrid implicit explicit difference technique and pseudospectral scheme. The maximum time-step size in this method is only determined by spatial discretization Δx and Δy, which only needs two cells per wavelength. The numerical performance of the method is demonstrated through numerical examples by comparing with the FDTD. For solving these problems both with fine structures and electrically large structure, the HIE-PSTD method will be more efficient than the FDTD methods in terms of computer memory and computation time.

ACKNOWLEDGMENT

This work was supported by National Natural Science Foundations of China (No. 61231003 and 61471292), the Natural Science Foundation of Shanxi Province, China (No. 2016 JM6001) and also supported by the Fundamental Research Funds for the Central University.

REFERENCES

[1] K. S. Yee, "Numerical solution of initial boundary value problems involving Maxwell's equations in isotropic media," *IEEE Trans. Antennas Propagat.*, vol. 14, pp. 302-307, May 1996.

[2] A. Taflove, *Computational Electrodynamics*. Norwood, MA, USA: Artech House, 1995.

[3] K. P. Ma, M. Li, J. L. Drewniak, T. H. Hubing, and T. P. VanDoren, "Comparison of FDTD algorithms for sub cellular modeling of slots in shielding enclosures," *IEEE Trans. Electromagn. Compat.*, vol. 39, no. 5, pp. 147-155, May 1997.

[4] J. Chen and J. Wang, "A 3-D hybrid implicit-explicit FDTD scheme with weakly conditional stability," *Microw. Opt. Tech. Lett.*, vol. 48, pp.

2291-2294, Nov. 2006.

[5] J. Chen and J. Wang, "A three-dimensional semi-implicit FDTD scheme for calculation of shielding effectiveness of enclosure with thin slots," *IEEE Trans. Electromagn. Compat.*, vol. 49, no. 2, pp. 354-360, Feb. 2007.

[6] J. Chen and J.Wang, "Numerical simulation using HIE-FDTD method to estimate various antennas with fine scale structures," *IEEE Trans. Antennas Propagat.*, vol. 55, no. 12, pp. 3603-3612, Dec. 2007.

[7] Q. H. Liu, "Large-scale simulations of electro-magnetic and acoustic measurements using the pseudospectral time-domain (PSTD) algorithm," *IEEE Trans. Geosci. Remote Sensing*, vol. 37, no. 2, pp. 917-926, Mar. 1999.

[8] Z. Lin, "The optimal spatially-smoothed source patterns for the pseudospectral time-domain method," *IEEE Trans. Antennas Propagat.*, vol. 58, no. 1, pp. 227-229, Jan. 2010.

[9] Q. H. Liu, "The PSTD algorithm: A time-domain method requiring only two cells per wavelength," *Microw. Opt. Tech. Lett.*, vol. 15, no. 3, June 20, 1997.

[10] Q. L. Li and Y. C. Chen, "Application of the PSTD for scattering analysis," *IEEE Trans. Antennas Propag.*, vol. 50, no. 9, pp. 1317-1319, Sep. 2002.

[11] J. P. Berenger, "A perfectly matched layer for the absorption of electromagnetic waves," *J. Computat. Phys*., vol. 114, pp. 185-200, 1994.

[12] J. Chen and J. G. Wang, "Weakly conditionally stable and unconditionally stable FDTD schemes for 3D Maxwell's equations," *Progr. Electromagn. Res. B*, vol. 19, pp. 329-366, 2010.

[13] J. Chen and J. G. Wang, "A novel hybrid implicit explicit – pseudospectral time domain method for TMz waves," *IEEE Trans. Antennas Propag*., vol. 61, no. 7, July 2013.

[14] J. Chen and J. G. Wang, "A three-dimensional HIE-PSTD scheme for simulation of thin slots," *IEEE Trans. Electromagn. Compat.*, vol. 55, no. 6, Dec. 2013.

[15] J. Chen and J. G. Wang, "A WCS-PSTD method for solving electromagnetic problems both with fine and electrically large structures," *IEEE Trans. Antennas Propag.*, vol. 62, no. 5, May 2014.

[16] W. K. Leung and Y. Chen, "Transformed-space non-uniform PSTD algorithm," *Microwave Opt. Technol. Lett*., vol. 28, 2003.

Jianying Guo received the B.S. degree in Electronic Technique from Henan Normal University, Xin'xiang, China, in 1996, and is currently working toward the Ph.D. degree in Electromagnetic Fields and Microwave Techniques at Xi'an Jiaotong University, Xi'an, China.

Her current research interests include computational electromagnetics, especially the FDTD method, microwave devices design and terahertz electronics.

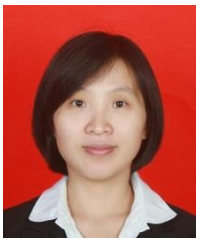

Juan Chen was born in Chongqing, China, in 1981. She received the Ph.D. degree in Electromagnetic Field and Microwave Techniques from the Xi'an Jiaotong University, Xi'an, China, in 2008.

She is currently an Associate Professor at Xi'an Jiaotong University. Her research interests include numerical electromagnetic methods, antenna designs, and electromagnetic compatibility.

Development of a Low Profile and Wideband Backward-Wave Directional Coupler Using Neural Network

Z. S. Tabatabaeian and Mohammad H. Neshati *

Department of Electrical Engineering
Ferdowsi University of Mashhad, 91779-48974, Mashhad, Iran
ztaba14@gmail.com, neshat@um.ac.ir

Abstract ─ In this paper, a low profile and wideband backward-wave directional coupler is introduced. It operates similar to the composite right left handed (CRLH) couplers. Two different mechanisms including connections between the coupled lines to provide shunt inductance for odd mode and defected ground structure (DGS) to add series capacitance for even mode are applied to obtain high performance and wideband coupler. Neural network process is used to obtain the optimized parameters of the proposed coupler. The introduced coupler is then numerically investigated using full wave simulator software. A prototype of the proposed coupler is fabricated and successfully tested. The measured results are in a good agreement with those obtained by simulation. The measured coupling level is 0.49 dB over the frequency range from 6.5 GHz up to 14 GHz, which shows fractional bandwidth of 73.2%.

Index Terms ─ Defected ground structure, directional coupler, neural network.

I. INTRODUCTION

Microstrip coupled-line directional couplers are widely used in microwave and millimeter wave circuits, such as filters, power dividers, transformers and baluns [1-2] due to their attractive performances. These couplers have two kinds of coupling mechanisms [3], depending on the type of the employed transmission lines, constituting the structure of the coupled lines and distance between the lines.

The first type of the coupling is based on the difference between the even- and odd-mode characteristic impedances leading to backward couplers. The difference between these impedances can be increased by reducing the interspacing between the lines. However, this is difficult due to fabrication constrains. Therefore, backward couplers suffer from the low level of coupling.

The second type of the coupling mechanism is based on the difference between phase velocities of even- and odd-modes providing forward couplers. In these types of couplers, the coupling level could be as high as 0 dB, but there are two important drawbacks in implementing them using microstrip lines. The first one is the small difference between even- and odd-mode propagation constants, which require very long coupling length. The other one is non-identical characteristic impedances of even- and odd-modes, which reduce the coupling level of the structure and the directivity performance of the coupler is decreased. A widely used planar coupler providing both broad bandwidth and tight coupling is a Lange coupler [4]. However, it suffers from requiring bonding wires which introduce parasitic effects at high frequencies.

In recent years, the composite right left-handed (CRLH) couplers represent unique alternatives to the Lange couplers [5]. They offer tight coupling over a broad bandwidth using planar structure without requiring bonding wires. In these couplers, the even- and odd-mode characteristic impedances are purely imaginary over the coupling bandwidth. Therefore, the coupling level is related to the attenuation length of the modes instead of the electrical length of the coupled lines.

In this paper, a low profile and wideband backward-wave directional coupler is designed and optimized using neural network. The proposed coupler operates similar to the CRLH couplers over a wide bandwidth. Two different techniques are applied together, for the first time, to obtain a high performance and wideband coupler. The first one is connections between the coupled lines, which provide shunt inductance for odd-mode. The second one is adding series capacitance for even mode using the defected ground structure (DGS) patterns.

The proposed coupler is numerically investigated using High Frequency Structure Simulator (HFSS). A prototype of the coupler is fabricated and tested using network analyzer and its *S*-parameters are measured. Results show that the proposed coupler provides the advantages of wide bandwidth and high coupling level in addition to low profile, low weight and low fabrication cost.

Submitted On: September 25, 2015
Accepted On: October 25, 2016

II. BACKWARD WAVE COUPLED LINE COUPLER

The structure of the proposed coupler is shown in Fig. 1. The coupled lines width and length are *W* and *l* respectively, which are separated by *s*. The proposed coupler is symmetric at the middle of the structure. The connections between the lines are the same. The DGS patterns are etched at the bottom layer of the substrate and they are separated from each other by *t*. The thickness of the substrate is denoted by *h*.

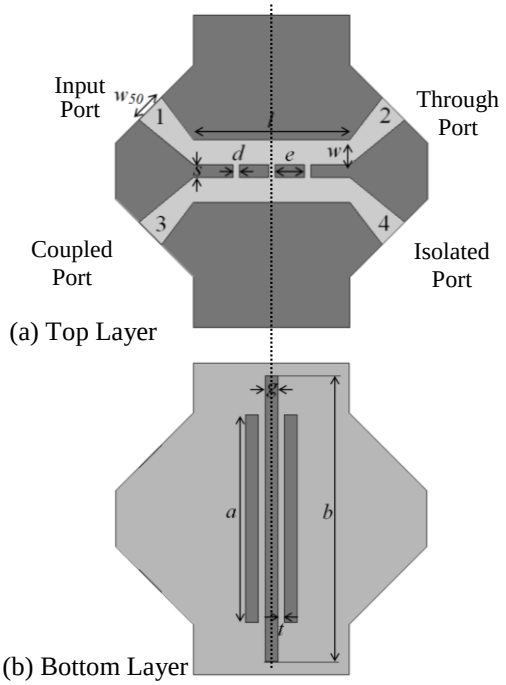

Fig. 1. The structure of the proposed coupler.

Because of the symmetry, the proposed four port coupler can be decomposed to even- and odd-mode two port structures. Even- and odd-mode equivalent circuit models correspond to the structure with perfect magnetic wall and perfect electric wall at the center of the coupler respectively. The equivalent circuit models for even- and odd-modes are shown in Figs. 2 (a) and 2 (b) respectively. For the microstrip coupled line, the propagation of odd-mode has low returned current density on the ground plane. The current of this mode is conducted from one of the coupled lines and returns from the other one. Nevertheless, in case of even-mode, the returned current density on the ground plane is high. This is due to direction of current which is the same for the two coupled lines, and the returned current is conducted by the ground. Hence, the current distribution pattern on the ground plane only affects the even-mode equivalent circuit. Therefore, the DGS patterns in the proposed coupler are modeled by resonating parallel *LC* circuits for only even-mode.

Connections between coupled lines are modeled by inductance and capacitance for odd- and even-modes respectively. However, because of the short length of the connections, the equivalent capacitances for even-mode can be neglected.

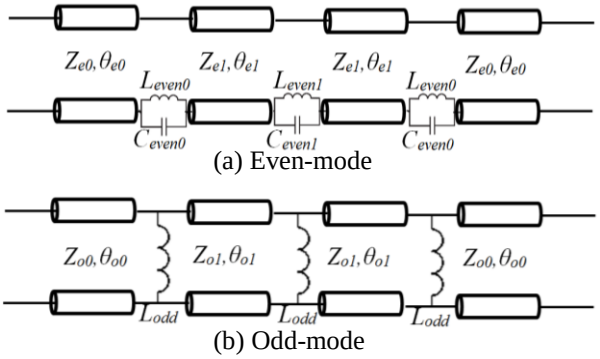

Fig. 2. The equivalent circuit of even- and odd-modes of the proposed coupler.

III. DESIGN PROCEDURE

The proposed coupler is designed based on the back propagation neural network (BPNN), which is normally used to estimate a complicated function of several variables [6] over an enclosed interval. In this work, the applied BPNN, as shown in Fig. 3, contains seven inputs regarding to the physical dimensions of the proposed coupler. In addition, fourteen neurons are used as the hidden layer of the proposed network. The coupling bandwidth, maximum magnitudes of S_{11} and S_{41} in pass band are considered to be the outputs of the BPNN network.

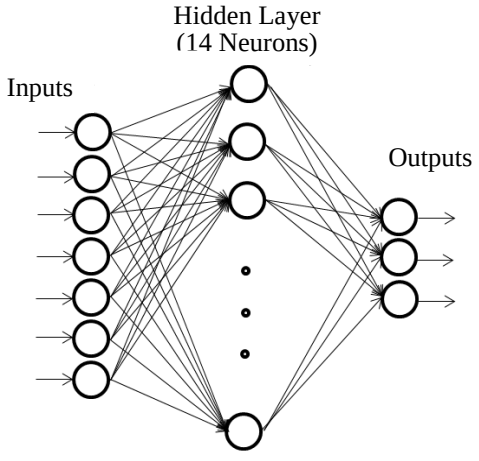

Fig. 3. Back propagation neural network model.

This network has to be trained. Input vectors and the corresponding target vectors are used to train the applied network. The BPNN uses a gradient descent

algorithm in which the network weights are moved along the negative portion of the gradient of the performance function. Using Matlab Neural Network Toolbox, trainbr function is chosen to train the applied network. This training function updates the weight and bias values according to Levenberg-Marquardt optimization process. It properly minimizes a combination of squared errors and weights, and then determines the correct combination of the weight and the bias values to obtain a network that can predict the best values of the outputs [7].

For training process of the BPNN, suitable values of input parameters of the neural network are chosen. In this procedure *b* is chosen from 18 mm to 22 mm, *g* is varied from 0.5 mm to 1.5 mm and *a* is selected from 14 mm to 18 mm. Moreover, the other values including *s*, *d*, *e* and *W* are set from 0.5 mm to 1.5 mm, 0.25 mm to 1.25 mm, 1 mm to 2.5 mm and 1.6 mm to 2.4 mm respectively. These are the input parameters of the BPNN network, whereas the coupling bandwidth and maximum magnitudes of S_{11} and S_{41} are the outputs of the network. Also, parameter *T* is defined by Equation (1):

$$T = \frac{BW}{MS_{11}MS_{41}}. \quad (1)$$

In Equation (1), *BW*, MS_{11} and MS_{41} are the coupling bandwidth with 1 dB flatness, maximum magnitudes of S_{11} and S_{41} in pass band respectively. It can be seen from Equation (1) that higher values of *T* lead to better performance for the coupler. Some selected values of the input training parameters including calculated *T* in each case are summarized in Table 1.

Table 1: Selected values of the training data for the designing procedure

g	*a*	*b*	*s*	*e*	*d*	*W*	*T*
0.5	14	18	1	2	1	2	107
0.75	16	18	0.5	1	0.75	1.8	143
1	14	18	0.75	1.5	0.5	2.2	166
1.25	18	20	1.25	1.75	0.25	1.6	82
1.5	18	22	1.5	1.25	1.25	2.4	93
0.75	14	20	1	2.25	0.5	1.6	59
1	16	22	0.75	1	1	2	98

g, *a*, *b*, *s*, *e*, *d* and *W* in mm.

The proposed coupler is numerically investigated using HFSS, which is a software package for solving complicated electromagnetic structure based on finite element method (FEM). The three dimensional structure is defined in HFSS. Using a full wave analysis, it predicts scattering parameters of the structure. *BW*, MS_{11} and MS_{41} in Equation (1) are obtained using HFSS. Testing data are shown in Table 2, which confirms that the BPNN outputs agree well with those obtained by HFSS.

After training the applied neural network, optimum values of the inputs to obtain maximum value of *T* is determined. The obtained optimum parameters of the proposed coupler are summarized in Table 3, which lead to the total length of $0.56\lambda_g$ for the proposed coupler.

Table 2: Testing data for the designing procedure

g	*a*	*b*	*s*	*e*	*d*	*W*	*T* BPNN	*T* HFSS
1.2	15	19	0.9	2.4	0.4	1.9	161	155
0.7	17	21	1.3	1.1	0.8	1.7	110	109
1.1	16	20	0.6	1.4	0.7	2.3	89	98
0.8	18	22	1	1.7	0.35	2.1	147	140
1.4	14	18	1.5	1.9	1.1	1.8	96	101
0.7	16	19	0.5	2.4	1	2	29	32
0.8	17	20	1.4	1.5	0.4	2.1	133	128

g, *a*, *b*, *s*, *e*, *d* and *W* in mm.

Table 3: The optimum parameters of the proposed coupler

Parameter	Value (mm)	Parameter	Value (mm)
g	1	*d*	0.5
a	16	*W*	1.9
b	22	*l*	12
s	1	*h*	0.787
e	2.25	*t*	0.5

IV. RESULTS AND DISCUSSIONS

A. Simulated results

The simulated *S*-parameters of the designed coupler versus frequency using the optimized parameters are shown in Fig. 4. It can be seen that the proposed coupler provides 0.58 dB coupling with 1 dB flatness over the frequency range from 6.5 GHz to 14 GHz, which corresponds to 73.2% fractional bandwidth. Maximum simulated return loss and coupler directivity in pass band are 11.62 dB and 13.83 dB respectively. Using the obtained results, *T* is calculated, which is 180.3 using simulation process. This agrees very well with the value of *T* = 188.7, which is obtained by the BPNN network.

To verify the cause of the high coupling strength over the predicted bandwidth, one can calculate even- and odd-mode complex propagation constants and characteristic impedances of these modes, using Equations (2) and (3) respectively [8]:

$$e^{\gamma_i d} = \frac{1 - S_{11,i}{}^2 + S_{21,i}{}^2 + \sqrt{\left(1 + S_{11,i}{}^2 - S_{21,i}{}^2\right)^2 - \left(2S_{11,i}\right)^2}}{2S_{21,i}}, \quad (2)$$

$$\gamma_i = \alpha_i + j\beta_i$$

$$Z_i = Z_0 \sqrt{\frac{\left(S_{21,i}{}^2 - S_{11,i}{}^2 - 1\right) - 2S_{11,i}}{\left(S_{21,i}{}^2 - S_{11,i}{}^2 - 1\right) + 2S_{11,i}}}. \quad (3)$$

In the above equations, i corresponds to even- or odd-mode, and Z_0 represents port impedances which is normally 50 Ω. Moreover, the coupling strength can be calculated using Equation (4) in a backward coupler:

$$C_z = S_{31} = \frac{(Z_e - Z_o)\tanh(\alpha + j\beta)l}{2Z_0 + (Z_e + Z_o)\tanh(\alpha + j\beta)l}. \quad (4)$$

The variation of $\tanh(\alpha + j\beta)l$ versus frequency is plotted in Fig. 5. It can be seen that in pass band, this function is equal to 1, except from 10 GHz to 13 GHz; and so, the coupling in pass band is determined using Equation (5):

$$C_z = S_{31} = \frac{Z_e - Z_o}{2Z_0 + (Z_e + Z_o)}. \quad (5)$$

The simulated imaginary and real parts of even and odd impedances, Z_e and Z_o, are shown in Fig. 6. It can be seen that the real parts of the impedances are negligible in the pass band, except over the frequency range from 10 GHz to 13 GHz. In addition, the imaginary parts in this band have opposite signs, which lead to obtain tight coupling of 0 dB over the mentioned frequency range.

Moreover, over the frequency range of 10 GHz to 13 GHz, $\tanh(\alpha + j\beta)l$ is not equal to 1. However, in this case the imaginary and real parts of Z_e are much greater than the imaginary and real parts of Z_o respectively. Therefore, the coupling coefficient, C_z is equal to 0 dB over the mentioned frequency range.

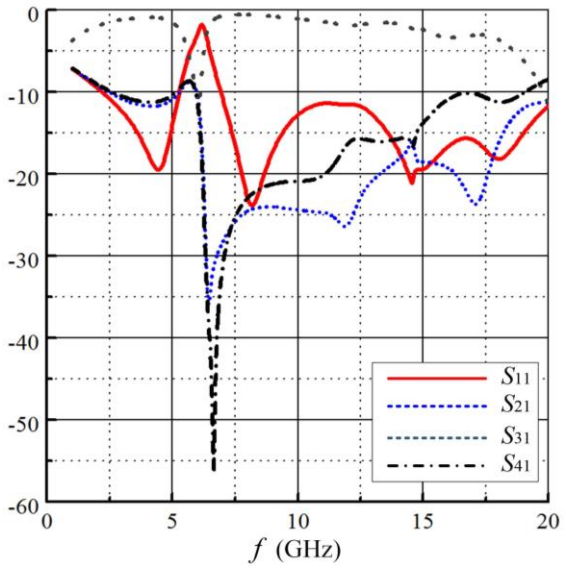

Fig. 4. The simulated *S*-parameters of the proposed coupler.

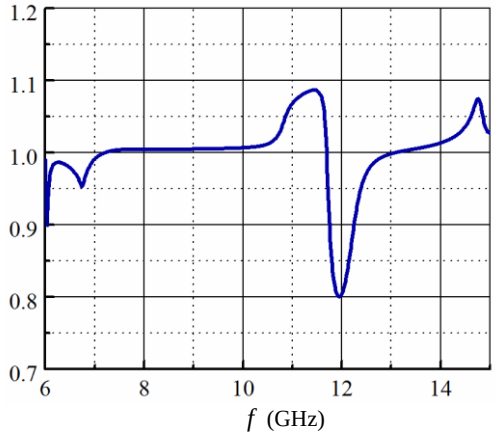

Fig. 5. Variation of $\tanh(\alpha + j\beta)l$ versus frequency.

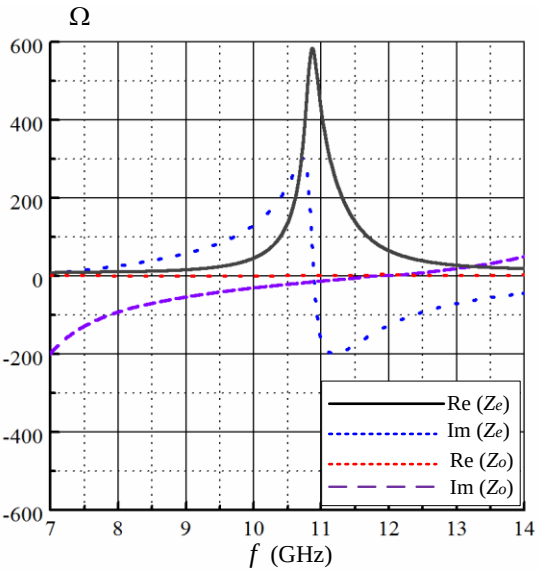

Fig. 6. The simulated imaginary and real parts of even and odd impedances versus frequency.

B. Measured results

To evaluate the designed procedure for the coupler, a prototype of the proposed coupler is fabricated using TLY031 substrate with electrical characteristics of ε_r=2.2, h=0.787 mm and loss tangent of 0.009. A photo of the fabricated coupler and the measurement test bench are shown in Fig. 7.

The measured results for the *S*-parameters of the designed coupler are shown in Figs. 8 (a) and 8 (b), including the simulation results for comparison. It can be seen that the measured coupling is 0.49 dB with maximum 2 dB variation over the desired bandwidth. In addition, measured return loss is better than 12.45 dB and measured directivity is better than 13.5 dB over the pass band. It can be seen that a very good agreement is obtained between measurement and simulation results.

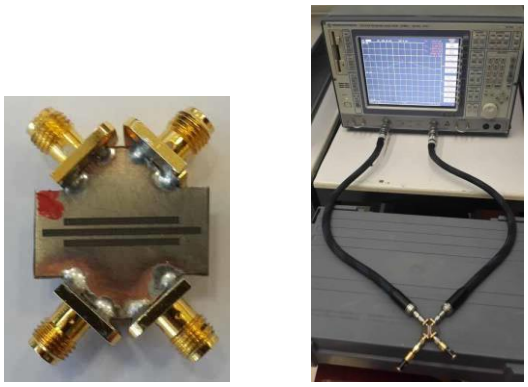

(a) (b)

Fig. 7. (a)The photo of the fabricated proposed coupler, and (b) the measurement test bench.

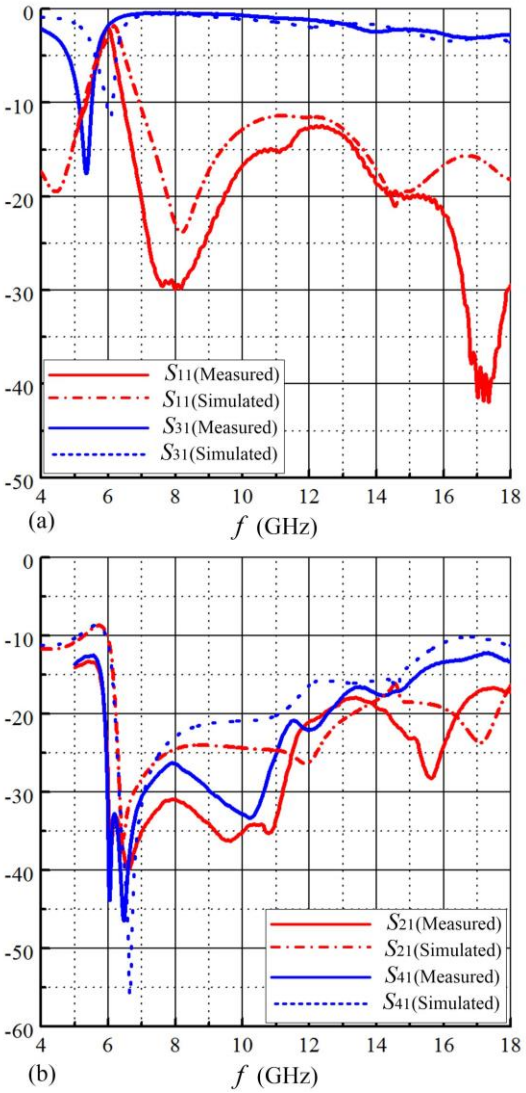

Fig. 8. The measured results of the proposed coupler: (a) S_{11} and S_{31}, and (b) S_{21} and S_{41}.

C. Comparison with the recently published research

The measured results of the proposed coupler are summarized in Table 4, including the measured performance of the recently published research of couplers for comparison. It can be seen that the proposed coupler provides a tight coupling over a very wide bandwidth with a reasonable short length. Although, it suffers from the low directivity compared to that of presented coupler in [14], but the obtained bandwidth is much more.

Table 4: Comparison of the measured results of the proposed coupler with the recently published research

Coupler	FBW (%)	Coupling (dB)	Directivity (dB)	Length (mm)
[9]	84.6	16.6	8	$1.85\lambda_g$
[10]	25.8	0.52	10	$1.50\lambda_g$
[11]	40.0	1.36	10	$7.67\lambda_g$
[12]	72.2	15.1	25	$0.50\lambda_g$
[13]	18.1	0	20	-
[14]	11.1	0	35	$2.26\lambda_g$
[15]	8.7	0.54	20	$0.50\lambda_g$
This paper	73.2	0.49	13.5	$0.56\lambda_g$

V. CONCLUSIONS

A new type of wideband backward-wave directional coupler is presented in this paper. The proposed coupler operates similar to the CRLH couplers. Two techniques, for the first time, including adding shunt inductance in odd mode and series capacitance in even mode are applied together to obtain a high performance and wideband coupler. Neural network based on the BPNN optimization procedure is used for designing process. The proposed coupler is also analyzed using HFSS software. A prototype of the proposed coupler is made and it is successfully tested. The measured results agree well with those obtained by simulation. It is shown that the coupling strength of 0.49 dB with maximum 2 dB flatness, return loss of better than 12.45 dB and directivity of at least 13.5 dB over the pass band are obtained. The proposed coupler provides the advantage of small size and high level of coupling over a very wide bandwidth and it is a good candidate in microwave and millimeter wave circuits.

ACKNOWLEDGMENT

The authors wish to express appreciation to Research Deputy of Ferdowsi University of Mashhad for supporting this project by Grant No. 3/33862.

REFERENCES

[1] L. K. Yeung and K. Wu, "A dual-band coupled line balun filter," *IEEE Transactions on Microwave Theory and Techniques*, vol. 55, pp. 2406-2411,

2007.

[2] A. M. Qaroot and N. I. Dib, "General design of N-way multi-frequency unequal split Wilkinson power divider using transmission line transformers," *Progress In Electromagnetics Research C*, vol. 14, pp. 115-129, 2010.

[3] C. Caloz and T. Itoh, *Guided-Wave Applications*. in Electromagnetic Metamaterials: Transmission Line Theory and Microwave Applications, 1st ed., Ed. New Jersey: John Wiley & Sons, pp. 227-249, 2006.

[4] J. Lange, "Interdigital stripline quadrature hybrid," *IEEE Trans. Microwave Theory Tech*., vol. 17, no. 12, pp. 1150-1151, Dec. 1969.

[5] C. Caloz, A. Sanada, and T. Itoh, "A novel composite right/left-handed coupled-line directional coupler with arbitrary coupling level and broad bandwidth," *IEEE Trans. Microwave Theory Tech*., vol. 52, no. 3, pp. 980-992, Mar. 2004.

[6] Z. S. Tabatabaeian and M. H. Neshati, "Design investigation of an X-band SIW H-plane band pass filter with improved stop band using neural network optimization," *The Applied Computational Electromagnetics Society Journal*, vol. 30, no. 10, pp. 1083-1088, Oct. 2015.

[7] D. J. C. MacKay, *Bayesian Interpolation, Neural Computation*. MIT Press Journals, vol. 4, no. 3, pp. 415-447, May 1992.

[8] W. R. Eisenstadt and Y. Eo, "S-parameter-based IC interconnect transmission line characterization," *IEEE Trans. Comp., Hybrids, Manufact. Technol*., vol. 15, pp. 483-490, Aug. 1992.

[9] M. Hrobak, M. Sterns, E. Seler, M. Schramm, and L. P. Schmidt, "Design and construction of an ultra-wideband backward wave directional coupler," *IET Microwaves, Antennas & Propagation*, vol. 6, pp. 1048-1055, Oct. 2012.

[10] Y. Ma, H. Zhang, and Y. Li, "Novel symmetrical coupled-line directional coupler based on resonant-type composite right/left handed transmission lines," *Progress In Electromagnetics Research*, vol. 140, pp. 213-226, 2013.

[11] M. Chudzik, I. Arnedo, A. Lujambio, I. Arregui, F. Teberio, D. Benito, T. Lopetegi, and M. A. G. Laso, "Design of EBG microstrip directional coupler with high directivity and coupling," *Proceedings of the 42nd European Microwave Conference*, pp. 483-486, 2012.

[12] H. Mextorf and R. Knöchel, "The intrinsic impedance and its application to backward and forward coupled-line couplers," *IEEE Transactions on Microwave Theory and Techniques*, vol. 62, pp. 224-233, 2014.

[13] R. Islam and G. V. Eleftheriades, "Review of the microstrip/negative-refractive-index transmission-line coupled-line coupler," *IET Microwaves, Antennas & Propagation*, vol. 6, pp. 31-45, 2012.

[14] C. Liu and W. Menzel, "A microstrip diplexer from metamaterial transmission lines," *IEEE MTT-S International Microwave Symposium Digest*, pp. 65-68, 2009.

[15] A. Pourzadi, A. R. Attari, and M. S. Majedi, "A directivity-enhanced directional coupler using epsilon negative transmission line," *IEEE Trans. Microwave Theory Tech.*, vol. 60, no. 11, pp. 3395-3402, Nov. 2012.

Zahra Sadat Tabatabaeian was born in Mashhad, Iran, on May 7, 1988. She received her B.Sc. and M.Sc. degree in Electrical Engineering from Ferdowsi University of Mashhad, Iran in 2010 and 2012 respectively, and she is currently working toward the Ph.D. degree in Electrical Engineering at Ferdowsi University of Mashhad. Her research interests include microwave passive circuit design and meta-materials.

Mohammad H. Neshati was born in Yazd, Iran. He received his B.Sc. in Electrical Engineering from Isfahan University of Technology, Isfahan, Iran; M.Sc. degree from Amir-Kabir University of Technology, Tehran, Iran, and Ph.D. from the University of Manchester (UMIST), England in 2000. Since 2006, he has been with the Department of Electrical Engineering of Ferdowsi University of Mashhad Iran, where he is an Associate Professor. His current research includes electromagnetic, antenna theory and design, microwave active and passive circuit design.

Planar Dual-Band WLAN MIMO Antenna with High Isolation

Hui Li *, Le Kang, Yuan Xu, and Ying-zeng Yin

Science and Technology on Antenna and Microwave Laboratory
Xidian University, Xi'an, Shaanxi, 710071, China
*huiyuezai@163.com

Abstract ─ In this paper, a dual-band multiple-input multiple-output (MIMO) antenna with a planar and rotational symmetric structure is presented. The proposed antenna comprises two via-fed monopole antennas arranged orthogonally in cross-pairs. When each monopole is excited, the other can be employed as a parasitic element. By properly adjusting the antenna dimensions, two resonant modes can be generated at about 2.45 and 5.6 GHz. Besides, the radiation patterns of two monopoles are orthogonal to each other, resulting in good pattern diversity and high isolation without using additional decoupling methods. Measured results show that two operating bands ranging from 2.3-2.75 and 5.09-6.16 GHz are obtained, which can cover the whole (2.4/5.2/5.8-GHz) wireless local area network (WLAN) bands. Port-to-port isolation is more than 24 and 22 dB at the lower and higher operating bands, respectively. Envelope correlation coefficient is studied as well.

Index Terms ─ Dual-band, high isolation, MIMO, via-fed monopole, WLAN.

I. INTRODUCTION

Nowadays, combining the existing wireless communication systems such as wireless local area networks (WLAN) with multiple-input multiple-output (MIMO) technology is a hot topic. Due to the limited space available in wireless terminals, multi-antennas are often closely packed in MIMO systems and strong mutual coupling is caused. In order to suppress the mutual coupling in MIMO antennas, various types of methods have been developed, which include the lumped decoupling circuit [1], parasitic element [2], neutralization line [3], defected ground structure [4], electromagnetic band gap [5] and ground stub [6]. However, all these methods require additional space for the decoupling structures and some of the structures are wavelength-related, which makes them difficult to be integrated in the portable devices. To achieve high isolation without the use of complex decoupling methods, MIMO antennas with orthogonal polarizations/modes could be a promising choice [7-9]. Though the antennas [7, 8] exhibit good isolation performance, the impedance matching and radiation characteristics are different between ports. Owing to the orthogonal and symmetrical placement of the antenna [9], identical matching characteristics and orthogonal radiation patterns with low correlation are realized at two ports. Nevertheless, this antenna with a single resonant mode at 2.4 GHz just covers the lower-band WLAN operation. The WLAN MIMO antenna [10] produces dual-band matching as well as a built-in decoupling mechanism. However, the antenna exhibits an isolation level less than 15 dB.

In this work, a small and planar MIMO antenna is proposed for the 2.4/5.2/5.8-GHz WLAN applications. The antenna consists of a cross-pair of via-fed monopole elements. When each antenna port is excited, two resonances at 2.45 and 5.6 GHz are generated by the excited antenna element and the other parasitic element, respectively. Parasitic dipole antenna has also been adopted in [11] to excite an additional resonance and thus extend the impedance bandwidth. Compared with the design in [11], the proposed antenna with via-fed monopole elements has planar and simple feeding structures. Since the two ports are orthogonally fed, the radiation patterns appear rotated by 90° and produce low mutual coupling between antenna elements. Without using any extra decoupling methods, the antenna achieves isolation of above 24 and 22 dB at the 2.4- and 5-GHz band, respectively. Moreover, the antenna maintains a total size of 43×43×0.8 mm^3 and a full planar structure.

II. ANTENNA DESIGN AND ANALYSIS

A. Antenna structure

Geometry of the proposed antenna is shown in Fig. 1. The antenna is implemented with a low-cost FR4 substrate with a relative permittivity of 4.4 and a thickness of 0.8 mm. The MIMO antenna is composed of two perpendicularly crossed via-fed monopole elements, which are identical in configuration and arranged on both sides of the substrate without physical overlaps.

For each monopole, a 50-Ω transmission line is printed on one side of the substrate and connected to the tapered radiator on the other side through a shorting via. Each monopole itself is capable of generating a lower resonance at around 2.45 GHz. Then a higher resonant

Submitted On: May 15, 2016
Accepted On: September 28, 2016

mode at about 5.6 GHz is excited by the other perpendicular monopole. By appropriately designing the detailed dimensions of the MIMO antenna, dual-band operation can be realized for WLAN applications. In addition, since one monopole element is horizontally polarized and the other is vertically polarized, orthogonal radiation patterns are obtained inherently at two ports and this weakens the coupling between antenna elements without additional decoupling structures. Based on the above analysis, the final parameters are optimized as follows (in millimetres): $W = L = 43$, $W_1 = 10$, $W_2 = 1.5$, $W_3 = 2$, $L_1 = 26.8$, $L_2 = 16.5$, $L_3 = 20.5$, $D = 5.7$, and $H = 0.8$.

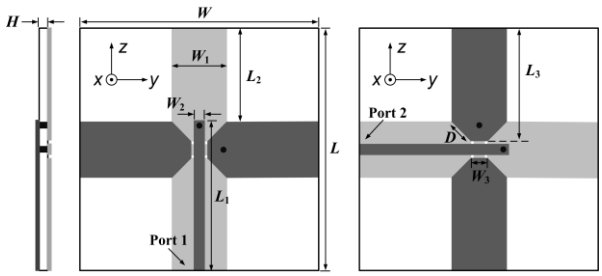

Fig. 1. Geometry of the proposed MIMO antenna.

B. Working mechanism

To clarify the dual-band excitation mechanism, the simulated current distributions of the proposed antenna are illustrated in Fig. 2. At 2.45 GHz, when only Port 1 is excited, most surface current is concentrated on the radiator as well as the ground plane of the vertically oriented monopole element. It is noted that the electrical length of the radiator is close to a quarter-wavelength at 2.45 GHz. It also can be seen that at 5.6 GHz, larger current is distributed along the tapered edges of the two crossed monopoles, and strong induced currents can be observed on the horizontally arranged monopole. It is revealed that the horizontal monopole can be viewed as a parasitic element, which leads to the appearance of an additional resonance. This resonant mode is sensitive to the electromagnetic coupling between the monopoles at the two sides of the substrate, which is controlled by adjusting the coupled length.

Figure 3 displays the simulated 3-D radiation patterns of the proposed antenna. It can be found from Figs. 3 (a) and (b) that, orthogonal radiation patterns are obtained at 2.45 GHz when different ports are excited. The two patterns have little influence on each other, which consequently leads to coupling reduction. Similar results are observed at 5.6 GHz, as indicated in Figs. 3 (c) and (d). The antenna provides two different radiation patterns to receive signals from different directions, hence ensuring pattern diversity with good isolation.

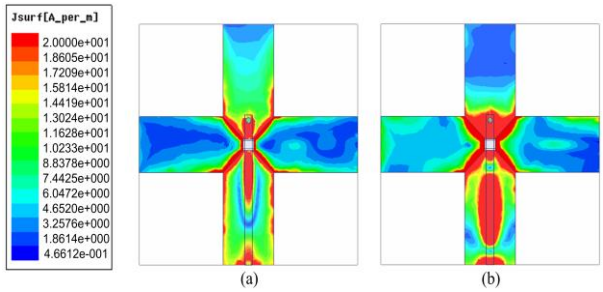

Fig. 2. Surface current distributions at: (a) 2.45 and (b) 5.6 GHz.

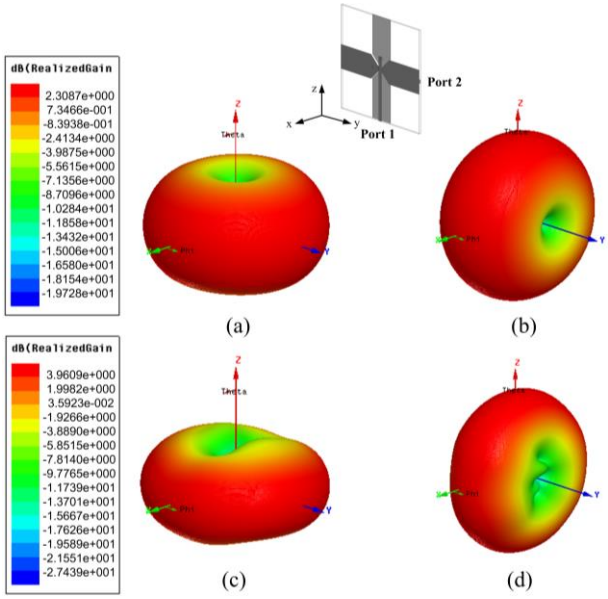

Fig. 3. Simulated 3-D radiation patterns at: (a), (b) 2.45 GHz, and (c), (d) 5.6 GHz.

The effects of the important design parameters on antenna performance are investigated through simulation, as presented in Fig. 4. It can be found from Fig. 4 (a) that, both the resonant bands at about 2.45 and 5.6 GHz shift towards lower frequencies when L_3 are influenced by increasing the total length of the tapered radiator (L_3). The change of the mutual coupling with the variation of L_3 is slight. In Fig. 4 (b), with the increase of D, the higher resonant band shifts to lower frequencies while the lower band almost remains unchanged. Meanwhile, the mutual coupling remains below -25 and -20 dB at the two bands, respectively. It is demonstrated that the coupled length (D) significantly affects the higher resonant band.

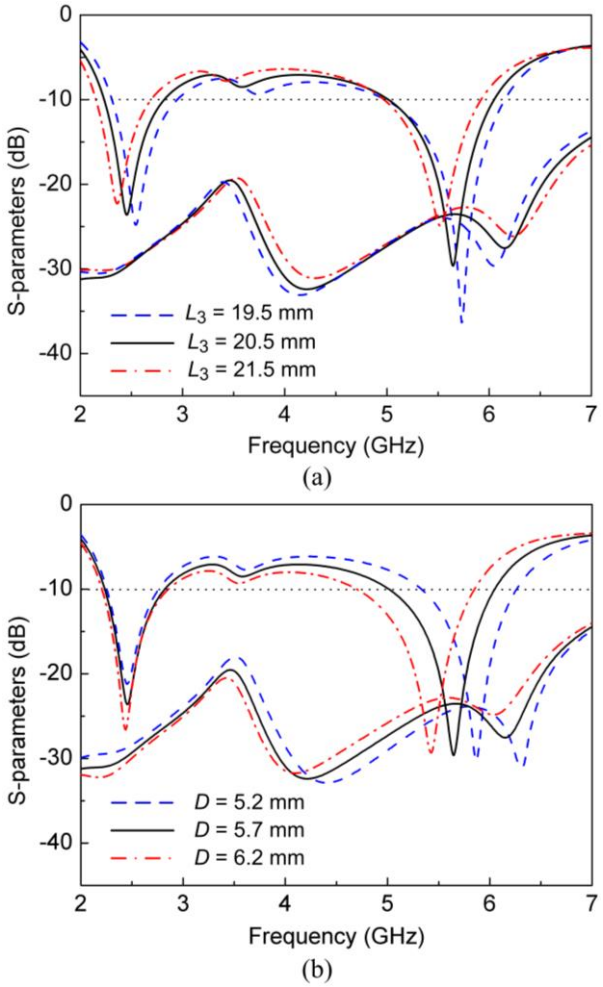

Fig. 4. Parametric study with different values of: (a) L_3 and (b) D.

III. RESULTS AND DISCUSSION

A. S-parameters

In order to examine the design above, an antenna prototype is fabricated and shown in Fig. 5. The reflection coefficient (S_{11} & S_{22}) and mutual coupling (S_{12} & S_{21}) are displayed in Figs. 6 (a) and (b), respectively. As can be observed, the discrepancies between measurement and simulation are very slight, which proves the design structure has a good and stable performance. The measured bandwidths with -10 dB reflection coefficient are 450 MHz (2.3-2.75 GHz) and 1070 MHz (5.09-6.16 GHz), which can cover the entire WLAN operating bands. It is also shown that the measured port isolation is more than 24 dB at the 2.4-GHz band and 22 dB at the 5.2/5.8-GHz band.

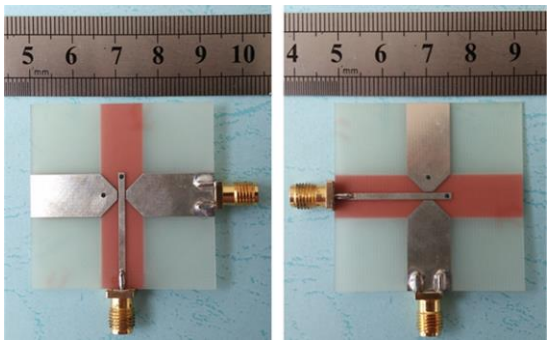

Fig. 5. Photographs of the fabricated antenna.

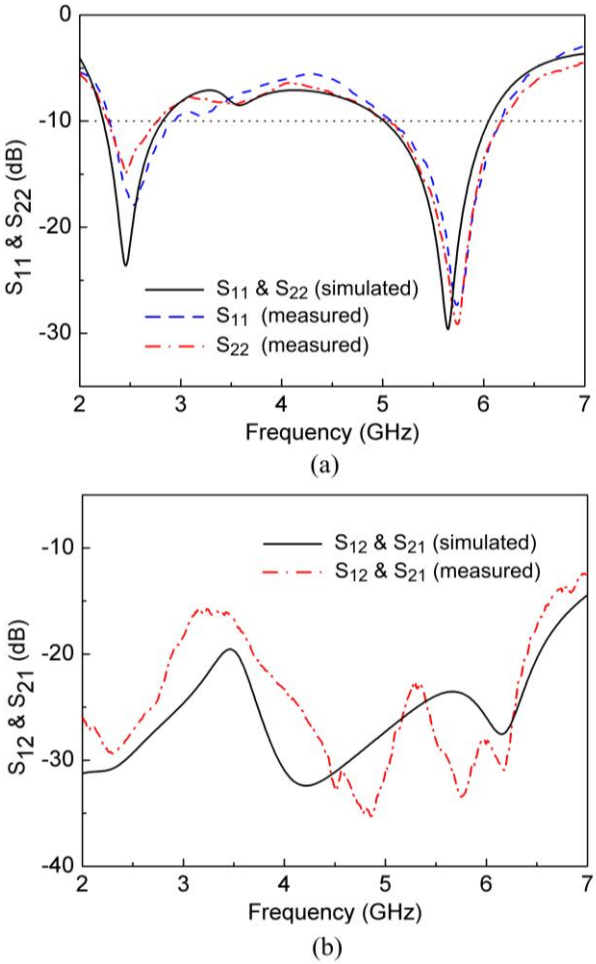

Fig. 6. Measured and simulated S-parameters.

B. Radiation characteristics

Since the antenna has a planar and rotational symmetric configuration, the radiation characteristics

are measured with a single port excited. The normalized radiation patterns are depicted in Fig. 7. It is observed that the radiation patterns are quasi-omnidirectional in the *H*-plane (*xoy*-plane of Port 1 and *xoz*-plane of Port 2) and nearly dumb-bell shaped in the *E*-plane (*xoz*-plane of Port 1 and *xoy*-plane of Port 2). In the *yoz*-plane, the patterns at two ports exhibit good complementary properties.

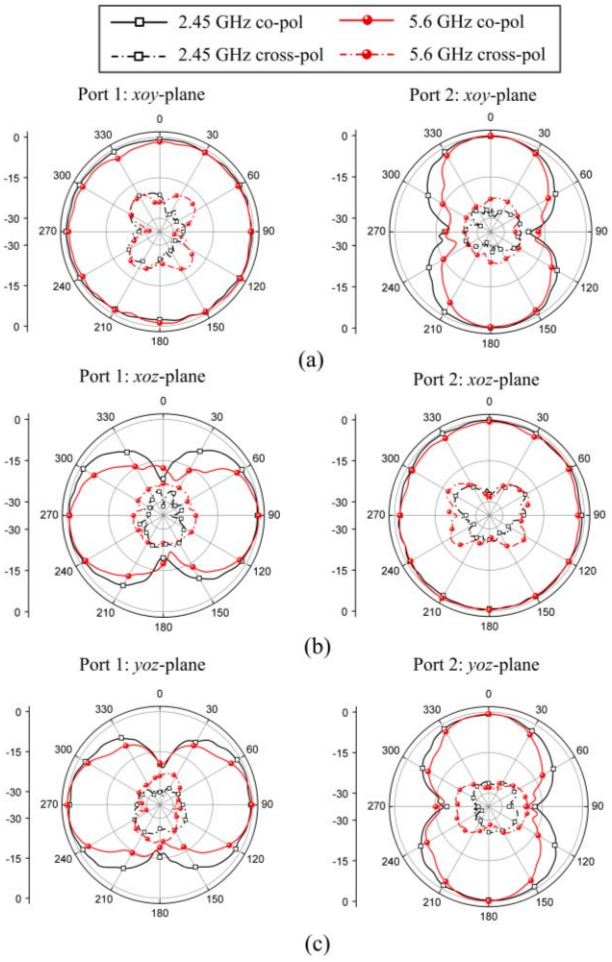

Fig. 7. Measured far-filed radiation patterns at 2.45 and 5.6 GHz: (a) *xoy*-plane, (b) *xoz*-plane, and (c) *yoz*-plane.

The measured results agree well with the simulation in Fig. 3. Therefore, the antenna produces both orthogonal and complementary patterns, which weaken the channel correlation and strengthen the power of the reception.

As shown in Fig. 8, the peak gain varies from 1.93 to 2.28 and 3.07 to 3.94 dBi at the lower and higher bands, respectively. Besides, the antenna provides radiation efficiency better than 80% at low-frequency range. At higher frequencies, the efficiency deceases to around 73%.

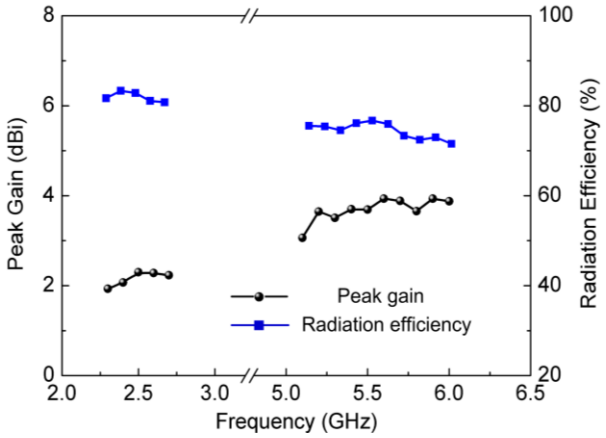

Fig. 8. Measured gain and radiation efficiency.

C. Diversity performance

An envelope correlation coefficient (ECC) level of below 0.5 is set as a widely accepted limit for diversity conditions [12]. Assuming that the antenna operates in a uniform multipath environment, the ECC value (denoted by ρ_e) is calculated from the measured results [13]:

$$\rho_e = \frac{\left|S_{11}^* S_{12} + S_{21}^* S_{22}\right|^2}{(1-(|S_{11}|^2+|S_{21}|^2))\,(1-(|S_{22}|^2+|S_{12}|^2))\eta_{rad1}\eta_{rad2}}. \quad (1)$$

As observed in Fig. 9, the ECC value between ports is found to be below 0.01 at the two bands of interest, which is much less than 0.5.

To estimate the loss of channel capacity in MIMO antenna systems, the capacity loss (C_{loss}) is obtained using the correlation matrix of the receiving antenna [14]:

$$C_{loss} = -\log_2 \det(\Psi^R), \quad (2)$$

where

$$\Psi^R = \begin{bmatrix} \rho_{11} & \rho_{12} \\ \rho_{21} & \rho_{22} \end{bmatrix}, \quad (3)$$

and

$$\rho_{ii} = 1-(|S_{ii}|^2+|S_{ij}|^2),\ \rho_{ij} = -(S_{ii}^* S_{ij} + S_{ji}^* S_{ij}),\ \text{for } i, j = 1 \text{ or } 2. \quad (4)$$

It also can be seen from Fig. 9 that the C_{loss} is less than 0.28 b/s/Hz, and it is well below the threshold value of 0.4 b/s/Hz. Therefore, the results above indicate that good diversity performance can be achieved

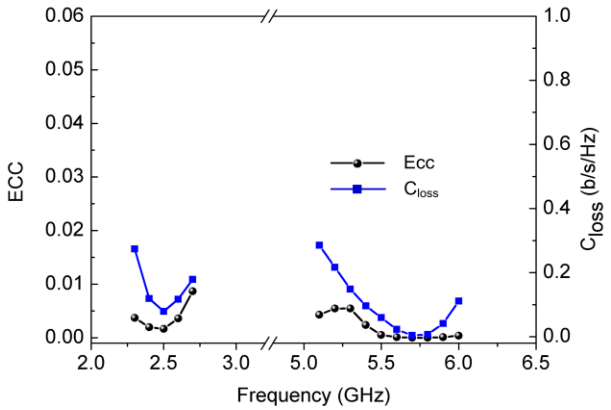

Fig. 9. Measured envelope correlation coefficient and capacity loss.

IV. CONCLUSION

A dual-port MIMO antenna using a planar rotational symmetric structure has been proposed and investigated. By employing a cross-pair of via-fed monopole elements, dual-band resonant characteristics can be obtained. Meanwhile, orthogonal radiation patterns are achieved when feeding different ports, which leads to low correlation in reception. According to the measured data, the antenna operates from 2.3 to 2.75 and 5.09 to 6.16 GHz, along with port isolation of better than 24 and 22 dB at the lower and higher working bands. The envelop correlation coefficient and capacity loss are better than 0.01 and 0.28 b/s/Hz, respectively. Furthermore, the planar structure and simple configuration make the antenna easy to be manufactured and integrated.

REFERENCES

[1] S. C. Chen, Y. S. Wang, and S. J. Chung, "A decoupling technique for increasing the port isolation between two strongly coupled antennas," *IEEE Trans. Antennas Propag.*, vol. 56, no. 12, pp. 3650-3658, Dec. 2008.

[2] A. C. K. Mak, C. R. Rowell, and R. D. Murch, "Isolation enhancement between two closely packed antennas," *IEEE Trans. Antennas Propag.*, vol. 56, no. 11, pp. 3411-3419, Nov. 2008.

[3] A. Chebihi, C. Luxey, A. Diallo, P. L. Thuc, and R. Staraj, "A novel isolation technique for closely spaced PIFAs for UMTS mobile phones," *IEEE Antennas Wireless Propag. Lett.*, vol. 7, pp. 665-668, 2008.

[4] F. G. Zhu, J. D. Xu, and Q. Xu, "Reduction of mutual coupling between closely-packed antenna elements using defected ground structure," *Electron. Lett.*, vol. 45, no. 12, pp. 601-602, June 2009.

[5] C. C. Hsu, K. H. Lin, and H. L. Su, "Implementation of broadband isolator using metamaterial-inspired resonators and T-shaped branch for MIMO antennas," *IEEE Trans. Antennas Propag.*, vol. 59, no. 10, pp. 3936-3939, Oct. 2011.

[6] L. Liu, S. W. Cheung, and T. I. Yuk, "Compact MIMO antenna for portable devices in UWB applications," *IEEE Trans. Antennas Propag.*, vol. 61, no. 8, pp. 4257-4264, Aug. 2013.

[7] J. Malik, A. Patnaik, and M. V. Kartikeyan, "Novel printed MIMO antenna with pattern and polarization diversity," *IEEE Antennas Wireless Propag. Lett.*, vol. 14, pp. 739-742, 2015.

[8] W. W. Li, B. Zhang, J. H. Zhou, and B. Q. You, "High isolation dual-port MIMO antenna," *Electron. Lett.*, vol. 49, no. 15, pp. 919-921, July 2013.

[9] H. Wang, Z. J. Zhang, and Z. H. Feng, "Dual-port planar MIMO antenna with ultra-high isolation and orthogonal radiation patterns," *Electron. Lett.*, vol. 51, no. 1, pp. 7-8, Jan. 2015.

[10] S. M. Wang, L. T. Hwang, C. J. Lee, C. Y. Hsu, and F. S. Chang, "MIMO antenna design with built-in decoupling mechanism for WLAN dual-band applications," *Electron. Lett.*, vol. 51, no. 13, pp. 966-968, June 2015.

[11] Q. X. Chu, D. L. Wen, and Y. Luo, "A broadband ±45° dual-polarized antenna with Y-shaped feeding lines," *IEEE Trans. Antennas Propag.*, vol. 63, no. 2, pp. 483-490, Jan. 2015.

[12] R. G. Vaughan and J. B. Andersen, "Antenna diversity in mobile communications," *IEEE Trans. Veh. Technol.*, vol. 36, no. 4, pp. 149-172, Nov. 1987.

[13] H. Paul, "The significance of radiation efficiencies when using S-parameters to calculate the received signal correlation from two antennas," *IEEE Antennas Wirel. Propag. Lett.*, vol. 4, no. 1, pp. 97-99, Jan. 2005.

[14] Y. K. Choukiker, S. K. Sharma, and S. K. Behera, "Hybrid fractal shape planar monopole antenna covering multiband wireless communications with MIMO implementation for handheld mobile devices," *IEEE Trans. Antennas Propag.*, vol. 62, no. 3, pp. 1483-1488, Mar. 2014.

Hui Li received the B.S. and M.S. degrees from Xidian University, Xi'an, China, in 2008 and 2012, respectively. She is currently pursuing the Ph.D. degree in Electromagnetic Field and Microwave Technology from the National Laboratory of Science and Technology on Antennas and Microwaves, Xidian University, Xi'an, China

Her research interests include multiband antennas, ultra-wideband antennas, tightly coupled antennas and MIMO technologies.

Le Kang received the B.S. and M.S. degrees from Xidian University, Xi'an, China, in 2008 and 2011, respectively. He is currently pursuing the Ph.D. degree in Electromagnetic Field and Microwave Technology from the National Laboratory of Science and Technology on Antennas and Microwaves, Xidian University, Xi'an, China.

His research interests include microstrip antennas, MIMO antennas, and phased array antennas.

Yuan Xu received the B.S. degrees from Xi`an University of Posts & Telecommunications, Xi'an, China, in 2014. She is currently pursuing the M.S. degree in Electromagnetic Field and Microwave Technology from the National Laboratory of Science and Technology on Antennas and Microwaves, Xidian University, Xi'an, China.

Her research interests include multiband antennas, UWB antennas, and wideband unidirectional antenna.

Ying-zeng Yin received the B.S. degree, M.S. degree and Ph.D. degree in Electromagnetic Wave and Microwave Technology from Xidian University, Xi'an, China, in 1987, 1990, and 2002, respectively. From 1990 to 1992, he was a Research Assistant and an Instructor at the Institute of Antennas and Electromagnetic Scattering, Xidian University. From 1992 to 1996, he was an Associate Professor in the Department of Electromagnetic Engineering, Xidian University. Since 2004, he has been a Professor at Xidian University.

His research interests include design of microstrip antennas, artificial magnetic conductors, phased array antennas, and computer aided design for antennas.

A Compact Planar Ultra Wideband Antenna with Triple-Notched Bands Using Capacitive Coupled and Parallel LC Elements

Amin Araghi

Department of Electrical Engineering, Islamic Azad University, Urmia, Iran
Amin_araghi_1368@yahoo.com

Abstract ─ Overlapping of frequency bands such as Worldwide Interoperability for Microwave Access (WiMAX), Wireless Local Area Network (WLAN) and International Telecommunication Union (ITU) bands with Ultra Wide Band (UWB) cause serious interference problems. As an attempt to reduce the effect of this coexistence, a triple band-notched monopole antenna is presented. A modified semi ellipse element with two I-shaped slots is used as the ground plane. A U-shaped slot, a pair of inverted L-shaped strips, and a modified G-slot structure which act as parallel LC circuit and capacitive-coupled elements, are embedded in feed line and radiation patch to create the triple band notch characteristics. The notched bands position can be controlled by tuning the dimensions of the foregoing filtering elements. The proposed antenna has been fabricated and measured. According to the measured results, the antenna operates over the frequency band of 2.5-16.5 GHz with three notched bands at the 5-6.2 GHz (WLAN), 3.1-4 GHz (WiMAX), and 7.15-8.1 GHz (X-band).

Index Terms ─ Capacitive-coupled elements, parallel LC circuits, triple band-notched antenna, Ultrawideband (UWB) antenna.

I. INTRODUCTION

Among the printed UWB antenna designs, the planar monopole antennas have gained great popularity due to their attractive characteristics such as wide impedance bandwidth (BW), simple structure and omni-directional radiation patterns [1]–[5], along with multitasking capabilities such as multiband and multi notched applications. However, due to the existence of many narrow frequency bands such as HIPERLAN/2 WLAN operating in the 5.15-5.825 GHz band, wireless local-area network (IEEE 802.11a), WiMAX IEEE 802.16 operating in the 3.3-3.7 GHz [3], and X-band in the 7.25-7.75 GHz over the UWB frequency range and the consequent interference problem, the need for techniques to filter the foregoing bands from UWB has been emerged. Band notched antennas, a new category of antenna structures, have been proved as a promising solution to the interfering problem. Many researches have been carried out and different techniques have been proposed to reach the filtering property. Embedding various geometrical shaped slots on the radiation patch [1], inverted L-, G-, and Γ-shaped strips, modified G-slot structures, rectangular subs and parasitic elements, are some of these techniques to suppress the dispensable bands [1], [4], [6].

This paper aims to design a novel antenna with triple band notched capability with increasing the bandwidth. By using the modifying ground plane and radiation patch, the bandwidth of antenna is increased. First, two symmetrical I-shaped slots are inserted on the ground plane with bandwidth enhancement purpose. Then, to achieve the filtering characteristics and improve the antenna bandwidth, U-shaped slot, two symmetrical inverted L-shaped strips, and a modified G-slot structure are added to the antenna structure. The mentioned elements act as parallel circuit and capacitive-coupled elements. The notched frequency bands are generated in the 5-6.2 GHz (WLAN), 3.1-4 GHz (WiMAX), and 7.15-8.1 GHz (X-band) over the 2.5-16.5 GHz (152%) operating frequency band. These may be controlled by changing the dimensions of the filtering structures. The rest of the paper will be as follows: Section II discusses the antenna design process. The simulated and measured results and discussion on them are presented in Section III.

II. ANTENNA DESIGN AND CONIFURATION

Figure 1 shows the geometrical configurations of the proposed antenna, which consists of a semi-ellipse shaped ground plane with two symmetrical I-shaped slots. The antenna is implemented on cheap FR4-epoxy substrate with a compact size of $19\times22\times1$ mm^3 and permittivity of 4.4. To achieve 50-ohm characteristic impedance, the length (L_f) and width (W_f) of the μ-strip feed line are fixed at 5.7 mm and 1.95 mm respectively. To analyze the antenna precisely, the antenna design is explained in Fig. 2 in five steps. These structures have been analyzed using Ansoft High Frequency Structure Simulator (HFSS). Figure 3 shows the S_{11} and VSWR curves for Antenna 1-5. It can be observed from Fig. 3

Submitted On: December 12, 2014
Accepted On: June 17, 2016

that, the antenna 1 has poor VSWR in the frequency range of 10-15 GHz frequency. Therefore to improve the impedance matching in the frequency range of 10-15 GHz, two I-shaped slots in the ground plane is embedded. Then, by using of modifying radiation patch, triple band notch antenna created and the impedance matching at the upper edge frequency is improved. As shown in Fig. 2, the addition of the I-shaped slots on the ground plane leads to the excitation of new resonances and bandwidth enhancement. As it is depicted in Fig. 2, U-shaped slot, two symmetrical inverted L-shaped strips, and a modified G-slot structure are embedded in Antenna 3; Antennas 4 and Antenna 5 which realize the notched bands in WLAN, WiMAX and X-band respectively. According to the results, the proposed triple band notch antenna structure covers the frequency band from 2.5 to 16.5 GHz with VSWR<2 (S_{11}< -10 dB) and the band notch frequencies covering the 5-6.2 GHz, 3.1-4 GHz, and 7.15-8.1 GHz.

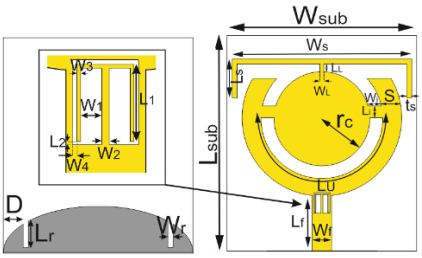

Fig. 1. Configuration of the proposed triple band-notched antenna: W_{sub}=19, L_{sub}=22, W_f=1.95, L_f=5.7, W_i=1.35, L_i=1.2, W_L=0.4, L_L=0.8, W_s=18, L_u=19, t_s=0.5, L_s=4, W_1=0.5, W_2=0.2, W_3=0.1, S=1.95, W_4=0.1, L_1=1.93, L_2=0.07, W_r=0.5, L_r=2.7, D=2, r_c=4.8; (all dimensions are expressed in mm).

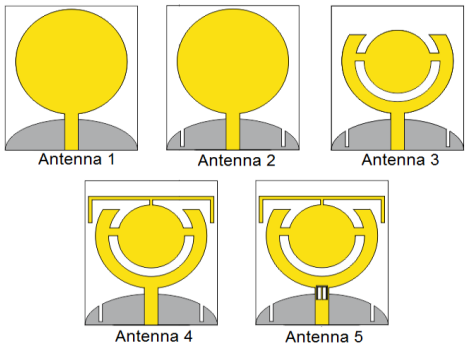

Fig. 2. The antenna design process.

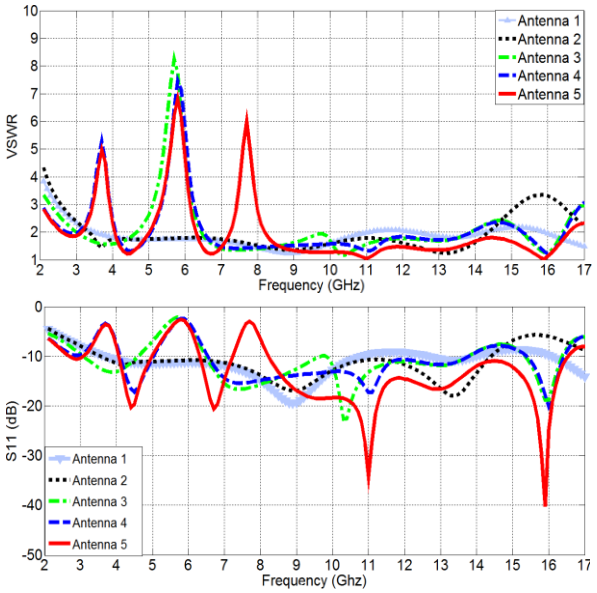

Fig. 3. S_{11} and VSWR curves for Antenna 1-5.

III. RESULTS AND DISCUSSION

A. Full band antenna

In this section, the bandwidth enhancement process to reach the full band antenna is studied in detail. As it was mentioned earlier, the basic structure of the proposed UWB antenna is composed of a circular radiation patch and a semi-ellipse shaped ground plane with a pair of I-shaped slots. As the insertion of the I-shaped slots helps the bandwidth enhancement, it is expected that antenna performance be a function of the I-shaped slots dimensions, named as L_r and W_r. Figure 4 shows simulated VSWR curves for different values of L_r and W_r. It is seen that even in the case that there is no slot on the ground plane, the UWB frequency band is covered. By inserting the slots and tuning their dimensions, upper edge frequency has been noticeably tended toward higher frequency bands, leading to bandwidth improvement. The lower edge frequency is remained almost constant and seems to be insensitive to this change. The widest bandwidth is obtained when L_r=2.7 mm and W_r=0.5 mm. To have a deeper insight of the antenna bandwidth enhancement process, surface current distribution is shown in Fig. 5. It is seen that at 13.2 GHz, where the new resonance is appeared, the current is concentrated around the two I-shaped slots, leading to performance improvement.

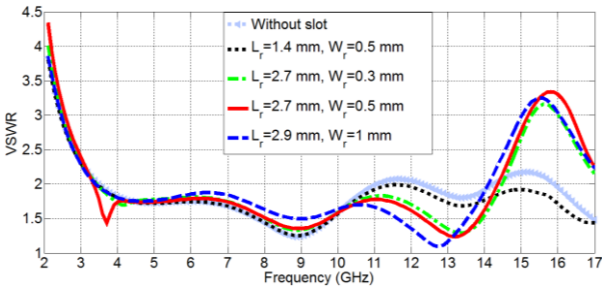

Fig. 4. Simulated VSWR curves of proposed antenna for different values of L_r and W_r.

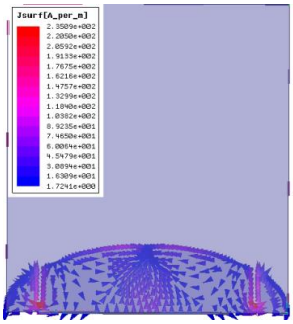

Fig. 5. Simulated current distribution on the ground plane at 13.2 GHz.

B. UWB monopole antenna with three band notched frequency characteristics

To obtain the band-notched functions, the concept of the parallel LC circuit is applied. In this technique, the desired impedance mismatch near the notch frequency may be achieved by increasing the input impedance [2]. In this antenna, the first notched band at 3.6 GHz, the second notched band centered at 5.7 GHz and the third notched-band functions at 7.15-8.1 GHz are realized using a pair of symmetrical inverted L-shaped strips at the top of the circular patch, a U-shaped slot inside the patch and a modified G-slot structure respectively as shown in Fig. 1. The modified G-slot acts as a parallel LC circuit. Hence, just by adjusting the capacitor and inductor values the desired notched frequency bandwidth can be achieved. Figure 6 shows the simulated current distribution at the centre of the three notch bands. As shown in Fig. 6 (a), where U-shaped slot is embedded in the antenna structure, the surface currents are more dominant around the slot and they are oppositely directed between the interior and exterior edges. Therefore, at the vicinity of the desired notch frequency the resultant radiation fields override, and high attenuation is produced. Figure 6 (b) shows the current distribution at 3.6 GHz, where by the addition of two inverted-L shaped elements, the first notched band is obtained. According to the results, the current flows in opposite directions at two edges of the inverted L-shaped strips leading to filtering mechanism [6]. Results in Fig. 6 (c) show that the surface current distribution at 7.6 GHz is disturbed around G-shaped slot and as a consequence, the frequency range of 7.15-8.1 GHz is blocked.

To investigate the parameters variation effects on the antenna performance, a parametric study is carried out. The position of the notched 5 to 6.2 GHz depends on the length of L_u. Figure 7 studies the VSWR curves for different values of L_u. When length of L_u is increased, the notched band moves toward lower frequencies and when L_u is fixed at 19 mm, the complete blockage is reached. The dependency of the position of the notched band from 3.1 to 4 GHz to L_s is shown in Fig. 8. It is clearly seen that when length of L_s is increased, centre of the notched band tends to the lower frequencies. The third notched band from 7.15 to 8.1 GHz depends on the values of L_1 and W_1. Figure 9 shows the VSWR curves for different values of L_1 and W_1. The results show that when L_1=1.95 mm and W_1=0.5 mm, the best performance is obtained.

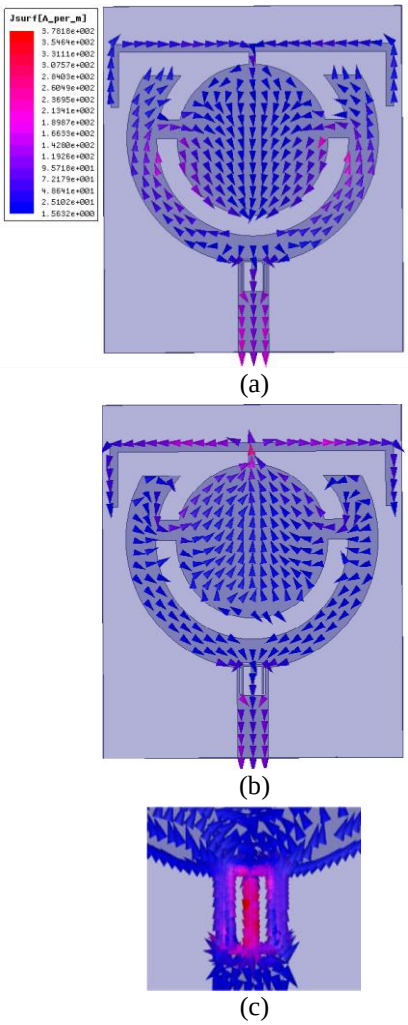

(a) (b) (c)

Fig. 6. Simulated current distribution on the radiation patch at: (a) 5.7 GHz, (b) 3.6 GHz, and (c) 7.6 GHz.

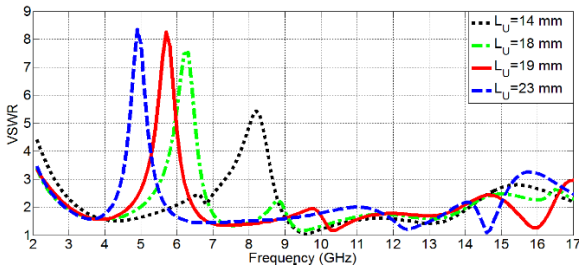

Fig. 7. Simulated VSWR curves for different values of Lu.

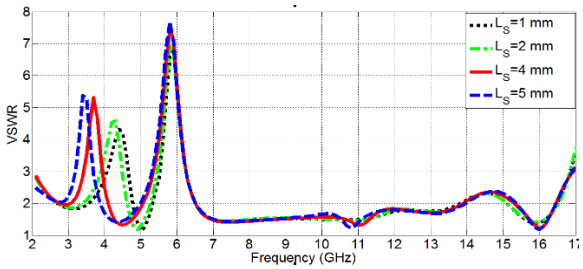

Fig. 8. Simulated VSWR curves for different values of Ls.

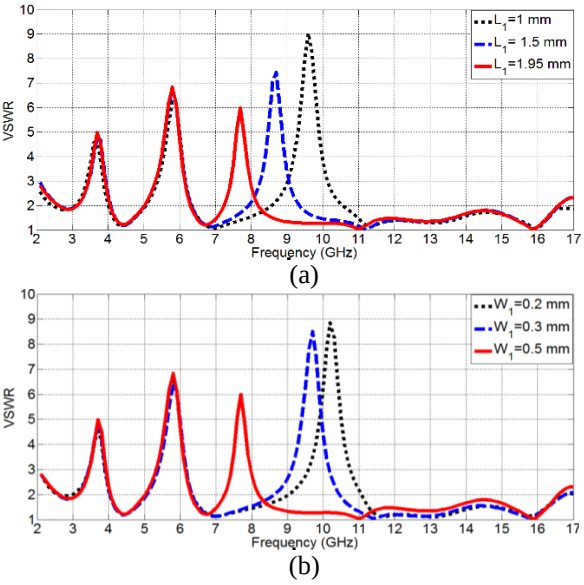

Fig. 9. Simulated VSWR curves for different values of: (a) L1 and (b) W1.

C. Measured results

The antenna with the given parameter values in Fig. 1, has been fabricated and is shown in Fig. 10. The fabricated prototype has been measured to validate the results from simulation. Agilent 8722ES network analyser has been used. The simulated and measured VSWR results of the proposed triple band-notched antenna are illustrated in Fig. 10. VSWR is a function of the reflection coefficient, which describes the power reflected from the antenna. If the VSWR is under 2, the antenna match is very good. As VSWR increases, more power is reflected to the radio and the antenna has poor impedance matching. Figure 10 shows that the proposed antenna has the acceptance VSWR curves over the frequency bands and has poor impedance matching at the notch frequency bands at 3.6, 5.7, and 7.6 GHz. Measured radiation patterns of antenna at 4.2 GHz, 6.3 GHz, and 12 GHz sample frequencies are plotted in Fig. 11. As shown in Fig. 11, omnidirectional radiation patterns with low cross polarization levels are obtained which are suitable for UWB applications. Gain of the antenna has been measured and is shown in Fig. 12. The simulated and measured gain from 2.5 to 16.5 GHz indicates acceptable and flat gain with variation less than 3 dB except for three notched bands. The group delay for the proposed antenna with 10 cm separation between two similar antennas as receiver and transmitter, was simulated in Fig. 13. Group delay variation less than 0.3 ns over the entire band except for notched bands ensure a good performance for the proposed antenna.

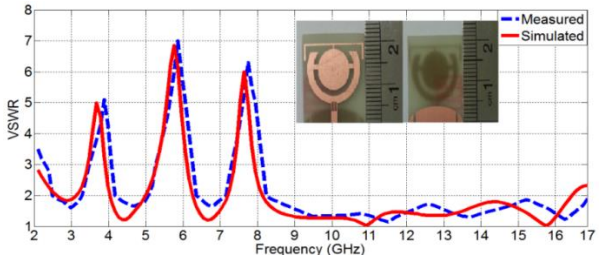

Fig. 10. Simulated and measured VSWR of the proposed antenna.

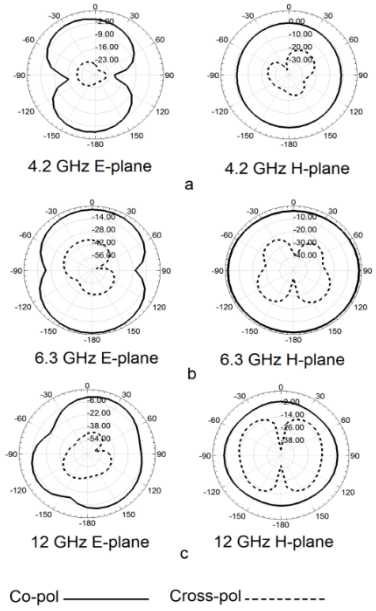

Fig. 11. Measured E-plane and H-plane radiation pattern for: (a) 4.2 GHz, (b) 6.3 GHz, and (c) 12 GHz.

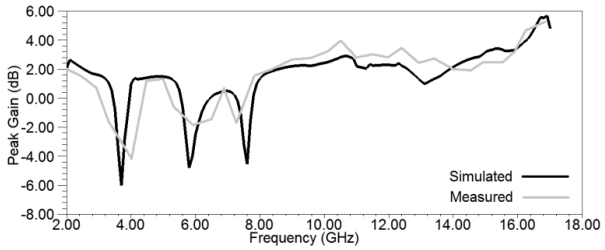

Fig. 12. Simulated and measured peak gain of the proposed triple band notch monopole antenna.

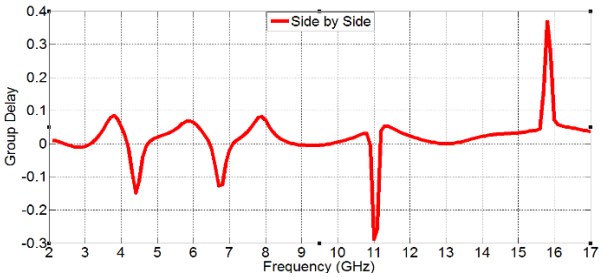

Fig. 13. Simulated group delay for side by side orientation.

IV. CONCLUSION

A printed UWB monopole antenna with triple band notched characteristics has been presented. The novelty of the proposed antenna is the antenna shape, size, and bandwidth. By using the modifying ground plane and modifying radiation patch, impedance matching is increased and the three notched frequency bands are achieved. The proposed antenna has a very small size of 19×22×1 mm^3 and operates over the frequency range of 2.5-16.5 (152%) GHz with triple band notched characteristics at 5-6.2 GHz (WLAN), 3.1-4 GHz (WIMAX) and 7.15-8.1 GHz (X-BAND). A parallel LC circuit is used to produce impedance mismatching at the desired frequencies.

The simulated and measured results are in good agreement with each other. The results certify this antenna as a promising candidate for UWB systems that is able to cancel the interference of three bands. The presented antenna is equipped with salient features such as wide bandwidth, multi-notch functions and a constant gain that highlight the potential of the studied antenna for multi task systems.

REFERENCES

[1] R. Movahedinia and M. N. Azarmanesh, "Ultra-wideband band-notched printed monopole antenna," *IET Microw. Antennas Propag.*, vol. 4, iss. 12, pp. 2179-2186, 2010.

[2] C.-Y. Hong, C.-W. Ling, I.-Y. Tarn, and S.-J. Chung, "Design of a planar ultrawideband antenna with a new band-notch structure," *IEEE Trans. Antennas Propag.*, vol. 55, no. 12, 2007.

[3] J. Pourahmadazar, Ch. Ghobadi, J. Nourinia, and H. Shirzad, "Multi-band ring fractal antenna for mobile devices," *IEEE Antenna Wireless Propag. Lett.*, vol. 9, no. 4, Sep. 2010.

[4] M. Abdollahvand, G. Dadashzadeh, and D. Mostafa, "Compact dual band-notched printed monopole antenna for UWB application," *IEEE Antennas Wireless Propag. Lett.*, vol. 9, pp. 1148-1151, 2010.

[5] M. Majidzadeh and Ch. Ghobadi, "Compact microstrip-fed monopole antenna with modified slot ground plane for UWB applications," *Applied Computational Electromagnetics Society Journal*, vol. 27, no. 10, pp. 801-807, 2013.

[6] M. Moosazadeh, A. M. Abbosh, and Z. Esmati, "Design of compact planar ultrawideband antenna with dual-notched bands using slotted square patch and pi-shaped conductor-backed plane," *IET Microw. Antennas Propag.*, vol. 6, iss. 3, pp. 290-294, 2012.

Amin Araghi Department of Electrical Engineering, Islamic Azad University, Urmia, Iran.

A Four-Leaf Clover Shape MIMO Antenna for UWB Applications

Wang Yao [1], Helin Yang [1], Xiaojun Huang [1,2], and Zetai Yu [1]

[1] College of Physical Science and Technology
Central China Normal University, Wuhan 430079, P. R. China
emyang@mail.ccnu.edu.cn

[2] College of Physics and Electrical Engineering
Kashgar University, Kashgar, 844000, P. R. China,
hxj0212@126.com

Abstract ─ This paper proposes a quad-element multiple-input multiple-output (MIMO) antenna for handheld wireless Ultra-wideband (UWB) devices, which has pocket dimensions of 40 mm × 40 mm. An elaborate tapered slot antenna fed by a gradient microstrip acts as the single radiation element. The slots evolved from exponential function are to achieve the UWB properties, and the four slots which aim to four directions constitute the four-leaf clover shape. The UWB antenna shows good impedance (S_{11} < -10 dB) match in a UWB band from 4 GHz to 13 GHz and performs high efficiency (above 80%) and high isolation (S_{21}, S_{31} < -20 dB). Realized gain is around 3 ~ 5 dB. The envelope correlation coefficient (ECC) is also investigated and it is within acceptance limits.

Index Terms ─ High isolation, multiple input multiple output (MIMO) antennas, slot antenna, Ultra-wideband (UWB).

I. INTRODUCTION

Ultra-wideband (UWB) technique provides some superiority such as high-speed data transmission, low cost and easily manufacture. However such a popular topic of technology suffers from multipath fading in the practical applications [1], [2]. Precisely, the multiple input multiple output (MIMO) technique was raised to resolve this issue, MIMO antennas are employed to enhance the channel capacity [2]. According to the requirement of the wireless communication, compact, wide operation band and high isolation MIMO antenna is an urgent demand in the mobile terminal and the portable applications [3], [4]. When the different antenna elements function in a cramped space, the inter-coupling between the antennas comes out to be intense and the MIMO antenna cannot achieve good impedance match and high isolation in a wide operating band under normal conditions [5], [6]. Several dual or quad elements UWB MIMO antennas are reported in recent years, plenty of methods are employed to eliminate coupling and enhance the isolation between the different elements [7], [8]. Some high isolation antennas were achieved by increasing the distance of the different antenna elements [9], and some others papers were to introduce the decoupling components such as parasitical slots or strips among the radiation elements or ground plane to achieve high isolation [10]-[13]. However, for most of compact devices where the space is very limited and they need the simplified structure for easier manufacture. Thus, establishing a compact and capable MIMO antenna in ultra-wideband with high isolation is still desired.

In this paper, an ultra-wideband quad-element MIMO antenna is proposed, realized demands mentioned above. The compact antenna possesses very high isolation while the four elements are distributed very close and without any decoupling component. Each element is transformed from tapered slot antenna thus the UWB properties are ensured. The feeding lines are optimized for the proper shape to actualize the radiation element has good impedance match in an ultra-wideband. The ingenious configuration of the radiation elements and feeding line increases the isolation of the proposed MIMO antenna significantly, and the envelope correlation coefficient (ECC) is also limited to the minimum.

II. ANTENNA DESIGN

The proposed quad-elements MIMO antenna is printed on Rogers RO4003 substrate with the thickness of 0.813 mm, dielectric constant of 3.38 and loss tangent of 0.0027. The structures of each layer are illustrated in Fig. 1. On the top of the substrate, the four tapered slot elements are arranged toward four different directions, at the back distributes four gradient feeding line and they vertical to the four slots respectively. Shorting vias connects the feeding line and the top metal layer. The slots are distributed vertically made the metal patch looks like a four-leaf clover.

The edge curves of the tapered slots are following the exponential function illustrated in Fig. 1 (a). Figure 2 shows the exponential functions with different bases

Submitted On: July 21, 2016
Accepted On: October 11, 2016

lead to different S-parameter curves. The results are simulated by CST MICROWAVE STUDIO. To ensure the Ultra-wideband properties, we choose the base (a = 1.4) in our final scheme and the S_{11} is less than -10 dB from 4 ~ 15 GHz, as shown in Fig. 2 (b).

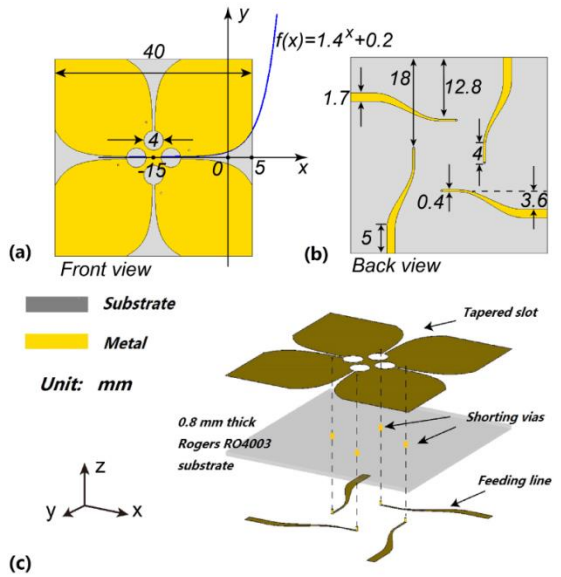

Fig. 1. The dimensions (a), (b) and analyze geometry (c) of the proposed four-leaf shape MIMO antenna.

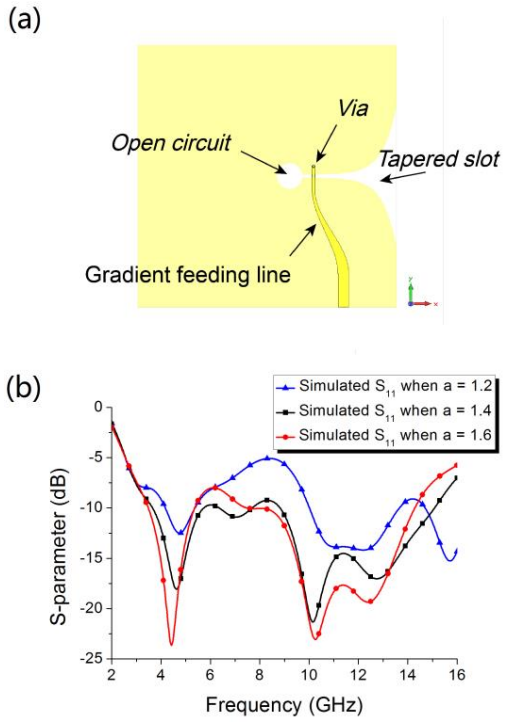

Fig. 2. The single radiation element (a), (b) is the simulated S_{11} with different bases of the exponential function.

For more compact dimensions, the shorting via and the ground are in different location at axis *X*, the feeding line must be curved and unequal in width to ensure the wide bandwidth. The gradient feeding line we adopted can contribute the realization of the slot antenna's UWB properties [14]. The S-parameter of feeding line with right angle, gradual change straightly, and gradient curve are illustrated in Figs. 3 (a), (b), and (c). From the figure, the third feed method shows more satisfactory impedance match from 4 ~ 14 GHz band than the others.

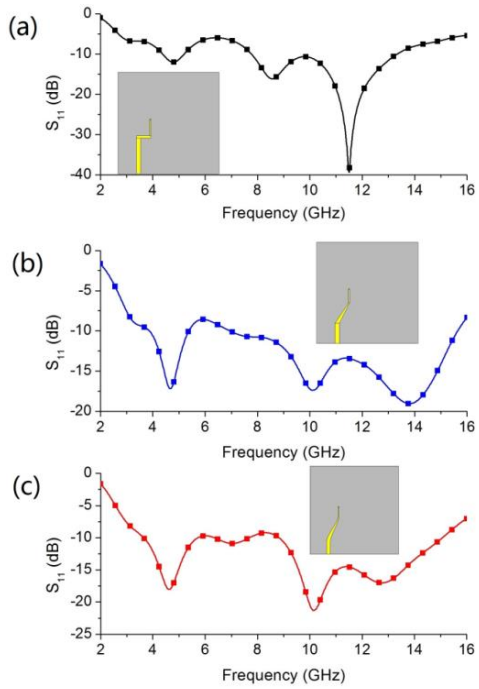

Fig. 3. The S-parameter from the single element with different feeding line.

III. RESULTS AND ANALYSES

A prototype is fabricated and measured to authenticate the characteristic of the proposed MIMO antenna. The prototype is shown in Fig. 4. The four leaves serve as the radiation element as well as the ground plane. Such a design can shrink the dimensions and make the antenna compact. Considering that the four elements of the four-leaf shape MIMO antenna are centro-symmetry and the results from all ports are similar, thus the port 1 results represent the single port results; the results from port 1 and 2 represent the dual-port results which are adjacent; the results from port 1 and 3 represent the dual-port results which are opposite.

The simulated and measured S-parameter of single and multiple ports are illustrated in Fig. 5. The measurement is performed on Agilent E8362B network analyzer. This figure shows that the measurements match well with the simulations, the S_{11} lower than -10 dB covers from 4 ~ 13 GHz (shown in Fig. 5 (a)). Meanwhile,

S_{21} and S_{31} are basically lower than -20 dB in this band (shown in Fig. 5 (b)). Thus, the proposed MIMO antenna can be sufficient to provide anticipated impedance match and slight inter-coupling for UWB MIMO devices.

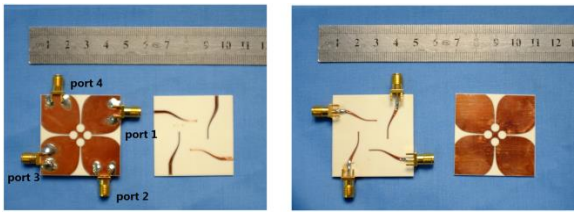

Fig. 4. Demonstration of the fabricated four-leaf shape MIMO antenna.

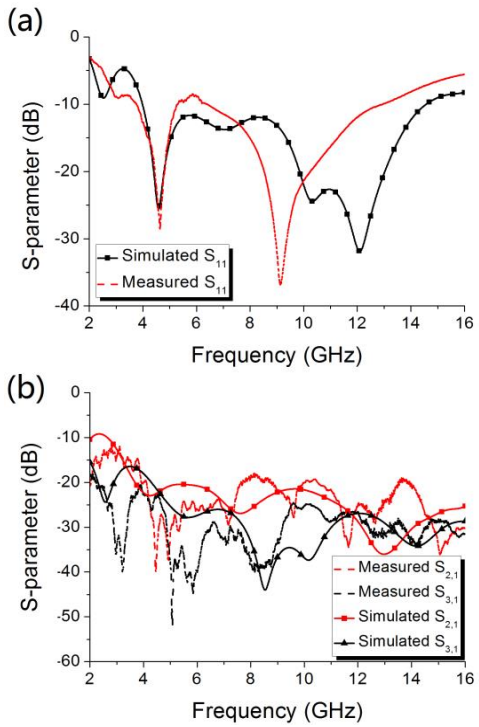

Fig. 5. Simulated and measured: (a) S_{11} and (b) S_{21}, S_{31} of the four-leaf shape MIMO antenna.

The surface current distributions for port 2 at the four frequencies are illustrated in Fig. 6. The currents mainly distribute at the edge of the tapered slot, and the gradient feeding line of the port 2. Even though the four elements are close, currents on the other elements are rarely founded, and that means very slight mutual coupling occurred between the different elements. The gain and efficiency is also simulated as the results shown in Fig. 7. The realized gain changes from 3 dB to 5 dB and the efficiency are above 80% through the entire band.

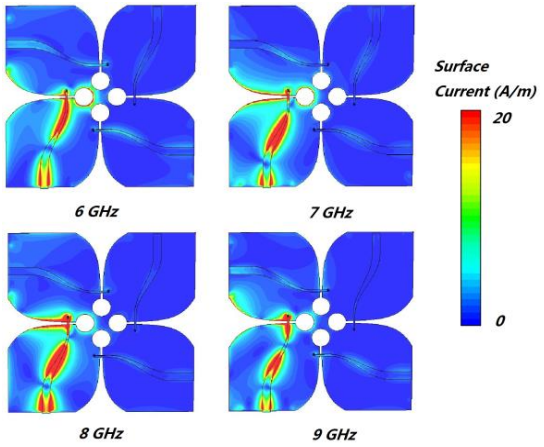

Fig. 6. Current distribution for port 2 in four different frequencies.

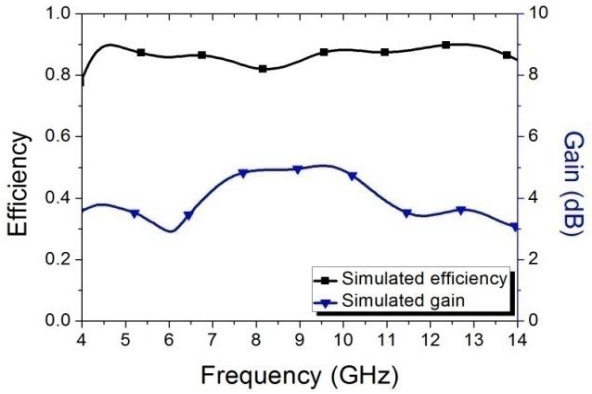

Fig. 7. Simulated gain and efficiency of the four-leaf shape MIMO antenna.

Since the back to back distribution of the four elements and the slots are toward four directions, the radiation patterns from the four elements are forced to radiate to four directions, as shown in Fig. 8. The ignorable overlaps from the four radiation patterns ensure the low correlation of the proposed MIMO antenna. The radiation patterns of the MIMO antenna at the three frequencies in *xoz*- and *xoy*-plane are measured and illustrated in Fig. 9. Since the high consistency of radiation patterns from the four ports, port 1 radiation patterns are measured as present. In the measurement, a broadband horn antenna (1 ~ 18 GHz) is employed as a receiving antenna, and the port 1 of the proposed MIMO antenna is used as transmitting antenna respectively. It can be seen that the radiation patterns of different frequencies are broadly the same and the patterns have directionality in *xoy*-plane, what suits well with the simulation results.

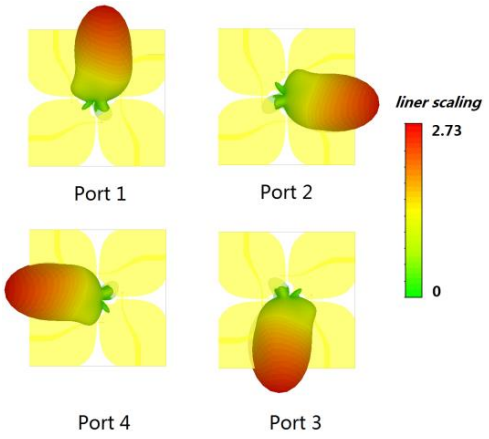

Fig. 8. Simulated 3-D radiation pattern of the four ports of the MIMO antenna at 7 GHz.

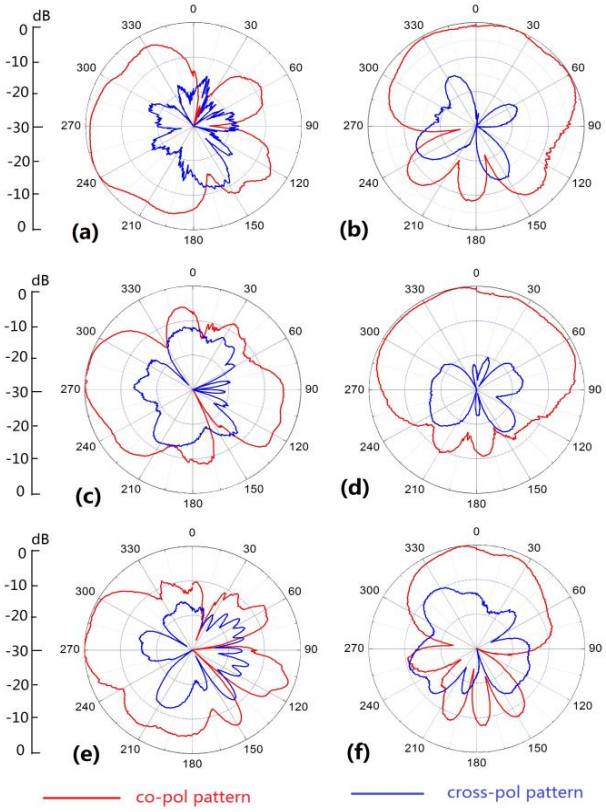

Fig. 9. Measured co-pol and cross-pol polarization of radiation pattern: (a) 6 GHz xoy-plane, (b) 6 GHz xoz-plane, (c) 7 GHz xoy-plane, (d) 7 GHz xoz-plane, (e) 9 GHz xoy-plane, and (f) 9 GHz xoz-plane.

The envelope correlation coefficient (ECC) is to judge multiple port performance of the MIMO antenna. The correlation among the embranchment signals received by different antennas is evaluated by this parameter, and lower ECC means more diversified patterns as a rule [15]. An acceptable standard for a desirable MIMO system is ECC < 0.5, and it could be calculated from the S-parameters and radiation efficiency of the MIMO antenna [16]:

$$\rho_{e,ij} = \frac{\left|S_{ii}^{*}S_{ij} + S_{ji}^{*}S_{jj}\right|^2}{\left(1-\left|S_{ii}\right|^2-\left|S_{ji}\right|^2\right)\left(1-\left|S_{jj}\right|^2-\left|S_{ij}\right|^2\right)\eta_{radi}\eta_{radj}}. \quad (1)$$

In which η_{radi} is the radiation efficiency of the port i radiation element. The simulated and measured ECC are illustrated in Fig. 10. The results of measurement agree well with the simulation and the values are below the 0.05 in the entire band. It verified the excellent properties of the proposed MIMO antenna. The comparison of the existing compact UWB MIMO antennas with the proposed four-leaf shape MIMO antenna is illustrated in Table 1. In comparison, the superiorities of this work are appeared both in size and isolation.

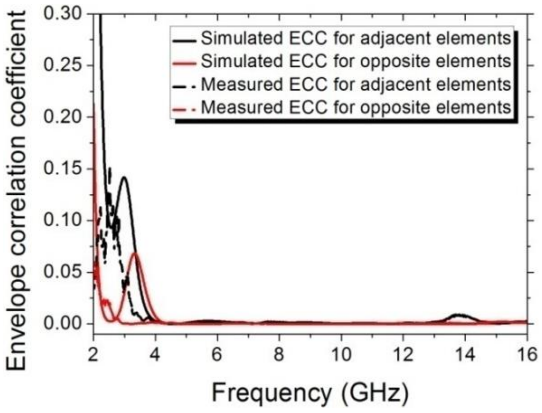

Fig. 10. Simulated and measured ECC of the four-leaf MIMO antenna.

Table 1: Comparison of compact UWB MIMO antennas

Ref.	Number of Ports	Planar Size (mm^2)	Bandwidth (%)	Isolation (dB)
[11]	4	40×40	60.6	-10
[13]	4	$\pi\times80^2$	42.2	-15
[17]	2	26×26	109.5	-15
This work	4	40×40	105.6	-20

IV. CONCLUSION

An Ultra-wideband (UWB) quad-element MIMO antenna with a four-leaf clover shape is proposed hereof, which is adapted from planar tapered slot antenna. The edge curves following the exponential function and achieved the UWB property. The dimensions of the proposed MIMO antenna are 40×40×0.813 mm. The measured results show that 105.6% (4 ~ 13 GHz) bandwidth and obtain a high isolation levels (S_{21}, S_{31} < -20 dB) since the four directional radiation properties of

the individual antenna elements. Efficiency is above 80% and the realized gain changes from 3 dB to 5 dB. Very low ECC value is provided by the MIMO antenna which guarantees the excellent multiple-input multiple-output performance of the four-leaf shape MIMO antenna in the relevant applications.

ACKNOWLEDGMENT

This work was supported by the National Natural Science Foundation of China (No. 41474117) and by self-determined research funds of CCNU from the colleges' basic research and operation of MOE (No. CCNU15GF005).

REFERENCES

[1] S. H. Choi, et al., "A new ultra - wideband antenna for UWB applications," *Microw. Opt. Techn. Let.*, vol. 40, no. 5, pp. 399-401, 2004.

[2] D. Chen and C.-H. Cheng, "A novel compact ultra-wideband (UWB) wide slot antenna with via holes," *Prog. Electromagn. Res.*, vol. 94, pp. 343-349, 2009.

[3] K. Zhao, et al., "Body-insensitive multimode MIMO terminal antenna of double-ring structure," *IEEE Trans. Antennas Propag.*, vol. 63, no. 5, pp. 1925-1936, 2015.

[4] B. Mun, et al., "A compact frequency-reconfigurable multiband LTE MIMO antenna for laptop applications," *IEEE Antenn. Wirel. Pr.*, vol. 13, pp. 1389-1392, 2014.

[5] S. H. Simon and A. L. Moustakas, "Optimizing MIMO antenna systems with channel covariance feedback," *IEEE J. Sel. Area. Comm.*, vol. 21, no. 3, pp. 406-417, 2003.

[6] B. N. Getu and J. B. Andersen, "The MIMO cube-a compact MIMO antenna," *IEEE T. Wirel. Commun.*, vol. 4, no. 3, pp. 1136-1141, 2005.

[7] G. Zhai, Z. N. Chen, and X. Qing, "Enhanced isolation of a closely spaced four-element MIMO antenna system using metamaterial mushroom," *IEEE Trans. Antennas Propag.*, vol. 63 no. 8, pp. 3362-3370, 2015.

[8] M. A. Abdalla and A. A. Ibrahim, "Compact and closely spaced metamaterial MIMO antenna with high isolation for wireless applications," *IEEE Antenn. Wirel. Pr.*, vol. 12, pp. 1452-1455, 2013.

[9] J.-F. Li, et al., "Compact dual band-notched UWB MIMO antenna with high isolation," *IEEE Trans. Antennas Propag.*, vol. 61, no. 9, pp. 4759-4766, 2013.

[10] R. Chandel and A. Gautam, "Compact MIMO/ diversity slot antenna for UWB applications with band-notched characteristic," *Electron. Lett.*, 2016.

[11] H. Wang, et al., "A wideband compact WLAN/ WiMAX MIMO antenna based on dipole with V-shaped ground branch," *IEEE Trans. Antennas Propag.*, vol. 63, no. 5, pp. 2290-2295, 2015.

[12] M. S. Sharawi, et al., "A dual-element dual-band MIMO antenna system with enhanced isolation for mobile terminals," *IEEE Antenn. Wirel. Pr.*, vol. 11, pp. 1006-1009, 2012.

[13] Y. S. Chen and C. P. Chang, "Design of a four-element multiple-input–multiple-output antenna for compact long-term evolution small-cell base stations," *IET Microw. Antenna P.*, vol. 10, no. 4, pp. 385-392, 2016.

[14] H. G. Schantz, *The Art and Science of Ultra-wideband Antennas*. Artech House, 2015.

[15] S. Zhang, et al., "Reduction of the envelope correlation coefficient with improved total efficiency for mobile LTE MIMO antenna arrays: Mutual scattering mode," *IEEE Trans. Antennas Propag.*, vol. 61, no. 6, pp. 3280-3291, 2013.

[16] P. Hallbjörner, "The significance of radiation efficiencies when using S-parameters to calculate the received signal correlation from two antennas," *IEEE Antenn. Wirel. Pr.*, vol. 4, pp. 97-99, 2005.

[17] J. Y. Zhang, et al., "ACS-fed UWB-MIMO antenna with shared radiator," *Electron. Lett.*, vol. 55, no. 17, pp. 1301-1302, 2015.

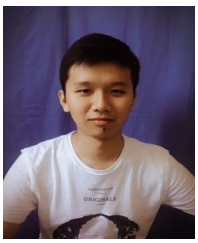

Wang Yao received the B.S. degree in Applied Physics from Yangtze University, Jingzhou, China, in 2014. He is currently working toward the Master's degree in Circuits and Systems from Central China Normal University, Wuhan, China.

His research interests include high-gain antenna design with metasurface and compact wearable antenna.

Transparent Flexible Antenna for UWB Applications

Mohammad Reza Haraty [1], Mohammad Naser-Moghadasi [1], Abbas Ali Lotfi-Neyestanak [2], and Alireza Nikfarjam [3]

[1] Faculty of Engineering, Science and Research Branch
Islamic Azad University, Tehran, 14778-93855, Iran
m.haraty@srbiau.ac.ir, mn.moghaddasi@srbiau.ac.ir

[2] Department of Electrical Engineering, Yadegar-e-Imam Khomeini (RAH) Shahre Rey Branch
Islamic Azad University, Tehran, 18155-144, Iran
*aalotfi@ieee.org

[3] Faculty of New Sciences & Technologies
University of Tehran, P.O. Box: 14395-1561, Tehran, Iran
a.nikfarjam@ut.ac.ir

Abstract ─ In this paper, a flexible circular slot transparent antenna which can be used in ultra wideband applications is presented. A CPW-fed circular disc monopole is used to excite the circular slot aperture. The antenna is designed and fabricated using ITO coated on a flexible Polyethylene Terephthalate (PET) substrate. It can operate with different curvature angles at UWB frequencies with 125% bandwidth. Simulation and measurement results show that the radiation pattern does not change if the antenna is being rolled, and also confirm its effective performance as a flexible transparent antenna with low profile.

Index Terms ─ Coplanar waveguide (CPW) fed antennas, flexible antenna, Indium Tin Oxide (ITO), Polyethylene Terephthalate (PET), transparent antenna, transparent conductive.

I. INTRODUCTION

Due to the widespread development of wireless communication systems in recent years, particularly in wearable and smart coating systems, demand for small-size, light, and flexible antennas has increased. Once, for the first time in 2002, FCC (Federal Communications Commission) allocated frequency range of 3.1-10.6 GHz to UWB applications, numerous UWB antenna designs on inflexible and non transparent sub layers were proposed [1-4]. Soon after, various complex antennas with more flexible structures designed and implemented [5-6]. As literature survey confirms flexible microstrip antennas have significant impact on different wireless applications such as cellular phones, airplanes, satellite, and *etc*.

Most of flexible antennas investigated in the literature are fabricated on non-transparent conductors, for instance, copper, silver and gold; therefore in case of placing them on an electrical circuit such as solar cell, they will reduce the system efficiency and degrade the system functionality. Although the proposed flexible antenna in [7, 8] has been fabricated using PET substrate, it uses a non-transparent conductors such as copper layer. In the recent years, due to the extensive applications of transparent antenna in wireless industry, such as touch panel control, display panels of wireless communications equipment, car windshields, building windows, integrated solar cell systems with transparent antenna, the use of such antennas is becoming more attractive [9]. Transparent antennas are often made of transparent conductor films such as Indium Tin Oxide (ITO), Fluorine-doped Tin Oxide (FTO) and silver coated polymer (AgHT) films. Among them, ITO is more desirable as it offers reasonable trade-off between optical transparency and conductivity. [10]. Most of transparent antennas have rigid and inflexible substrate and those with less rigid substrates cannot be used in applications where flexible transparent antennas are required [11-14].

In this paper, we proposed a flexible transparent antenna with PET substrate and ITO transparent conductor, which not only is flexible and can be placed on curved surfaces, but also is light and its 85% optical transparency does not degrade the system functionality.

II. ANTENNA DESIGN

The geometry and parameters of the proposed antenna are given in Fig. 1. This antenna is a slotted

Submitted On: October 12, 2015
Accepted On: September 9, 2016

circular patch with a CPW fed. This antenna is made of: 1) an ITO film with 100 nm thickness, 15 Ω/sq and above 85% transparency. 2) PET polymer with 0.28 mm thickness and dielectric constant of 3.4. To achieve high transparency and high flexibility, higher ITO sheet resistance than AgHT has been used. Although some transparent conductors such as AgHT-4 or AgHT-8 have lower sheet resistance, according to [12], in order to design an effective antenna from AgHT films, the transparency has to be sacrificed. Figure 2 shows the transparency of ITO at different wavelengths. As it can be seen the transparent conductor has 85% transparency at wavelength of 550 nm. The antenna is positioned in the xy plane and has a size of 40*40 mm^2. The fabricated antenna is depicted in Fig. 3. In order to achieve input impedance of 50 Ω, we have used CPW fed with width of W_f =1.3 mm, which is separated from the CPW ground by a gap of 0.65 mm. Once a conventional planar antenna is being rolled, impedance mismatch occurs within a frequency bands. The more the antenna is being rolled, the higher impedance mismatch can be seen. To overcome this problem, here we have tuned two key parameters, *i.e.*, L_s and R_1. Figure 4 shows the reflection coefficient of the antenna for different values of R_1 and L_s. Optimized dimension and characteristics of the antenna are given in Table 1.

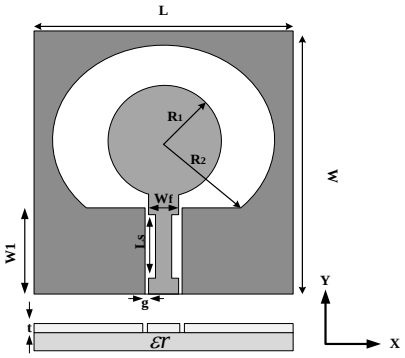

Fig. 1. Schematic of the antenna.

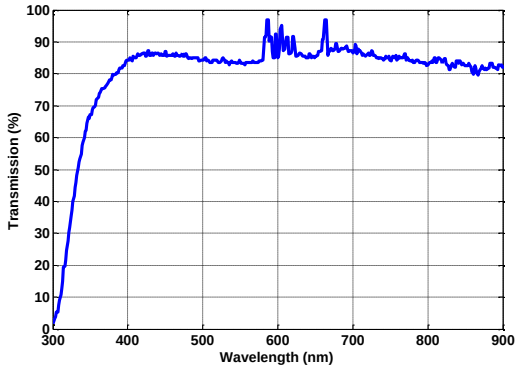

Fig. 2. Measured optical transparency of the antenna for various wavelengths.

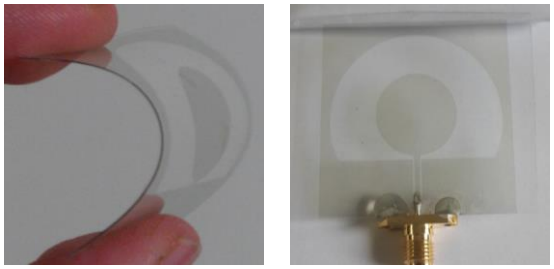

Fig. 3. Schematic of the fabricated antenna.

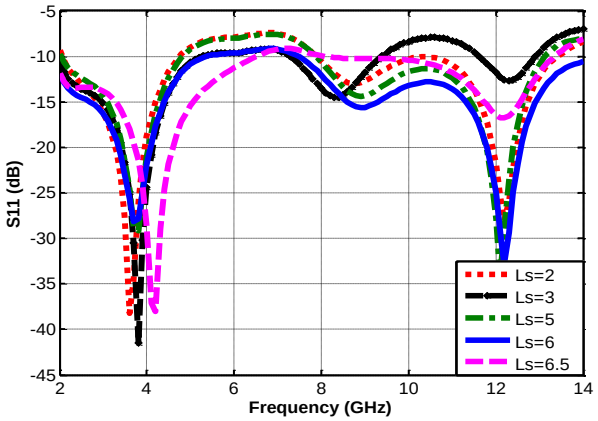

(a)

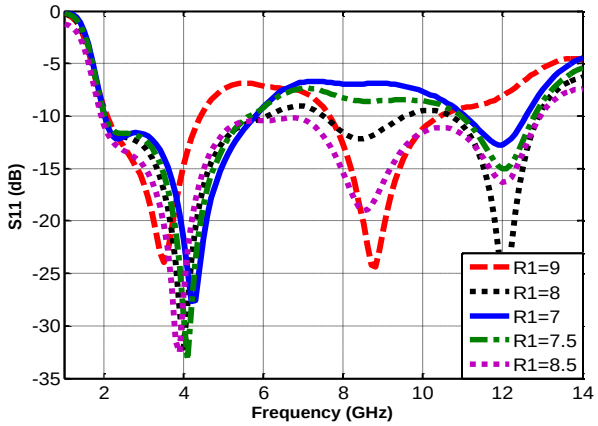

(b)

Fig. 4. Reflection coefficient of the antenna for: (a) different values of L_s, and (b) different values of R_1.

Table 1: Antenna parameters

Parameter	L	W	W_1	L_s	R_1	R_2	R_s
Units (mm)	40	40	11.1	6.5	8.5	18	0.8

III. SIMULATION AND FABRICATIONS

The antenna shown in Fig. 1 is fabricated using parameter values given in Table 1. The antenna is simulated with Ansoft's High-Frequency Structure Simulator (HFSS™). The reflection coefficient (S_{11} dB) is measured by Agilent 8722ES network analyzer (50 MHz-40 GHz). To ensure the antenna performance,

it has been assessed for three curvature angles: 0°, 45°, 90° in the z-axis.

Figure 5 compares the measured and simulated reflection coefficient of the antenna for different curvature angles using HFSS and CST Microwave studio. As the reflection coefficient plots show, rolling the proposed flexible antenna causes less impedance mismatch compared to the planar one. More importantly, considering optimized parameter values for the antenna, it can sustain its 10 dB bandwidth over the whole UWB range for different curvature angels. The slight deviation of the simulation and measurement results can be due to the impact of fabrication process, for instance, silver paste used to attach the connector to the antenna. In spite of this slight deviation, it is a good candidate because it does not suffer from low efficiency of common flexible antennas. Also, the effect of the silver paste has been shown for the curvature angles of 0°in Fig. 5 (a).

Figure 6 shows radiation patterns of the proposed antenna at two frequencies of 4 GHz and 8 GHz, for both co- and cross-polarizations and three curvature angles of: (a) 0°, (b) 45°, and (c) 90°. As can be seen, it is omni-directional on the *H*-plane while it is bi-directional on the *E*-plane. Moreover, for different curvature angles its radiation patterns do not change significantly.

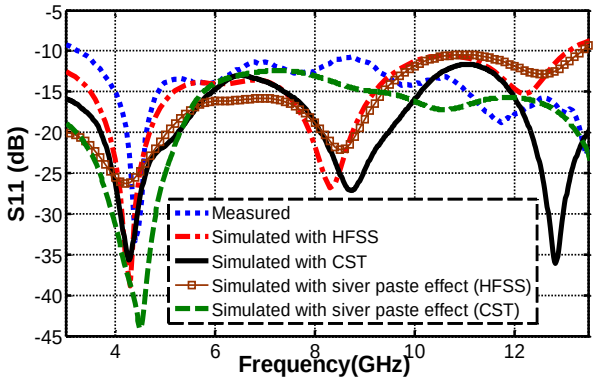

(a) Curvature angle of 0°

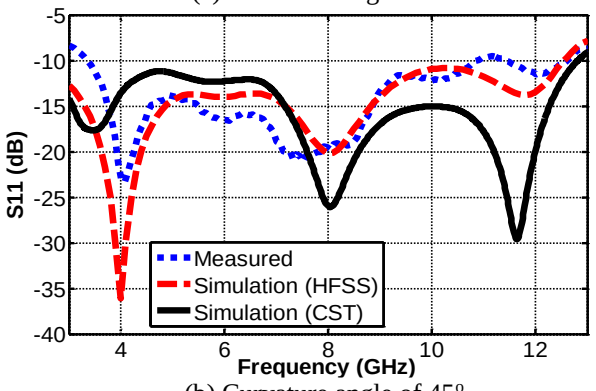

(b) Curvature angle of 45°

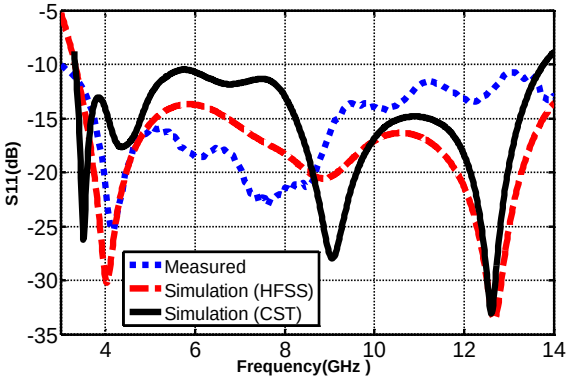

(c) Curvature angle of 90°

Fig. 5. Reflection coefficient of the antenna for several curvature angles.

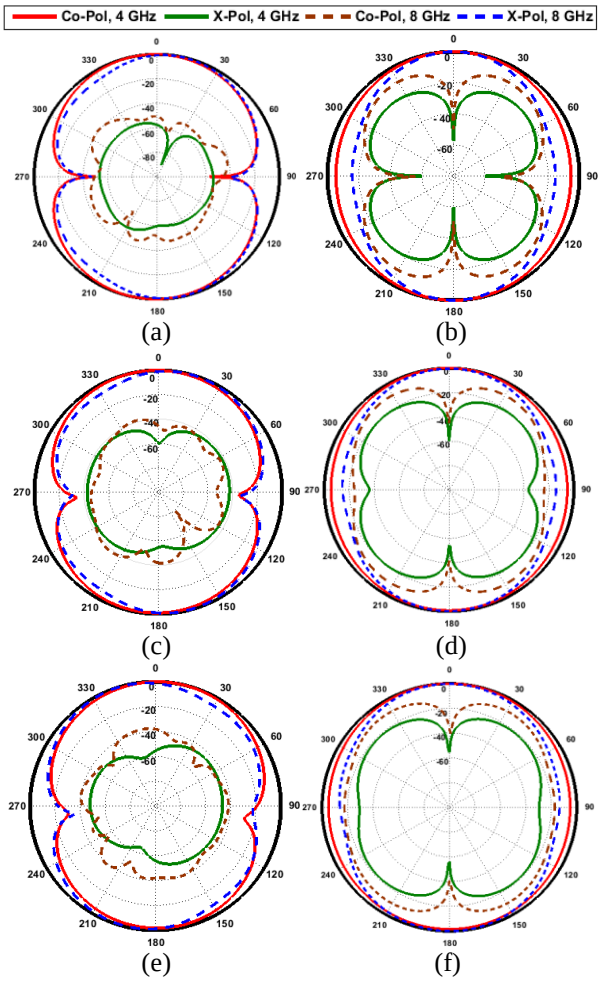

Fig. 6. Co-polar and cross-polar normalized radiation patterns at 4 GHz and 8 GHz for: (a) *E*-plane at 0°, (b) *H*-plane at 0°, (c) *E*-plane at 45°, (d) *H*-plane at 45°, (e) *E*-plane at 90°, and (f) *H*-plane at 90°.

IV. CONCLUSION

In this paper, a flexible transparent circular slot antenna excited by a circular disc CPW-fed monopole, is proposed. This antenna which is fabricated using ITO on a transparent, very light, and flexible PET substrate, can be used for UWB applications. Simulation results are validated with measurement, and confirm that the proposed antenna has a bandwidth of 125% and is omni- directional in the *H*-plane and bi-directional in *E*-plane. Its great features such as being light, low profile, highly transparent, and flexible have made it a suitable candidate for applications where an antenna needs to be placed on non coplanar surfaces or wearable electronic systems.

REFERENCES

[1] FCC, "First report and order, revision of part 15 of the commission's rules regarding ultra-wideband transmission system," FCC02-48, Apr. 2002.

[2] C. M. Dikmen, S. Cimen, and G. Cakir, "Planar octagonal-shaped UWB antenna with reduced radar cross section," *IEEE Transactions on Antennas and Propagation*, vol. 62, no. 6, pp. 2946-2953, June 2014.

[3] M. R. Haraty, S. M. Seyed-Momeni, and R. A. Sadeghzadeh, "Candelabra shaped microstrip antenna for ultra-wideband applications," *Microw. Opt. Technol. Lett.*, vol. 53, no. 3, pp. 669-672, Mar. 2011.

[4] A. A. Lotfi-Neyestanak, M. R. Azadi, and A. Emami-Forooshani, "Compact size ultra wideband hexagonal fractal antenna," *Proceedings of the 25th Queen's Biennial Symposium on Communications (QBSC'10)*, pp. 387-390, May 2010.

[5] D. Betancourt and J. Castan, "Printed antenna on flexible low-cost PET substrate for UHF applications," *Progress in Electromagnetics Research C*, vol. 38, pp. 129-140, 2013.

[6] Y. Bayram, Y. Zhou, B. Shim, S. Xu, J. Zhu, N. Kotov, and J. Volakis, "E-Textile conductors and polymer composites for conformal lightweight antennas," *IEEE Trans. on Antenna and Propagation*, vol. 58, no. 8, pp. 2732-2736, Aug. 2010.

[7] A. Collado and A. Georgiadis, "Conformal hybrid solar and electromagnetic energy harvesting rectenna," *IEEE Transactions on Circuits and Systems-I: Regular Papers*, vol. 60, no. 8, pp. 2235-2234, Aug. 2013.

[8] H. K. Yoon, Y. J. Yoon, H. Kim, and C. H. Lee, "Flexible ultra-wideband polarization diversity antenna with band-notch function," *IET Microw. Antennas Propag*, vol. 5, no. 12, pp. 1463-1470, Sep. 2011.

[9] R. Saberin and C. Furse, "Challenges with optically transparent patch antennas," *IEEE Antennas and Propagation Magazine*, vol. 54, no. 3, pp. 10-16, June 2012.

[10] T. Peter, T. A. Rahman, S. W. Cheung, R. Nilavalan, F. H. Abutarboush, and A. Vilches, "A novel transparent UWB antenna for photovoltaic solar panel integration and RF energy harvesting," *IEEE Transactions on Antennas and Propagation*, vol. 62, no. 4, pp. 1844-1853, Apr. 2014.

[11] M. R. Haraty, M. Naser-Moghadasi, A. A. Lotfi-Neyestanak, and A. Nikfarjam, "Circular ring optically transparent antenna for ultra wideband applications," *ACES Journal*, vol. 30, no. 2, pp. 208-212, Feb. 2015.

[12] M. R. Haraty, M. Naser-Moghadasi, A. A. Lotfi-Neyestanak, and A. Nikfarjam, "Improving the efficiency of transparent antenna using gold nano layer deposition," *IEEE Antennas Wireless Propag. Lett.*, vol. 15, pp. 4-7, Feb. 2016.

[13] T. Peter, R. Nilavalan, H. F. A. Tarboush, and S. W. Cheung, "A novel technique and soldering method to improve performance transparent polymer antennas," *IEEE Antennas Wireless Propag. Lett.*, vol. 9, pp. 918-921, Sep. 2010.

[14] T. Yasin, R. Baktur, and C. Furse, "A comparative study on two type of transparent patch antenna," *General Assembly and Scientific Symposium*, 2011 XXXth URSE, pp. 1-4, Aug. 13-20, 2011.

Mohammad Reza Haraty was born in Tehran, Iran, in 1984. He received his B.Sc. degree in Electrical Engineering (Communication) from Yadegare-Imam Khomeini (RAH) Shahre-Rey Branch, Islamic Azad University, Tehran-Iran in 2008 and M.Sc. and Ph.D. degree in Electrical Engineering (Communication) from Islamic Azad University, Science & Research Branch, Tehran, Iran, in 2011 and 2014, respectively. From 2010 he was teaching in the Department of Electrical Engineering at the Yadegar-e-Imam Khomeini (RAH) Shahre-Rey Branch, Islamic Azad University, Tehran-Iran. His main areas of research interest are Microstrip antenna, Microwave passive and active circuits, Transparent antenna and shielding, Optimization methods in electromagnetic, Microwave measurement, Numerical methods in electromagnetic problems and RF MEMS.

Mohammad Naser-Moghadasi was born in Saveh, Iran, in 1959. He received the B.Sc. degree in Communication Eng. in 1985 from the Leeds Metropolitan University (formerly Leeds Polytechnic), UK. Between 1985 and 1987, he worked as an RF Design Engineer for the

Gigatech Company in Newcastle Upon Tyne, UK. From 1987 to 1989, he was awarded a full scholarship by the Leeds Educational Authority to pursue an M.Phil. studying in CAD of Microwave Circuits. He received his Ph.D. in 1993, from the University of Bradford, UK. He was offered then a two years Post Doc. to pursue research on Microwave Cooking of Materials at the University of Nottingham, UK. From 1995, Naser-Moghadasi joined Islamic Azad University, Science & Research Branch, Iran, where he currently is an Associate Professor and Head of Postgraduate Studies. His main areas of interest in research are Microstrip antenna, Microwave passive and active circuits, RF MEMS. Naser-Moghadasi is Member of the Institution of Engineering and Technology, MIET and the Institute of Electronics, Information and Communication Engineers (IEICE). He has so far published over 140 papers in different journals and conferences.

Abbas Ali Lotfi-Neyestanak was born in Tehran, Iran. He received his B.Sc. degree in Communication Eng. (1993) and M.Sc. degree in Electronic Engineering (1997) and Ph.D. degree in Communication Engineering (2004) from Iran University of Science and Technology (IUST) Tehran, Iran, respectively. From 1997 he was teaching in the Department of Electrical Engineering at the Yadegare-Imam Khomeini (RAH) Shahre-Rey Branch, Islamic Azad University, Tehran-Iran. In 2011, he joined the Radio Science Lab at the University of British Columbia as Visiting Researcher. Currently, he is collaborating with the Department of Electrical Engineering, University of Waterloo, Ontario, Canada. His main areas of research interest are Microstrip antenna, Microwave passive and active circuits, Electronic circuits design, EMC & EMI in High voltage, Optimization methods in electromagnetic, Radio wave propagation, Microwave measurement, Numerical methods in electromagnetic problems, RF MEMS and bio electromagnetic. Lotfi-Neyestanak is a Senior Member of IEEE and has published two books and more than 110 papers in international journals and conferences.

Alireza Nikfarjam was born in Tehran on 1975. He obtained his B.Sc. and M.Sc. degrees in Electronics both in Iran in 1998 and 2001, respectively. In 2007 he obtained his Ph.D. in Microelectronics from K. N. Toosi University of Technology. He joined the Sharif University of Technology in Tehran in 2009 as Post-Doctoral Researcher to work on nano-sensors. Then he joined the Faculty of New Sciences and Technologies of University of Tehran in Tehran in 2011 as Assistant Professor. His research interests are semiconductor micro & nano-devices, especially gas sensors, MEMS & NEMS and Organic Electronics.

Design of a Planar Surface Wave Antenna with a Bidirectional Pattern Based on Periodic Structures for Telemetry Applications

I. Mazraeh-Fard [1], M. Maddahali [1], Z. H. Firouzeh [1], and H. Khayam Nekoei [2]

[1] Dept. of Electrical and Computer Engineering
Isfahan University of Technology (IUT), Isfahan 8415683111, Iran
i.mazraeh@ec.iut.ac.ir, maddahali@cc.iut.ac.ir, zhfirouzeh@cc.iut.ac.ir

[2] Avionics Research Institute
Isfahan University of Technology (IUT), Isfahan, Iran
h.khayam@ec.iut.ac.ir

Abstract ─ A planar surface wave antenna (PSWA) that realizes a bidirectional radiation pattern with a low profile configuration is designed, fabricated and measured. The antenna consists of a planar dielectric slab loaded with periodic spiral patches and EBG structure, which are designed to support the propagation of the surface waves in the desired direction. The diffraction of surface waves at the edges of the ground plane generates a bidirectional radiation pattern. The radiation mechanism and performance of the PSWA are described and simulated with commercial CST software. The proposed antenna with only 1.6 mm thickness is fabricated and tested, which resonates at 2.4 GHz. The antenna is especially attractive for telemetry applications because of its low profile and weight.

Index Terms ─ Bidirectional radiation pattern, planar antenna, periodic structure, surface wave antenna.

I. INTRODUCTION

Wire inverted F antennas (WIFAs) are commonly used on small unmanned aerial vehicles (UAVs) for telemetry and command signals because of their bidirectional pattern [1]. However, the wire inverted F antennas similar to other wire antennas have disadvantages such as high aerodynamic drag and a high degree of electromagnetic coupling to the fuselage [2]. Another approach is to use the low profile surface wave antennas (SWAs) [3-8] and electromagnetic band gap (EBG) structures [9-15] to suppress the surface wave propagating along one side and support it along another side.

In [9-15], the surface waves are suppressed with EBG structures that made with periodic mushroom-like structure. Thus, in these antennas side-lobe falls down and the gain of broadside direction rises up. But in [3-8], the surface waves have important role in the low profile surface wave antennas. In these antennas, mushroom-like structure without via supports the surface waves. The surface waves propagate in a ground plane and diffraction rays from opposite edges will cancel each other in the broadside direction, resulting in a radiation null. Thus, an omnidirectional monopole-like radiation is generated. So, the low profile surface wave antenna can be a good idea to realize a bidirectional radiation pattern, like WIFA pattern.

In this paper, a novel planar surface wave antenna with a bidirectional radiation pattern based on low-profile SWA and EBG structure is proposed. The SWA consists of two parts: a patch to excite the surface waves, and a thin dielectric slab loaded with periodic spiral patches to support the surface waves. The EBG structure in the two lateral sides of the periodic patches can suppress the surface waves. Consequently, strong surface waves propagate in central side and their diffractions at the boundary of the ground plane form a bidirectional pattern. PSWA pattern is similar to the pattern of the WIFAs; however, PSWA is low-profile without aerodynamic drag. In fact, the PSWA is superior to the disadvantages of the WIFAs. The proposed planar surface wave antenna is so attractive for telemetry applications. The artificial ground plane is studied in details in Section II, then the radiation mechanism of the planar surface wave antenna is described in Section III and experimentally verified in Section IV.

II. THE NEW ARTIFICIAL GROUND PLANE

A. Surface waves in the structure

In [3], a thin slab loaded with periodic square patches and EBG structure has been discussed separately. A unique feature of the proposed antenna in this paper is an incorporation both of the thin grounded dielectric slab loaded with periodic spiral patches and the EBG

Submitted On: October 12, 2015
Accepted On: October 4, 2016

structures to make a novel artificial ground as shown in Fig. 1. The dimensions of the periodic structure for the desired application are as follows:

s = 0.8 mm, p = 6.8 mm, g = 0.5 mm, r = 0.31 mm, (1)

where s is the gap width of the spiral line, p is the period of the periodic structure, g is the gap width between two spiral patches, r is the via-radius of the EBG structure. The substrate thickness, h, is 1.574 mm (62 mil) and the dielectric constant of the substrate, ε_r, is 2.2. Figure 2 shows the dispersion diagrams [3] of the two different periodic artificial surfaces using the CST software. The vertical axis shows the frequency and the horizontal axis represents the values of transverse wave numbers; *i.e.*, k_x and k_y. As shown in Fig. 2 (a), the surface wave is suppressed between 2.3 GHz and 2.5 GHz for the EBG structure of Fig. 1; *i.e.*, all the patches are connected to the ground with vertical vias. In contrast, for the patch loaded grounded slab, since the vertical vias are removed, the first surface wave mode exists in the desired frequency range as shown in Fig. 2 (b).

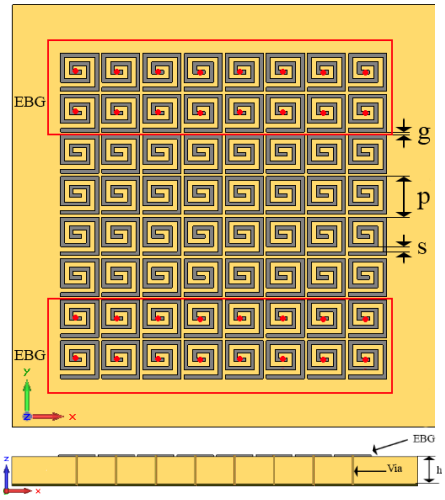

Fig. 1. The geometry of the novel proposed artificial ground plane.

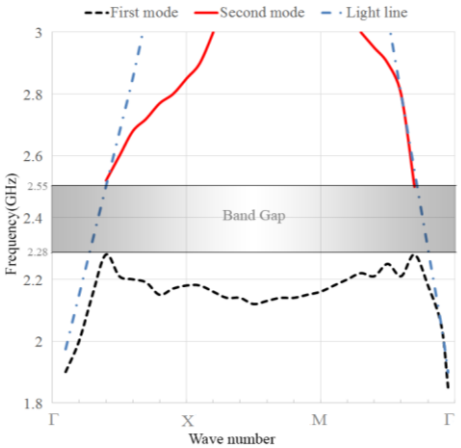

(a)

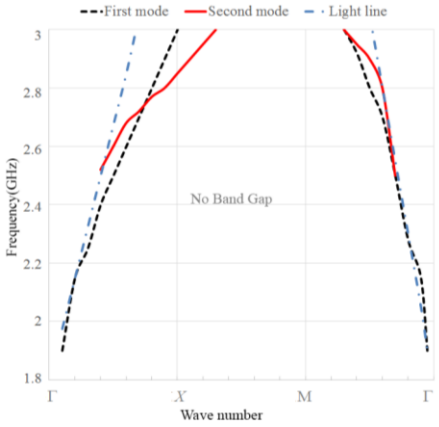

(b)

Fig. 2. Dispersion diagram of the two artificial surfaces: (a) a EBG structure (with vias), and (b) a dielectric slab loaded with patches (without vias). Along the horizontal axis, Γ: $k_x = 0$, $k_y = 0$; X: $k_x = \pi/p$, $k_y = 0$; M: $k_x = \pi/p$, $k_y = \pi/p$.

These structures are combined to make a new artificial ground plane as shown in Fig. 1. There are four rows of periodic patches in the middle of the ground plane to support the propagation of the surface waves along $\pm x$ directions and two rows in each lateral side to suppress the surface wave propagating along $\pm y$ directions. In summary, with the novel artificial ground plane, the surface wave can be directed along one side.

B. Parametric studies of the unit cell

The unit-cell EBG structure is shown in Fig. 3, which includes a layer with metallization layout and shorted with the ground through a center via connection. In contrast to the traditional square patch layout [15], a spiral type is proposed for the size reduction. The layouts with number of turns N = 0, 1, 2, are shown in Figs. 3 (a)-(c), respectively. Other important parameters for the unit-cell spiral EBG are the gap s and width w of the spiral line [16]. According to Table 1, changing square patch to spiral patch results in that the frequency band gap decreases. Also, an increase of s causes the frequency band gap to decrease. Therefore, s = 0.8 mm is selected to obtain the band gap 2.3-2.5 GHz as shown in Fig. 3 (c). As a result, surface waves will be suppressed in this structure at frequency of 2.4 GHz. Note that in this parametric studies, other dimensions are the same as given in (1).

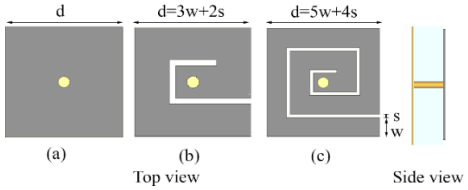

Fig. 3. A unit-cell EBG with: (a) rectangular layout (N = 0), (b) spiral layout (N = 1), and (c) spiral layout (N = 2) [16].

Table 1: Band gap of the three different unit-cell EBG

Unit Cell		Band Gap	
		f1 (GHz)	f2 (GHz)
a	-	5.70	7.80
b	S=0.2 mm	4.90	5.90
c	S=0.2 mm	2.55	2.85
	S=0.6 mm	2.40	2.68
	S=0.8 mm	2.28	2.55

III. THE PLANAR SURFACE WAVE ANTENNA

A PSWA based on the proposed periodic structure is designed to radiate at 2.4 GHz as shown in Fig. 4. The input reflection coefficient of the antenna is about 30 dB at 2.4 GHz as shown in Fig. 5. The PSWA consists of two parts; a circular patch fed by a 50 Ω coax cable to excite surface waves, and a thin dielectric slab loaded with 20×20 periodic spiral patches and EBG structure. There are 16 rows of periodic patches in the middle of the ground plane to support the propagation of the surface waves along ±*x* directions and in each lateral side there are 2 rows of periodic patches with via to suppress the surface waves propagating along ±*y* directions. Consequently, the surface waves will be propagated only along ±*x* direction, it is observed clearly in Fig. 6, which shows the surface current of the antenna in two cases; before and after adding vias. The surface waves excited by the circular patch are radiated from the edge of the ground plane, and diffraction rays from the opposite edges will cancel each other in the broad-side direction. Thus, a bidirectional radiation is generated, as observed in Fig. 7. The maximum realized gain of the antenna is about 8.7 dB in xz plane and about 0.7 dB in yz plane. This pattern has a deep null in the broad-side direction and the antenna beams are at θ = 36° (-40°) with a realized gain of 8.7 dB (8.5 dB).

The antenna is simulated with the 14 cm×14 cm square ground plane. The circular patch of the antenna has a radius of 49.6 mm and its height from PEC ground is 0.787 mm. The periodic patches dimensions and dielectric substrate properties are the same as given in (1).

In order to see the effect of vias or EBG structure on the radiation pattern, the pattern of the PSWA are plotted in two cases; with and without vias as shown in Fig. 8. As can be observed, the gain increases 4 dB in xz plane and decreases about 4.3 dB in yz plane, by adding vias to the antenna.

In order to compare the properties of the proposed PSWA with those of a WIFA antenna, the WIFA antenna as shown in Fig. 9 is designed and simulated at 2.4 GHz. The antenna PEC ground plane is a 110×110 mm^2 square and other dimensions of the WIFA are as follows:

H = 13 mm, S = 4.1 mm, L = 18.5 mm.

The gain and input reflection coefficient of both antennas are presented in Fig. 10 and Fig. 12, respectively. It is observed from Fig. 10 that, the maximum gain of the proposed antenna is increased at about 4 dB than that of the WIFA antenna.

In order to compare the properties of the proposed PSWA with those of a new WIFA antenna, the loaded WIFA antenna as shown in Fig. 11 is compared at 2.4 GHz. The antenna PEC ground plane is a 60×60 mm^2 and other dimensions of the WIFA are as follows (unit of these parameters are mm) [17]:

l = 28, t = 6, t_1 = 6, h_1 = 15, h_2 = 2, w = 2, s = 0.4.

The properties of the above antennas are presented in Table 2. From this table, although the gain of the loaded WIFA antenna is more than the WIFA antenna (from 4.7 dB to 8.9 dB), its thickness is increased. While with the proposed planar surface wave antenna (PSWA), we can increase gain and decrease antenna thickness.

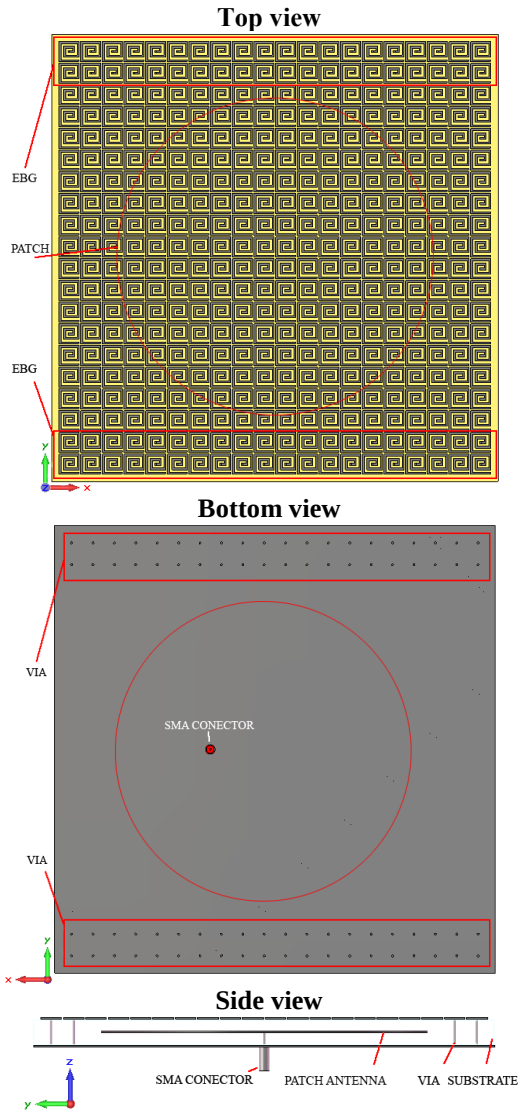

Fig. 4. The geometry of the PSWA.

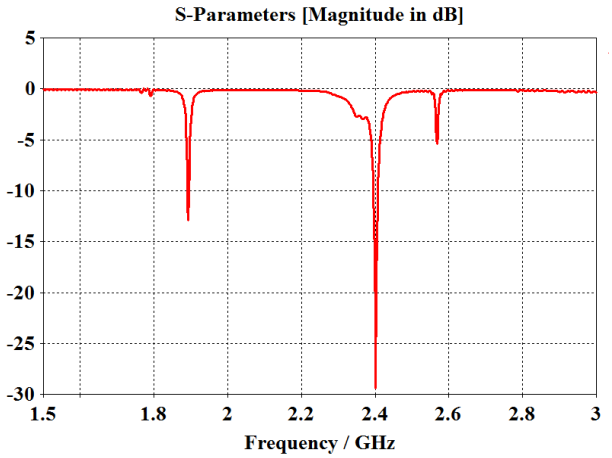

Fig. 5. Reflection coefficient of the proposed PSWA.

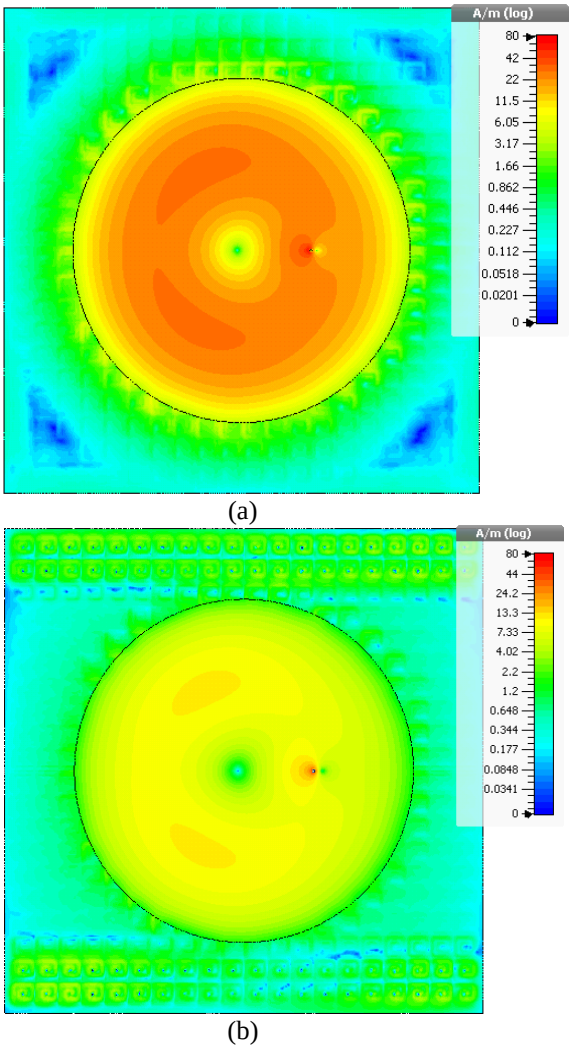

Fig. 6. The surface currents of the PSWA: (a) with vias and (b) without vias.

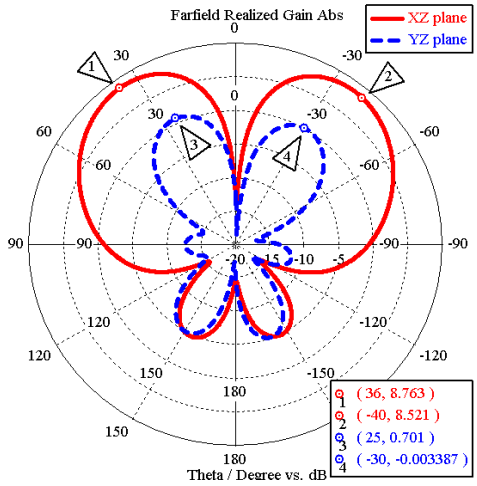

Fig. 7. The 2D radiation patterns of the PSWA.

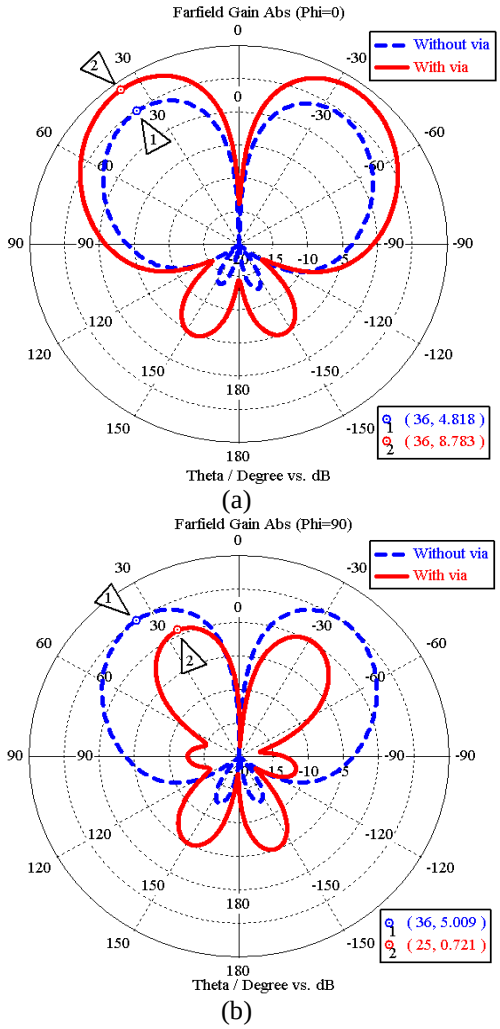

Fig. 8. Radiation patterns of the PSWA: (a) xz plane and (b) yz plane.

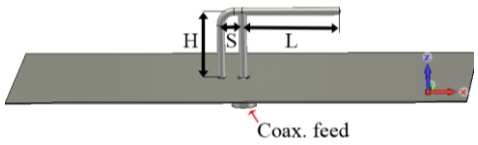

Fig. 9. The geometry of the WIFA.

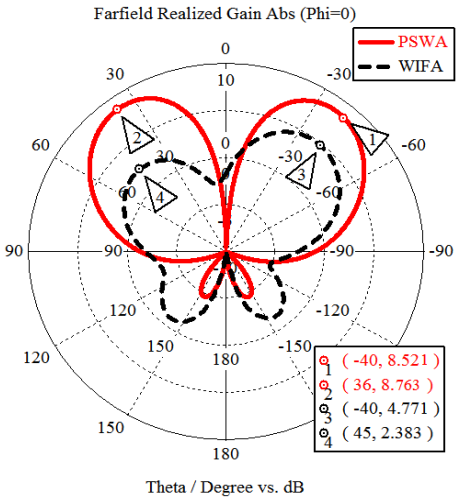

Fig. 10. The 2D radiation patterns of the PSWA and the WIFA (xz plane).

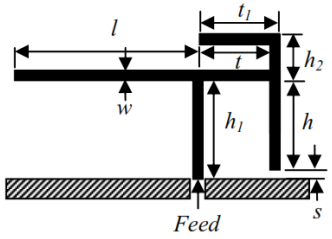

Fig. 11. The geometry of the loaded WIFA [17].

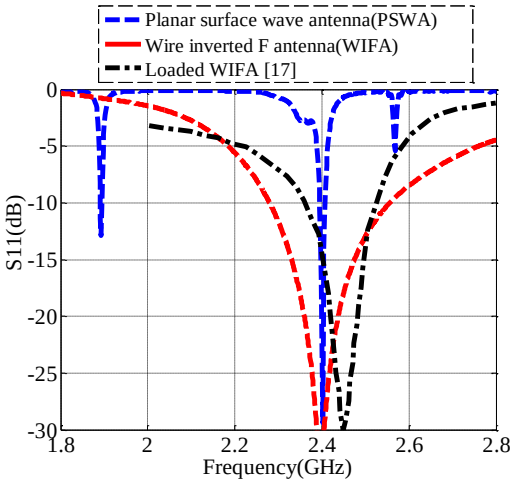

Fig. 12. Reflection coefficient of the PSWA, the WIFA and the loaded WIFA.

Table 2: The properties of the proposed PSWA, the WIFA and the loaded WIFA

Properties	Proposed Antenna	WIFA Antenna	Loaded WIFA [17]
Max. gain (dB)	8.7 (back & front)	4.7 (front) 2.3 (back)	8.9
Return loss	Narrower	Wide	Narrow
Dimensions (mm^2)	140×140	110×110	60×60
Thickness	1.6 mm	13 mm	17 mm
Aerodynamic drag	Very low	High	Higher
Pattern-type	Bidirectional	~Omni.	Omni.

Figure 13 illustrates the realized gain of the both antennas over frequency range of 2300 MHz to 2500 MHz. From this figure, it is obvious that the proposed antenna has very sensitive dimensions versus the operational frequency. If we shift from 2.4 GHz, the gain is decreased dramatically. Therefore, this fact is a disadvantage of the proposed antenna where there is not this range of sensitivity in the WIFAs. However, when the operational frequency is 2.4 GHz or very near it, the proposed low profile PSWA can be a good idea to realize a bidirectional radiation pattern. Because the gain is increased from 4.7 dB to 8.7 dB and the antenna thickness is reduced from 13 mm to 1.6 mm against the WIFA antenna. In fact, the PSWA is superior to the disadvantages of the WIFA such as high aerodynamic drag and a high degree of electromagnetic coupling to the fuselage. Therefore, the proposed antenna exhibits a great potential when a high gain bidirectional radiation pattern and a low-profile antenna are desired.

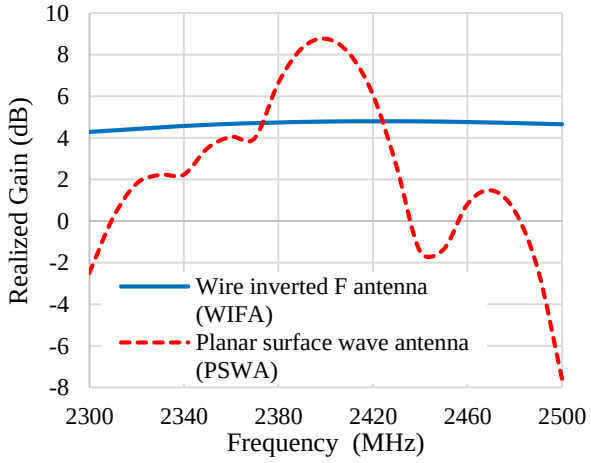

Fig. 13. The realized gain of the PSWA and the WIFA.

IV. EXPERIMENTAL RESULTS

To verify the concept of the PSWA, an antenna prototype with the same dimensions as given in Section III is fabricated and measured.

Figure 14 (a) shows the photo of the 20×20 periodic

spiral patches fabricated on the RT/duroid 5880 high-frequency laminate ($\varepsilon_r = 2.2$). Figure 14 (b) shows a back view of the fabricated PSWA and a 50 Ω SMA connector that is soldered to the patch embedded in middle of dielectric slab. The connector is shifted 20 mm along $+x$ direction.

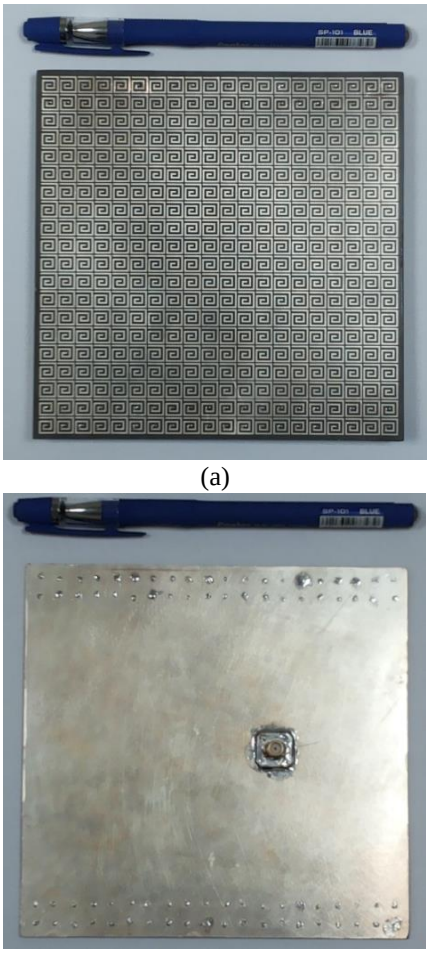

(a)

(b)

Fig. 14. Photos of a fabricated PSWA: (a) top view and (b) back view.

Figure 15 presents the measured return loss of the PSWA with a comparison with the CST simulation results. According to the measured results, the antenna resonates at 2.38 GHz with a return loss of about -18 dB, which agrees with the simulation results. The radiation patterns of the PSWA are measured at the resonant frequency of 2.38 GHz. The measured radiation patterns agree well with the CST simulations in Fig. 16, and a WIFA-like pattern has been obtained. The pattern has a deep null in the broad-side direction and the antenna beam is at about θ = ± 38°direction with a gain of 8 dB. The cross-polarisation is about -20 dB lower than the co-polarization in the beam direction. As shown in Fig. 16, because of existence of vias, the gain of yz plane decreases than the xz plane. As shown in Fig. 16 (b), this reduction is about 7.2 dB in measured result and about 4 dB in simulated result. It shows that in practice, the vias reduce the surface wave less than measured result. But the reduction is enough to make a WIFA-like pattern.

Figure 17 shows the comparison between simulated and measured gain of the PSWA. The difference of maximum gain is 0.75 dB in the both cases. The presented experimental results verify the simulation results and demonstrate the radiation performance of the PSWA.

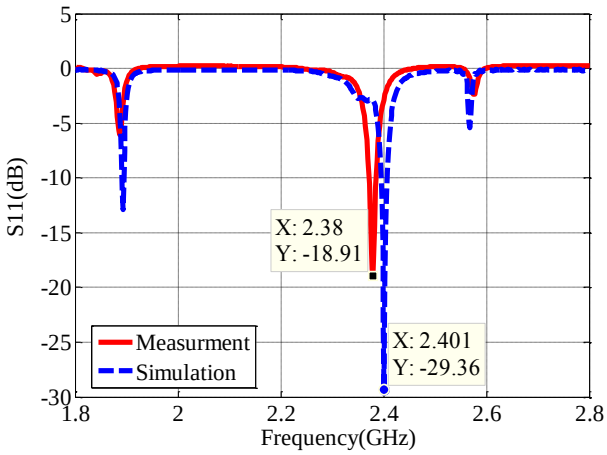

Fig. 15. Comparison between the simulated and measured return loss of the PSWA.

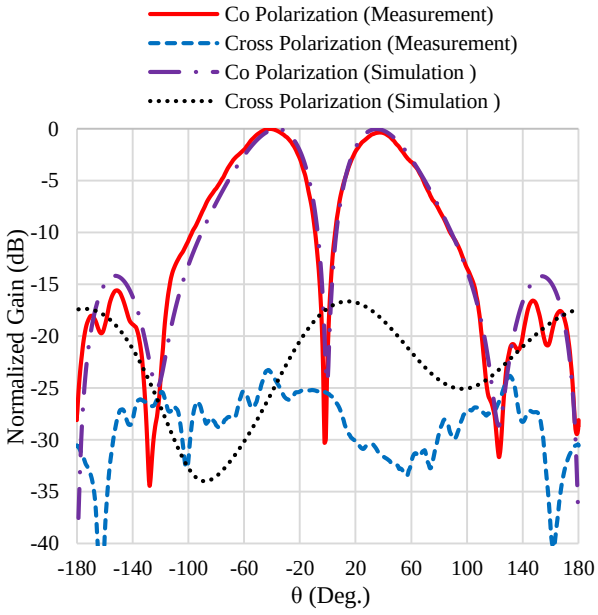

(a)

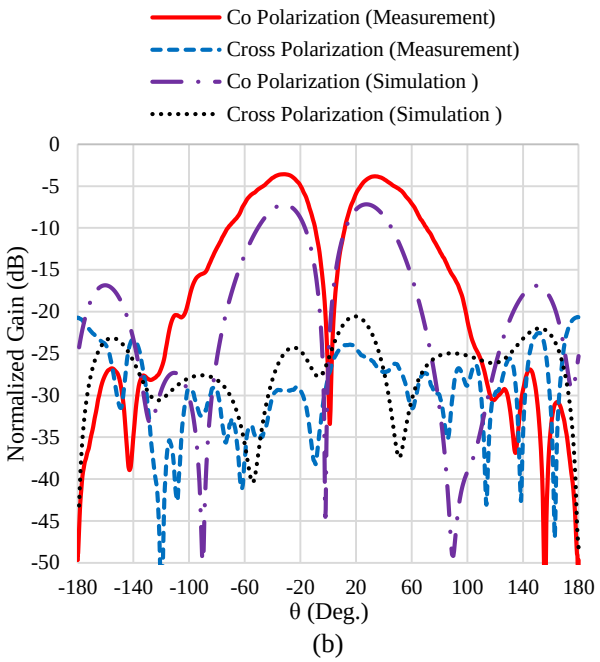

Fig. 16. Comparison between the simulated and measured normalized gain of the PSWA: (a) xz plane and (b) yz plane.

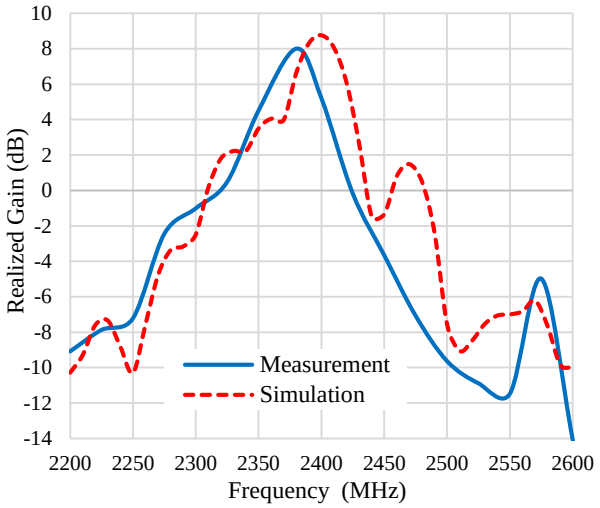

Fig. 17. Comparison between simulated and measured realized gain of the PSWA.

V. CONCLUSION

This paper has presented a planar surface wave antenna (PSWA) that radiates a bidirectional radiation pattern with a low-profile configuration. The low-profile property has been realized using a novel artificial ground plane. The radiation performance of the PSWA was described and parametric studies were performed. An antenna prototype was fabricated and tested, which resonated at 2.38 GHz with a gain of 8 dB and WIFA-type radiation pattern. In contrast to the WIFA, the PSWA has low-profile configuration without a high aerodynamic drag. The proposed planar surface wave antenna exhibits a great potential for telemetry applications when a bidirectional radiation pattern and a low-profile antenna are desired.

ACKNOWLEDGMENT

The authors would like to thank Research Center for Avionics, Isfahan University of Technology, Iran to support of this project.

REFERENCES

[1] H. Nakano, Y. Asano, and J. Yamauchi, "A wire inverted F antenna on a finite-sized EBG material," *IEEE International Workshop on*, pp. 13-16, Mar. 2005.

[2] B. R. Motlhabane and D. Gray, "TE-monopole radiation pattern DRA for UAVs," *Antennas and Propagation (ISAP), International Symposium on*, pp. 499-502, Oct. 29, 2012-Nov. 2, 2012.

[3] F. Yang, A. Aminian, and Y. Rahmat-Samii, "A novel surface-wave antenna design using a thin periodically loaded ground plane," *Microw. Opt. Technol. Lett.*, vol. 47, pp. 240-245, Nov. 2005.

[4] F. Yang, Y. Rahmat-Samii, and A. Kishk, "Low-profile patch-fed surface wave antenna with a monopole-like radiation pattern," *Microwaves, Antennas & Propagation, IET*, vol. 1, pp. 261-266, Feb. 2007.

[5] A. Al-Zoubi, F. Yang, and A. Kishk, "A low-profile dual-band surface wave antenna with a monopole-like pattern," *Antennas and Propagation, IEEE Transactions on*, vol. 55, no. 12, pp. 3404-3412, Dec. 2007.

[6] F. Yang, A. Aminian, and Y. Rahmat-Samii, "A low profile surface wave antenna equivalent to a vertical monopole antenna," *IEEE Antennas Propag. Soc. Symp. 2004.*, vol. 2, 2004.

[7] F. Yang, Y. Rahmat-Samii, and A. Kishk, "A novel surface wave antenna with a monopole type pattern: A thin periodically loaded slab excited by a circular disk," in *IEEE Antennas and Propagation Society, AP-S International Symposium (Digest)*, vol. 1 A, pp. 742-745, 2005.

[8] F. Y. F. Yang, A. Al-Zoubi, and A. Kishk, "A dual band surface wave antenna with a monopole like pattern," *2006 IEEE Antennas Propag. Soc. Int. Symp.*, 2006.

[9] D. Sievenpiper, L. Zhang, R. F. J. Broas, N. G. Alexopolous, and E. Yablonovitch, "High-impedance electromagnetic surfaces with a forbidden frequency band," *IEEE Transactions on Microwave Theory & Techniques*, vol. 47, no. 11, pp. 2059-74, Nov. 1999.

[10] F. Yang and Y. Rahmat-Samii, *Electromagnetic*

Band Gap Structures in Antenna Engineering. Cambridge University Press, Cambridge, UK, 2009.

[11] C. R. Simovski, P. de Maagt, and I. V. Melchakova, "High-impedance surfaces having stable resonance with respect to polarization and incidence angle," *IEEE Trans. Antennas Propag.*, vol. 53, pp. 908-914, 2005.

[12] H. Mosallaei and Y. Rahmat-Samii, "Periodic bandgap and effective dielectric materials in electromagnetics: Characterization and applications in nanocavities and waveguides," *IEEE Trans. Antennas Propag.*, vol. 51, pp. 549-563, 2003.

[13] R. Abhari and G. V. Eleftheriades, "Metallo-dielectric electromagnetic bandgap structures for suppression and isolation of parallel-plate noise in high-speed circuits," *IEEE Trans. Microw. Theory Tech*., vol. 51, no. 6, pp. 1629-1639, June 2003.

[14] T. Kamgaing and O. M. Ramahi, "A novel power plane with integrated simultaneous switching noise mitigation capability using high impedance surface," *IEEE Microw. Wireless Compon. Lett.*, vol. 13, no. 1, pp. 21-23, Jan. 2003.

[15] S. Shahparnia and O. M. Ramahi, "Simple and accurate circuit models for high-impedance surfaces embedded in printed circuit boards," in *Proc. IEEE Antennas Propagat. Symp.*, vol. 4, pp. 3565-3568, June 2004.

[16] C.-L. Wang, G.-H. Shiue, W.-D. Guo, and R.-B. Wu, "A systematic design to suppress wideband ground bounce noise in high-speed circuits by electromagnetic-bandgap-enhanced split powers," *IEEE Trans. Microw. Theory Tech*., vol. 54, no. 12, pp. 4209-4217, Dec. 2006.

[17] D. K. Karmokar and K. M. Morshed, "Analysis of inverted-F and loaded inverted-F antennas for 2.4 GHz ISM band applications," *Journal of Electrical Engineering, IEB*, vol. EE 36, no. 2, pp. 4-9, 2009.

A Novel Tunable Graphene Based Terahertz Absorber with Polarization Insensitive

Sv. Masuminia, Ch. Ghobadi, J. Nourinia, M. Karamirad, and B. Mohammadi

Department of Electrical Engineering
Urmia University, Urmia, Iran
{sv.masuminia, ch.ghobadi, j.nourinia, m.karamirad}@urmia.ac.ir, b.m.mohammadi@ieee.org

Abstract ─ A novel design of the four-band graphene based terahertz (THz) absorber is presented. The pattern is formed by a graphene ring and orthogonal elliptical sheets on the top of a ground plate separated by a dielectric layer. Numerical results reveal that the graphene based absorber has four absorption peaks whose peaks are all over 99%. Besides, the absorption coefficient of the proposed absorber is insensitive to the polarization of the incident wave. And also, variation of geometrical parameter gives considerable freedom to change the resonance frequencies of the absorber. Moreover, the results reveal that the absorption spectra can be extended by tuning the chemical voltage of the graphene layer.

Index Terms ─ Absorber, grapheme, polarization insensitive, terahertz (THz), tunable.

I. INTRODUCTION

With recent ongoing progress in the next generation communications, absorbers attract more attention [1], [2]. Recently, THz absorbers have been used in applications such as security, medical imaging, and communications. Besides, graphene has attracted more consideration owing to its unique electrical, mechanical, and optical properties. Graphene is a two dimensional material with hexagonal structure which has excellent properties such as high electron mobility and flexibility. Furthermore, the Fermi energy of the graphene sheet can be controlled by electrochemical potential. In fact, owing to its impedance variation by tuning bias voltage, it can be used in electromagnetic devices such as absorber [3]. Researchers have been working on graphene based absorbers such as [4] and [5]. In [4], a narrow bandwidth absorption spectra is obtained by using a stack of graphene-dielectric-grounded metal. In order to expand the bandwidth, two or more layers are employed in [6] and [7-9].

New group of graphene based absorbers such as graphene nano disk [10], micro ribbons [11], and hereterostructures [12] have been studied. Since, these papers mentioned above indicate that the bandwidth of the absorbers are narrow, so, the broadband functionality is more attracted. Therefore, more broadband graphene based absorbers such as multiple graphene nano resonators [13] are proposed. Although, the broadband attitude of the absorber is practical, the tunable of absorption is more important in many applications. In order to control the tunability, the voltage control technique is suitable. The bias voltage controls the absorption energy of the absorber over a narrow frequency band [14, 15]. Recently, both multiband and broadband tunable absorbers were investigated [16, 17]. However, no design focused on tuning the narrowband to broadband through changing various bias voltages in multiband graphene based absorber with polarization insensitive in the terahertz region. In particular, converting narrowband to broadband in absorbers promises application opportunities in terahertz sensor network such as [18] and communications.

In this paper, a dynamically frequency-tunable graphene based terahertz absorber is presented, which consists of a single layer periodically patterned graphene structure over a metal ground plane separated by a polyamide dielectric layer. In order to obtain polarization insensitive and wideband frequency bandwidth, the structure should be symmetrical and curved, respectively. Due to structure of the proposed absorber, an identical absorption spectra is obtained for both TE and TM incident EM wave. By suitable parametric study, average absorption coefficients greater than 99% for the four distinct absorption peaks can be achieved. The distinguish property of the proposed absorber is expanding the bandwidth of the absorption spectra by tuning the applied bias voltage. The absorber with these performances has sufficient potential in medical imaging, communications, sensing, and most practical applications.

II. DESIGN AND CONFIGURATION

The proposed four-band THz absorber based on graphene is shown in Fig. 1; which unit cell consists of two orthogonal concentric elliptical graphene rings at the center and quarter orthogonal concentric elliptical graphene sheets at the corners. The pattern is on the metallic ground plate separated by a thick dielectric

Submitted On: August 10, 2016
Accepted On: October 25, 2016

layer. The pattern is periodic in x- and y-direction with periodicity of W_{cell} = 150 um and L_{cell} = 150 um. All the optimized parameters are specified as follows: R_1 = 60 um, R_2 = 30 um, R_3 = 27 um, R_4 = 12 um, w = 5 um, h = 25um, t = 0.4 um. The refractive constant of the dielectric polyamide layer is 1.68 + *i*0.06 [8]. The thickness of the metal (Gold) layer is set to $t = 0.4\ \mu m$ whose frequency independent conductivity is $\sigma = 4.5\times10^7\ S/m$.

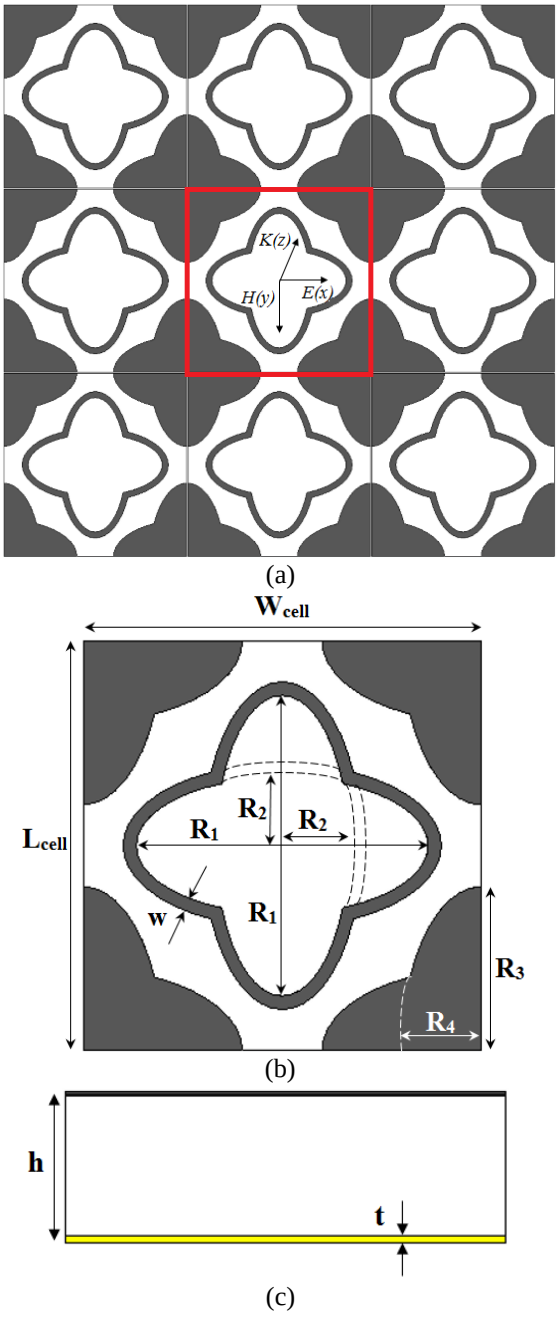

Fig. 1. (a) Structure schematic of the proposed four-band graphene based THz absorber. (b) Red line is presented a unit cell. (c) Cross sectional view of a unit cell.

Graphene can be electromagnetically investigated by modeling a single layer as ultrathin surface characterized by a two dimensional complex surface conductivity. In this study, the complex conductivity of graphene can be calculated by Kubo formula as [18]:

$$\sigma(\omega,E_f)=\frac{je^2(\omega-2j\Gamma)}{\pi\hbar^2}\left[\frac{1}{(\omega-2j\Gamma)^2}\times\int_0^\infty\varepsilon\left(\frac{\partial f_d(\varepsilon)}{\partial\varepsilon}-\frac{\partial f_d(-\varepsilon)}{\partial\varepsilon}\right)d\varepsilon-\int_0^\infty\frac{f_d(-\varepsilon)-f_d(\varepsilon)}{(\omega-2j\Gamma)^2-4(\frac{\varepsilon}{\hbar})}d\varepsilon\right], \quad (1)$$

where ω, E_f, e, ε, h, and Γ are the radian frequency, Fermi energy level, electron charge, carriers energy, reduced Plank's constant, and phenomenological scattering rate, respectively. The Fermi-Dirac function can be calculated as [19]:

$$f_d(\varepsilon)=\left(1+\exp\left[\frac{\varepsilon-\mu_c}{k_BT}\right]\right)^{-1}, \quad (2)$$

where μ_c, k_B, and T are chemical potential, Boltzmann constant, and temperature, respectively. Besides, for the lower THz band at room temperature, the conductivity of graphene can be described as [19]:

$$\sigma=\frac{e^2E_f}{\pi\hbar^2}\frac{j}{\omega+j/\tau}. \quad (3)$$

Here, τ is the relaxation time. Chemical potential (μ_c) of graphene layer is defined as [19]:

$$|\mu_c|\approx\hbar\upsilon_F\left\{\pi C_g|V_A-V_{Dirac}|\right\}^{\frac{1}{2}}, \quad (4)$$

where $V_{Dirac}=0.8V$, $\upsilon_F=106m/s$, and V_A are Dirac voltage offset, fermions Fermi velocity, and applied voltage.

III. RESULTS AND DISCUSSIONS

The absorption spectra of the proposed four-band graphene based absorber as a function of frequency for *x*- and *y*-polarized of incident wave is presented in Fig. 2. As shown in Fig. 2, there are four absorption peaks at 1.84 THz (f_1), 2.23 THz (f_2), 2.46 THz (f_3), and 2.61 THz (f_4) whose peaks are average over 99%, for *x*-polarized wave. The bandwidth of resonance frequency defined as full width at half maximum (FWHM), are 0.3 THz, 0.17 THz, 0.19 THz, and 0.2 THZ for mode f_1, f_2, f_3, and f_4, respectively. Owing to the narrowband absorption obtained by above results, the four-band graphene based absorber has potential in imaging and sensing applications. Besides, the absorption spectra for the *y*-polarized wave is shown in Fig. 2. It is found that, the proposed absorber has the same resonance frequencies as in *x*-polarized case. Therefore, the absorption spectra of the proposed graphene based absorber is not limited to the polarization of the incident wave.

The sensitivity of the absorption spectra on proposed

graphene based absorber at various angles of incident TE and TM polarized wave from 25° to 40° is shown in Figs. 3 (a) and (b). As shown in Figs. 3 (a) and (b), it is found that the presented four-band absorption is not limited to the normal incident wave. Besides, the proposed absorber remains almost stable for both TE and TM polarized incident wave to 40°.

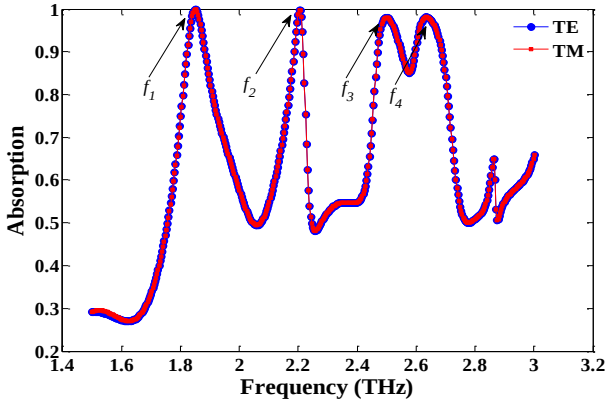

Fig. 2. The absorption spectra of the proposed terahertz absorber for TE and TM polarization.

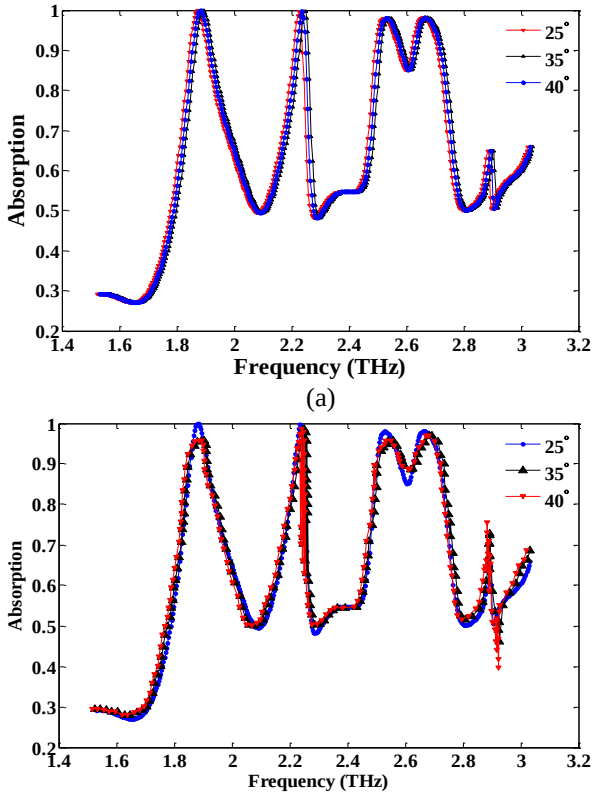

Fig. 3. Dependence of the absorption spectra on different incident angles for: (a) TE and (b) TM configurations, respectively.

In order to reveal the better understanding of the multi band absorption mechanism, the electric field (|E| and real E_z) distributions corresponding to four-band absorption peaks, are presented in Fig. 4. As shown in Fig. 4 (a_1), at 1.84 THz (mode f_1) the electric field is mainly focused on the outer edges of the quarter orthogonal concentric elliptical graphene sheets. Great enhancement of electric field on the corners of the pattern provides the large accumulation of opposite charges on the edges of the orthogonal elliptical pattern, as shown in Fig. 4 (b_1). For mode f_3 (2.46 THz), the electric field distribution is concentrated on the upper and bottom (near the minor axes) of the horizontal elliptical ring, as shown in Fig. 4 (a_2). Besides, the opposite charges are mostly accumulated on both inner and outer edges of the horizontal elliptic (Fig. 4 (b_2)). For mode (f_4), the electric field is focused on the major axes (upper and bottom) of the vertical elliptical ring (Fig. 4 (a_3)). Thus, the opposite charges are accumulated on both inner and outer edges of the pattern (Fig. 4 (b_3)). Owing to the electric field distributions, the fundamental modes are attributed to the main resonance frequency of the orthogonal, horizontal, and vertical elliptical patterns, respectively.

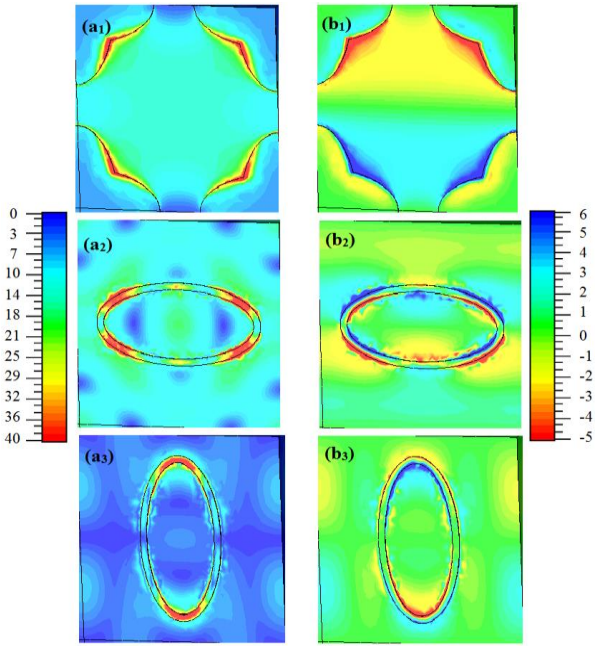

Fig. 4. Distributions of the electric fields (|E| and $|E_z|$) for the quarter orthogonal elliptical nano-disk (a_1 and b_1), horizontal elliptical ring (a_2 and b_2), and vertical elliptical ring (a_3 and b_3) in modes f_1, f_3, and f_4, respectively.

In order to gain the better understanding of the behavior of absorption mechanism of the proposed graphene based four-band absorber, the electric field (|E| and $|E_z|$) distributions, are presented in Fig. 5 and

Fig. 6. The distributions of electric field on the edges of the quarter orthogonal elliptical sheets, provide the accumulation of opposite charges on the edges of the pattern (Fig. 5 (a_1) and Fig. 6 (b_1)). Besides, some weak real ($|E_z|$) electric field distributions can be found on the inner ring. Therefore, the fundamental mode is mainly affected by the quarter orthogonal elliptical sheets. The modes f_2 and f_3 are due to the resonance frequency of the inner ring, because, the electric field distribution is focused on the right and left sides of the ring (mostly near the horizontal axes of the ring), which results the opposite charges accumulation on the inner and outer edges of the ring (Figs. 5 (a_2)-(a_3) and Fig. 6 (b_2)-(b_3)). For mode f_2, the opposite charges are accumulated on the bottom of the elliptical ring, as shown in Fig. 6 (b_2). Furthermore, owing to the large accumulation of opposite charges on the major axes (upper) of the elliptical ring, the mode f_2 is changed to mode f_3, as shown in Fig. 6 (b_3). For mode f_4, the great enhancement of the electric field on the upper and bottom of the ring, provide the large accumulation of opposite charges on the inner edge (Fig. 5 (a_4) and Fig. 6 (b_4)). Therefore, based on the electric field distributions on the structure pattern, the four-band graphene based absorber can be obtained.

Furthermore, in order to verify the explanation of the absorption mechanism, the effect of the geometrical parameter the resonance frequency is investigated. As mentioned above, the resonant frequency of the four-band graphene based absorber mainly depends on the radius of each elliptical pattern. Thus, with the other geometric parameters fixed, the radius variation of the ring can shift or change the modes f_2 and f_3. The effect of the radius R ($R = R_1 + 2.5\ \mu m$ and $R = R_2 + 32.5\ \mu m$) on the resonance frequency of the absorption coefficient, is shown in Fig. 7. The term R indicates the variations of radius R_2 and R_3. It is obvious that the resonant frequencies of the modes f_3 and f_4 gradually decreases with the increase of radius R, while the frequency changes of the modes f_1 and f_2 are neglected. Therefore, the geometrical parameter variation of the structure pattern provides the considerable freedom to control the resonance frequency of the proposed absorber.

In order to achieve the frequency tunability of the proposed graphene based absorber, the absorption spectra in terms of frequency is depicted in Fig. 8 for different values of the chemical potential. From (4), the graphene's chemical potential in various applied bias voltages is tabulated in Table 1. As shown in Fig. 8, when the chemical voltage increases, the bandwidth of the near unity absorption spectra at low frequencies becomes wide from 1.5 THz to 2.1 THz (with FWHM of 0.87 THz). Therefore, the absorber with tunability property is desirable in sensing applications.

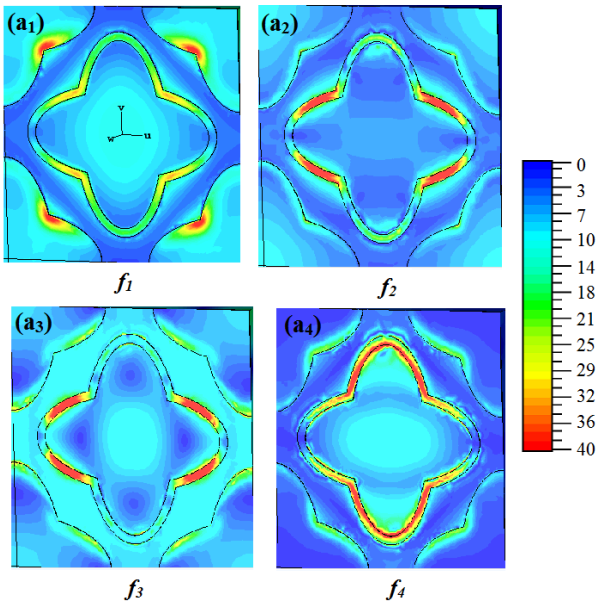

Fig. 5. (a_1)-(a_4) show the distributions of the electric fields |E| for the proposed four-band THz absorber at modes f_1, f_2, f_3, and f_4, respectively.

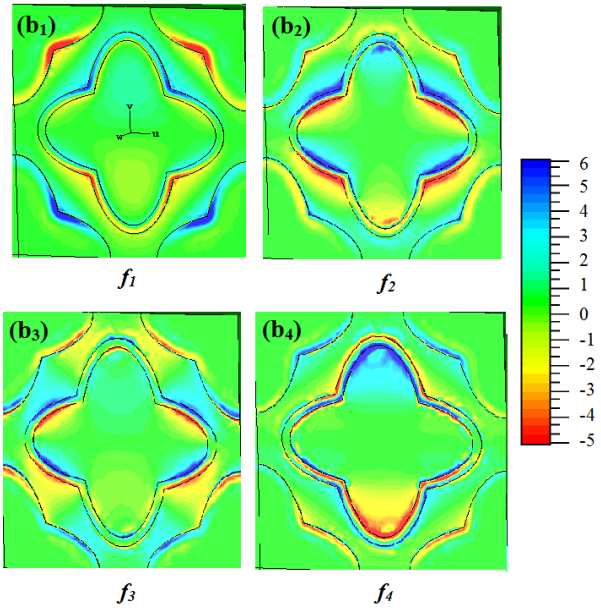

Fig. 6. (b_1)-(b_4) show the distributions of the electric field real $|E_z|$ for the proposed four-band THz absorber at modes f_1, f_2, f_3, and f_4, respectively.

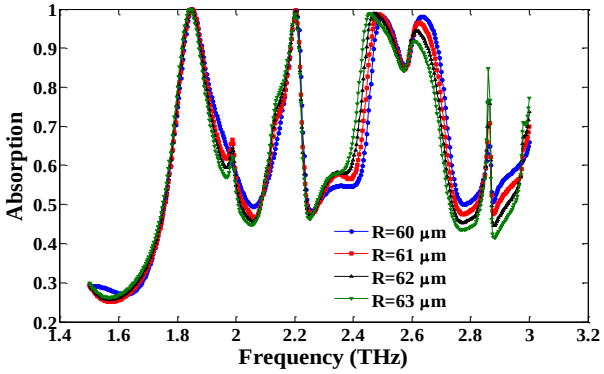

Fig. 7. Dependence of the absorption spectra of the proposed four-band THz absorber on the size changes of the R.

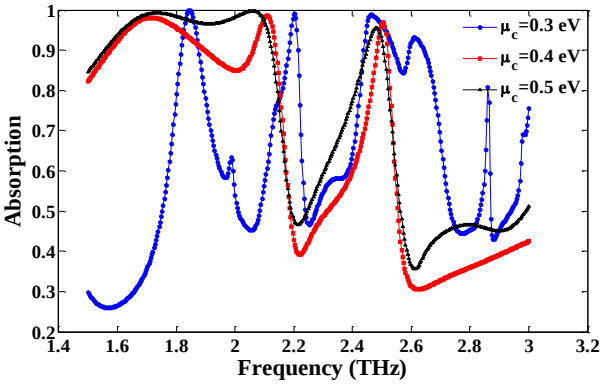

Fig. 8. Dependence of the absorption spectra of the proposed four-band THz absorber on the variation of the chemical potential.

Table 1: Chemical potential of the graphene layer

$\mu_c\,(eV)$	0.3	0.4	0.5
$V_A\,(V)$	6.3	8.5	10.3

IV. CONCLUSION

In conclusion, we proposed a near unity graphene based THz absorber. Four distinct absorption peaks are found at 0.3 THz, 0.6 THz, 0.816 THz, and 2.52 THz with the average absorption over 99% when the Fermi energy is $E_f = 0.2$ eV. The results show that the absorption spectra is insensitive to the incident polarization. Moreover, the bandwidth of the absorption coefficient can be expanded by applying different biasing voltages. The proposed absorber with these performances can be used in imaging and sensing applications.

ACKNOWLEDGMENT

The authors thank the Northwest Antenna and Microwave Research Laboratory (NAMRL) for their beneficial and professional help.

REFERENCES

[1] D. R. Smith and N. Kroll, "Negative refractive index in left-handed materials," *Phys. Rev. Lett.*, vol. 85, pp. 2933, 2000.

[2] A. Ali and Z. Hu, "Metamaterial resonator based wave propagation notch for ultra wide band filter applications," *IEEE Atennas Wireless Propagat. Lett.*, vol. 7, pp. 210-212, 2008.

[3] R. Alaee, M. Farhat, C. Rockstuhl, and F. Lederer, "A perfect absorber made of a graphene micro-ribbon metamaterial," *Optics Express*, vol. 20, pp. 28017-28024, 2012.

[4] M. Pu, P. Chen, Y. Wang, Z. Zhao, C. Wang, C. Huang, et al., "Strong enhancement of light absorption and highly directive thermal emission in graphene," Optics Express, vol. 21, pp. 11618-11627, 2013.

[5] B.-Z. Xu, C.-Q. Gu, Z. Li, and Z.-Y. Niu, "A novel structure for tunable terahertz absorber based on graphene," Optics Express, vol. 21, pp. 23803-23811, 2013.

[6] M. Amin, M. Farhat, and H. Bağcı, "An ultra-broadband multilayered graphene absorber," Optics Express, vol. 21, pp. 29938-29948, 2013.

[7] S. He and T. Chen, "Broadband THz absorbers with graphene-based anisotropic metamaterial films," *Terahertz Science and Technology, IEEE Transactions on*, vol. 3, pp. 757-763, 2013.

[8] J. Grant, Y. Ma, S. Saha, A. Khalid, and D. R. Cumming, "Polarization insensitive, broadband terahertz metamaterial absorber," *Optics Letters*, vol. 36, pp. 3476-3478, 2011.

[9] G. W. Hanson, "Dyadic Green's functions and guided surface waves for a surface conductivity model of graphene," *Journal of Applied Physics*, vol. 103, pp. 064302, 2008.

[10] S. Thongrattanasiri, F. H. Koppens, and F. J. G. de Abajo, "Complete optical absorption in periodically patterned graphene," *Physical Review Letters*, vol. 108, pp. 047401, 2012.

[11] R. Alaee, M. Farhat, C. Rockstuhl, and F. Lederer, "A perfect absorber made of a graphene micro-ribbon metamaterial," *Optics Express*, vol. 20, pp. 28017-28024, 2012.

[12] X.-H. Deng, J.-T. Liu, J. Yuan, T.-B. Wang, and N.-H. Liu, "Tunable THz absorption in graphene-based heterostructures," *Optics Express*, vol. 22, pp. 30177-30183, 2014.

[13] S. Yi, M. Zhou, X. Shi, Q. Gan, J. Zi, and Z. Yu, "A multiple-resonator approach for broadband light absorption in a single layer of nanostructured graphene," *Optics Express*, vol. 23, pp. 10081-10090, 2015.

[14] F. Bonaccorso, Z. Sun, T. Hasan, and A. Ferrari, "Graphene photonics and optoelectronics," *Nature Photonics*, vol. 4, pp. 611-622, 2010.
[15] H. Yan, X. Li, B. Chandra, G. Tulevski, Y. Wu, M. Freitag, et al., "Tunable infrared plasmonic devices using graphene/insulator stacks," *Nature Nanotechnology*, vol. 7, pp. 330-334, 2012.
[16] S. He and T. Chen, "Broadband THz absorbers with graphene-based anisotropic metamaterial films," *IEEE Transactions on Terahertz Science and Technology*, vol. 3, pp. 757-763, 2013.
[17] Z. Su, J. Yin, and X. Zhao, "Terahertz dual-band metamaterial absorber based on graphene/MgF 2 multilayer structures," *Optics Express*, vol. 23, pp. 1679-1690, 2015.
[18] D. Ahmadian, C. Ghobadi, and J. Nourinia, "Tunable plasmonic sensor with metal–liquid crystal–metal structure," *IEEE Photonics Journal*, vol. 7, pp. 1-10, 2015.
[19] A. Fallahi and J. Perruisseau-Carrier, "Design of tunable biperiodic graphene metasurfaces," *Physical Review B*, vol. 86, pp. 195408, 2012.

Sayed Vahid Masuminia was born in Urmia, Iran 1976. He received his B.Sc. in Electrical Engineering from Azad University of Urmia, Iran, in 1994 and M.Sc. degrees in Electrical Engineering Telecommunication from Azad University of Tehran, Iran, in 2002, and he is a currently Ph.D. Student at Urmia University, Urmia, Iran. His primary research interests are in radar, microwave circuits, MIMO systems.

Changiz Ghobadi received his B.Sc. in Electrical Engineering-Electronics and M.Sc. degrees in Electrical Engineering from Isfahan University of Technology, Isfahan, Iran, and Ph.D. degree in Electrical-Telecommunication from University of Bath, Bath, UK in 1998. From 1998 he was an Assistant Professor and now he is a Professor in the Department of Electrical Engineering of Urmia University, Urmia, Iran. His primary research interests are in antenna design, radar and adaptive filters.

Javad Nourinia received his B.Sc. in Electrical and Electronic Engineering from Shiraz University and M.Sc. degree in Electrical and Telecommunication Engineering from Iran University of Science and Technology, and Ph.D. degree in Electrical and Telecommunication from University of Science and Technology, Tehran Iran in 2000. From 2000 he was an Assistant Professor and now he is a Professor in the Department of Electrical Engineering of Urmia University, Urmia, Iran. His primary research interests are in antenna design, numerical methods in electromagnetic, microwave circuits.

Mohsen Karamirad received the M.Sc. degree in Electrical Engineering Microwave, Antenna and Propagation from USB University, Iran, in 2013. He is currently working toward the Ph.D. degree at Urmia University, Urmia, Iran. He is with Northwest Antenna and Microwave Research Laboratory (NAMRL) as a Microwave Engineering. His research interests include Floquet Analysis and Periodic Structures, Microwave Components, Optimization Methods, MIMO and electrically small antennas and Measurements.

Bahman Mohammadi received the B.Sc. degree in Electrical Engineering-Telecommunication from Tabriz University, Tabriz, Iran, in 2011 and M.Sc. degree in Electrical Engineering-Microwave, Antenna and Propagation from Urmia University, Urmia, Iran, in 2013 (1 honor or award). He is with Northwest Antenna and Microwave Research Laboratory (NAMRL) as a Microwave Engineer since March 2011. His research interests include Floquet Analysis and Periodic Structures, Microwave Components, Optimization Methods, MIMO and Measurements.

Multiband and Perfect Absorber with Circular Fishnet Metamaterial and its Variations

Yusuf Ozturk [1,2] and A. Egemen Yilmaz [2]

[1] The Scientific and Technological Research Council of Turkey
ULAKBİM, Ankara, 06539, Turkey
yusuf.ozturk@tubitak.gov.tr

[2] Department of Electrical and Electronics Engineering
Ankara University, Ankara, 06830, Turkey
aeyilmaz@eng.ankara.edu.tr

Abstract — In this study, a composite metamaterial unit cell is introduced based on experimentally proven circular fishnet metamaterials (CF-MMs) and its stripped versions to implement an absorber for Ku band microwave regime. The offered MM absorber shows the perfect absorptivity (99.9%), the near perfect absorptivity (96.2%) and the standard absorptivity (58%) over narrow band frequencies 14.28, 14.77 and 15.2 GHz, respectively. We offered a method to create a composite metamaterial unit cell consisting of resonant type metamaterial sub-unit cells that are not suitable for absorber implementations in normal conditions. The physical mechanism behind multi-band resonances in the left-handed medium (LHM) regime is explained in detail by revealing the reverse behavior in the right-handed medium (RHM) regime keeping a single resonance feature, based on cancellation of impinging electric fields and preservation of circulating electric fields around the MM space. A detailed analysis is performed to explore and compare the power losses due to imperfect dielectric and non-ideal conductor.

Index Terms — Absorptivity, dielectric loss, composite multiband metamaterial, metamaterial perfect absorber, Q-factor, surface loss.

I. INTRODUCTION

Metamaterials are artificial materials engineered to gain their properties from design challenges such as shape, geometry, size or orientation rather than from their chemistry or composition. By combining electric and magnetic responses together, metamaterials allow for the explicit design of the effective macroscopic parameters. Practical outcome is a negative refractive index (NRI) or double-negative material (DNM) whose effective electric permittivity (ε_{eff}) and magnetic permeability (μ_{eff}) are negative simultaneously in a certain frequency range [1, 2]. Creating an effective medium with controllable permittivity and permeability makes this metamaterials very interesting for many applications, such as superlenses [3, 4], phase shifters [5], antennas [6, 7], cloaking [8, 9], as well as many other devices which have been designed and studied. For many other applications, a key metamaterial performance would be desirable to minimize the metamaterial losses [10, 11]. On the other hand, absorbers focus on maximizing these losses to avoid all types of scattering electromagnetic fields outward the inclusion. An absorber is a device in which all incident radiations including transmissivity, reflectivity and scattering are absorbed at the desired frequency. Electromagnetic (EM) wave absorbers can be categorized into two types: resonant absorbers and broadband absorbers [12]. Resonant absorbers require the material interacting with the incident radiation in a resonant way at a specific frequency, ω_0 (where the wavelength corresponding to ω_0 defined as $\lambda_0 = 2\pi c/\omega_0$ and c is the speed of light in vacuum). Broadband absorbers generally rely on materials whose properties are non-dispersive and therefore can absorb radiations over a large bandwidth. The absorbers employed in everyday applications based on the Salisbury screen [13] are usually backed by a metallic plate to avoid power transmission on the other side of the absorber. In the Salisbury screen layout, a 377 Ω-resistive sheet is placed a quarter-wavelength apart from the metallic plate, where the tangential component of the electric field has its maximum amplitude. Suitable boundary conditions create a reflected component, when combined with the impinging wave, cancels out the reflection from the screen.

The first metamaterial perfect absorber (MPA) consists of three layers, two metallic layers and a dielectric, and demonstrated a simulated absorptivity of $A \approx 99\%$ at 11.48 GHz [14]. Other examples of resonant absorbers were also proposed lately containing three or more layers of symmetrical coupling structures and exhibiting narrow-band absorptivity [15, 16]. Absorbers

Submitted On: August 1, 2016
Accepted On: October 7, 2016

based on the regular split-ring resonators (SSRs) disposed in an array configuration are shown to reach thickness of the order of $\lambda_0/20$ [17]. On the other hand, some of multiband metamaterial absorbers take place as good examples, which are composed of six close rings distributed in two metallic layers separated by FR-4 substrates [18], dipole mode electric resonators coupled by microwave diodes on one side of a dielectric substrate and metallic ground plane on the other side [19], 2×2 array of eSRRs oriented in different directions [20]. Physical explanations for absorbance mechanism include lossy substrates and the destructive interference of EM wave with superposition and counteraction for different components [21], plasmonic perfect absorbance based on a Fabry–Perot cavity bounded by a resonator mirror and metallic film [22], or the weak surface current area to avoid the radiation property deterioration [23].

In this study, we designed a multiband metamaterial absorber based on the circular fishnet metamaterial (CF-MM) structure which is shown double-negative (DNG) properties experimentally and theoretically [24]. The dispersive transmission line parameters explain a complex resonance behavior or loss/gain mechanism for CF-MM [25]. At first glance, CF-MM structure shows resonant type transmission properties and the transmission/ reflection coefficients have mutual-exclusive mode that is an undesirable feature for absorber design. To avoid this obstacle, we designed a novel composite CF-MM cell containing itself and stripped variations together. All sheets are designed to operate at a distinct wavelength, and thus, each sheet is separated by approximately λ/9, producing multiple reflection minima around some center frequency. As a contribution, the main reason for multiband features is explained in physical meaning. Additionally, power losses are calculated for each non-ideal conductor sheets and imperfect dielectric layer, separately.

II. STRUCTURE DESIGN AND FABRICATION

Firstly, circular fishnet metamaterial (CF-MM) operating independent of the incident polarization is designed, fabricated and measured in order to characterize its behavior completely. Polarization independency of the structure is due to its symmetric configuration. A schematic view of unit cell, multilayer and equivalent slab pair forms of CF-MMs are depicted in Fig. 1.

The structure consists of the low-loss Teflon substrate (ε_r=2.16 and loss tangent of tanδ=0.005) with a transparent view and the highlighted metal parts as copper layer. The lower tangent loss value is vital to achieve left-handed resonance behavior, therefore FR-4 like substrates are not suitable to create CF-MM in the same dimensions. The Teflon layer as a substrate and the copper layer has t=1 millimeter and 20 micrometer respectively. The unit cell as shown Fig. 1 (a), has the complementary parameters wherein choosing the dimensions as a_x=a_y=a=14 mm and the radius r=0.25×a result in a fully circular and polarization-independent inclusions. The unit cell is replicated nine times in x and y directions to obtain the whole one-layer CF-MM structure including 10×10 cells. For multilayer deployment of CF-MM's as in Fig. 1 (b), the distance between stacked layers shall be set as a_z=2 mm. The incident EM wave propagates along the z-direction perpendicular to the $\boldsymbol{E}$-field parallel to the y-axis and the $\boldsymbol{H}$-field parallel to the x-axis.

In Fig. 1 (b), 1-Stripped CF-MM inclusion (1S-CFMM) is introduced with two complementary design parameters: the strip width (w=0.5 mm) and the gap width between the strip and the main block of copper layer (g=0.2 mm). Due to simplicity, 2-Stripped (2S-CFMM) and 3-Stripped CF-MMs (3S-CFMM) are not presented as stand-alone graphics, indeed they are shown in the composite unit cell (C-CFMM) in Fig. 1 (c). In fact, there are two alternatives to create a composite metamaterial unit cell: sub-modules are placed on the same plate an example of a single planar cell [20] or cascaded form as depicted in [26]. The first one is not applicable for our design due to touching effect of copper layers resulting in a single material rather than a composite metamaterial.

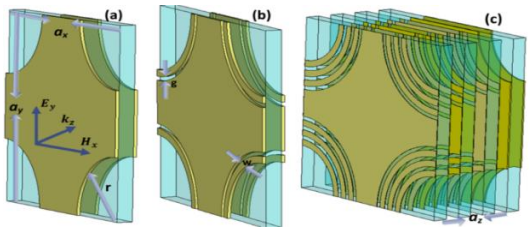

Fig. 1. Schematic representation of CF-MMs as: (a) unit cell, (b) 1-stripped form of the unit cells, and (c) composite CF-MM cell consists of unit cell, 1-stripped, 2-stripped and 3-stripped form of CF-MM cell.

III. EXPERIMENTAL RESULTS AND NUMERICAL CALCULATIONS

First, we investigate the resonance behavior of structure to satisfy the desired operation conditions of DNG medium properties. Due to experimental limitations, the 0-Stripped CF-MM sheet was merely fabricated and measured (Fig. 2). We excite the unit cell displayed in Fig. 1 (a) with a waveguide port and obtain the transmission amplitudes by another waveguide port. The distance between the device under test and the waveguide ports is a_z/2=1 mm. The propagation direction is along +z and electric field vector ($\boldsymbol{E}$) is directed to +y. Moreover, open boundary conditions are employed along the propagation direction (+z and -z). All tangential electric fields in y direction and all tangential magnetic fields in x direction are set to zero to realize electric

boundary conditions and magnetic boundary conditions, respectively. As depicted in Fig. 3 (a), the unit cell has a LHM and RHM resonance centered around 13.8 GHz and 18.5 GHz, respectively. In order to further investigate the properties of CF-MM and its stripped variations, the standard retrieval procedure [27] is applied to extract the effective permittivity and permeability values. The related retrieved effective parameters are shown in Fig. 3 (b). The calculated DNG regions for CF-MM and its variations (1S-CFMM, 2S-CFMM, and 3S-CFMM) are placed at 13.8, 14.2, 14.7, and 15.2 GHz, respectively.

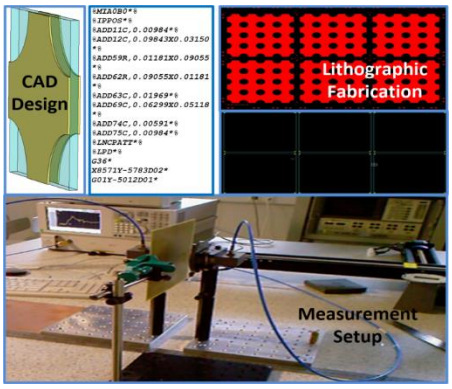

Fig. 2. Schematic representation of the whole process explaining design, sample gerber file, fabrication and measurement of CF-MMs.

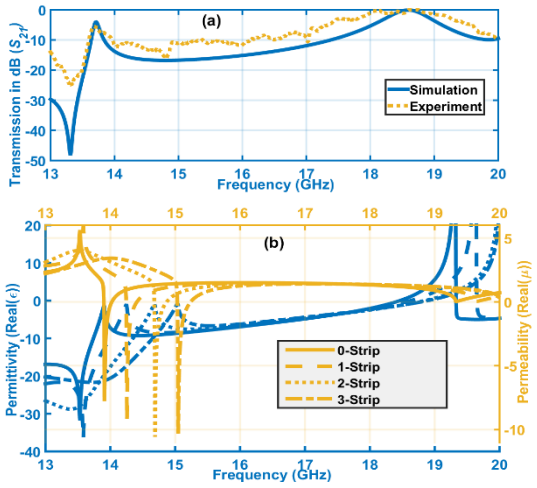

Fig. 3. Numerical and experimental results for $r = 0.25a$: calculated transmission (the blue solid line), measured transmission (the orange dashed) (a), and calculated effective macroscopic parameters (b).

During simulations, the same behaviors of LHM and RHM regimes are obtainable for 1S-CFMM, 2S-CFMM, and 3S-CFMM unit cells except from a frequency-shipping coming from the additional strip capacitance and inductance values. The LHM resonance values in the transmission spectra are calculated 14.22, 14.75, and 15.2 GHz for these inclusions. The phase advance and lag characteristics are also observable in the similar manner. Figure 4 (a) presents the transmission spectra of the composite CF-MM inclusion where S_{11} and S_{21} denote the reflection and transmission coefficients. After this operation, the impedance of the C-CFMM is calculated according to Eq. (1) and compared to the free space impedance:

$$Z(\omega) = \sqrt{\frac{(1+S_{11})^2 - {S_{21}}^2}{(1-S_{11})^2 - {S_{21}}^2}}. \quad (1)$$

The experiments for the CF-MM absorber are performed in free space and at room temperature by using two standard-gain horn antennas. The distance between the horn antennas was kept fixed at 30 cm, away and the absorber under test consisting of 10×10 cells was located at the centeral position. Firstly, a TRL calibration procedure was implemented on the network analyzer in order to eliminate the environmental noises. After the calibration, the transmission spectra have been measured at the same position.

It is necessary to check real and imaginary parts of the retrieved line impedance to control the well-known passive medium requirements. As depicted in Fig. 4 (b), the matching performance of the device reveals the normalized line impedance as 1.5, 1, 0.5, and 0.1 ohms for the resonances 13.8, 14.22, 14.75, and 15.2 GHz, respectively. At around 14.22 GHz, the expected impedance values are easy to achieve for perfect metamaterial absorber applications.

The frequency characteristics of absorption can be calculated by Eq. (2) where A denotes absorber performance. In this equation, S_{21} coefficient must be taken into account under the condition of lacking a backed metallic plate. Accordingly, there are four distinct absorptive peaks belonging to each internal modules with absorption values as 96.2%, 99.99%, 58%, and the negligible one 2.5%. As can be seen from the results in Fig. 4 (c), perfect absorption only occurs with very narrow band at resonant frequency centered at 14.28 GHz, and nearly perfect absorber at 13.82 GHz:

$$A(\omega) = 1 - R(\omega) - T(\omega) = 1 - {S_{11}}^2 - {S_{21}}^2. \quad (2)$$

Obviously, the designed MM absorber has narrow-band absorptivity, and it is possible to achieve perfect absorption in different resonance frequency points by changing the sizes of the structures and dielectric of the substrate materials by supplying sub-wavelength criteria. According to some previous studies [28, 29], the effect is that it acts as a resonant absorber over multiple wavelengths, achieving a broadband response. The bandwidth should increase with each added layer; however, this has the undesirable effect of making the absorber thick and bulky. In our design, the layered unit cells do not play a critical role to change bandwidth of the absorber, clearly.

Power losses inside C-CFMM structure are calculated for each resonance frequency to better

understand the composite unit cell. The results were plotted in Fig. 5 as a bubble graphic. Based on the surface currents created on the each variation of CF-MM cells in the LC resonant mode, the maximum power loss calculations conform with the previous results to a great extent. For 13.82 GHz, the maximum power losses were occurred in the CF-MM module with no-strip. On the other hand, the frequencies of 14.28/14.77/15.2 GHz were correspondent to 1S-CFMM, 2S-CFMM and 3S-CFMM sub-modules as expected.

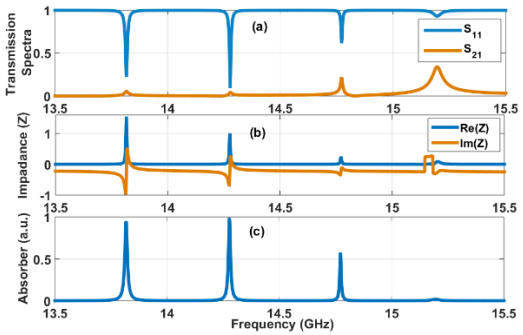

Fig. 4. Calculated transmission/reflection coefficients (a), impedance values (b), and absorbance performance (c) for the C-CFMM unit cell.

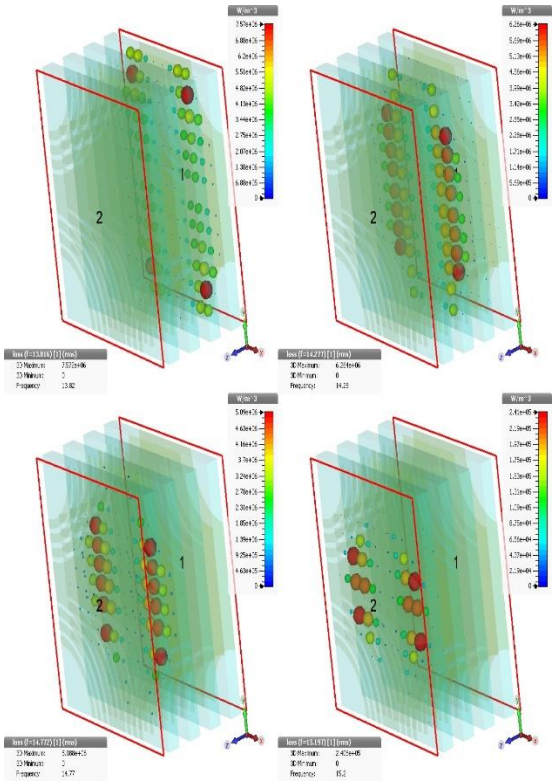

Fig. 5. Power loss density calculations inside the C-CFMM structure for 13.82 GHz (a), 14.28 GHz (b), 14.77 GHz (c), and 15.2 GHz (d).

IV. PHYSICAL EXPLANATIONS

In this section, a detailed physical examination is performed to understand the actual behavior of multiband metamaterial absorbers. First of all, we focus on the question how every sub-module keeps its own behavior like an isolated device. It is easy to observe the omitted fringing electric field intensities in the LHM regime; along the circular sides of CF-MM [24]. As a basic physical explanation, the relationship between the electrical permittivity ε_r and the electric polarization $\boldsymbol{P}$ is defined with the basic formula of $\boldsymbol{D} = \varepsilon_0\boldsymbol{E} + \boldsymbol{P}_e = (1+\chi_e)\varepsilon_0\boldsymbol{E}$. In the situation $\chi_e < -1$, ε_r becomes negative satisfying the homogenization subwavelength conditions. This effect results in that the electric polarization $\boldsymbol{P}$ overcomes the electric flux density term of $\varepsilon_0\boldsymbol{E}$. The same approach can be used in order to analyze the relationship between the effective magnetic susceptibility χ_m and the magnetic flux density $\boldsymbol{B}$ with the second complementary formula $\boldsymbol{B} = \mu_0(\boldsymbol{H} + \boldsymbol{P}_m) = (1+\chi_m)\mu_0\boldsymbol{H}$. This cancellation of the horizontal electric field components produced by circular slots and the corresponding anti-parallelism changes in the surface currents.

On the other hand, the fringing electric fields and the relevant parallel surface currents reshape dispersive nature of multiband absorber. By using a single CF-MM unit cell (shown as blue transparent), electric field components are calculated for LHM (13.8 GHz) and RHM (18.5 GHz) as depicted in Fig. 6, where the numbers "1" and "2" are the waveguide port numbers normal to the surface plane of CF-MM. The distance between the unit cell and the waveguide ports is set to $5xa_z$=10 mm to observe the electric field distributions. The excitation with arbitrary $e^{i\beta r}e^{-i\omega t}$ plane-wave, E-fields are assumed uniformly distributed all over the array according to homogeonization approach. This assumption supplies an averaged space-time distribution of the induced fields with the same $e^{i\beta r}e^{-i\omega t}$ dependence, in which the variables ω and β are independent of each other.

Similar anaysis is performed for causality properties of metamaterial to check Kramers-Kronig relations [30]. The interesting point is that the variables r and β may have corresponding dependency based on Fig. 6. For LHM region, C-CFMM is breaking homogenization approach and each sub-module has own dispersive β characteristics. On the other hand, the same parameters obey homogeonization scheme completely for RHM bands in that conditons there is single RHM resonance different from multiple LHM resonances. Similar composite metamaterial cells can be analyzed with this approach.

Lastly, MPA performance is analyzed here to consider realistic losses in the metals (called as surface loss power and denoted as P_W) and volume losses in the

dielectric substrates (called as volume loss power and denoted as P_D). In the simulations and power loss calculations, the structure has been simulated employing CST Microwave Studio, a full-wave commercial code based on the finite integration technique, with periodic boundary conditions [31]. In order to solve the integral form of Maxwell's equations numerically a finite calculation domain is defined, enclosing the considered application problem. Then, this domain is split up into several small grid cells to create a useful mesh system. Waveguide ports are handled inside the structure, which is quite useful for simulations and physical excitations. The dissipated power on the imperfect dielectric layer strongly depends on the parameters the loss-tangent value taken as $tan\delta = 0.005$ and the electric permittivity taken as $\varepsilon_r = 2.16$ in Eq. (3.1). In normal conditions, the copper layers are assumed to behave as PEC in microwave regimes. During a detailed investigation, the absorbed power due to the nonideal surface losses is calculated with help of the specified conductivity of copper as $\sigma = 5.8x10^7 \mathrm{S/m}$ in Eq. (3.2) [32]:

$$P_D = \pi f tan\delta \varepsilon_0 \varepsilon_r \int |\boldsymbol{E}|^2 \, \partial V, \tag{3.1}$$

$$P_W = \frac{1}{2}\sqrt{\frac{\pi\mu f}{\sigma}} \int |\boldsymbol{H}|^2 \, \partial S. \tag{3.2}$$

The results of the loss power calculations for 14.28 GHz and 14.77 GHz are presented in Table 1, showing very good agreement with the resonances in Fig. 3 and simulations in Fig. 5. According to the table, the surface losses (46.4% and 46.2% for the 1S-CFMM resonance at 14.28 GHz and the 2S-CFMM resonance at 14.77 GHz, respectively) are comparable to the volumetric losses (53.6% and 53.8% for 14.28 GHz and 14.77 GHz, respectively). The maximum surface losses can be seen in 1S-CFMM Copper Surface (33%) and 2S-CFMM Copper Surface (33.5%) for their own LHM resonances as expected. By using this results, Q-factor of device is equal to:

$Q = 2\pi f \times (average\ energy\ stored)/(total\ power\ loss)$.

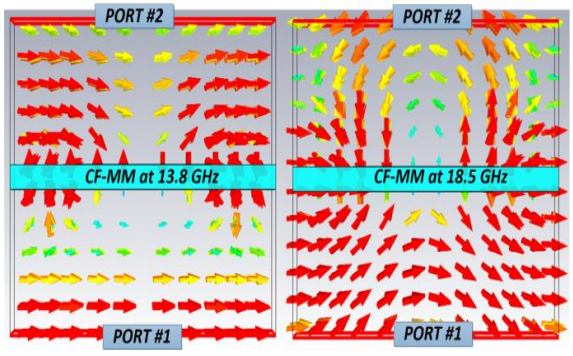

Fig. 6. Top view of the calculated electric field components inside and around the CF-MM structure for 13.8 GHz (left panel) and 18.5 GHz (right panel).

Table 1: Power loss calculation for the C-CFMM inclusion

Loss Region	Loss/W (Peak) at 14.28 GHz	Loss/W (Peak) at 14.77 GHz
CF-MM copper surface	4.8567×10^{-3}	3.9969×10^{-3}
1S-CFMM copper surface	6.1259×10^{-1}	9.3417×10^{-3}
2S-CFMM copper surface	3.5518×10^{-2}	3.4556×10^{-1}
3S-CFMM copper surface	3.6165×10^{-3}	3.4972×10^{-2}
Total surface loss power (P_W)	8.4762×10^{-1}	4.7555×10^{-1}
Total volume loss power (P_D)	9.8087×10^{-1}	5.5461×10^{-1}

V. CONCLUSIONS

In summary, a polarization-independent and narrow-band absorber with triple bands has been successfully designed and tested by using composite circular fishnet metamaterial cells. The resonant inclusions are considered to match the impedance of the absorber to free space and achieve large energy dissipation, minimizing the wave refection and transmitting under the assumption that the scattering is negligible (the roughness of the surface $R \ll \lambda$). The proposed structure does not require a separate resistive sheet or backed metal plate. It is shown that different LHM resonances can occur simultaneously based on cancellation of impinging electric fields. This gives opportunity to design composite unit cells for multiband absorber operations. Power loss calculations result in comparability between metal and dielectric layers of composite circular fishnet metamaterial.

REFERENCES

[1] D. R Smith, W. J. Padilla, D. C. Vier, S. C. Nemat-Nasser, and S. Schultz, "Composite medium with simultaneously negative permeability and permittivity," *Physical Review Letters*, vol. 84, no. 18, pp. 4184, 2000.

[2] R. A. Shelby, D. R. Smith, and S. Schultz, "Experimental verification of a negative index of refraction," *Science*, vol. 292, no. 5514, pp. 77-79, 2001.

[3] K. Aydin, I. Bulu, and E. Ozbay, "Subwavelength resolution with a negative-index metamaterial superlens," *Appl. Phys. Lett.*, vol. 90, no. 25, pp. 254102, 2007.

[4] X. Zhang and L. Zhaowei, "Superlenses to overcome the diffraction limit," *Nat. Mater.*, vol. 7, no. 6, pp. 435-441, 2008.

[5] M. A. Antoniades and G. V. Eleftheriades, "Compact linear lead/lag metamaterial phase shifters for broadband applications," *IEEE Antennas Wirel. Propag. Lett.*, vol. 2, no. 1, pp. 103-106,

2003.

[6] A. Erentok, P. L. Luljak, and R. W. Ziolkowski, "Characterization of a volumetric metamaterial realization of an artificial magnetic conductor for antenna applications," *IEEE Trans. Antennas Propag.*, vol. 53, no. 1, pp. 160-172, 2005.

[7] L. Sungjoon, C. Caloz, and T. Itoh, "Metamaterial-based electronically controlled transmission-line structure as a novel leaky-wave antenna with tunable radiation angle and beamwidth," *IEEE Trans. Microwave Theory Techn.*, vol. 53, no. 1, pp. 161-173, 2005.

[8] W. Cai, U. K. Chettiar, A. V. Kildishev, and V. M. Shalaev, "Optical cloaking with metamaterials," *Nat. Photonics*, vol. 1, no. 4, pp. 224-227, 2007.

[9] A. Alu and N. Engheta, "Plasmonic and metamaterial cloaking: Physical mechanisms and potentials," *J. Opt. A*, vol. 10, no. 9, pp. 093002, 2008.

[10] S. Wuestner, A. Pusch, K. L. Tsakmakidis, J. M. Hamm, and O. Hess, "Overcoming losses with gain in a negative refractive index metamaterial," *Phys. Rev. Lett.*, vol. 105, no. 12, pp. 127401, 2010.

[11] J. Zhou, T. Koschny, and C. M. Soukoulis, "An efficient way to reduce losses of left-handed metamaterials," *Opt. Express*, vol. 16, no. 15, pp. 11147-11152, 2008.

[12] C. M. Watts, X. Liu, and W. J. Padilla, "Metamaterial electromagnetic wave absorbers," *Adv. Mater.*, vol. 24, no. 23, pp. OP98-OP120, 2012.

[13] W. W. Salisbury, "Absorber Body for Electromagnetic Waves," *U.S. Patent* 2599944, June 10, 1952.

[14] N. I. Landy, S. Sajuyigbe, J. J. Mock, D. R. Smith, and W. J. Padilla, "Perfect metamaterial absorber," *Phys. Rev. Lett.*, vol. 100, no. 20, pp. 207402, 2008.

[15] H. Tao, C. M. Bingham, A. C. Strikwerda, D. Pilon, D. Shrekenhamer, N. I. Landy, et al., "Highly flexible wide angle of incidence terahertz metamaterial absorber: Design, fabrication, and characterization," *Phys. Rev. B*, vol. 78, no. 24, 2008.

[16] N. I. Landy, C. M. Bingham, T. Tyler, N. Jokerst, D. R. Smith, and W. J. Padilla, "Design, theory, and measurement of a polarization-insensitive absorber for terahertz imaging," *Phys. Rev. B*, vol. 7, no. 9, 2009.

[17] F. Bilotti, A. Toscano, K. B. Alici, E. Ozbay, and L. Vegni, "Design of miniaturized narrowband absorbers based on resonant-magnetic inclusions," *IEEE Trans. Electromagn. Compatibility*, vol. 53, no. 1, pp. 63-72, 2011.

[18] L. Huang and H. Chen, "Multi-band and polarization insensitive metamaterial absorber," *Prog. Electromagn. Res.*, vol. 113, pp. 103-110, 2011.

[19] B. Zhu, C. Huang, Y. Feng, J. Zhao, and T. Jiang, "Dual band switchable metamaterial electromagnetic absorber," *Prog. Electromagn. Res.*, vol. 24, pp. 121-129, 2010.

[20] M. Li, H. L. Yang, X. W. Hou, Y. Tian, and D. Y. Hou, "Perfect metamaterial absorber with dual bands," *Prog. Electromagn. Res.*, 108, pp. 37-49, 2010.

[21] S. J. Li, X. Y. Cao, J. Gao, T. Liu, Y. J. Zheng, and Z. Zhang, "Analysis and design of three-layer perfect metamaterial-inspired absorber based on double split-serration-rings structure," *IEEE Transactions on Antennas and Propagation*, vol. 63, no. 11, pp. 5155-60, 2015.

[22] K. Bhattarai, Z. Ku, S. Silva, J. Jeon, J. O. Kim, S. J. Lee, A. Urbas, and J. Zhou, "A large-area, mushroom-capped plasmonic perfect absorber: Refractive index sensing and Fabry–Perot cavity mechanism," *Advanced Optical Materials*, vol. 3, no. 12, pp. 1779-1786, 2015.

[23] S. J. Li, J. Gao, X. Y. Cao, Y. Zhao, Z. Zhang, and H. X. Liu, "Loading metamaterial perfect absorber method for in-band radar cross section reduction based on the surface current distribution of array antennas," *IET Microwaves, Antennas & Propagation*, vol. 9, no. 5, pp. 399-406, 2014.

[24] Y. Öztürk, A. E. Yılmaz, E. Çolak, and E. Özbay, "Characterization, slab-pair modeling and phase analysis of circular fishnet metamaterials," *Phot. Nano. Fund. Appl.*, vol. 10, no. 4, pp. 624-631, 2012.

[25] Y. Öztürk, A. E. Yılmaz, and E. Özbay, "Conversion from constitutive parameters to dispersive transmission line parameters for multi-band metamaterials," *Waves in Random and Complex Media*, vol. 26, no. 2, pp. 223-235, 2016.

[26] E. Ekmekci, K. Topalli, T. Akin, and G. Turhan-Sayan, "A tunable multi-band metamaterial design using micro-split SRR structures," *Opt. Express*, vol. 17, no. 18, pp. 16046-16058, 2009.

[27] X. Chen, T. M. Grzegorczyk, B. I. Wu, J. Pacheco, and J. A. Kong, "Robust method to retrieve the constitutive effective parameters of metamaterials," *Phys. Rev. E.*, vol. 70, pp. 016608, 2004.

[28] G. T. Ruck, D. E. Barrick, and W. D. Stuart, *Radar Cross Section Handbook*. vol. 2, New York, Plenum Press, New York, 1970.

[29] B. A. Munk, P. Munk, and J. Pryor, "On designing Jaumann and circuit analog absorbers for oblique angle of incidence," *IEEE Trans. Ant. Prop.*, vol. 55, pp. 186-193, 2007.

[30] A. Alù, "First-principles homogenization theory for periodic metamaterials," *Phys. Rev. B*, vol. 84, no. 7, pp. 075153, 2011.

[31] CST Microwave Studio, ver. 2015, Computer

Simulation Technology, Framingham, MA, 2016.
[32] R. Bansal, *Fundamentals of Engineering Electromagnetics*. CRC Press, pp. 233-235, 2006.

Yusuf Ozturk received his B.Sc., M.Sc. and Ph.D. in Electrical and Electronics Engineering from Ankara University in 1997, 2002, and 2014 respectively. His research interests include image processing, networking technologies, applied electromagnetics, photonics and metamaterials. He is working at the Scientific and Technological Research Council of Turkey (TUBITAK).

Asim Egemen Yilmaz was born in 1975. He received his B.Sc. degrees in Electrical-Electronics Engineering and Mathematics from the Middle East Technical University in 1997. He received his M.Sc. and Ph.D. degrees in Electrical-Electronics Engineering from the same university in 2000 and 2007, respectively. He is currently with the Dept. of Electronics Engineering in Ankara University, where he is an Associate Professor. His research interests include computational electromagnetics, nature-inspired optimization algorithms, knowledge-based systems; more generally software development processes and methodologies.

Novel Mathematical Formulation of the Antenna Array Factor for Side Lobe Level Reduction

Oussama Gassab and Arab Azrar

Department of Electronic, Institute of Electrical & Electronics Engineering
University of M'Hamed BOUGARA of Boumerdes, Boumerdes, 35000, Algeria
oussamagassab@yahoo.com, take_azrar_2007@yahoo.com

Abstract ─ In this article a new approach is used to improve the performance of antenna arrays. The antenna array performance is improved when its directivity is increased and its side lobes are decreased. To do this, a concept of array hybridization (mixing two distinct arrays) is presented and applied to uniform arrays to generate a new array for satisfying the requirement. Two new arrays are generated using the proposed principle. The first is obtained from two arrays with different number of elements (UUDNH). The second generated array is based on the use of two arrays with different spacing between their elements (UUDdH).

The obtained arrays parameters (array factor, side lobe levels, directivity and excitation coefficients) are given in closed form expressions. Furthermore, performances of the proposed arrays exceed that of Tschebyscheff arrays with the same number of elements.

Index Terms─ Antenna array, array factor, convolution, directivity, distance conversion, feeding currents, first null bandwidth, Fourier transform, hybridization, side lobe.

I. INTRODUCTION

In this modern era, the telecommunications become an important research field because all the new physical cosmological phenomena are happening in the far field. To collect the electromagnetic signals coming from these phenomena without any interference and any noise a high directive antenna with very low side lobes is needed. A single element antenna cannot be used to obtain the needed radiation pattern and the required results. For this reason an antenna array is used in order to have large number of controllable parameters to obtain the needed pattern that satisfies the desired specifications [1-2]. The uniform array is the simpler and the well-known array that offers high directivity, but unfortunately with very high side lobes levels. Previously, many methods have been used to improve the antenna array performance [3]. In [3], the non-uniform arrays have been studied and the obtained distributions are quite complicated for practical implementation. Other works also exist for the same purpose and most of them are based on the use of Genetic Algorithm (GA) or other optimization techniques [4-9]. The results obtained by using optimization techniques are reasonably satisfactory but the feeding currents and the elements positions are randomly distributed and the implementation of the array using these distributions is very hard and costly.

The present work is based on mathematical derivation of the array factor of linear antenna array based on linear systems techniques [10]. The idea may be viewed as hybridization of two distinct uniform antenna arrays; in which the current excitation for each element is viewed as one term that belongs to an overall discrete sequence in given coordinate system. By applying the Fourier transform and convolution properties the hybridization (mixing) can be performed between two different arrays yielding a new array (Fig. 1) having high directivity with very low side lobe levels. Furthermore, the feeding currents are given by closed form expression that can easily be practically implemented.

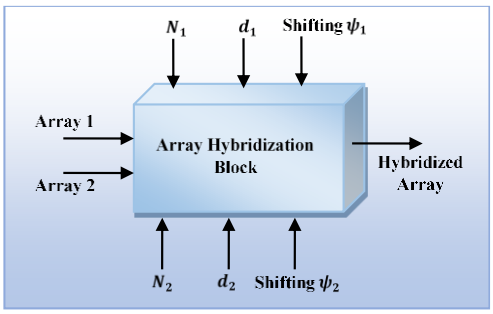

Fig. 1. The Hybridization block diagram where (N_1, d_1, ψ_1) and (N_2, d_2, ψ_2) are the controllable parameters of the array 1 and the array 2 respectively; N_i is the number of the elements, d_i is the spacing distance, and ψ_i is the array shifting $\left(A(\psi - \psi_i)\right)$ of array i (i = 1 or 2).

II. MATHEMATICAL THEORY OF HYBRIDIZATION

As already stated, the hybridization is performed between two distinct uniform arrays. The array factor of

Submitted On: June 6, 2016
Accepted On: October 7, 2016

a linear array is given by the following relation:

$$A(\psi) = \sum_n a_n e^{j\psi n}, \quad (1)$$

where a_n is complex sequence that represent the feeding current (excitation coefficients) of each antenna element, and ψ is the array digital wave number ([2] at chapter 18). A linear antenna aligned along the z-axis has a digital wave number $\psi = kdcos(\theta)$; where d is the spacing distance and θ is the elevation angle.

Now the proposed method starts by replacing the term a_n by the term $x[n]$, which is more general than a_n, because n can be negative, and it indicates the existence of coordinate. So, the array factor is written in the following form:

$$A(\psi) = \sum_n x[n] e^{j\psi n}. \quad (2)$$

The relation (2) represents the discrete Fourier transform $D\mathcal{F}$:

$$A(\psi) = D\mathcal{F}\{x[n]\}_{\psi \to -\psi}. \quad (3)$$

The property of convolution given in the following equation is applied in the coming sections:

$$D\mathcal{F}\{x_1[n] * x_2[n]\} = A_1(\psi) A_2(\psi). \quad (4)$$

A. Application of convolution on the array elements

We consider an array $A_1(\psi)$ with five identical elements positioned along z-axis with equal spacing d between them. The total electric field $\vec{E}_{T_1}$ is given as ($\vec{E}_0$ is the electric field of an individual element):

$$\vec{E}_{T_1} = \vec{E}_0 A_1(\psi), \quad (5)$$

where the array factor is given by:

$$A_1(\psi) = \sum_{n=-2}^{+2} x_1[n] e^{j\psi n}. \quad (6)$$

Let's take a step further by considering the array as one antenna and we repeat the arraying process (using the array factor $A_2(\psi)$) over the first array and we obtain the following results:

The total electric field would be $\vec{E}_{T_2} = \vec{E}_{T_1} A_2(\psi)$, where $A_2(\psi)$ is the array factor of the second array. Consequently the following result is obtained:

$$\vec{E}_{T_2} = A_1(\psi) A_2(\psi) \vec{E}_0. \quad (7)$$

The resulted array factor is $A_T(\psi) = A_1(\psi) A_2(\psi)$.

The resulted feeding currents are simply obtained by convolution between the currents of the first and the second arrays. This process may be seen as the shift of the first array along the second one as represented by Fig. 2 (for illustration the second array has three elements). The application of the shifting process produces superposition of some elements on each other as shown in Fig. 3.

The superposed elements in one given position are replaced by one element antenna. This element is fed by all the currents of the superposed antennas. When the first array is translated along the second array elements positions, the first array is scaled by the second array coefficients at its corresponding position as shown in Fig. 4.

The feeding current of the obtained array is:

$$x[n] = x_1[n] * x_2[n]. \quad (8)$$

The obtained array has a total number of elements and is given by following equation:

$$N_T = N_1 + N_2 - 1, \quad (9)$$

where $\boldsymbol{N_T}$, $\boldsymbol{N_1}$, **and** $\boldsymbol{N_2}$ are the number of elements of the resulted, the first and the second arrays respectively.

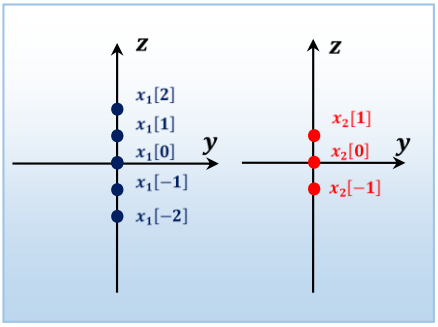

Fig. 2. The first array has five elements the second array has three elements.

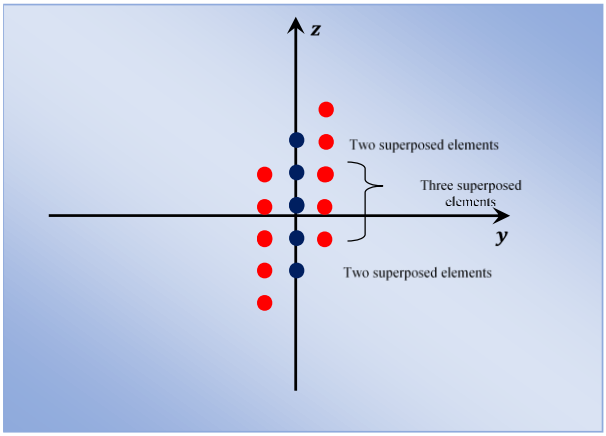

Fig. 3. Translating the first array along the positions of the second array's elements.

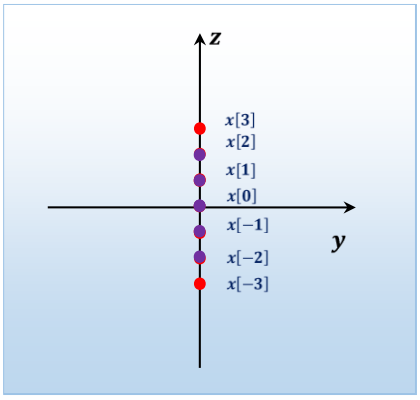

Fig. 4. There is superposed element when the translation is performed.

B. Arrays with different spacing

In this section, the hybridization is performed between two uniform arrays which have distinct spacing between their elements. For this case the multiplication of the array factors does not lead to the convolution of the feeding currents like the case of equidistance arrays. To overcome this problem, a mathematical trick is used and it is named, *distance conversion* [10].

When two array factors with different spacing ($d_1 \neq d_2$) are multiplied then,

$$A(\psi_1, \psi_2) = A_1(\psi_1)A_2(\psi_2), \tag{10}$$

where

$$\begin{cases} \psi_1 = kd_1 cos(\theta) \\ \psi_2 = kd_2 cos(\theta) \end{cases}, \tag{11}$$

where k is the wave number $k = \frac{2\pi}{\lambda}$ and λ is the signal wavelength.

The relation between ψ_1 and ψ_2 can be written as:

$$\frac{\psi_2}{\psi_1} = \frac{d_2}{d_1} = \frac{p}{q}, \tag{12}$$

where p and q are positive integers different from zero.

The new value of ψ and the new distance d can be defined as:

$$\psi = \frac{\psi_2}{p} = \frac{\psi_1}{q}, \tag{13}$$

$$d = \frac{d_2}{p} = \frac{d_1}{q}. \tag{14}$$

The feeding currents expression is obtained by performing the following analysis.

The array factor of the first array is given by:

$$A_1(\psi_1) = \sum_n x_1[n] e^{j\psi_1 n},$$

$$\Rightarrow A_1(\psi_1) = \sum_n x_1[n] e^{j\frac{\psi_1}{q}(qn)}.$$

By putting $m = qn$, where $\psi = \frac{\psi_1}{q}$ the following result is obtained:

$$A_1(\psi) = \sum_m x_1^{\frac{d_1}{q}}[m] e^{j\psi m}, \tag{15}$$

where

$$x_1^{\frac{d_1}{q}}[m] = \begin{cases} x_1\left[\frac{m}{q}\right]; & m = kq \\ 0 \quad ; & otherwise \end{cases}. \tag{16}$$

Similar result can be obtained for the case of the second array as:

$$x_2^{\frac{d_2}{p}}[m] = \begin{cases} x_2\left[\frac{m}{p}\right]; & m = kp \\ 0 \quad ; & otherwise \end{cases}, \tag{17}$$

where the notation $x_1^{\frac{d_1}{q}}[m]$ denote the distance conversion $d_1 \xrightarrow{converted} \frac{d_1}{q}$.

The equation (10) implies that $A(\psi_1, \psi_2) = A(\psi) = A_1(\psi)A_2(\psi)$:

where

$$\begin{cases} A_1(\psi) = \sum_n x_1^{\frac{d_1}{q}}[n] e^{j\psi n} \\ A_2(\psi) = \sum_n x_2^{\frac{d_2}{p}}[n] e^{j\psi n} \end{cases}. \tag{18}$$

The obtained array feeding currents will be the convolution between $x_1^{\frac{d_1}{q}}[n]$, and $x_2^{\frac{d_1}{p}}[n]$:

$$x^d[n] = x_1^{\frac{d_1}{q}}[n] * x_2^{\frac{d_2}{p}}[n]. \tag{19}$$

The distance conversion is explained in Fig. 5 by adopting some imaginary elements with feeding currents with amplitude of zero.

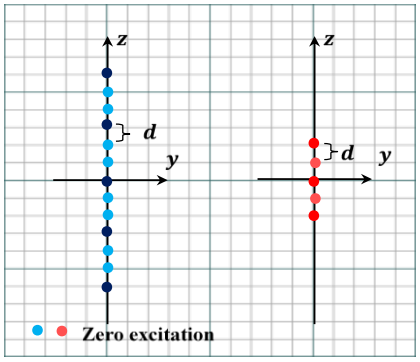

Fig. 5. Elements positions of the first and second arrays after distance conversion.

To apply the distance conversion, we propose the following definitions:

1) Elements with zero excitation are called "imaginary elements"; their number denoted by N_i.
2) Elements with non-zero excitation are called "real elements"; their number denoted by N.
3) The total number of elements is called "theoretical elements"; $N' = N_i + N$.

After applying the distance conversion, the theoretical number of elements is given by:

$$N' = q(N-1) + 1, \tag{20}$$

where $"q"$ is the distance conversion factor.

The convolution $x^d[n] = x_1^{\frac{d_1}{q}}[n] * x_2^{\frac{d_2}{p}}[n]$ can be represented graphically as shown in Fig. 6.

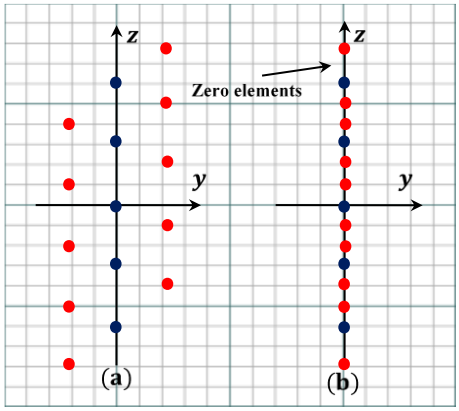

Fig. 6. (a) Translating the first array along the second array's positions. (b) The real elements of the obtained array.

C. Array with even number of elements

When the number of the elements in the array is even and the array is centered at the origin, the array elements are located at fractional numbers $(-\frac{3}{2}, -\frac{1}{2}, \frac{1}{2}, \frac{3}{2})$ and the notation $x[n]$ cannot be used because n is an integer. Consequently, the convolution cannot be applied between even array-even array elements, even array-odd array elements. To overcome this dilemma, the distance conversion can be performed $(d \xrightarrow{converted} \frac{d}{2})$. This conversion makes the notation $x[n]$ applicable and the convolution can be used.

Let's take $x[n]$, the relative feeding current with even number array elements. By applying the distance conversion, the theoretical number of the array elements will be odd as shown in Fig. 7. The expression of conversion is shown below:

$$x^{\frac{d}{2}}[n] = \begin{cases} x\left[\frac{n}{2}\right]; & n \text{ is odd} \\ 0\ ; & n \text{ is even} \end{cases}. \tag{21}$$

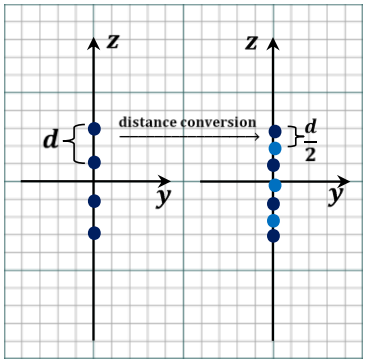

Fig. 7. The distance conversion is applied to array with even number of elements to obtain an array with odd number of elements.

III. APPLICATION OF THE HYBRIDIZATION CONCEPT

Now the theory of hybridization discussed in the forgoing sections is applied to two uniform arrays with specified criteria to obtain new arrays with improved parameters.

A. Array factor multiplication with different number of elements

The hybridization will be performed by multiplying two uniform arrays. Each array has its own number of elements (N_1 and N_2) where the two arrays have the same spacing distance. To design the hybridized array with desired specification the ratio, ${}^{N_1}/_{N_2}$ should be chosen as explained below:

$$A_T(\psi) = A_1(\psi)A_2(\psi),$$

where $A_1(\psi) = \frac{\sin\left(\frac{N_1}{2}\psi\right)}{N_1 \sin\left(\frac{\psi}{2}\right)}$, and $A_2(\psi) = \frac{\sin\left(\frac{N_2}{2}\psi\right)}{N_2 \sin\left(\frac{\psi}{2}\right)}$.

The total array factor is given by:

$$A_T(\psi) = \frac{\sin\left(\frac{N_1}{2}\psi\right)}{N_1 \sin\left(\frac{\psi}{2}\right)} \frac{\sin\left(\frac{N_2}{2}\psi\right)}{N_2 \sin\left(\frac{\psi}{2}\right)}. \tag{22}$$

To minimize side lobes, N_1 and N_2 should be chosen so that the zeros of the first array eliminate the side lobes maxima of the second array and vice-versa as illustrated by Fig. 8. To achieve this requirement, the following condition must be satisfied:

$$\frac{2\pi}{N_1} = \frac{3\pi}{N_2}. \tag{23}$$

The condition (23) will adjust the first zero of the first array over the first minor lobe maximum of the second array yielding a hybridized array with very low side lobes. From Equation (23), the following relation can be deduced:

$$2N_2 = 3N_1 = 6N. \tag{24}$$

This imply the following:

$$\begin{cases} N_1 = 2N \\ N_2 = 3N \end{cases}. \tag{25}$$

The total array factor of the obtained array can be written under the following relation:

$$A_T(\psi) = \frac{\sin(N\psi)\sin\left(\frac{3N}{2}\psi\right)}{6N^2 \sin^2\left(\frac{\psi}{2}\right)}. \tag{26}$$

The total number of elements in the hybridized array is found by using relation (9):

$$N_T = 5N - 1. \tag{27}$$

The side lobe will be minimized after the multiplication as shown in the Fig. 8.

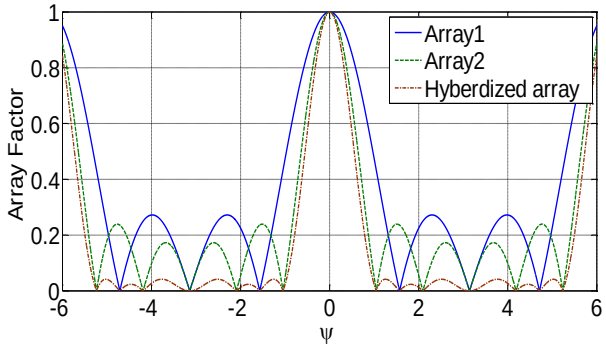

Fig. 8. Array factors in terms of ψ ($N = 2, N_T = 9$).

The hybridized array parameters are given below.

Side Lobe Level (SLL)

The first side lobe maxima position is located between the first and the second nulls. The minor lobe maxima position is approximated as $\psi_{SLM} \cong \frac{\psi_{null1}+\psi_{null2}}{2}$, where $\psi_{null1} = \frac{2\pi}{N_1} = \frac{\pi}{N}$, and $\psi_{null2} = \frac{2\pi}{N_2} = \frac{2\pi}{3N}$. The side lobe maxima position is $\psi_{SLM} \cong \frac{5\pi}{6N}$. The side lobe level of the hybridized array is given under the following expression:

$$|A_T(\psi_{SLM})| \cong \frac{\sqrt{2}}{24\, N^2 \sin^2\left(\frac{5\pi}{12N}\right)}. \tag{28}$$

Directivity

The directivity of the hybridized array can be evaluated in terms of the parameter $''N''$. The radiated power is evaluated by $P_{rad} = \oiint_{\Omega} |A_T(\psi)|^2 d\Omega$. By using Equation (26) we get the following:

$$P_{rad} = 2\pi \int_0^{\pi} \left| \frac{sin(N\psi)}{2N\, sin\left(\frac{\psi}{2}\right)} \frac{sin\left(\frac{3N}{2}\psi\right)}{3N\, sin\left(\frac{\psi}{2}\right)} \right|^2 \sin(\theta) d\theta. \quad (29)$$

In the absence of grating lobes in the visible region, we can use the approximation $\frac{sin\left(N\frac{3\psi}{2}\right)}{N\, sin\left(\frac{\psi}{2}\right)} \cong \frac{sin\left(N\frac{3\psi}{2}\right)}{N\frac{\psi}{2}}$, and letting $z = Nkd\, cos(\theta)$, the radiated power is written in the following form:

$$P_{rad} = \frac{2\pi^2}{Nkd} \int_{-Nkd}^{Nkd} \left(\frac{sin(z)}{z}\right)^2 \left(\frac{sin\left(\frac{3}{2}z\right)}{\frac{3}{2}z}\right)^2 dz. \quad (30)$$

This integral can be performed by using the properties of convolution and Fourier transform and the directivity expression is obtained as:

$$D = \frac{27\, Nkd}{7\, \pi}. \quad (31)$$

When the relation (27) is used, the directivity is written in terms of the total number of element in the array, N_T as:

$$D = \frac{27\, (N_T+1)kd}{35\, \pi}. \quad (32)$$

Feeding Currents

To implement this antenna array, the feeding current in each antenna must be determined. The hybridized array factor is found under the relation $A_T(\psi) = A_1(\psi)A_2(\psi)$, where

$$\begin{cases} A_1(\psi) = \frac{sin\left(\frac{N_1}{2}\psi\right)}{N_1\, sin\left(\frac{\psi}{2}\right)} \;;\; N_1 = 2N \\ A_2(\psi) = \frac{sin\left(\frac{N_2}{2}\psi\right)}{N_2\, sin\left(\frac{\psi}{2}\right)} \;;\; N_2 = 3N \end{cases}$$

, since the first array has always an even number of elements, the position of the array elements will be located at fractional numbers. The notation $x_1[n]$ cannot be used because n must be integer. In this case the distance conversion will be applied.

$$d \longrightarrow d' = \frac{d}{2} \;\Leftrightarrow\; \psi \longrightarrow \psi' = \frac{\psi}{2}.$$

The conversion is performed by adding zero imaginary elements between the real elements.

Theoretically, the total number of elements will be, for the first array:

$$N_1' = N_1 + N_{i_1} = N_1 + (N_1 - 1) = 4N - 1;$$

for the second array:

$$N_2' = N_2 + N_{i_2} = N_2 + (N_2 - 1) = 6N - 1.$$

By applying the distance conversion the feeding current will have the following form.

When N is even:

$$x_1^{\frac{d}{2}}[n] = \begin{cases} \begin{cases} \frac{1}{2N} \;;\; n\ odd \\ 0 \;;\; n\ even \end{cases} ; -(2N-1) \le n \le (2N-1) \\ 0 \quad ; \quad otherwise \end{cases}, \quad (33)$$

$$x_2^{\frac{d}{2}}[n] = \begin{cases} \begin{cases} \frac{1}{3N} \;;\; n\ odd \\ 0 \;;\; n\ even \end{cases} ; -(3N-1) \le n \le (3N-1) \\ 0 \quad ; \quad otherwise \end{cases}. \quad (34)$$

The feeding current can be represented in its matrix form:

$$x_1^{\frac{d}{2}}[n] = \frac{1}{2N} \overbrace{\left[1\,0\,1\,0\,1 \ldots \underbrace{0}_{-2,} \underbrace{1}_{-1,} \underbrace{0}_{n=0,} \underbrace{1}_{1,} \underbrace{0}_{2} \ldots 1\,0\,1\,0\,1 \right]}^{4N-1},$$

$$x_2^{\frac{d}{2}}[n] = \frac{1}{3N} \overbrace{\left[1\,0\,1\,0\,1 \ldots \underbrace{0}_{-2,} \underbrace{1}_{-1,} \underbrace{0}_{n=0,} \underbrace{1}_{1,} \underbrace{0}_{2} \ldots 1\,0\,1\,0\,1 \right]}^{6N-1}.$$

When N is odd:

$$x_1^{\frac{d}{2}}[n] = \begin{cases} \begin{cases} \frac{1}{2N} \;;\; n\ odd \\ 0 \;;\; n\ even \end{cases} ; -(2N-1) \le n \le (2N-1) \\ 0 \quad ; \quad otherwise \end{cases}, \quad (35)$$

$$x_2^{\frac{d}{2}}[n] = \begin{cases} \begin{cases} \frac{1}{3N} \;;\; n\ even \\ 0 \;;\; n\ odd \end{cases} ; -(3N-1) \le n \le (3N-1) \\ 0 \quad ; \quad otherwise \end{cases}. \quad (36)$$

The feeding current can be represented in its matrix form:

$$x_1^{\frac{d}{2}}[n] = \frac{1}{2N} \overbrace{\left[1\,0\,1\,0\,1 \ldots \underbrace{0}_{-2,} \underbrace{1}_{-1,} \underbrace{0}_{n=0,} \underbrace{1}_{1,} \underbrace{0}_{2} \ldots 1\,0\,1\,0\,1 \right]}^{4N-1},$$

$$x_2^{\frac{d}{2}}[n] = \frac{1}{3N} \overbrace{\left[1\,0\,1\,0\,1 \ldots \underbrace{1}_{-2,} \underbrace{0}_{-1,} \underbrace{1}_{n=0,} \underbrace{0}_{1,} \underbrace{1}_{2} \ldots 1\,0\,1\,0\,1 \right]}^{6N-1}.$$

The feeding currents of the hybridized array is determined by performing the convolution:

$$x_T^{\frac{d}{2}}[n] = x_1^{\frac{d}{2}}[n] * x_2^{\frac{d}{2}}[n]. \quad (37)$$

By evaluating the convolution (37), the following results are obtained.

When N is even:

$$x_T^{\frac{d}{2}}[n] = \frac{(-1)^n + 1}{2} \begin{cases} -\frac{1}{12N^2}(|n| - 5N) \;;\; N \le |n| \le 5N-2 \\ \frac{1}{3N} \quad ; \quad |n| \le N \\ 0 \quad ; \quad otherwise \end{cases}, \quad (38)$$

When N is odd

$$x_T^{\frac{d}{2}}[n] = \frac{(-1)^{n+1}+1}{2}\begin{cases} -\frac{1}{12N^2}(|n|-5N)\,; N \le |n| \le 5N-2 \\ \frac{1}{3N} \quad ; \quad |n| \le N \\ 0 \quad ; \quad otherwise \end{cases}, \quad (39)$$

where $N = \frac{N_T+1}{5}$, N_T is the total number of the array. Note that for N is even $a_n = x_T^d[n] = x_T^{\frac{d}{2}}[2n]$, for $n \ge 0$, when N is odd $a_n = x_T^d[n] = x_T^{\frac{d}{2}}[2n-1]$, for $n \ge 1$.

The proposed array is named as **UUDNH,** which is the abbreviation of "**Uniform with Uniform Different-N Hybridization**".

For illustration, the feeding currents of Equations (38) and (39) are drawn for N = 4 and 5 in Fig. 9 and the corresponding array factors are illustrated in Fig. 10. To avoid the appearance of the grating lobes in the visible region of $(-kd \le \psi \le kd)$, the following condition should be satisfied:

$$kd \le 2\pi - \psi_{first\ null}. \quad (40)$$

For the proposed array case, the first null is situated at $\psi_{first\ null} = \frac{2\pi}{3N}$, and this condition becomes $kd \le 2\pi\frac{3N-1}{3N}$.

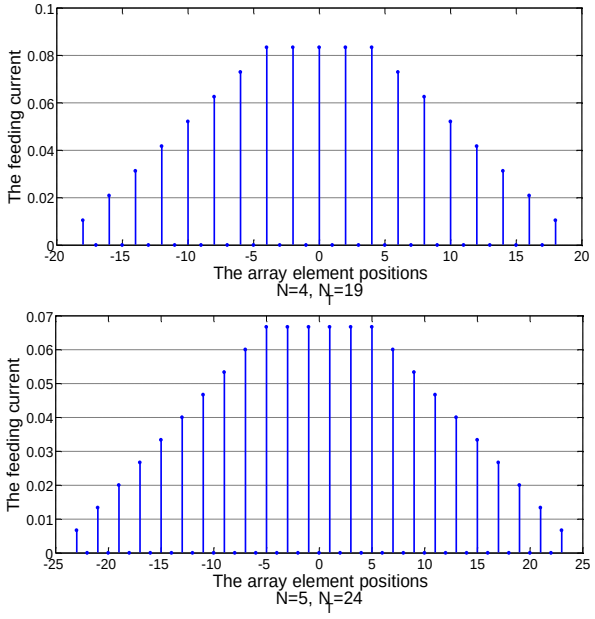

Fig. 9. Excitation coefficients of the hybridized array for N = 4 and 5.

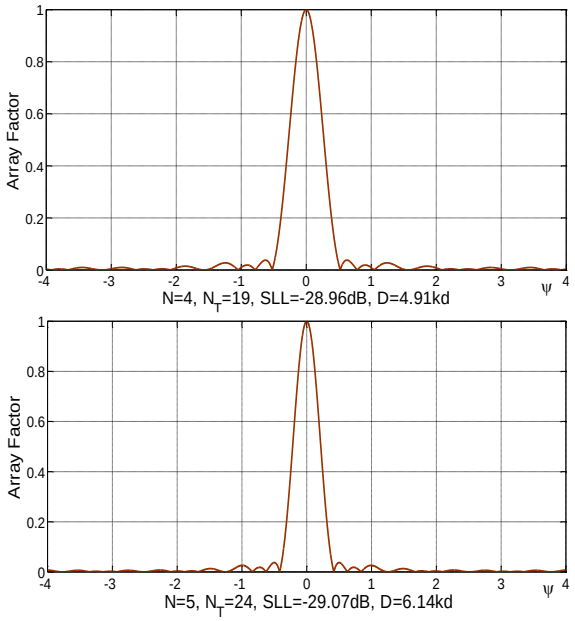

Fig. 10. Array pattern of the hybridized array (UUDNH) in terms of ψ for N = 4 and 5, where the directivities is given in terms of the wave number k and the distance between the elements d.

B. Array factor multiplication with different spacing

Previously, the hybridization between two uniform arrays with different number of elements is performed. Here, the hybridization between two uniform arrays with different spacing is proposed. To do this, a condition on the ratio of the two spacing is set as illustrated in coming sections. Similarly, the new array factor is simply given as:

$$A(\psi_1, \psi_2) = A_1(\psi_1)A_2(\psi_2),$$

where $\psi_1 = kd_1\cos(\theta), \psi_2 = kd_2\cos(\theta)$, and by letting $s = kcos(\theta)$,

then $$A_T(s) = A_1(sd_1)A_2(sd_2). \quad (41)$$

Therefore, the array factor is given by:

$$A_T(s) = \frac{sin\left(N\frac{sd_1}{2}\right)}{N\,sin\left(\frac{sd_1}{2}\right)} \times \frac{sin\left(N\frac{sd_2}{2}\right)}{N\,sin\left(\frac{sd_2}{2}\right)}. \quad (42)$$

To minimize side lobes, d_1 and d_2 should be chosen so that the zeros of the first array eliminate the side lobes maxima of the second array. To achieve this, $\frac{3\pi}{Nd_1} = \frac{2\pi}{Nd_2}$, is required. By satisfying this condition and applying the multiplication, the graph in Fig. 11 is obtained.

The condition $\frac{3\pi}{Nd_1} = \frac{2\pi}{Nd_2}$ implies that:

$$d = \frac{d_1}{3} = \frac{d_2}{2}. \quad (43)$$

By replacing it in relation (42) and $\psi = kdcos(\theta) = sd$ then,

$$A_T(\psi) = \frac{sin\left(3N\frac{\psi}{2}\right)}{N^2\, sin\left(\frac{3\psi}{2}\right)} \times \frac{sin(N\psi)}{sin(\psi)}. \quad (44)$$

Using the condition of Equation (20), the theoretical elements have a total number:

$$N_T{}' = (3(N-1)+1) + (2(N-1)+1) - 1,$$
$$\Rightarrow N_T{}' = 5N - 4.$$

Since there is two elements with zero feeding exactly as shown in Fig. 6, the actual number of elements in the array is $N_T = N_T{}' - 2$, so that,

$$N_T = 5N - 6. \quad (45)$$

For $N = 5$, the array pattern is given in Fig. 12. The visible region must be chosen to avoid the appearance of the side lobes with the highest level. This attained when $\leq \frac{2\pi}{3} - \frac{2\pi}{3N}$; where $\frac{2\pi}{3}$ is the period of the function $\frac{sin\left(3N\frac{\psi}{2}\right)}{N\, sin\left(\frac{3\psi}{2}\right)}$ and $\frac{2\pi}{3N}$ is its first zero.

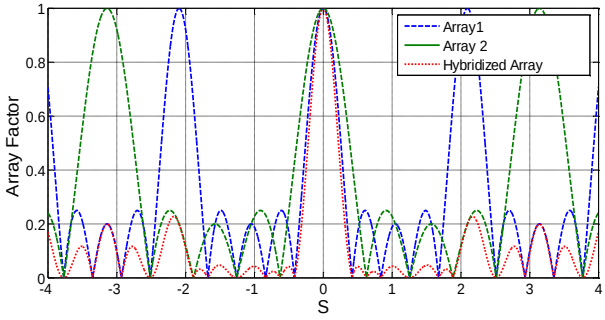

Fig. 11. Array factors and the hybridized array in terms of "s".

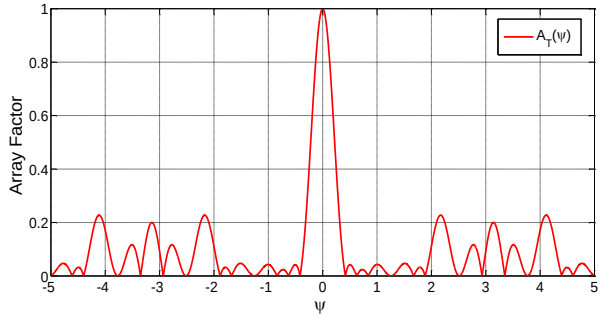

Fig. 12. Array factors in terms of "ψ" for N = 5.

The hybridized array parameters are given below.

Side Lobe Level (SLL)

The side lobe maxima position is given by $\psi_{SLM} \cong \frac{\psi_{null1} + \psi_{null2}}{2}$ yielding:

$$\psi_{SLM} \cong \frac{5\pi}{6N}. \quad (46)$$

Consequently, the side lobe level is given by the following expression:

$$|A_T(\psi_{SLM})| \cong \frac{\sqrt{2}}{4N^2\left|\sin\left(\frac{5\pi}{4N}\right)\sin\left(\frac{5\pi}{6N}\right)\right|}. \quad (47)$$

Directivity

The radiated power is given as:

$$P_{rad} = 2\pi \int_0^{\pi} \left|\frac{sin\left(3N\frac{\psi}{2}\right)}{N^2\, sin\left(\frac{3\psi}{2}\right)} \frac{sin(N\psi)}{sin(\psi)}\right|^2 \sin(\theta)\, d\theta. \quad (48)$$

Then the directivity is given under the following expression:

$$D = \frac{27\, Nkd}{7\,\pi}. \quad (49)$$

Since $N = \frac{N_T+6}{5}$, the directivity is expressed in terms of the total number of the elements in the array as:

$$D = \frac{27\,(N_T+6)kd}{35\,\pi}. \quad (50)$$

Feeding Currents

Since the proposed array factor is multiplication of $A_1(\psi) = \frac{sin\left(3N\frac{\psi}{2}\right)}{N\, sin\left(\frac{3\psi}{2}\right)}$, and $A_2(\psi) = \frac{sin(N\psi)}{N\, sin(\psi)}$, and using $d = \frac{d_1}{3} = \frac{d_2}{2}$, the feeding currents may be expressed, for N is odd, as:

$$x_T^d[n] = x_1^{\frac{d_1}{3}}[n] * x_2^{\frac{d_2}{2}}[n], \quad (51)$$

where

$$x_1^{\frac{d_1}{3}}[n] = \mathcal{F}^{-1}\{A_1(\psi)\}$$
$$= \begin{cases} \begin{cases} \frac{1}{N} & ;\ n = 3p \\ 0 & ;\ n \neq 3p \end{cases} & ; -\frac{3}{2}(N-1) \leq n \leq \frac{3}{2}(N-1) \\ 0 & ;\ otherwise \end{cases}, \quad (52)$$

$$\mathcal{F}^{-1}\{A_2(\psi)\} = x_2^{\frac{d_2}{2}}[n]$$
$$= \begin{cases} \begin{cases} \frac{1}{N} & ;\ n = 2p \\ 0 & ;\ n \neq 2p \end{cases} & ; -(N-1) \leq n \leq (N-1) \\ 0 & ;\ otherwise \end{cases}, \quad (53)$$

$x_1^{\frac{d_1}{3}}[n]$ and $x_2^{\frac{d_2}{2}}[n]$ can be represented in their matrix form as shown below:

$$x_1^{\frac{d_1}{3}}[n] = \frac{1}{N}\Big[\overbrace{1\,0\,0\,1\,0\,0\,1 \ldots \underbrace{1}_{-3}\ \underbrace{0}_{-2}\ \underbrace{0}_{-1}\ \underbrace{1}_{n=0}\ \underbrace{0}_{1}\ \underbrace{0}_{2}\ \underbrace{1}_{3} \ldots 1\,0\,0\,1\,0\,0\,1}^{3(N-1)+1}\Big],$$

$$x_2^{\frac{d_2}{2}}[n] = \frac{1}{N}\Big[\overbrace{1\,0\,1\,0\,1 \ldots \underbrace{1}_{-2}\ \underbrace{0}_{-1}\ \underbrace{1}_{n=0}\ \underbrace{0}_{1}\ \underbrace{1}_{2} \ldots 1\,0\,1\,0\,1}^{2(N-1)+1}\Big].$$

For the case of N even, the distance conversion must be applied leading to the following results (with the number of ones in each matrix remain equal to N):

$$x_1^{\frac{d_1}{6}}[n] = \frac{1}{N}\Big[\overbrace{1\,0\,0\,0\,0\,0\,1\,\ldots\underbrace{1}_{-3}\,\underbrace{0}_{-2}\,\underbrace{0}_{-1}\,\underbrace{0}_{n=0}\,\underbrace{0}_{1}\,\underbrace{0}_{2}\,\underbrace{1}_{3}\ldots 1\,0\,0\,0\,0\,0\,1}^{6(N-1)+1}\Big],$$

$$x_2^{\frac{d_2}{4}}[n] = \frac{1}{N}\Big[\overbrace{1\,0\,0\,0\,1\,\ldots\underbrace{1}_{-2}\,\underbrace{0}_{-1}\,\underbrace{0}_{n=0}\,\underbrace{0}_{1}\,\underbrace{1}_{2}\ldots 1\,0\,0\,0\,1}^{4(N-1)+1}\Big].$$

Consequently, the feeding currents for that case are given as:

$$x_T^{\frac{d}{2}}[n] = x_1^{\frac{d_1}{6}}[n] * x_2^{\frac{d_2}{4}}[n]. \tag{54}$$

The resulted array may be named as **UUDdH**, which is the abbreviation of "**Uniform with Uniform Different-d Hybridization**". Evaluation of these equations reveals that the excitation coefficients of the proposed array are distributed simply in a countable number of discrete levels. This number is found to be M whose values is given by:

$$M = \left\lceil \frac{N}{3} \right\rceil, \tag{55}$$

where $\left\lceil \frac{N}{3} \right\rceil$ denotes the ceiling function and it is defined as:

$$\lceil x \rceil = n \quad if \quad n-1 < x \le n. \tag{56}$$

The levels of the coefficients are given by:

$$\frac{L}{N^2} \quad ; \quad L \in \{1\,,2\,,3\,,\ldots M\}, \tag{57}$$

where L denotes the level state.

Now, the values of excitation coefficients of the proposed array are determined analytically as:

$$w = \frac{5N+7}{2} - 6\left\lceil \frac{N}{3} \right\rceil.$$

When N is odd:

$$x_T^{d}[n] = \begin{cases} f[n] \quad ; \quad |n| \le w \\ \frac{\lceil \frac{N}{3} \rceil - 1}{N^2} - \frac{1}{N^2}\delta[|n| - (w+5)] \;\; ; \; |n| \epsilon\, I_1 \\ \frac{\lceil \frac{N}{3} \rceil - 2}{N^2} - \frac{1}{N^2}\delta[|n| - (w+11)] \;\; ; \; |n| \epsilon\, I_2 \\ \vdots \\ \frac{\lceil \frac{N}{3} \rceil - m}{N^2} - \frac{1}{N^2}\delta[|n| - (w+6m-1)] \;\; ; \; |n| \epsilon\, I_m \\ \vdots \\ \frac{1}{N^2} - \frac{1}{N^2}\delta[|n| - (w+6(M-1)-1)] \;\; ; \; |n| \epsilon I_{M-1} \end{cases}, \tag{58}$$

where $I_m = [w+6m-5\,;w+6m]$, and

$$f[n] = \begin{cases} \frac{\lceil \frac{N}{3} \rceil}{N^2} - \frac{1}{N^2}\delta[|n| - (w-1)] \quad ; \quad N = 3P \\ \frac{1}{N^2}\left(1 - \frac{2}{\sqrt{3}}\left|sin\left(\frac{2\pi}{3}n\right)\right|\right) + \frac{\lceil \frac{N}{3} \rceil - 1}{N^2} \; ; \; N = 3P+1 \\ \frac{1}{N^2}\left|\frac{2}{\sqrt{3}} sin\left(\frac{2\pi}{3}n\right)\right| + \frac{\lceil \frac{N}{3} \rceil - 1}{N^2} \quad ; \quad N = 3P+2 \end{cases}.$$

When N is even:

$$x_T^{\frac{d}{2}}[n] = \frac{1-(-1)^n}{2}\begin{cases} g[n] \quad ; \quad |n| \le 2w \\ \frac{\lceil \frac{N}{3} \rceil - 1}{N^2} - \frac{1}{N^2}\delta[|n| - (2w+10)] \;\; ; |n| \epsilon\, I_1 \\ \frac{\lceil \frac{N}{3} \rceil - 2}{N^2} - \frac{1}{N^2}\delta[|n| - (2w+22)] \;\; ; \; |n| \epsilon I_2 \\ \vdots \\ \frac{\lceil \frac{N}{3} \rceil - m}{N^2} - \frac{1}{N^2}\delta[|n| - (2w+12m-2)] \;\; ; \; |n| \epsilon I_m \\ \vdots \\ \frac{1}{N^2} - \frac{1}{N^2}\delta[|n| - (2w+12(M-1)-2)] \;\; ; |n| \epsilon I_{M-1} \end{cases}, \tag{59}$$

where $I_m = [2w+12m-11\,;2w+12m]$, and

$$g[n] = \begin{cases} \frac{\lceil \frac{N}{3} \rceil}{N^2} - \frac{1}{N^2}\delta[|n| - (2w-2)] \quad ; \quad N = 3P \\ \frac{1}{N^2}\left(1 - \frac{2}{\sqrt{3}}\left|sin\left(\frac{2\pi}{3} \times \frac{|n|+3}{2}\right)\right|\right) + \frac{\lceil \frac{N}{3} \rceil - 1}{N^2} \; ; \; N = 3P+1, \\ \frac{1}{N^2}\left|\frac{2}{\sqrt{3}} sin\left(\frac{2\pi}{3} \times \frac{|n|+3}{2}\right)\right| + \frac{\lceil \frac{N}{3} \rceil - 1}{N^2} \quad ; \; N = 3P+2 \end{cases} \tag{60}$$

P is positive integer and $\delta[n]$ is the discrete Dirac delta function. For illustration, the feeding currents of Equations (58) and (59) are drawn for $N = 4$ and 5 in Fig. 13 with their corresponding array factors in Fig. 14. The visible region is taken for $\left(kd = \frac{2\pi(N-1)}{3N} \Leftrightarrow d = \frac{\lambda}{3}\frac{N-1}{N}\right)$, which is the maximum value of d so that there is no high side lobes in the visible region.

IV. RESULTS AND DISCUSSION

To see the evidence of the proposed arrays, a comparison with Tschebyscheff array is carried out in this section. In this comparison, the chosen total number of elements in each array is $N_T = 19$. The obtained feeding coefficients distributions for the both proposed arrays are shown in Fig. 13 (for UUDNH case) and Fig. 9 (for UUDdH case). These coefficients in addition to their calculation, which is easy, they are not highly varying; this makes the realization in the electronic circuit generating these amplitudes simple and inexpensive and economical.

The obtained array factors are also drawn in Fig. 15 together with the Tschebyscheff array factor with $SLL = -28\ dB$. The figure shows clearly that the proposed array obtained from hybridization between two uniform arrays with different spacing has performances exceeding that of Tschebyscheff array with simplicity in realization.

For deeper comparison using numerical values, in addition to the two proposed arrays, two Tschebyscheff arrays are considered. The first Tschebyscheff array with side lobe level of $-27\ dB$, whereas the second one with $-28\ dB$. The obtained numerical results are summarized in the Table 1 below. Form this table, it is clear that the proposed UUDdH has highest directivity with side lobe

level comparable to Tschebyscheff. Furthermore, the very interesting result is that the excitation coefficients of UUDdH are constructed from only few levels as shown in Fig. 13; and in case of 19 elements, there are only two levels (0.0400 and 0.0800) as shown in the table and the Fig. 13. This result gives us the opportunity to implement the feeding circuit of the array using simply a digital circuit.

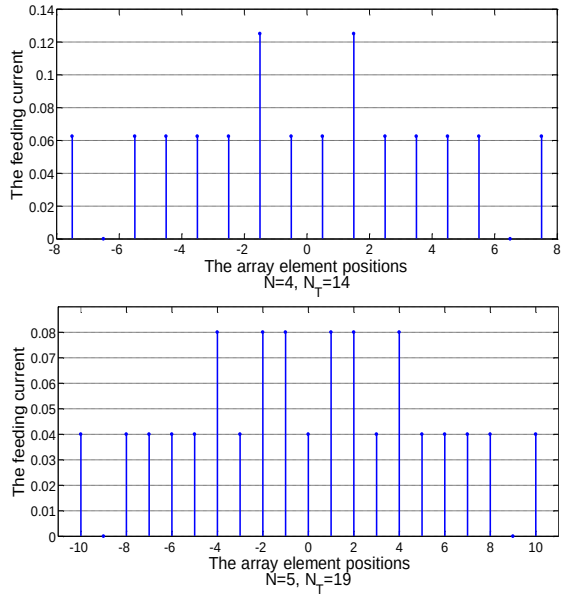

Fig. 13. Excitation coefficients of the hybridized array for N = 4 and 5.

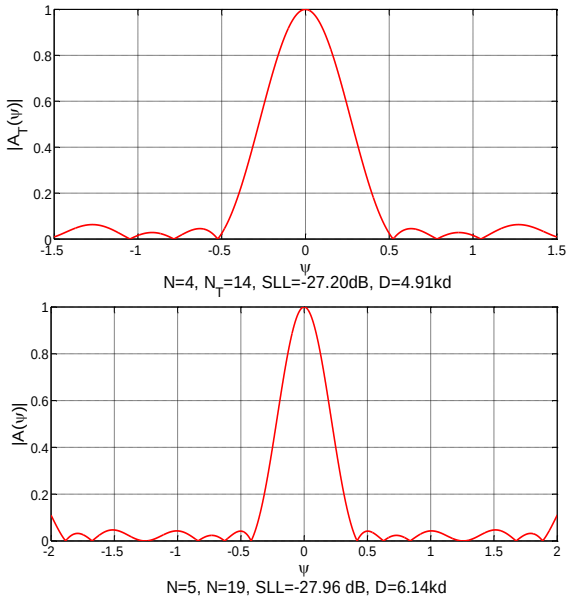

Fig. 14. Array pattern of the hybridized array (UUDdH) in terms of ψ for N = 4 and 5 where the directivities is given in terms of the wave number k and the distance between the elements d.

Table 1: Excitation coefficients, side lobe levels and directivity of the proposed arrays and two Tschebyscheff arrays with 19 elements in each (note that $x^d[9] = 0$ is not counted as an elements because it has zero feeding)

Tschebyscheff Array 1		Tschebyscheff Array 2
$N_T = 19$		$N_T = 19$
$x^d[0] = 0.0777$		$x^d[0] = 0.0763$
$x^d[1] = 0.0765$		$x^d[1] = 0.0752$
$x^d[2] = 0.0730$		$x^d[2] = 0.0719$
$x^d[3] = 0.0675$		$x^d[3] = 0.0666$
$x^d[4] = 0.0602$		$x^d[4] = 0.0598$
$x^d[5] = 0.0518$		$x^d[5] = 0.0518$
$x^d[6] = 0.0428$		$x^d[6] = 0.0431$
$x^d[7] = 0.0337$		$x^d[7] = 0.0343$
$x^d[8] = 0.0251$		$x^d[8] = 0.0259$
$x^d[9] = 0.0304$		$x^d[9] = 0.0333$
SLL $= -28$ dB		$SLL = -27\ dB$
$\boldsymbol{d = \frac{\lambda}{4}}$	$D = 8.50$	$D = 8.62$
$\boldsymbol{d = \frac{\lambda}{3}}$	$D = 11.31$	$D = 11.47$
$\boldsymbol{d = \frac{\lambda}{2}}$	$D = 16.89$	$D = 17.10$
Our Array 1 UUDNH		Our Array 2 UUDdH
$N_T = 19$		$N_T = 19$
$x^d[0] = 0.0833$		$x^d[0] = 0.0400$
$x^d[1] = 0.0833$		$x^d[1] = 0.0800$
$x^d[2] = 0.0833$		$x^d[2] = 0.0800$
$x^d[3] = 0.0729$		$x^d[3] = 0.0400$
$x^d[4] = 0.0625$		$x^d[4] = 0.0800$
$x^d[5] = 0.0521$		$x^d[5] = 0.0400$
$x^d[6] = 0.0417$		$x^d[6] = 0.0400$
$x^d[7] = 0.0313$		$x^d[7] = 0.0400$
$x^d[8] = 0.0208$		$x^d[8] = 0.0400$
$x^d[9] = 0.0104$		$x^d[9] = 0.0000$
		$x^d[10] = 0.0400$
$\boldsymbol{SLL = -28.96\ dB}$		$\boldsymbol{SLL = -27.96\ dB}$
$\boldsymbol{d = \frac{\lambda}{4}}$	$\boldsymbol{D = 7.68}$	$\boldsymbol{D = 9.45}$
$\boldsymbol{d = \frac{\lambda}{3}}$	$\boldsymbol{D = 10.24}$	$\boldsymbol{D = 12.37}$
$\boldsymbol{d = \frac{\lambda}{2}}$	$\boldsymbol{D = 15.36}$	$\boldsymbol{D = 16.90}$

For the case of the proposed UUDNH array, the table indicates the very low level of the side lobes compared to other arrays with relatively acceptable directivity. The importance of this array resides in the very simple expressions of the excitation coefficients that simple at the same time the calculations of these coefficients and their practical implementation.

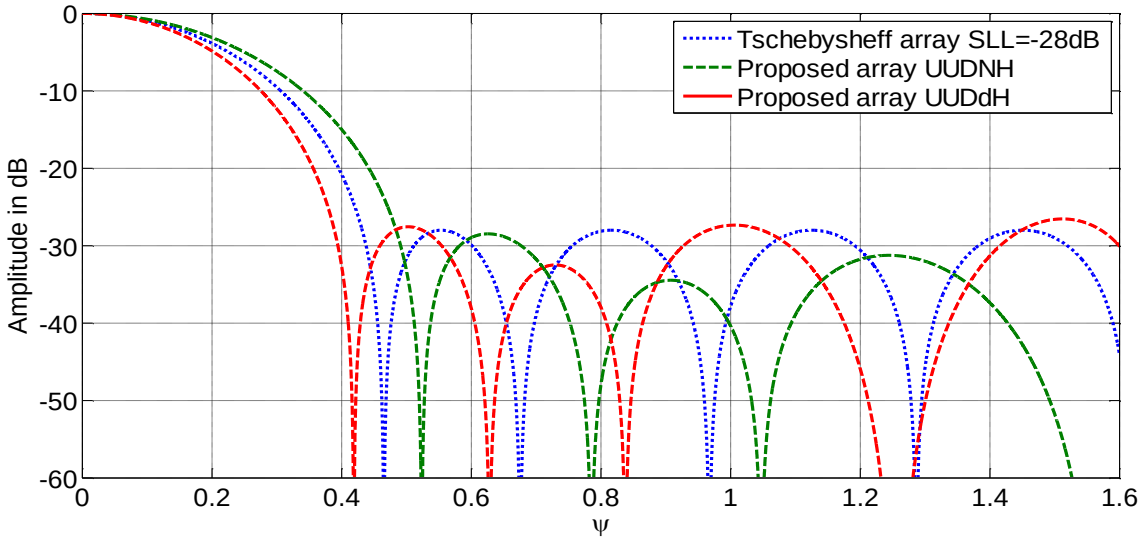

Fig. 15. Comparison between Tschebyscheff array ($SLL = -28\ dB$) and the proposed arrays for 19 elements each.

V. CONCLUSION

In this work a concept of array hybridization (mixing two distinct arrays) is presented and applied to uniform arrays to generate a new array that presents good compromise between its directivity and the level of the secondary lobes. The choice uniform array is dictated by its high directivity; and also restricting the generation problem to only reduction of the side lobes levels. As compared to the existing techniques for solving such problem which are based on optimization approaches, the proposed ones are solely based on mathematical procedures using known analytical expressions which are presented in details.

The hybridization is applied twice on two uniform arrays. At the beginning the two hybridized arrays are chosen to have different number of elements (UUDNH). The resulted array has good compromise between the directivity and its side lobe level as required. In addition to this the excitation coefficients are not highly varying. The second generated array is based on the use of two uniform arrays with different spacing between their elements (UUDdH). The obtained array satisfies also the requirements. Furthermore, the excitation coefficients are distribution in very few levels.

The obtained arrays are compared with Tschebyscheff arrays having the same number of elements. The UUDNH generated array has comparable performances with respect to Tschebyscheff array whereas, the second, UUDdH arrays has better performances. In addition to this, the excitation coefficients of the generated arrays are not highly varying as compared to Tschebyscheff ones and this simplifies their realization.

It should also be noted that all the arrays parameters (array factor, side lobe levels, directivity and excitation coefficients) are expressed in very elegant closed form expressions leading to easy use of the proposed arrays.

REFERENCES

[1] C. A. Balanis, *Antenna Theory: Analysis and Design*. John Wiley & Sons, 2016.

[2] S. J. Orfanidis, *Electromagnetic Waves and Antennas*. New Brunswick, NJ: Rutgers University, 2002.

[3] A. Azrar, A. Chemsa, and R. Aksas, "Novel analysis and design approaches of the planar antenna arrays," *Annals of Telecommunication*, vol. 62, no. 9-10, pp. 1053-1078, Oct. 2007.

[4] G. Bipul and D. Mandal, "Nulls and side lobe levels control in a time modulated linear antenna array by optimizing excitations and element locations using RGA," *Journal of Microwaves, Optoelectronics and Electromagnetic Applications*, vol. 12, no. 2, pp. 238-255, Dec. 2013.

[5] A. Recioui and A. Azrar, "Use of genetic algorithms in linear and planar antenna array synthesis based on Schelkunoff method," *Microwave and Optical Technology Letters*, vol. 49, no. 7,pp. 1619-1623, May 2007.

[6] C. Liu and H. Wu, "Synthesis of thinned array with side lobe levels reduction using improved binary invasive weed optimization," *Progress In Electromagnetics Research M*, vol. 37, pp. 21-30, June 2014.

[7] V. Shreni and P. Raikwar, "Optimization of reduction in side lobe level using genetic algorithm," *International Journal of Emerging Technology and Advanced Engineering*, vol. 2, no 12, Dec. 2012.

[8] M. M. Khodier and C. G. Christodoulou, "Linear array geometry synthesis with minimum side lobe

level and null control using particle swarm optimization," *IEEE Trans. Antennas Propag*., vol. 53, pp. 2674-2679, Aug. 2005.

[9] D. W. Boeringer and D. H. Werner, "Particle swarm optimization versus genetic algorithms for phased array synthesis," *Antennas and Propagation, IEEE Transactions on*, vol. 52, no. 3, pp. 771-779, Mar. 2004.

[10] Alan V. Oppenheim A. S. Willsky, and S. H. Nawab, *Signals and Systems*. Pearson, 2014.

Oussama Gassab was born on February 14, 1990, in Djelfa, Algeria. He received his B.Sc. in Electrical and Electronic Engineering from the National Institute IGEE, Boumerdes, Algeria in 2013 and M.Sc. degree in Telecommunications from the same institute in 2015. His main fields of interest are Microwave, Antennas, Radio waves, Information theory. He is also interested in the fields of Mathematics and Modern physics.

Arab Azrar was born in Takerboust, Bouira, Algeria, on August 2, 1971. He received the B.S. degree in Electrical and Electronic Engineering form National Institute of Electricity and Electronics of Boumerdes Algeria in 1995 and the MS and Doctorate degrees from National Polytechnic School of El-Harrach, Algeria respectively in 1998 and 2004. Currently, he is a Senior Professor in the Institute of Electrical and Electronic Engineering of Boumerdes University and his fields of interest include Antennas, Wave Propagation, and Microwaves.